UNIVERSITETET I AGDER

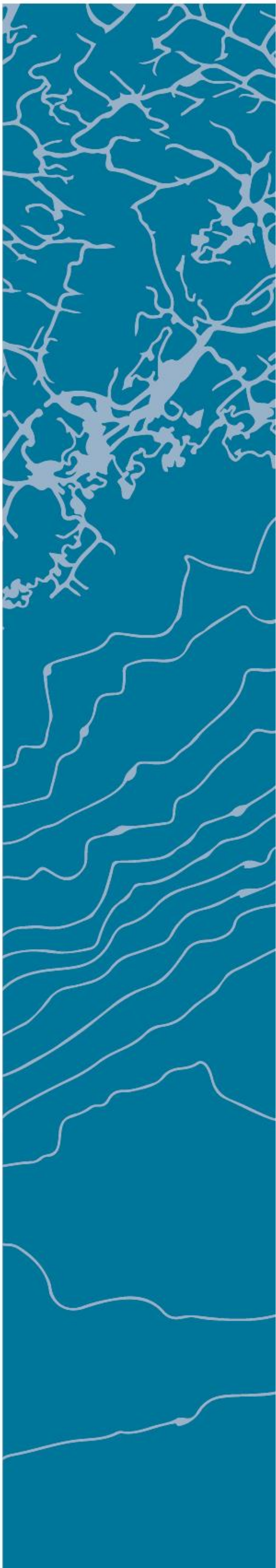

Experimental and finite element analysis of the shear behaviour of UHPC beams

HAIDAR HOSAMO

PEROOZ SARWARI

SUPERVISORS

Katalin Vertes

Ingrid Lande Laresen

University of Agder, [2019]

Faculty of engineering and science

Obligatorisk egenerklæring/gruppeerklæring

Den enkelte student er selv ansvarlig for å sette seg inn i hva som er lovlige hjelpemidler, retningslinjer for bruk av disse og regler om kildebruk. Erklæringen skal bevisstgjøre studentene på deres ansvar og hvilke konsekvenser fusk kan medføre. Manglende erklæring fritar ikke studentene fra sitt ansvar.

1.	Jeg/vi erklærer herved at min/vår besvarelse er mitt/vårt eget arbeid, og at jeg/vi ikke har brukt andre kilder eller har mottatt annen hjelp enn det som er nevnt i besvarelsen.	☒
2.	Jeg/vi erklærer videre at denne besvarelsen: - ikke har vært brukt til annen eksamen ved annen avdeling/universitet/høgskole innenlands eller utenlands. - ikke refererer til andres arbeid uten at det er oppgitt. - ikke refererer til eget tidligere arbeid uten at det er oppgitt. - har alle referansene oppgitt i litteraturlisten. - ikke er en kopi, duplikat eller avskrift av andres arbeid eller besvarelse.	☒
3.	Jeg/vi er kjent med at brudd på ovennevnte er å betrakte som fusk og kan medføre annullering av eksamen og utestengelse fra universiteter og høgskoler i Norge, jf. Universitets- og høgskoleloven §§4-7 og 4-8 og Forskrift om eksamen §§ 31.	☒
4.	Jeg/vi er kjent med at alle innleverte oppgaver kan bli plagiatkontrollert.	☒
5.	Jeg/vi er kjent med at Universitetet i Agder vil behandle alle saker hvor det forligger mistanke om fusk etter høgskolens retningslinjer for behandling av saker om fusk.	☒
6.	Jeg/vi har satt oss inn i regler og retningslinjer i bruk av kilder og referanser på biblioteket sine nettsider.	☒

Publiseringsavtale

Fullmakt til elektronisk publisering av oppgaven

Forfatter(ne) har opphavsrett til oppgaven. Det betyr blant annet enerett til å gjøre verket tilgjengelig for allmennheten (Åndsverkloven. §2).
Alle oppgaver som fyller kriteriene vil bli registrert og publisert i Brage Aura og på UiA sine nettsider med forfatter(ne)s godkjennelse.

Oppgaver som er unntatt offentlighet eller tausehetsbelagt/konfidensiell vil ikke bli publisert.

Jeg/vi gir herved Universitetet i Agder en vederlagsfri rett til å
gjøre oppgaven tilgjengelig for elektronisk publisering: ☒JA ☐NEI

Er oppgaven båndlagt (konfidensiell)? ☐JA ☒NEI
(Båndleggingsavtale må fylles ut)
- Hvis ja:
Kan oppgaven publiseres når båndleggingsperioden er over? ☐JA ☐NEI

Er oppgaven unntatt offentlighet? ☐JA ☒NEI
(inneholder taushetsbelagt informasjon. Jfr. Offl. §13/Fvl. §13)

Preface

The work performed in this master thesis, was prepared as partial fulfillment of the requirements for the Master of Science Degree in Construction Engineering at the University of Agder. It is a continuation of our work on Ultra-High Performance Fibre-Reinforced Concrete conducted during the first semester.

The present study has been carried out between January 2019 and May 2019 at the Department of engineering sciences, University of Agder (UiA), Norway. Investigation of UHPC at UiA has been one of the most important fields. Our goal in the UHPC field is to design more sustainable construction, as well as enhance the work environment and cost efficiency during the whole service life of concrete buildings. In order to accomplish this , we tried to enhance our understanding of the shear behavior of UHPC, in order to achieve more effective construction techniques, develop preferred materials and unique design theories. Therefore, we decided to combine experimental and numerical analyzing to get more environmentally friendly material production.

First of all, we would like to thank our supervisor, Prof. Katalin Vertes, for creating an encouraging environment, and for the valuable discussions we have had throughout the study. We would also like to thank our supervisor, Ph.D. candidate Ingrid Larsen, for sharing her thorough knowledge and for giving valuable guidance. We would also like to extend our appreciation to Prof. Rein Terje Thorstensen, who has enthusiastically shared his comprehensive and profound knowledge, and to Anette Heimdal, who cannot be thanked enough for her patience with answering our constant flow of questions.

We would also like to extend our thanks to Paul Ragnar Svennevig and Rita Ditlefsen at the Department of engineering sciences, who have, in one way or another, assisted with several experimental obstacles encountered, as well as contributing with their great sense of humor, making the work more enjoyable.

Last, but not least, we would like to express our sincere gratitude to (Mogamed)(), for their involvement in the project. Furthermore, we thank our families for their endless support and for reminding us what is essential besides work.

It is our hope that this master thesis can contribute to enhance the development of a more environmentally friendly approach within the field of engineering and to be helpful for students during the coming years. We also hope that any viewpoints, comments, and suggestions regarding its content will be directed to us.

Oslo and Grimstad, 2019
Haidar Hosamo and Perooz Sawari

Summary

The flexural behavior of reinforced concrete beams is obviously defined and can be managed with reasonable accuracy. However, a solution has not been obtained for the shear capacity of beams, especially those without shear reinforcement, though numerous models have been established using different approaches. The reason is due to the complexity of shear behavior of reinforced concrete beams, where the load transfer through various components of concrete. In addition to this, there is also the effect of reinforcement and cross-section of the members which is linked with dowel action and geometric parameters. All these aspects cause a challenge in quantifying the contribution of each parameter towards shear strength. The uncertainties of these parameters are the reason for not having a principal shear model in the measurement of the shear capacity of reinforced or un-reinforced concrete beams.

This master thesis has therefore focused on enhancing the shear resistance of reinforced concrete beams, among a suitable fibre dosage, and the use of UHPC. Experiments, as well as numerical analyses, have been conducted in this thesis. The experiments were divided into 3 parts: cubic and cylinder specimens at different ages to determine the compressive strength, as well as the modulus of elasticity, a four-point bending test on beams to investigate shear strength, and lastly, a three-point bending test on small-scale prisms to determine the flexural tensile strength. In order to reach a deeper understanding of the shear behavior, finite element (FE) analyses were implemented utilizing the computer software ANSYS. Through ANSYS, several sets of analyses were completed on the simulation of four-point beam bending tests.

The large-scale beams were all tested at the mechatronic laboratory at the University of Agder, using the four-point bending test. The midspan deflection was measured based on the available machines and a computer was used to register the values. The digital image correlation technique was used to extract the load- deflection curve of several points near to the diagonal shear crack. The experimental results confirm that using the fibre in UHPC beams, will increase the shear strength and the ductility. Replacing stirrups completely with fibres, leads to a reduction of beam depth as well as a decrease in stirrup assembly time.

The results were compared with the estimations by Australian guideline, ACI 522, Sharma, Ashour et al., Narayana et al. and Imam et al. The results show that Ashour et al. and Narayana et al. formulas gave the most accurate prediction, while the formula proposed by Sharma was the the least accurate.

Most of the Finite element modeling results correlated well with our experimental results. Hence, using ANSYS may be the right solution in the future to investigate UHPC beams and to develop design theories of UHPFRC.

Table of contents

List of figures

List of tables

Symbols and abbreviations

Abbreviations

UHPC	Ultra-High-Performance Concrete.
UHPFRC	Ultra-High-Performance Fibre-Reinforced Concrete.
NC	Normal concrete.
W/B ratio	Water-Binder ratio.
COIN	Concrete Innovation Centre, SINTEF.
ACI	American concrete institute.
ASTM	American Society for Testing and Materials.
CMOD	Crack Mouth Opening Displacement.
EC 2	Eurocode 2
FEA	Finite Element Analysis
FEM	Finite Element Method
FRC	Fibre-Reinforced Concrete
GFRC	Glass Fibre Reinforced Concrete
HSC	High-Strength Concrete
FE modeling	Finite element modeling

Latin upper-case letters

M_{Rd}	Moment capacity
M_{Ed}	Design value of the applied internal bending moment
E	Young's Modulus
d	Effective depth
f_c	Compressive strength for concrete
f_{ck}	Characteristic cylinder compressive strength
f_{cm}	Mean cylinder compression strength
h	Height of the cross-section
A_{sw}	The cross-sectional area of the shear reinforcement
s	The stirrup spacing
f_{ywd}	The design yield strength of the shear reinforcement
a_{cw}	The coefficient which considers the form of the stress in the compression chord.
A_s	Cross-sectional area of reinforcement
$A_{s,min}$	Minimum cross-sectional area of reinforcement
A_{sw}	Cross sectional area of shear reinforcement
L	Length
b	Width of the cross-section
b_w	Width of the web
$V_{Rd,c}$	Shear capacity
V_{Ed}	Shear force
$S.D.$	Standard deviation

Greek letters

θ	Angle between the normal vector from the crack and the fiber orientation
ν	Poisson ratio
ø	Diameter of steel bar
ρ	Density
v_1	The strength reduction factor for concrete cracked in shear

1. Introduction

UHPFRC, a combination of steel fibre and UHPC, is a mix with preferred characteristics compared to standard concrete, which has been of concern during the last years [1]. Meaning, it has a compressive strength higher than 150 MPa, higher tensile strength, is non-brittle, and has a low water binding ratio. The essential principle on which UHPC is used, is to achieve a denser transition zone between the cement matrix and aggregate, in addition to reducing cracks and capillary pores in the cement matrix, which lead to a denser cement matrix [2].

Since the start of using conventional reinforced concrete (RC) structures, with its low tensile strength, brittle behavior, and high shrinkage, it has been studied, to try to eliminate its insufficiencies. The Fiber- Reinforced Concrete (FRC) materials appeared as a result of these challenges. These attempts culminated in the development of UHPC. Ultra-High-Performance Concrete has gained considerable recognition in applications in significant structures. It has superior properties, making it a promising alternative to standard concrete in important structures. Considering Norway's focus on an environmentally friendly approach in construction, it is important that UHPC is adopted and implemented in our essential structures.

However, to prevent the brittle behavior of UHPC concrete under shear failure in reinforced concrete beams, the shear strength and shear toughness of the concrete have to be improved. Then, an appropriate reinforcement must be used to hold the principal stress lower than the tensile strength of the concrete [3]. On the other hand, an essential improvement in shear strength, in ductile and brittle failure modes, can be obtained by adding a proper percentage and geometry of fibres. Hence, fibres can have the same effect in terms of shear strength and may be able to replace shear reinforcement partially [3]. Considering the high cost of the fibre used in UHPC, more research is needed in order to develop more cost effective designs and standards, so that UHPC may be available for unlimited use.

Although there are several guidelines, recommended test methods and structural design regulations in relation to Ultra-High-Performance Fibre Reinforced Concrete, there is no guidance on the shear capacity of UHPFRC beams. Despite that previous studies have confirmed the advantages of UHPC utilization, the experimental and numerical investigations in this field are essentially not sufficient as there are no adequate studies that have investigated the behavior of shear resistance of UHPC. Consequently, there are not enough recommendations and data within the literature on the shear behavior of UHPC and UHPFRC beams.

This thesis will investigate and discuss different models in determining the shear strength of UHPCFR beams without stirrups. Hence, an innovative system of structure can be established to recognize the benefits and restrictions of UHPFRC, including the amount **of** and bonding conditions of fibre, longitudinal reinforcement, concrete matrix along with dowel action, mix recipe type and amount.

2. The significance of the work

Nowadays, the importance of sustainable infrastructure systems is more understanding since a significant global environmental impact comes primarily from concrete [4]. Hence, high attention is placed on combining the sustainability thought into the structural design procedure which remains a challenging task. To overcome CO2 emissions and reach more sustainable construction and plan strategies, the concrete industry has discovered a unique solution by the application of high-performance materials to decrease the concrete quantity used for the infrastructures. UHPC is a material with high compressive strength. It is composed of cement, Silica fume, Quartz powder, superplasticizer, water, and steel fibers. Generally, UHPC can improve the performance and extend the service life of new structures due to its high mechanical, durability properties and sustainability. Thus, the construction using UHPC, affording a green solution for more advanced civil infrastructures [5] [6].

Using UHPC, allows the design of more slender, stronger and more durable structural members at the same time. This leads to less material consumption, demolition waste, demands on transportation and lower environmental impacts [7]. Due to its dense components, UHPC enhanced protection to corrosion and lead to less maintenance and repairs. Thus, UHPC is an innovative material that withstands the? unusual environmental loads, earthquakes, floods, and strong winds and can be used for large span structures [5].

Achieving these superior characteristics of UHPC required many efforts. The homogeneity was improved by using much finer particles instead of coarse aggregate; the superplasticizer used to reduce water to cement ratio; making the cement denser by using pozzolan such as silica fume and find the proper curing regime [2]. The previous ingredients can be found easily but unfortunately not in a high amount such as fine quartz sand and silica fume. Therefore, the search for local materials as an alternative is ongoing [2].

These properties lead to increase of UHPC applications in the structural field [8]. For instance, in steel-reinforced structures, UHPC can prevent brittle failure, result in higher ductility, higher shear resistance and reduce the requirement of shear reinforcement. Also, UHPC proved to be an ultimate solution for prefabricated elements compared to the conventional concrete which has several limitations [9].

On the other hand, one disadvantage of UHPC, is that it requires several hours before it begins to set. The reason is that the dwell time before the initiation of the cement hydration reactions, can be influenced by factors such as temperature and chemical accelerators [6].

Another disadvantage may be that UHPC alone is a brittle material. Therefore, fibre needs to be added to secure the ductility behavior. The casting of fibre is influenced to a large extent in the mixing procedure. Thus, internal vibration is not allowed which will affect the dispersion and orientation of the fibre. However, a limited vibration on the surface may be allowed to release the air bubbles. Wrong oriented fibre may lead to a catastrophic result where structures can fall while applying the loads. Therefore, it is very important to ensure the orientation of fiber as possible in the concrete elements [6].

UHPC also has some damages to the surrounding since it contains two times cement than a conventional concrete type [10]. More amounts of cement, means more energy consumption at the manufacturing phase, which in turn, leads (in turns) to higher environmental impact. Also, it is an expensive material. To limit this problem, the right amount of materials needs to be calculated in the project [11].

3. Theory and literature review

3.1. UHPFRC properties and characteristics

3.1.1. History and background of UHPFRC

During the 1930s, Eugene Freyssinet illustrated that compressing concrete during setting, could improve its strength. In the 1960's compressive strengths up to 650 MPa were gained in smaller concrete and mortar specimens by pressing and giving heat in a water environment at the same time [12]. The evolution of what is called as UHPFRC began in the 1970s by Brunauer, Odler, and Yudenfreund. They inquired high strength cement pastes with water-cement ratios as small as 0.2-0.3. The mentioned low w/c ratios resulted in concrete with low porosities causing the compressive strengths up to 200 MPa and small dimensional changes.

Ultra-High Performance Fibre-Reinforced Concretes have been developed as consequences of research that was initiated in 1930. The purpose of this research was to find a method for concrete production with high compressive strength [12]. There is no detailed description of UHPFRC in the reviewed literature, but there is an approach that this type of concrete is a concrete type with a compressive strength above 150 MPa. It is not enough to have an Ultra-High compressive strength alone, because above mentioned concretes are fugitive, the performance of the concrete should be Ultra-High.

The following features of concrete are standard in the literature;

- Direct tensile strength above 7-8 MPa.
- W/B ratio smaller than 0.25, and usually between 0.16 and 0.20.
- High content of the binder, which causes an absence of capillary porosity.
- Using the fibers to maintain a ductile characteristic [10] [13].

Ultra-High-Performance Fibre Reinforced Concrete (UHPFRC), is a mixed material which is different from standard concrete in many aspects. Mechanical characteristics like compressive and tensile strengths are much more significant than regular concrete. This enables the making of slender structures because a smaller cross-section can distribute and tolerate the same amount of load as a bigger cross-section.

3.1.2. Steel fibers

Concrete is naturally brittle. Typical stresses like impact, fatigue and loading, lead to cracking and eventual failure. Adding reinforcement to the concrete helps to absorb these stresses and to limit the formation of cracks, increasing the load bearing capacity and ductility of the concrete structure. There are several ways of reinforcing concrete. There are a lot of focus on rebar and steel mesh. However, steel fiber is more durable and reliable. Since its introduction over 40 years ago, steel fiber reinforcement has proven its merits in the most demanding structures and applications. The core difference between steel fiber and other reinforcement solutions, is that fibers are part of the concrete matrix, turning it into a composite material. Instead of providing strength in distinct locations, steel fibers form a reinforcing network throughout the entire concrete structure, increasing its overall ductility [14].

This can be translated into concrete behavior by taking a random concrete structure subjected to loading, compressive and tension stresses. Over time, small cracks will appear in places where the

stress reaches a critical point Steel fiber interacts within the concrete matrix, absorbing tensile stresses at any point and in any direction. As a result, steel fiber picks up small cracks much faster than traditional reinforcement. When a crack occurs, the ends of the fibers remain solidly anchored on each side of the crack, acting as a stress transfer media. Once the maximum bond strength of the concrete is reached, the pull out takes full effect. This enables the next fiber to take over, delaying cracks from growing. Different loads require different steel fibers. Each fiber has a different hook, strength, and ductility.
Consequently, they also behave slightly differently when dealing with stresses. Let us take a closer look at Dramix®, which was used in our research. When a small crack occurs, the fiber is firmly anchored inside the concrete matrix. As stress increases, the fiber slowly deforms. As soon as the fiber loses its bond with the concrete, the pull out takes full effect where the wire slowly elongates, until it reaches its maximum strength with a tensile strength of 1200 MPa. It can take high flexural stresses over a long period. We can conclude that Dramix® steel fibers effectively increase the load-bearing capacity of concrete. It can be used in almost any concrete structure with or without additional reinforcement, where the ductility of the concrete structure depends on the length/diameter ratio of the fibers and the number of fibers used per cubic meter [15]. It is essential that enough fibers overlap to create a continuous network in the concrete mix. Choosing the right fiber and determining the right dosage may help a lot in improving the concrete capacity.

The incorporation of steel fibers in UHPC mixture can ensure ductile behavior in tension and transform brittle failure to ductile failure in compression [16]. UHPC without fibers, exhibits very brittle failure with tensile strength values ranging between 7 MPa and 10 MPa, while UHPFRC poses higher tensile strength varying from 7 MPa to 15 MPa and ductile behavior in the post-cracking stage with a pronounced descending portion in the force-deformation diagram [16]. It has already been proven by many previous experimental studies that although the tensile performance of UHPFRC is affected by fiber characteristics, including fiber type, content, shape, aspect ratio, orientation and distribution, the increase in amount of fibers, results in the most significant improvement in the tensile strength, fracture energy capacity and post-cracking behavior [16]. However, in contradiction with some previous studies, there is a relatively small reduction of compressive strength when using higher volumes of steel fibers compared to UHPC without fiber [16].

Some UHPFRC include several sizes of fibers that may have complementary behaviors (microfiber improving the anchoring of larger fibers and sewing the first networks of microcracks). The high fiber content used in UHPFRC gives them quite interesting tensile and shear strength that allows traditional passive reinforcement frames to be dispensed with. The steel reinforcement is limited to acting principal forces on large sections. To enable the design of structures without any reinforcements, it was necessary to develop rules for specific calculations. This objective, necessary to produce a work in the public domain was one of the main motivations that led to the drafting of the AFGC (Association Français de Gènie Civil) recommendations on UHPFRC [14].
The most Common fiber shapes are illustrated in the following Figure 3-1. The most commonly used dimension of steel fibers is 13 mm in length and 0.20 mm in diameter [17] which is used in our thesis.

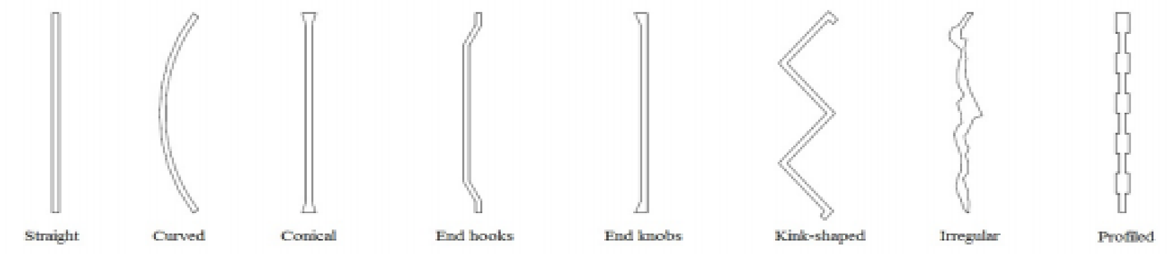

Figure 3-1 Different fiber shapes [16]

3.1.3. Thermal treatment

UHPFRC may meet a specific cure regime which is implemented a few hours after the concrete sets. This cure type involves giving heat to the element at a high temperature (Almost 90°C), with moisture near saturation for almost 48 hours [10]. When the UHPFRC has not undergone any form of heat treatment, it is classified STT. It should then be cured for 28 days, and the air temperature maintained at 20 ° C ± 2. Class TT1, TT2 and TT1 + 2 are when the concrete has been through a form of heat treatment. As UHPFRC classified TT1, it has undergone an acceleration of hydration through heat treatment which aims to reduce the time interval. This takes place right after the specimen is molded in at moderate heating. When UHPFRC is classified TT2, the heat treatment starts after several hours. The temperature is relatively high (in the order of 90°C), and the moisture content is higher than 90%. The average compressive strength at 28 days after such treatment, should not be less than the average compressive strength at 28 days without heat treatment. Class TT1 + 2 is given when the UHPFRC has successfully undergone both above heat treatments [18]. Hence, the degree of hydration in UHPC mixtures can be enhanced through correct heat treatment. The utilization of thermal processing proceeds pozzolanic reactions, heading to the generation of additional calcium silicate hydrates (C–S–H) [19] [20]. A 40 % average improvement in compressive strength was recognized for 90 °C heat treatment corresponded to that of untreated specimens [21]. Besides, the academic knowledge gained concerning UHPC and a hard regime emphasizes that curing at 90°C for 48 hours at high moisture enhances the compressive strength of UHPC and improves Young's modulus [22].

3.1.4. Tensile strength

The biggest challenge for UHPFRC, and what distinguishes them radically from the other concretes, is tensile strength. This concerns the strength of the material before cracking and the post-cracking resistance that involves mainly fiber strength. The tensile strength before cracking shows no real problem [6]. UHPC tensile stress-strain behavior has proposed by Graybeal as shown in Figure 3-2 [23]. This behavior is classified into four phases. Phase I is an elastic behavior. Phase II is the phase where several cracks develop in the UHPC matrix. At phase III, cracks grow in this phase. Finally, Phase IV arises when the fibers that are bridging cracks start to pull out of the matrix.

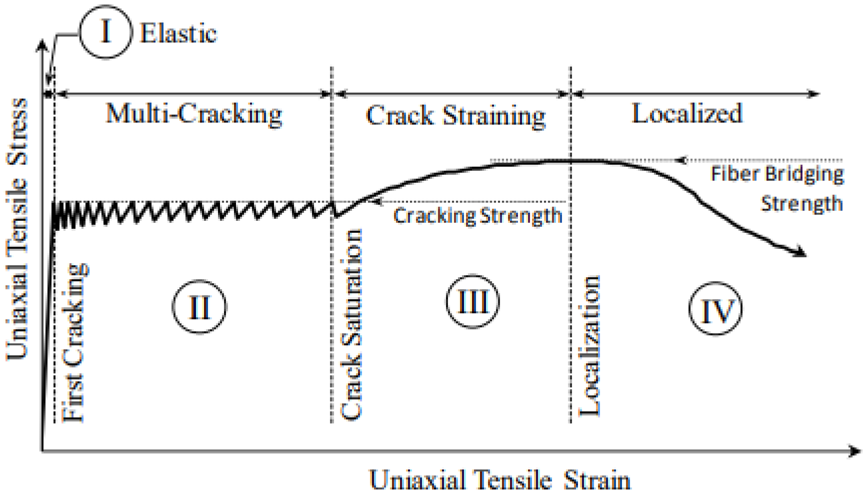

Figure 3-2 uniaxial tensile mechanical response of a UHPC [23]

The top of the curve in phase III represents the post-cracking strength which is the residual strength. Phase IV can be represented in another way by using σ-w curve; w is the crack width. By adding the fibers, the residual tensile strength will be increased dramatically due to the bridging mechanism. This increasing is profoundly affected by the orientation of the fiber and the casting method.

Figure 3-3 and Figure 3-4 show the stress and strain along with the depth of the UHPFRC section.

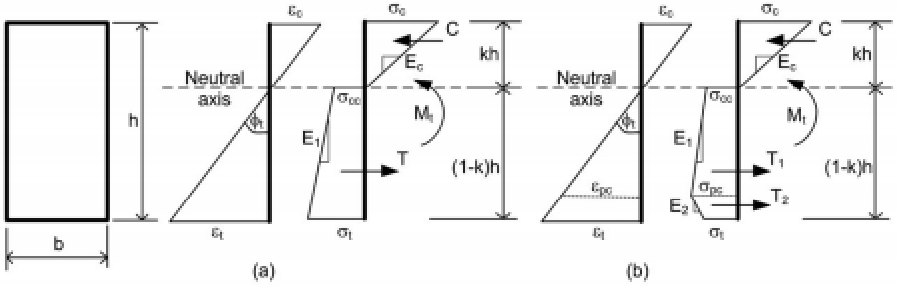

Figure 3-3 Strain and stress distribution along with the depth of section for strain-hardening UHPFRC: (a)$\varepsilon_{cc} \leq \varepsilon_t \leq \varepsilon_{pc}$ *(b)* $\varepsilon_{pc} \leq \varepsilon_t \leq \varepsilon_{cu}$ [24]

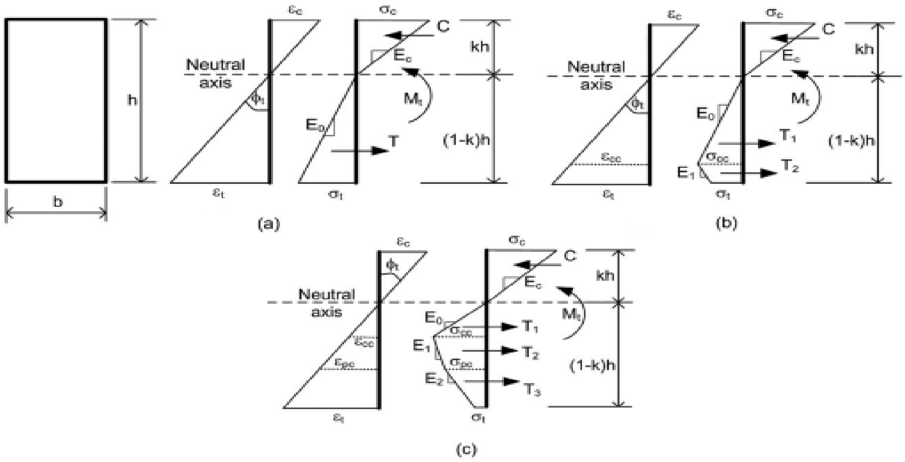

Figure 3-4 Strain and stress distribution along with the depth of section for strain-softening UHPFRC, $\varepsilon_{pc} > \varepsilon_{cc}$ *(a)* $0 \leq \varepsilon_t \leq \varepsilon_{cc}$ *(b)* $\varepsilon_{cc} \leq \varepsilon_t \leq \varepsilon_{pc}$*(c)* $\varepsilon_{pc} \leq \varepsilon_t \leq \varepsilon_{tu}$ [24]

3.1.5. DIC technique

UHPC is composite material which needs more advanced techniques to be applied in order to investigate deformation, strain and detect the crack propagation. The Digital Image Correlation (DIC) is a high-speed photography technique that tracks the movement of a random dot pattern that may be painted on the investigated specimens [25].

Usually, the DIC is used as an additional tool to the conventional one. The reason for that is by using LVDT (Linear Variable Differential Transformer) sensors; it is possible that the crack cannot be seen by the naked eye or several cracks initiate together within the study region. In this case, the DIC technique provides a continuous measuring of the cracks from the very first crack up to failure [26]. Moreover, as the LVDT sensors need cables and may be disconnected if the deflection becomes high, one more advantage is to provide here by the DIC technique. DIC in non-connected tool measurement which allows measuring all the required data with a low- cost.

Marina et al. studied three slab specimens. They measured the crack width and the vertical displacement in the middle of the span by using both, DIC and LVDT sensors. The results showed that for vertical displacements, DIC results differ from LVDT sensor results by only ± 1 %, but at low load levels the differences reach up to 3.3 % were noted. For crack width, the deviation reaches up to 7% compared to LVDT sensors results. Although the LVDT sensor was installed at the base surface and DIC- camera captured the side surface of the specimen, the results are reasonably correlated well [27].

Bora et al. conducted a test on a full-scale prestressed I-shaped beams by using conventional tools as well as digital image correlation technique. The results show that DIC data can provide very accurate and even more detailed results than the standard equipment [28].

David Corr et al. carried out two different experimental tests on the concrete block as a substrate for a carbon fiber sheet of size 75 mm by 150 mm by 200 mm and for the interfacial fracture. LDVT sensors were used along with a continuous observation under digital image correlation technique. They found that DIC measures the surface displacements very accurately of the tested specimens [29].

On the other hand, one should be conscious of the DIC data efficiency and its limitation. For instance, the camera should be stable from the beginning of the test to the end. Any undesired shift in the camera position will lead to unremoved error. Hence, high vibration isolation is required.

Out from the reviewed studies above, the results from the DIC technique are suitable to be utilized in estimating the vertical displacement and prediction the cracks propagation of the deformed specimens. Based on that, the DIC technique will be used in our thesis to investigate more accurately the vertical displacement of the studied beams.

3.1.6. Shear strength

Challenges of shear dimension calculation in concrete structures are influenced by several factors that make the calculations complex. Concrete strength, longitudinal reinforcement, and stress are among the most important factors that are included in dimensioning. Several regulations and models have been developed that satisfy laws and regulations for selected solutions. Today's formula in EC 2 for structural parts without the computational need for shear reinforcement is used. However, a common shear failure in a beam without shear reinforcement will start horizontally at the supports, then will the fracture move along with the longitudinal reinforcement, then to go up to the load point for approx. 45 degrees [30].

The transfer of force through the concrete and cracks in the UHPC are still uncertain. The transfer mechanics are something that must be determined to be possible to have a right way of determining shear for UHPC. The more detailed study had been prepared in our preliminary report in Annex D (section 3.10 and section 6) to describe the shear strength mechanism.

In general, to stop sudden, brittle failure and hinder the development of crack width which may follow the diagonal cracks, reinforced concrete beams should have enough shear strength. Therefore, minimum shear reinforcement is additionally needed to achieve ductile behavior prior to failure [31] [32]. However, there is no critical amount of shear reinforcement for coverage required strength to limit the crack width after failure. On the other hand, several equations, basically based on standards, have been established to predict the shear strength of beams.
Due to various formulas that have been conducted by researchers, it becomes challenging to pick a proper model for predicting shear strength [33]. Thus, a four-bending test on beams is implemented which is the conventional method for investigating the shear failure. The pure bending in this method is achieved between the two equal symmetrically concentrated loads P where there is no shear force whereas a constant shear force can be obtained within the shear spans which is the distance between the concentrated load and the support.

There are numerous investigations on shear behavior in the conventional reinforced concrete. If the fibre is involved, the investigation is limited. By taking UHPC into account, the researches become less. Therefore, Voo et al. examined eight I-section prestressed UHPFRC beams in shear. The results are compared to several proposed models to predict the shear strength of FRC beams where the variables are the quantity and type of steel fibers and the shear span-to-depth ratio [34].

Xia et al. tried to meet the lightweight and high strength conditions in bridge applications. Hence, they worked on the shear failure of UHPC beams reinforced with high strength steel. Experimental studies covered several parameters, including material properties, bond tests, tests on prisms and beams. Also, several formulas from the literature were used to determine the shear strength. The values from formulas were compared to the experimental results [35].

Kara applied an improved method to determine the shear capacity of fibre reinforced concrete beams without stirrups based on the Gene Expression Programming (GEP) technique. This manner presents an accurate solution in predicting the shear strength of FRP-reinforced concrete beams among the available formulas in articles [36].

Xia et al. investigated the contribution of the dowel action of longitudinal reinforcement in increasing the shear strength of UHPFRC beams without stirrups. The dowl action has almost a negligible effect on shear in standard concrete design. However, in UHPFRC beams without stirrups, the dowel action becomes significant in ensuring a non-brittle behavior of shear failure by enhancing the tensile strength on sides of the shear crack [37].

Baby et al. studied the shear behavior of UHPC beams including various parameters; with and without prestressing, vertical shear reinforcement and fibre [38] [39]. The results prove that fibers have a significant contribution as shear reinforcement in beams. The results also show that the AFGC recommendation for UHPFRC was conservative for the investigated beams [40].

Baby et al. investigated the ratio between the experimental shear force to the predicted shear force using RILEM equations. The results show that RILEM very conservative in determining the shear strength. The average ratio for prestressed UHPFRC beams was 3.36 while it was 4.56 for reinforced UHPFRC beam [39].

Khaloo et al. tested reinforced high-strength concrete beams without stirrups to determine shear capacity. The study includes several parameters such as six shear span-to-depth ratios and six percentages of longitudinal steel p. The result confirmed that ACI equations for predicting the shear capacity of beams with $l < a/d < 2.5$ are overly conservative [41].

Twenty-seven large-scale FRC beams without stirrups have been studied by Hai H. Dinh et al. to estimate their shear strength. Three types of hooked steel fibers were utilized. All test beams failed in shear except one beam. The ultimate failure of beams happened as a consequence of either a diagonal crack or by crushing of the beam compression zone [42].

Although an enormous number of articles focusing on UHPCFRC as some of them were studied here, there is no sufficient knowledge of shear strength.

3.2. Finite Element Modeling

The Finite Element Analysis (FEA) method, basically presented by Turner et al. (1956), has become a fundamental step in the design or modeling of cases in different engineering disciplines. FEA can be applied to produce results for various engineering issues; it has become a useful tool for analyzing stress [43].

Why use the Finite Element Method?
Some simple issues may cost money and consume time in order to be solved whether the finite element model is applied. Such issues have to be solved with simple methods. However, some applications are complicated and solving this problem applying the fundamentals principles becomes more challenging. As the complexity becomes higher, it will almost be impossible to get the correct solution. Here comes the importance of finite element analysis by solving complex issues which would be time-consuming and costly to solve analytically [44].
The finite element analysis technique needs the following significant steps [43]:

- Discretization of the field into a finite number of elements.
- Determination of additional functions.
- Development of the element matrix.
- Assembly of the element matrices to obtain the global matrix for the whole domain.
- Set the boundary conditions.
- A solution of equations.

Typical fundamental engineering issues and their FEA are illustrated in Figure 3-5.

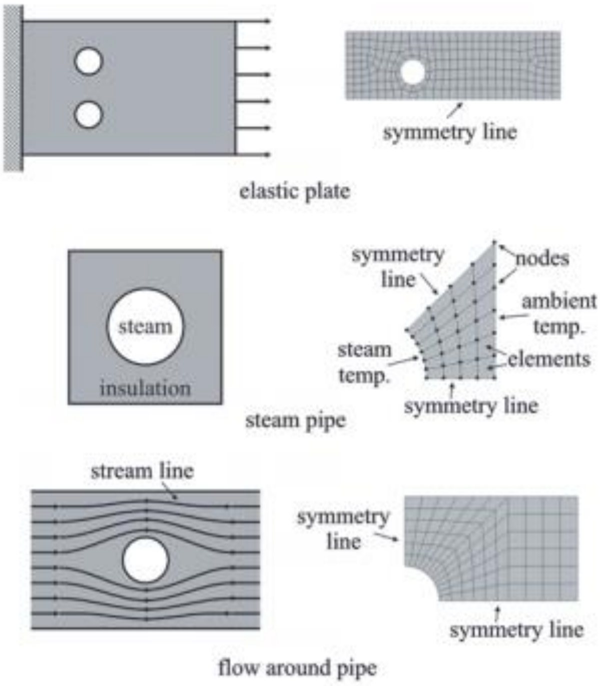

Figure 3-5 FEA representation of practical engineering problems [43]

In the early stages of using the finite element method, two-dimensional models were focused, but soon general cases of loading were involved. Even though the two-dimensional analysis gives enough and efficient results on many issues, the three-dimensional analysis provides a better representation of the non-linear behavior of materials in reinforced concrete structures.
In the three-dimensional analysis, the behavior of any element under loads is highly dependent on the material behavior of this element. Concrete and reinforcing steel act as a composite system

in which the steel is a uniform material has the same stress-strain curve in both tensile and compressive conditions, while concrete is known to be heterogeneous and highly dependent on each component properties. The nonlinear solution of specific elements can be therefore used to predict the behavior of concrete structures in elastic and plastic phases, cracking loads, post-crack loads and failure load.

In this study, ANSYS will be used to analyze the three-dimensional concrete element. Since the behavior of any structural element under loads depends mostly on the characteristics and behavior of the materials, this section will describe models and behavior of materials in Ansys.

3.2.1. Finite element formulation [43] [45]

Equilibrium equations in the nonlinear 3D analysis of installations under static loads are derived using the Virtual Work principle. For the deformable object to be in equilibrium, the Virtual Work performed by the external forces must be equal to the virtual work done by the internal forces Resulting from internal stresses.

$$\delta W_{int} - \delta W_{ext} = 0 \qquad 3\text{-}1)$$

δW_{int}: Internal virtual work.
δW_{ext}: External virtual work.

Internal virtual work

$$\delta W_{int} = \int_v \{\delta\varepsilon\}^T \{\sigma\}\, dv \qquad (3\text{-}2)$$

$\{\delta\varepsilon\}$: Virtual strain vector.
$\{\sigma\}$: Real stress vector.
dv: Infinitesimal volume.

Using the general stress-strain relationship, stress vector can be found from the corresponding strain vector.

$$\{\sigma\} = [D]\{\varepsilon\}$$

$[D]$: Matrix stiffness Material which contains an appropriate definition of the material properties. By using the two previous equations:

$$\delta W_{int} = \int_v \{\delta\varepsilon\}^T [D]\{\varepsilon\}\, dv$$

Local displacements within the element (U) are related to general displacement in node { a } with an approximate interpolation.

$$\{U\} = [N]\{a\}$$

$[N]$: Shape function materix.
$\{U\}$: Local displacement.
$\{a\}$: Global displacement.

Strain in elements can be linked to general displacements in nodes:

$$\{\varepsilon\} = [B]\{a\}$$

$[B]$: Stress-nodal displacement matrix.

$$\text{Then } \delta W_{int} = \{\delta a\}^T \int_v [B]^T [D][B]\{a\}\, dv$$

External virtual work

This work is caused by the nodal forces applied to the element and can be calculated as follows:

$$W_{ext} = \{a\}^T\{F\}$$

$\{F\}$: Nodal forces applied to the element.

Then

$$\{\delta a\}^T \int_v [B]^T [D][B]\{a\}\, dv = \{a\}^T\{F\} \qquad 3\text{-}3)$$

$\{\delta\alpha\}^T$: Arbitrary virtual displacement.
The previous equation can then simplify as follows:

$$[K^e].\{a\} = \{F\}$$

$$[K^e] = \int_v [B]^T [D][B]\, dv \qquad (3\text{-}4)$$

$[K^e]$: Element stiffens matrix.
$dv = dx.dy.dz$
Equation number 10 represents the equilibrium equation based on only one element.
The overall matrix of all the elements is adopted by adding the stiffness matrix for each element after converting the local coordinates to the global coordinates. This formula can be written as follows:

$$[K].\{a\} = \{F^a\} \qquad 3\text{-}5)$$

$[K] = \Sigma_n[K^e]$: Overall structural stiffness matrix.
$\{F\} = \{F^a\}$: Vector off applied loads.
n: Overall number of elements.

3.2.2. Classification of finite elements according to their dimensions [45]

Some important definitions need to be explained before moving to the element type.

Nodes

Each element has a set of distinctive points called nodes, located in corners, or on the bars, and at the endpoints of the element. It is useful in determining the geometric shape of the element (linear or non-linear) and determining degrees of freedom.

The geometric shape

The geometric shape of the element is defined by the position of the nodes. Most elements have simple geometric shapes. In general, there are four possible forms of elements: pointed, linear, surface and volumetric.

Degree of freedom

A degree-of-freedom (or DOF) is a method that a node is allowed to move or rotate. Each node has three possible degrees-of-freedom: translation (movement) in one direction, translation in another direction perpendicular to the first one, and rotation. However, particular directions may be restricted, either by a support reaction or by one of the connected members.

The degree of freedom of the element determines the scope of application (construction, thermal, magnetic, electric or fluids). By selecting the degrees of freedom required in the element, the response of the model is determined. The addition of unnecessary degrees of freedom increases the duration of the analysis and requires more storage. Selecting an element with unnecessary features, for example, using an element that has the advantage of plasticity for a solution in the elasticity field, only increases the time of analysis.

The finite elements can then be classified according to their dimensions into four types:

DOT Element

usually consisting of one node, as in the mass element.

1D Elements

The geometric shape here is a straight or curved consisting of two or three nodes, such as the elements (Link, Bar, Spar) used in tensile and pressure situations, as in the case of a truss element. In cases of bending (as in the case of a beam), the element Beam is used. These elements can be linear or quadratic, as shown in Figure 3-6.

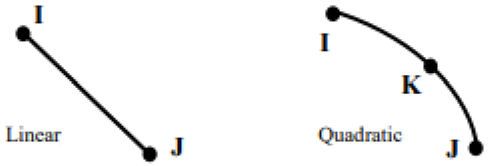

Figure 3-6 One dimensional elements [45]

2D elements

It has a triangular or quadratic geometric shape and may be caused by volumetric (2D solid element) or shell elements. The most prominent surface elements are the Plate and Shell elements.

The triangular element may be linear, consisting of 3 nodes or quadratic consisting of 6 nodes. The quadrilateral element, May be linear, consisting of (4) nodes, or quadratic composed of (8) nodes, as shown in Figure 3-7.

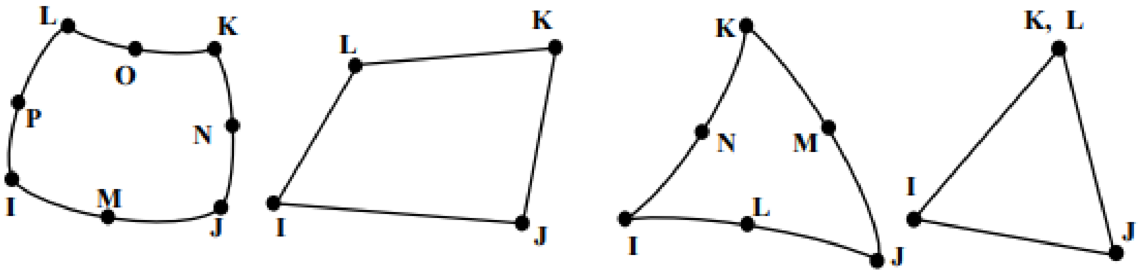

Figure 3-7 2D elements [45]

3D elements

The volumetric elements have several shapes as shown in Figure 3-8;

1- Tetrahedron: It may be linear, consisting of 4 nodes or quadratic consisting of 10 nodes.

2- Prism: It may be linear, consisting of 6 nodes or quadratic consisting of 15 nodes.

3- Pyramids: It may be linear, consisting of 5 nodes or quadratic consisting of 13 nodes.

4- Hexahedron: It may be linear, consisting of 8 nodes or quadratic consisting of 20 nodes.

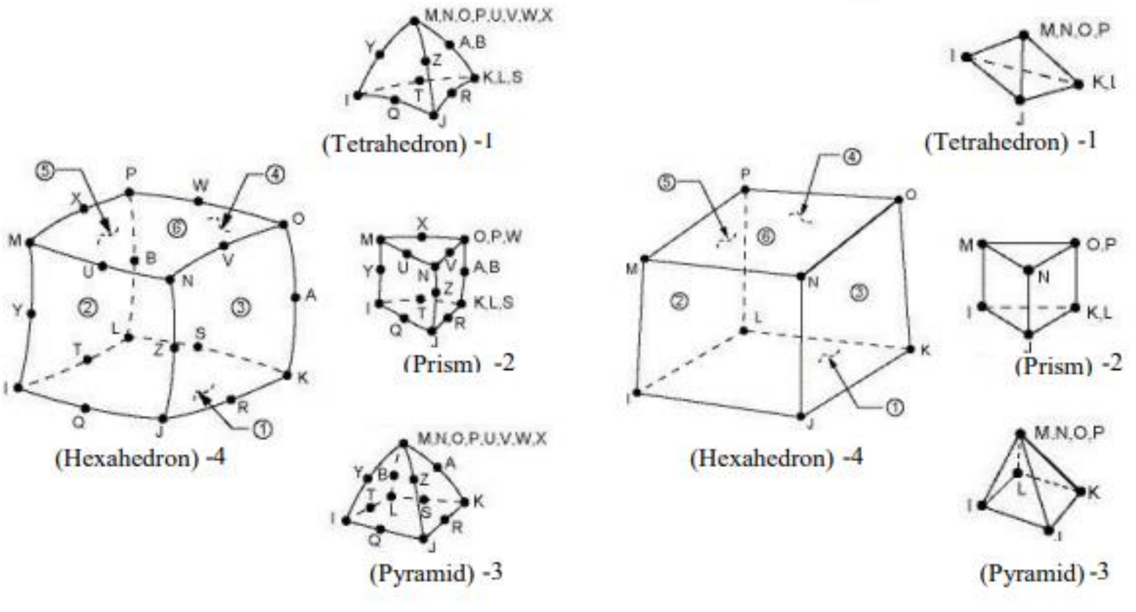

A. Quadratic

B. Linear

Figure 3-8 3D elements [45]

3.3. Nonlinearity

In dealing with nonlinearity, it is essential to distinguish between material nonlinearity, geometric nonlinearity and non-linearity due to specific boundary conditions [46].

3.3.1. Material nonlinearity

Means that a $\sigma - \varepsilon$ relationship is a nonlinear relationship and the basic forms of nonlinear response can be classified, Figure 3-9, as in the following cases:

1- Viscoplastic.
2- Viscoelastic.
3- Plastic.
4- Nonlinear elastic.

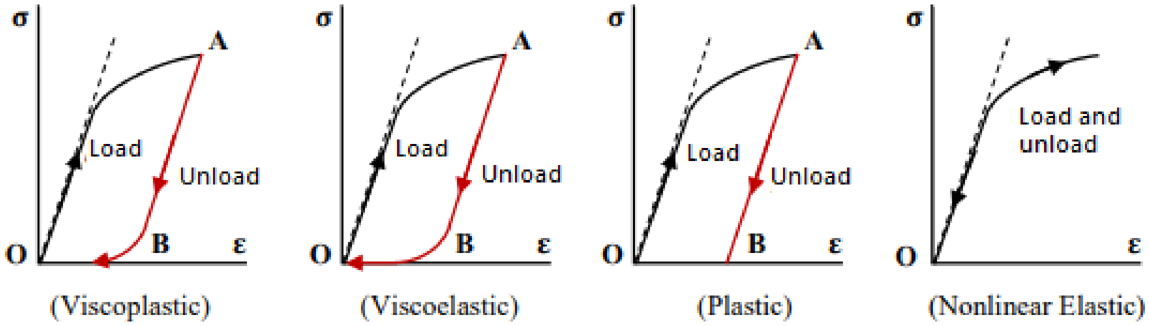

(Viscoplastic) (Viscoelastic) (Plastic) (Nonlinear Elastic)

Figure 3-9 Basic forms of nonlinear material response

The ideal computational methods for the behavior of nonlinear materials are illustrated in the following figure:

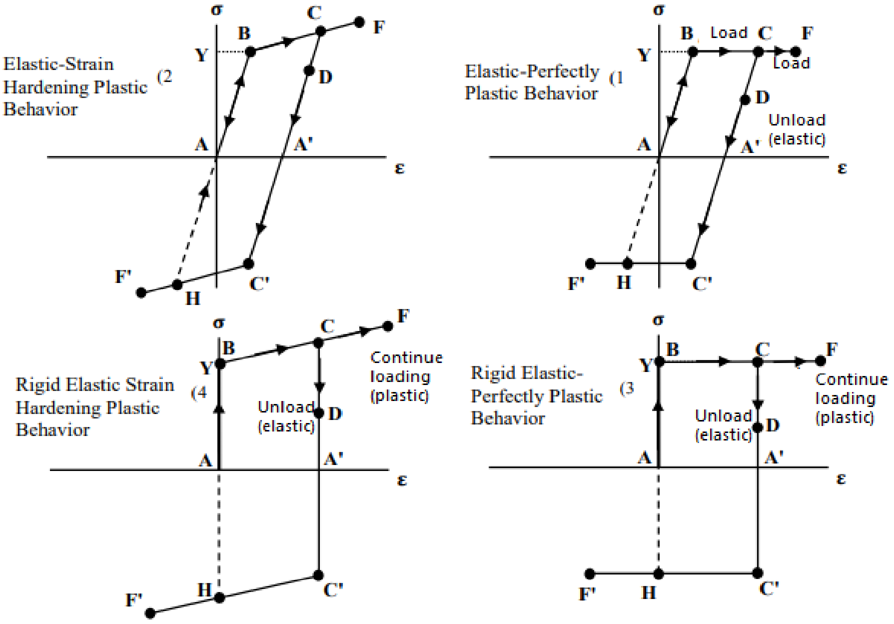

Figure 3-10 The ideal computational methods for the behavior of nonlinear materials

3.3.2. Geometric nonlinearity

Geometrical nonlinearity is the nonlinearity resulting from the change of shape during the transition of the structure or its components. In other words, the stiffness matrix is related to the transitions, so the stiffness matrix changes due to the change of shape or rotation in the material. (Example, cracks in the concrete cause a change in its stiffness matrix).

The most prominent cases in which engineering nonlinearity arises are:
P-delta: a situation where stress is significant, such as a large compressive force applied to a thin column, as the increase of this force from a certain limit occurs in buckling and weakens its stiffness.
Large Displacement: This situation arises when the span is large, primarily when the long-term transitions are assessed, and the creep effect is examined in the stiffness.
Stress stiffening: This condition occurs when stress in a particular direction affects the rigidity in the other direction, for example, the structural element that has low or no stiffness on the pressure while it has a good stiffness on the tensile as in the case of cables or membranes.

3.3.3. Non-linearity due to certain boundary conditions

Includes contact problems and all the other structures where the boundary conditions can change during the service time from the origin.

3.4. Meshing

The volumetric shape drawn from solid elements is converted to finite elements using the mesh command. This is because the program does not deal with the solid elements but with the finite elements consisting of separate structural units called elements and nodes.
Since the meshing has an important role on the accuracy of the results, it is often working on experimenting several measurements of meshing, and in the light of the results is adopted the proper meshing, which gives accurate results and takes an acceptable computational time when solving the models [43].

It is known that the smaller the meshing, the more accurate results will be given to a certain extent, then the results will be removed from the correct solution due to a large number of numerical errors.

In the case of a high concentration of the stresses due to the application of surface-focused load, the density of the division can be increased in the area of application of load and convert the concentrated load to a set of loads applied to nodes [43].

3.4.1. Main meshing methods

There are two main methods of meshing: Free and Mapped. See Figure 3-11.

1-Free Mesh:
- It has no Specific shape.
- Suitable for the meshing of complex areas or sizes.
- The high order tetrahedral consists of (10) nodes.

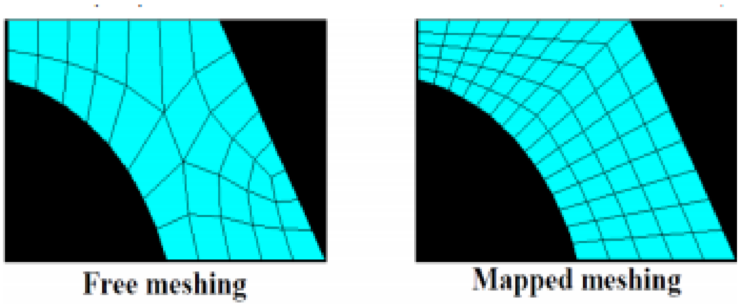

Figure 3-11 Mapped and free mesh

2-Mapped Mesh:
-Elements are made up of four quadrilateral shapes when dividing areas and hexahedra when dividing volumes.
-Generally, it has a regular pattern so that the elements are arranged regularly.
-Suitable for dividing regular rectangles or volumes.

3.4.2. The meshing density control

The program provides several tools to help control the increase in the intensity of the meshing, through the smart meshing called (Smart Sizing), the global element sizing, determining the maximum dimensions of the areas, and the maximum dimensions of the lines.

3.5. Analysis type

The program provides several types of analysis, including static analysis, model analysis, harmonic analysis, transitional analysis, spectrum analysis, buckling analysis... Etc.
The default analysis in the program is static analysis.

3.5.1. Static Analysis

Used to identify transitions, stresses, and strains. . . Etc., under the influence of constant loads and by neglecting the effect of inertia or damping which may be produced in the case of variable loads over time, this analysis takes into account the fixed inertial loads (such as gravity and rotational velocity) and the time-varying loads that can be considered as equivalent static loads (wind and earthquake which may be considered as equivalent static loads as is common in many building codes). This analysis can be linear or nonlinear. Nonlinearity can include large deflections, large strain, Hyperelasticity, contact surfaces, and creep [43].

The fixed loads assume that the loads change slowly for a time, and the types of payload that can be applied in this analysis [43]:
-External loads such as concentrated forces or distributed loads.
-Strong static inertia (such as terrestrial side, rotational velocity).
-Imposed transfers.
-Thermal loads (to observe thermal reactions).

3.6. Criteria of deformation

In structural engineering, a segment may be subjected to various kinds of forces/moments or a blend of them. Those forces and moments or their combinations increase various kinds of stresses at several points in the segments. Depending on the substance of the member and the stress generated, the segment may break due to an exceedance of various sorts of stresses. Consequently, it is important to understand the mechanism of failure of several kinds of materials so that the structure may be correctly managed to avoid the occurrence of that stress at the critical point.

Methods of failed attempt to determine the reason for the failure of a material due to an exceedance of various parameters. For all material, there is particularly one predominant form of failure and others are not correct. This is ordinarily controlled by using various theories of failure in various loading situations. The theory that perfectly predicts failure following different conditions is trusted for that material.

The most prominent criteria for judging reaching to the plasticity zone are Von Mises criterion and Tresca criterion.

3.6.1. Von Mises failure criteria

This theory states that failure in any material happens when the shear strain energy per unit volume saved in that material due to any loading passes the shear strain energy per unit volume saved in that material in the one-dimensional loading test.

Von suggested that the distortion energy should be divided into two parts, the first is volumetric and the second is related to the shape. He suggested that the plasticity criterion is only by the shape of deformation energy.

$$U_0 = \frac{1}{2E}[\sigma_1{}^2 + \sigma_2{}^2 + \sigma_3{}^2 - 2v(\sigma_1.\sigma_2 + \sigma_2.\sigma_3 + \sigma_3.\sigma_1)] \quad (3\text{-}6)$$

$$U_0 = U_V + U_D$$

$$U_V = \frac{(\sigma_1 + \sigma_2 + \sigma_3)^2}{18K}$$

$$U_D = \frac{(\sigma_1 - \sigma_2)^2 + (\sigma_2 - \sigma_3)^2 + (\sigma_3 - \sigma_1)^2}{12G}$$

$$K = \frac{E}{3(1 - 2v)}$$

U_v: Distortion energy related to a volumetric change.
U_D: Deformation energy related to a shape change.
E: Longitudinal elasticity factor.
G: Transverse elasticity factor.
v: Poisson's ratio.

Since Von Mises stress is equivalent stress which is usually utilized in design activity because it enables any random three-dimensional stress state to be expressed as a single positive stress value. Equivalent stress is a component of the maximum equivalent stress failure theory applied to expected yielding in a ductile material. Based on that, when the equivalent stress reaches the yielding stress the following equation can be found:

$$\sigma_e = \frac{1}{\sqrt{2}}\sqrt{(\sigma_1-\sigma_2)^2+(\sigma_2-\sigma_3)^2+(\sigma_3-\sigma_1)^2} \qquad (3\text{-}7)$$

σ_e: Von Mises stress.
$\sigma_1, \sigma_2, \sigma_3$: The principle stresses of the studied point in the structure.

Von Mises stress is given according to general coordinate and shear stresses as follows:

$$\sigma_e = \frac{1}{\sqrt{2}}\left[(\sigma_x-\sigma_y)^2+(\sigma_y-\sigma_z)^2+(\sigma_z-\sigma_x)^2+6(\tau_{xy}^2+\tau_{yz}^2+\tau_{zx}^2)\right]^{\frac{1}{2}} \qquad 3\text{-}8)$$

For the 2D case, the principal stresses will be as follows:

$$\sigma_{1,2} = \frac{\sigma_x+\sigma_y}{2} \pm \frac{1}{2}\sqrt{(\sigma_x-\sigma_y)^2+4\tau_{xy}^2}$$

Based on that Von Mises stress in X, Y plane is:

$$\sigma_e = \sqrt{(\sigma_x+\sigma_y)^2-3(\sigma_x.\sigma_y-\tau_{xy}^2)}$$

$$\sigma_z = \tau_{yz} = \tau_{zx} = 0$$

3.6.2. Tresca Yield Criterion

The Tresca yield criterion is another model of a basic criterion used for defining the maximum stress of material before yielding. Estimating yielding with Trescas method leads to a lower result compared to the von Mises method. It is generally recognized as a more conservative judgment on failure. Furthermore, it is understood as the greatest shearing stress yield criterion.

This criterion states that plasticity occurs in a 3D condition when the value of the shear stress is equal to the yielding stress of the 1D state.

$$\sigma_1 = Y$$
$$\sigma_2 = Y$$
$$\sigma_3 = Y$$
$$\tau_{max} = \frac{Y-0}{2} = \frac{Y}{2}$$

Maximum shear stresses in the 3D state:

$$\tau_1 = \frac{|\sigma_2-\sigma_3|}{2}$$
$$\tau_1 = \frac{|\sigma_3-\sigma_1|}{2}$$
$$\tau_1 = \frac{|\sigma_1-\sigma_2|}{2}$$
$$\tau_{max} = \max(\tau_1, \tau_2, \tau_3)$$

If we equalize previous relations, we find the Tresca yield criterion:

$$\sigma_2 - \sigma_3 = \pm Y$$
$$\sigma_3 - \sigma_1 = \pm Y$$
$$\sigma_1 - \sigma_2 = \pm Y$$

The following figure shows the Tresca and Von Mises criteria for plane case

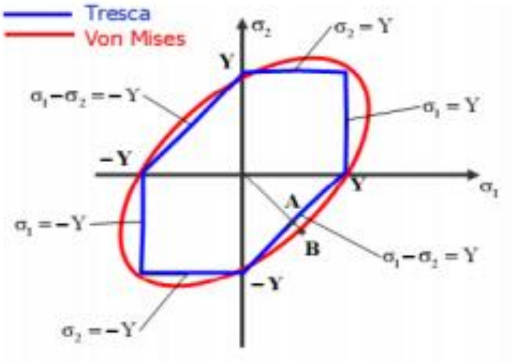

Figure 3-12 Tresca and Von Mises yield surface

3.7. Material Properties

The main goal of the current study is to clarify the relations and characteristics of the UHPCs beams. The nonlinear behavior of the model should be represented in a way that facilitates the process of numerical analysis to simulate the structural behavior of beams.

3.7.1. Concrete

Concrete is a semi-brittle material, and its behavior in compression is different from its behavior in tension. In tension, the stress-strain curve for concrete is approximate linearly elastic up to the maximum tensile strength. As the cracks initiate, the concrete strength declines steadily to zero [47] [48] [49] [50]. In compression, the stress-strain curve for concrete is linearly elastic up to approximately 30% of the maximum compressive strength. Over this point, the stress develops steadily up to the maximum compressive strength σ_{cu}. After that, the curve drops into a softening region, and finally, at an ultimate strain ε_{cu} crushing failure happens [51] [52]. Figure 3-13 presents typical uniaxial compressive and tensile stress-strain curve for concrete.

UHPC behaves more linearly than standard concrete at the same stress level but exhibits a more brittle behavior in the second part of the stress-strain curve after maximum compressive strength.

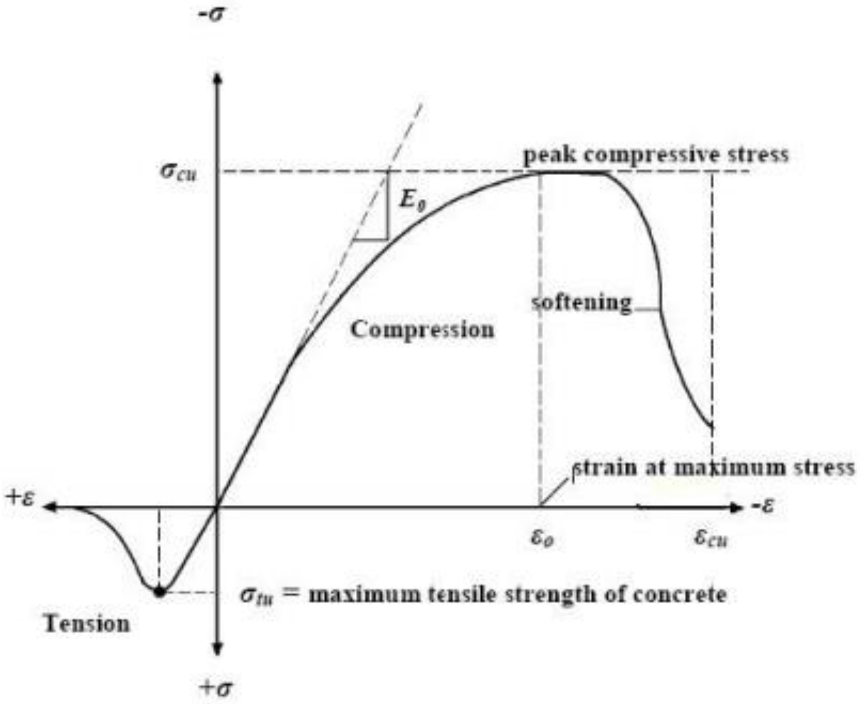

Figure 3-13 Typical stress-strain curve for concrete [47]

After yield, Figure 3-14, plastic behavior starts which permanently deforms the UHPFRC. Based on the properties of the fiber reinforcement, the plastic behavior will regularly either soften or harden the UHPFRC. For UHPC with 0% fiber, the strain range between yield point and failure is smaller corresponded to standard concrete, hence showing more brittle behavior [53].

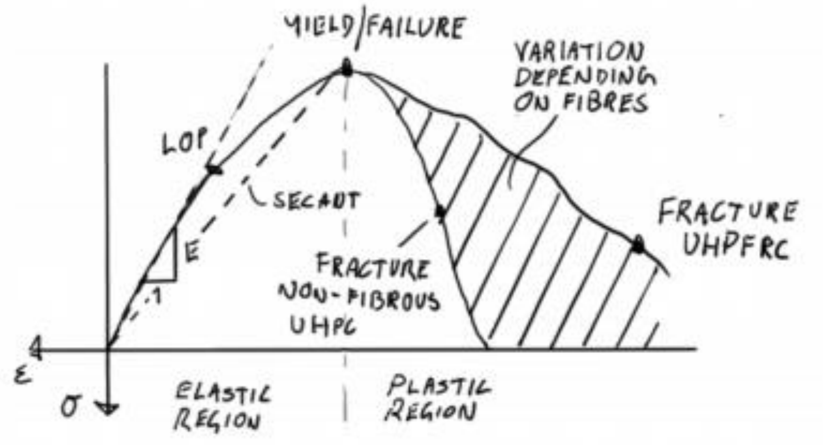

Figure 3-14 stress-strain diagram of UHPFRC with strain softening post-yield behavior [53]

FEM Input Data

As input data For concrete, ANSYS needs the following material characteristics:
Elastic modulus (Ec).
Ultimate uniaxial compressive strength (f’c).
Ultimate uniaxial tensile strength (modulus of rupture, fr).
Poisson’s ratio (ν).
Shear transfer coefficient (βt).
Compressive uniaxial stress-strain relationship for concrete.

Elastic modulus, Ultimate uniaxial compressive strength, modulus of rupture and Poisson's ratio were found based on laboratory test results. These results are listed in the method section. Poisson's ratio for UHPC was assumed to be 0.2 [6].

The shear transfer coefficient, βt, describes cases of the crack face. βt is between 0.0 to 1.0, with 0.0 expressing a smooth crack (complete loss of shear transfer) and 1.0 expressing a sharp crack (no loss of shear transfer) [45]. Several preliminary analyses were considered in this study with several values for the shear transfer coefficient. Many articles indicate to work performed by Kachlakev [54] who states the values for open cracks to be 0.2. For closed cracks value, it was also proposed and set to 0.8.

A tensile stress relaxation ratio at cracking can also be set. The default value of 0.6 is used in analyses [45].

Compressive Uniaxial Stress-Strain Relationship for Concrete

Laboratory experiments indicate that a uniaxial Stress-Strain relationship of compression in concrete has a nonlinear behavior even at low-stress levels. Several mathematical formulas are available to represent this behavior. One of these formulas is the mathematical equivalent of the second-order parabolic, starting from the elastic phase to the peak of the compressive stress at εc2 and then the linear relationship to the maximal strain at εcu2 as in Figure 3-15. This formula is provided from Eurocode 2 as follows [55]:

$$\sigma_c = f_{cd}\left[1-\left(1-\frac{\varepsilon_c}{\varepsilon_{c2}}\right)^n\right] \; for\; 0 \leq \varepsilon_c \leq \varepsilon_{c2} \qquad (3\text{-}9)$$

$$\sigma_c = f_{cd} \; for\; \varepsilon_{c2} \leq \varepsilon_c \leq \varepsilon_{cu2}$$

Where,

ε_{c2}: is the strain at reaching the maximum strength.

ε_{cu2}: is the ultimate strain.

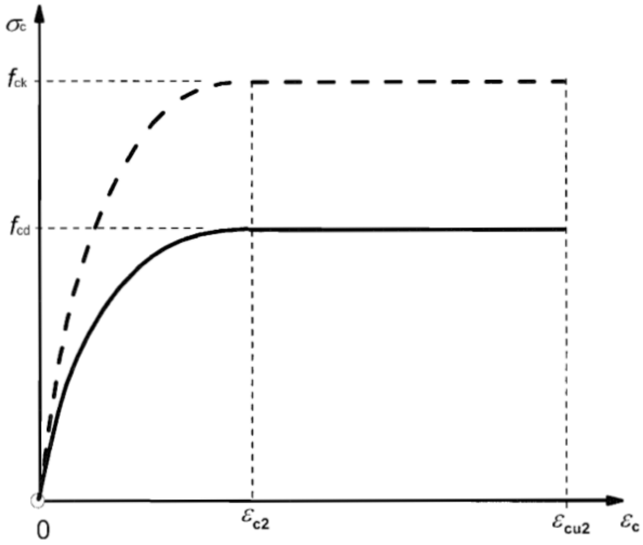

Figure 3-15 Parabola-rectangle diagram for concrete under compression [55]

UHPC has a high compressive strength between 150-250 MPa, but greater strength may also be achieved. The compressive strength is slightly affected by fiber reinforcement; whereas, the stress-strain relationship of compressive loading is significantly influenced by the fiber content [56].

However, the correct stress-strain response is remarkably challenging to accomplish due to the unstandardized mixture design of concrete which is, in turn, a heterogeneous material. In Figure 3-16 one can see Graybeal's research results which were performed on cylinder compression tests of UHPFRC [8]. An understanding of what a typical response would look like can be obtained out of his result. The non-linear relation between stress and strain may be then determined as follows;

$$f_c = \varepsilon_c E(1-\alpha) \qquad \text{3-10)}$$

$$\alpha = a e^{\frac{\varepsilon_c E}{b f_c'}} - a \qquad \text{3-11)}$$

Where,
f_c: Actual stress.
ε_c: Actual strain.
α: The percent stress decrease from linear elastic behavior.
E: Modulus of elasticity.
f_c': Compressive strength experimentally determined 28-day.

The strain at peak compressive strength can then be predicted as in Table 3-1.

Table 3-1 a and b values to draw the stress-strain curve [8]

	Steamed specimens at 90 degrees for 48 hours	Untreated specimens
a	0.001	0.011
b	0.24	0.44

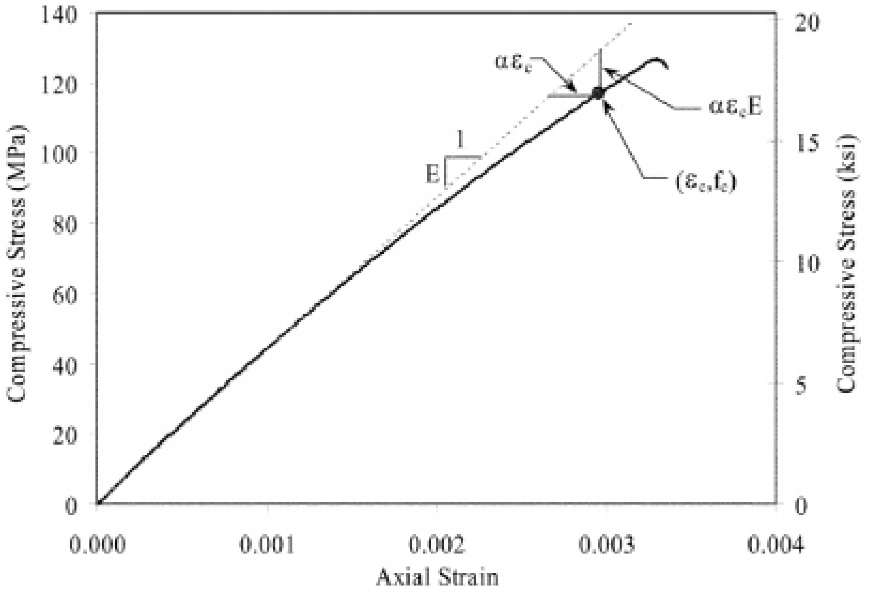

Figure 3-16 Typical stress-strain response for UHPFRC [8]

Modulus of elasticity

In 2007 Benjamin Graybeal [8] fulfilled research on the stress-strain curve of UHPFRC and the correlation between compressive strength and the modulus of elasticity. Three linear equations illustrating the relationship linking the E-module and the compressive strength at 28 days are shown, the first for normal strength concrete and the other two for UHPFRC. The equations that related to UHPFRC may be used in our case, but it is suited for compressive strength higher than 150 MPa.

$$E = 4730\sqrt{f_c'}\ (MPa) \qquad \text{3-12)}$$

$$E = 3320\sqrt{f_c'} + 6900\ (MPa) \qquad (3\text{-}13)$$

$$E = 19000\sqrt[3]{\frac{f_c'}{10}}\ \ (MPa) \qquad (3\text{-}14)$$

Following ASTM C469 at ages from 1 to 56 days, Graybeal conducted his compressive strength test on cylinders under different curing regimes. It was obvious that the modulus of elasticity for specimens cured under standard condition is smaller than those steamed cured, 42.7 GPa AND 50 GPa at 28 days, respectively. Whereas, the average measured values for modulus of elasticity under direct tension tests were 51.9 GPa for steam-treated specimens and 47.6 GPa for untreated specimens.

Graybeal proposed the following equation to calculate the modulus of elasticity for specimens which have compressive strength between 28-193 MPa [57];

$$E = 3840\sqrt{f_c'} \qquad (3\text{-}15)$$

where E: is the modulus of elasticity in MPa and f_c': UHPC compressive strength in MPa.

Failure Criteria for Concrete

When concrete exposed to stress, it shows resistance, but when these stresses reach their critical value, the concrete begins to fracture and fails. Concrete failure can be classified as cracking, crushing or both.

In 1974, Willam and Warnke formulated mathematical relationships for the failure criterion of concrete under multiaxial stresses as the following:

$$\frac{F}{f_c'} - S \geq 0 \qquad (\ 3\text{-}16)$$

Where:
F: The main stress function.
S: The surface function of the failure.

Both cracking and crushing failure modes are considered for the two input strength parameters – i.e., ultimate uniaxial tensile and compressive strengths – are needed to define a failure surface for the concrete. Consequently, a criterion for the failure of the concrete due to a multi-axial stress state can be calculated [58].

The function of F expresses the principal stresses ($\sigma_1 \geq \sigma_2 \geq \sigma_3$) while the surface function of S is defined by five coefficients, in addition to the hydrostatic pressure (σ_h^a). When the failure criterion is met (previous equation), the concrete cracks or crushes.
The relation between the main stress (F) and the surface of failure (S), as shown in Figure 3-17 and Figure 3-18, are expressed by:

$$\sigma_1 = Max(\sigma_{xp}, \sigma_{yp}, \sigma_{zp})$$

$$\sigma_3 = Min(\sigma_{xp}, \sigma_{yp}, \sigma_{zp})$$

Willam and Warnke's model is governed by 5 strength parameters:
f_c': Uniaxial compressive strength.
f_t': Uniaxial tensile strength.
f_{cb}: Biaxial compressive strength.
f_1: Uniaxial compressive strength at hydrostatic pressure σ_h^a.
f_2: Biaxial compressive strength at hydrostatic pressure σ_h^a.

The surface of the failure can be represented by two factors: uniaxial compressive and tensile strength, suggested by Willam and Warnke by the values below. These values are used when the following condition is met:$|\sigma_h| \leq \sqrt{3}f_c'$:

$$f_{cb} = 1.2f_c'$$

$$f_1=1.45f_c^{'}$$

$$f_2 = 1.725f_c'$$

The failure of the concrete is classified into four domains according to the type of applied stresses. Each domain depends on the stress function and the surface function of the failure to achieve the equation aa.

1- $0 \geq \sigma_{xp} \geq \sigma_{zp} \geq \sigma_{yp}$ (Compression- Compression- Compression)
2- $\sigma_{xp} \geq 0 \geq \sigma_{zp} \geq \sigma_{yp}$ (Tension- Compression- Compression)
3- $\sigma_{xp} \geq \sigma_{zp} \geq 0 \geq \sigma_{yp}$ (Tension- Tension- Compression)
4- $\sigma_{xp} \geq \sigma_{zp} \geq \sigma_{yp} \geq 0$ (Tension- Tension- Tension)

For instance, if σ_{xp} and σ_{yp} are both negative (compressive) and σ_{zp} is slightly positive (tensile), cracking would be predicted in a direction perpendicular to σ_{zp}. However, if σ_{zp} is zero or slightly negative, the material is assumed to crush [45].

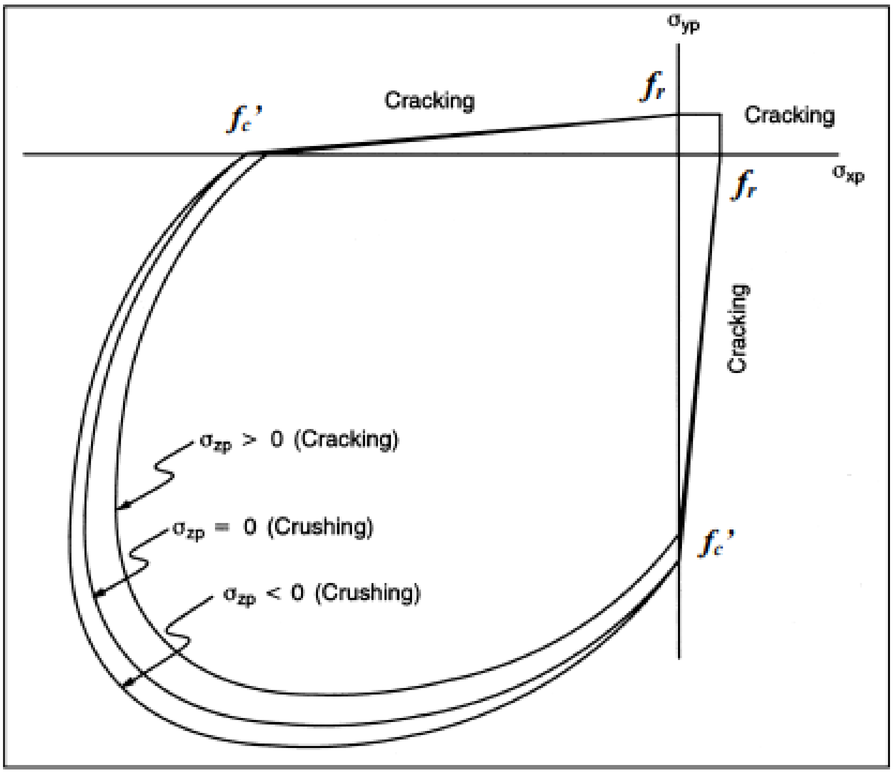

Figure 3-17 3-D failure surface for concrete [45]

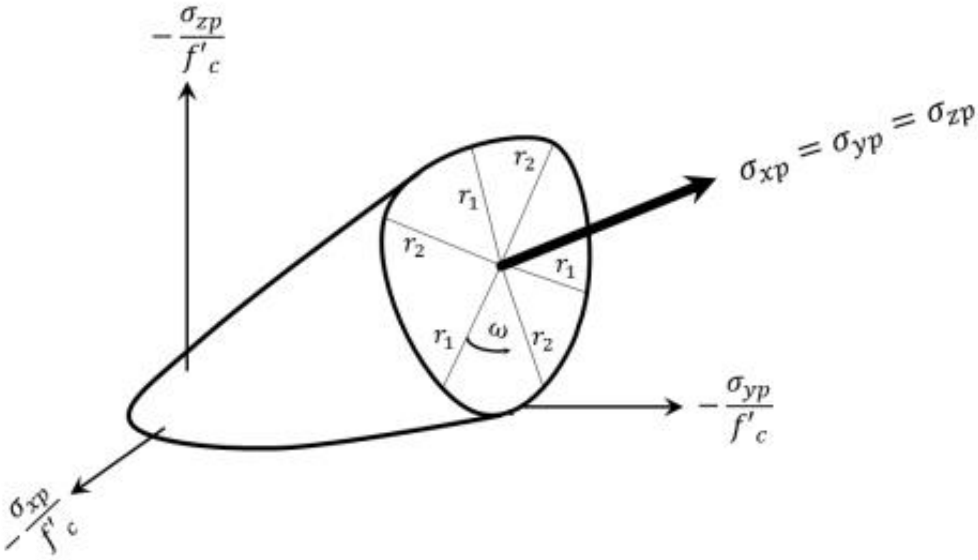

Figure 3-18 Three-dimensional failure surface in the principal stress space [45]

If equation (3-16) is not achieved, there is no crushing or cracking. Otherwise, the material will crack when the principal tensile stress in any direction lies outside the failure surface. Crushing occurs when all principal stresses lie outside the failure surface where compressive and the elastic modulus is set to zero. After cracking, in the direction parallel to the principal tensile stress direction, the elastic modulus of the concrete element is set to zero; consequently, the elastic modulus is set to zero in all directions [45].

In ANSYS, the parameters of influence in this model are the tensile strength in concrete (fr) (rupture modulus), the uniaxial compressive stress-strain curve for concrete, the shear transfer coefficient in open and closed cracks, the concrete elasticity modulus (E_c), and Poisson's ratio (v). It is clear that the first and second parameters have the most significant impact on the yield surface.

Throughout this study, it was noticed that if the crushing capability of the concrete is switched on, the crushing of the concrete began to grow in elements placed directly under the loads. Consequently, nearby concrete elements crushed within various load steps as well.

In a compression experiment, the specimen is subjected to a uniaxial compressive load. Secondary tensile strains caused by Poisson’s impact happen perpendicular to the load. Because concrete is comparatively weak in tension, these generate cracking and the ultimate failure [59] [60]. However, in this study, the crushing capability was kept on, and the failure of the finite element models was dominated by cracking and crushing of the concrete.

3.7.2. Crack modeling

Ngo and Scordelis [61] and Rashid [62] started the numerical simulation of concrete breakage in the late 1960s. They proposed discrete crack and smeared crack models, respectively. The discrete crack model represents the initiation and propagation of dominant cracks. On the other hand, the smeared crack model indicates that in concrete several small cracks gathered and later form one or more dominant cracks due to its heterogeneity and the presence of reinforcement.
The Cracking Discrete model is used in the analysis of simple concrete beams. The crack is represented by a physical separation along the element boundaries and nodes on either side of the crack as in Figure 3-19. However, the reason for limiting its use in the present study is the need to change the coordinates of the nodes of the elements by re-meshing after each development in the cracking process [61].

The second model is known as the Smeared Cracking model, which has been introduced by Rashid 1968. Through this type of model, an indeterminate number of cracked and parallel segments can be represented in the finite element as in Figure 3-20. The element is yet treated as a continuum. Hence there are no separations of elements and no need to make re-meshing for the model.
As a result, the Smeared Cracking model is used in most analytical studies of concrete members that use the finite element method, because there is no need to change the characteristics of the finite element during the analysis process through the crack's propagation in the concrete, but the relationship of (stress-strain) is updated in the concrete stiffness matrix when the cracks occur.
The Smeared Cracking was adopted in this study using the ANSYS software to represent cracks in concrete. To give a complete picture of this model, it is necessary to refer to the tensile strength, shear coefficient, opening and closing of the crack.

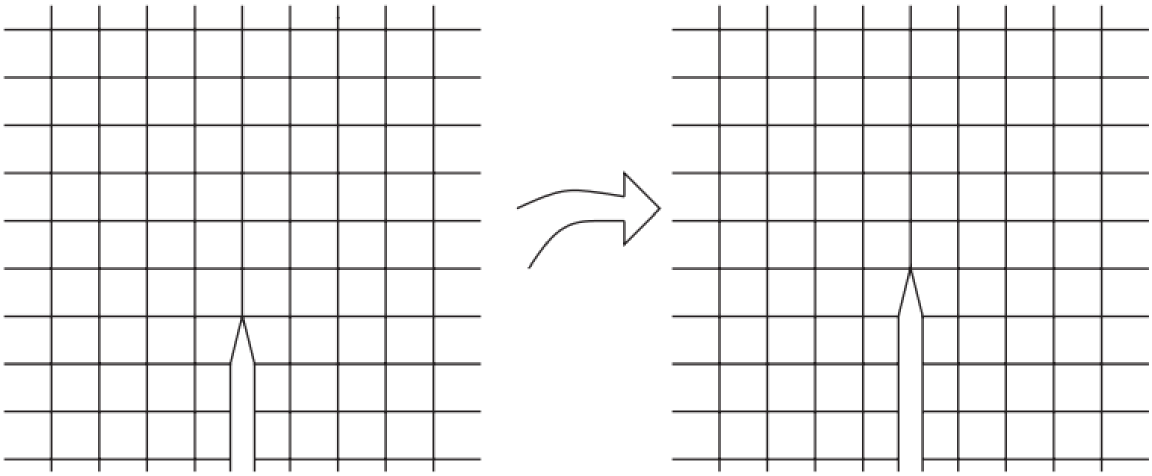

Figure 3-19 Early discrete crack modeling [63]

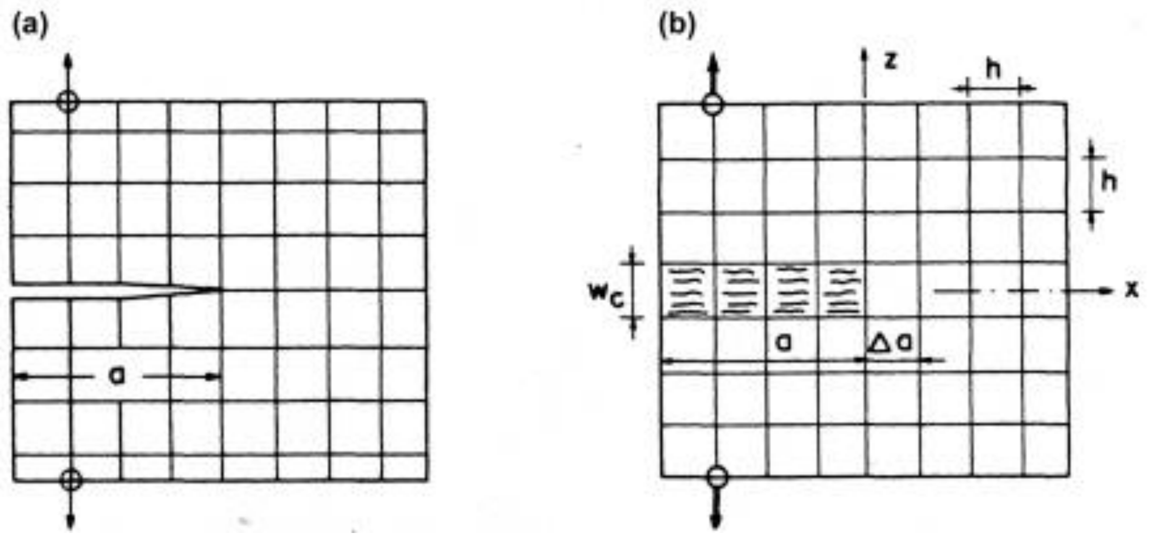

(a) (b)

Figure 3-20 (a) discrete crack model (b) smeared crack model [64]

3.7.3. Tension stiffening [65] [66] [67]

One of the most important mechanisms between concrete and reinforcing bars or fibers is the formation of cracks when both are exposed to tensile. A relative movement occurs between reinforcement and concrete while opening the crack resulting in shear forces.

These shear forces in the contact area between reinforcing bars and concrete, produce tension stresses in the concrete through the area between adjacent cracks. These tensile stresses are involved in the overall rigidity of the model. The rigidity resulting from tensile strength is therefore of great importance in reinforced concrete beams.

This lead to understanding the “stress relaxation” expression from Ansys. As from the cracks that will be formed in the concrete, a specific amount of tensile stress will be released from the section. This case is called “stress relaxation”. It serves to quicken the convergence of the computations throughout the crack period, represents the real behavior of concrete and helps stabilize the solution.

The amount of tensile stress relaxation can be input as a constant. This method was used in most analytical studies, and this method was used in the current study. ANSYS allows modeling the tensile strength of the reinforced concrete with the triangular model as in Figure 3-21.

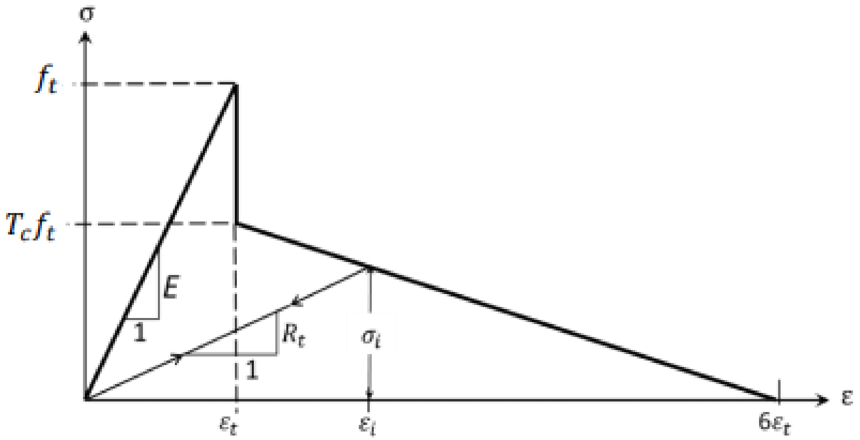

Figure 3-21 Post-cracking model of concrete due to tension [45]

Where:
f_t: Uniaxial tensile cracking strength.
T_c: Tensile crack factor (In the present study $T_c = 0.6$) [45].

3.7.4. Steel (Reinforcement and fibers)

The steel is a homogeneous material that holds the same resistance in tensile and compression. In this study, the stress-strain relationship of longitudinal reinforcement and steel fibers was indicated by an elastic-plastic behavior with strain hardening as in Figure 3-22. In the primary phase, it is assumed that the reinforcing steel has a linear elastic behavior with an initial module of elasticity (Es) up to the steel yield stress (fy). By additional loading, the material takes plastic linear behavior with strain hardening to steel ultimate strength (fu).

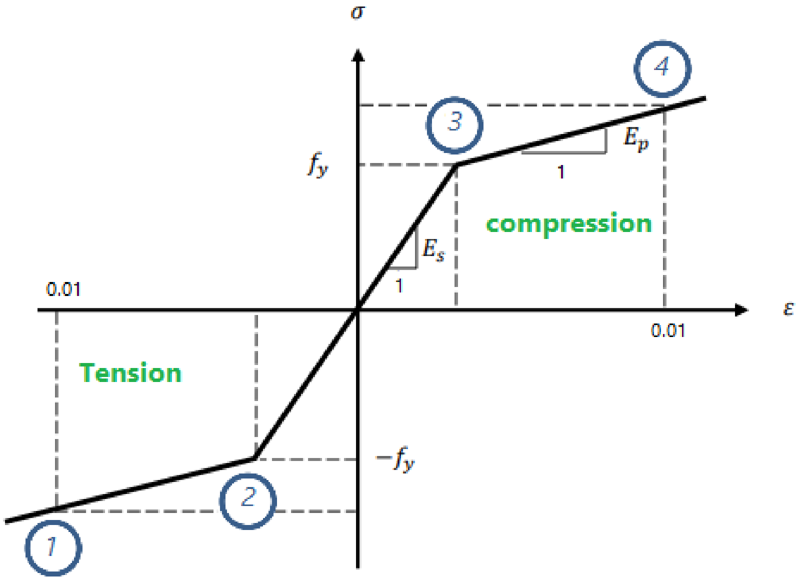

Figure 3-22 Stress-strain curve of steel in compression and tension [45]

3.7.5. Nonlinear Solution Techniques

The analysis is relatively simple for linear analysis problems by solving the equilibrium equations that represent the linear relationship between the loads and displacement. In contrast, the nonlinear analysis needs further knowledge of equation-solving methods. Several attempts and variations in approaches may be needed to achieve acceptable results for the study. The nonlinear behavior of the reinforced concrete structures is the result of the non-linear behavior of the material (stress-strain relationship), like cracking and yielding as well as the time-dependent effects like creep and shrinkage. It may also result from the significant change in the geometrical shape of the concrete. Therefore, it is the most reliable prediction of the response in a structure, but it is also very time-consuming [68].

General procedure for nonlinear solution

In linear elastic issues, the primary solution is to solve a set of algebraic equations in which the displacement vector is unknown as in the equation:

$$\{F\} = [K]\{\delta\} \qquad (3\text{-}17)$$

This method cannot be followed by nonlinear behavior. The K matrix is a function in terms of the properties of the material and the transitions of the building together, meaning that it is constantly changing. Therefore, the nonlinear system of equations must be solved iteratively until equilibrium has been reached. To perform this, ANSYS offers the well-known iteration schemes; Newton-Raphson.

The total load must be divided into several load increments (sub-steps). At the end of each step, the stiffness matrix is modified to reflect the nonlinear behavior before moving forward to the next step. For modifying and updating the stiffness matrix, ANSYS uses Newton-Raphson iterations method where it checks the convergence at the end of each step considering the tolerance limits. Newton-Raphson approach is shown in Figure 3-23.

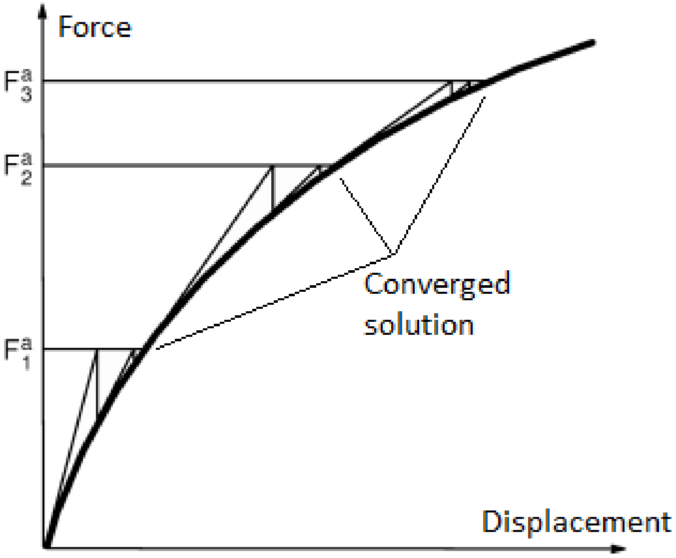

Figure 3-23 Newton-Raphson solution [45]

Convergence Criterion

Newton-Raphson method estimates the difference between the loads corresponding to the element stresses and the applied loads. Afterward, the program provides a linear solution and checks for convergence. If convergence criteria are not met, the stiffness matrix is updated, and a new solution is achieved. This iterative procedure continues until the problem converges [45]. If there is a variation from the essential path, the iterative procedure will be exhausted without reaching the required accuracy, and the solution will be interrupted and stopped.

In this study, the convergence criteria were based on the L2 norm. The L2 norm is the square root of the sum of the unbalanced forces or the increase in displacement; it is also called the "Euclidean norm". The convergence tolerance limits were raised to 0.5% for force checking, and 5% for displacement checking since the convergence of solutions was challenging to obtain due to the nonlinear behavior of reinforced concrete.

Failure Determination for FE Models

Non-linear analysis of reinforced concrete beams under static loads should include a mechanism to be terminated upon failure. In experimental tests, the failure occurs when no additional loads are recorded. This occurs in the numerical analysis when the iterative procedure continues without reaching convergence in solution. It is, therefore, necessary to identify an appropriate mechanism to stop the analysis.

Figure 3-24 illustrates the load-deflection curve of an example beam with four zones presenting various reinforced concrete behavior. In this study, the load step sizes were adjusted to achieve the convergence behavior of the models.

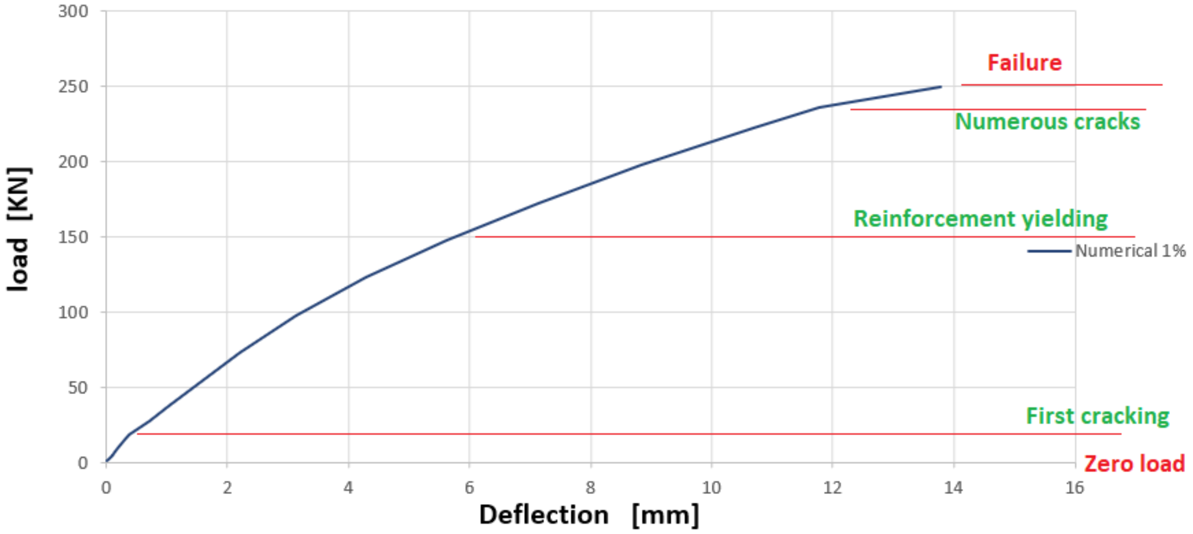

Figure 3-24 load-deflection curve of an example beam

4. Research question

This master thesis aims to provide a study on the issue of Ultra-High Performance FibreReinforced Concrete. This field is very wide. Therefore this thesis will attempt to concentrate on an individual part which is shear behavior and investigate it in details as the time permits. The thesis is a continues of our work that was held in the first semester within UHPC structural performance as well as material properties, and it will be the basis for further material advancement within these focus field. The thesis is mainly relevant for the development of UHPFRC and can additionally assist in achieving new structural theory concepts. Based on that, our main research question is as follows:

How to analyze the steel fiber content effect on the shear behavior of Ultra-High-Performance Concrete (UHPC)?

4.1. Sub-questions

- **How does the different fiber contents by volume (V_f = 0%, 0,5% and 1%) influence shear behavior of UHPC?**
- **How to build in a numerical model of an UHPC-beam with the help of Ansys?**
- **To what extent can some of the available formulas in literature predict the shear strength of UHPC beams?**

4.2. Limitation

1- The conducted analyses are based on one single type of fibre, namely a short straight steel fibre.
2- The capacity of the test machines available at UiA will determine how large beams that can be molded and tested.
3- The study considers one type of beams; same shear span and cross-section.
4- Limitations in the laboratory, both regarding time and materials.
5- Low amount of steel fibers and no shear reinforcement were implemented due to the capacity of the test machine so that a shear failure can be obtained.
6- The used material models were found directly in ANSYS.

5. Case/Materialer

5.1. Case

This thesis investigates the short steel fiber effects on the shear strength of UHPFRC beams. To answer the research question, a complementary work on pre-designed beams by us in our preliminary report (Annex D) should be carried out. The work will include applying a four-point bending test (Figure 5-1) to determine the shear capacity on beams F1, G1 and H1.

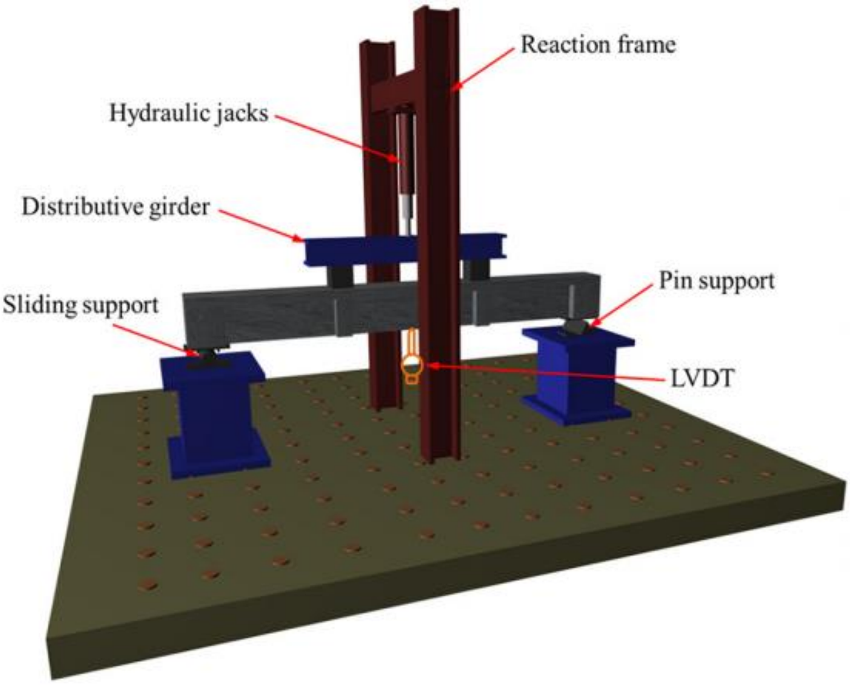

Figure 5-1 Four-point bending test setup [69]

Also, the numerical solution will consider two cases. The first one is to calibrate the beams that have been cast in the first semester; C1, C2, D1, D2, E1, and E2 (Annex D). The missing parameters in this case such as cylinders compressive strength, E-module, and stress-strain curves will be determined by using different formulas. The second case is to calibrate the beams that have been cast this semester; F1, G1, and H1 by using the results of this semester tests on the new specimens (cubes, cylinders, and prisms).

The mixing procedure for UHPC is quite similar to standard concrete. However, extra energy is required to fulfill the experiment. Therefore, high power mixer is needed to manage the procedure without overheating the mix. In our case, a Zyklos rotating pan mixer is utilized to carry out the mixing, Figure 5-2.

Figure 5-2 The used mixer in our experiments- Zyklos

5.2. Material

As shown in Figure 5-3, the used materials are Alborg rapid cement, Elkem micro silica, Dynamon SX-N superplasticizer, Dramix fibers, Velde filler, Water, tensile reinforcement and one side partial inclined shear stirrups. In addition, straight high strength steel fiber was used (13 mm long, 0.2 mm diameter and specified tensile strength of 2700 MPa), and longitudinal steel reinforcement with a yield point of 600 MPa.

Figure 5-3 UHPC materials that were used in the lab.

5.3. Recipe

The mix recipe of UHPC is developed by the University of Agder and provided in Table 5-1.

Table 5-1 UHPFRC recipe by University of Agder (UiA)

	0% Fiber	0.5% Fiber	1% Fiber
	Kg/m^3	Kg/m^3	Kg/m^3
Cement	727,709	724,071	720,432
Microsilica	181,930	181,020	180,111
filler(mellom)	1237,099	1230,913	1224,728
Water	144,380	143,658	142,936
SP	72,770	72,406	72,042
Steel fiber	0,000	39,000	78,000

A summarized of our results from the preliminarily report (Annex D) are shown in Table 5-2. The tests were held at 14 days after casting.

Table 5-2 Average properties results of UHPC specimens

Fibre volume %	Flowability (cm)	Compressive strength of cubes (MPa)	Flexural strength of small-scale prisms (MPa)
0	16.9	92	10.1
0.5	17.9	108	13.9
1	15.7	105	18.9

5.4. Casting program

5.4.1. Specimens

The casting program includes three types of fibre volume;

Type F With 0% fiber.
Type G With 0.5% fiber.
Type H With 1% fiber.
Type I With 0% fiber.
Type J With 0.5% fiber.
Type K With 1% fiber.

The number of specimens for every type is shown in Table 5-3.

Table 5-3 Number of specimens

Casting	Beam (cm) 10x20x150	Cube (cm) 10x10x10	Cylinder(cm) 10x20	Prism (cm) 15x15x60	Prism (cm) 4x4x16
F	1	6	6	3	6
G	1	6	6	3	6
H	1	6	6	3	6
I	-	-	12	-	-
J	-	-	12	-	-
K	-	-	12	-	-

5.4.2. Beams

Type F1 With 0% fiber, longitudinal reinforcement and inclined stirrups on one side.
Type G1 With 0.5% fiber, longitudinal reinforcement and inclined stirrups on one side.
Type H1 With 1% fiber, longitudinal reinforcement and inclined stirrups on one side

6. The method

This chapter covers the used methods to answer the research question. Several approaches have been used to study the shear behavior of structural elements. Background knowledge regarding the topic was first to gain from literature study to find how to address the different manners. Quantitative and qualitative methods have been adopted in the form of laboratory tests, numerical simulation and shear strength calculations. ANSYS has been applied to cover the finite element analysis. The procedure in ANSYS presented later in this chapter which is based on the results from our preliminary report and experimental work in this thesis.

6.1. Literature review

To get deep knowledge related to the main topic of the research, the emphasis was placed on several previous scientific articles within UHPC field. These articles should also be published in a scientific journal during the last few years. Only old researches on procedures and methods, such as the steps of conducting laboratory and statistical analysis and other methods that have been established and not been modified, can be utilized.

6.2. Experimental program

The experiments procedure had been described in more details within our preliminarily report (Annex D, section 6.5) and will be summarized in this section.

6.2.1. The test specimens

Three types of beams with longitudinal and no shear reinforcement, were investigated in this study. The longitudinal reinforcement, shear span to depth ratio and concrete type for each type of beams were kept constant. The variable parameter was the fibre volume;

Type F1 With 0% fiber, longitudinal reinforcement and inclined stirrups on one side.
Type G1 With 0.5% fiber, longitudinal reinforcement and inclined stirrups on one side.
Type H1 With 1% fiber, longitudinal reinforcement and inclined stirrups on one side.

6.2.2. Gravity and Absorption of the fine aggregate

The moisture content in aggregates can have a severe influence on the concrete compressive strength and durability. This influence is due to the moisture effect on the water/cement ratio. Therefore, identifying the moisture of aggregate may help to accurately calculate and adjust the amount of water to be added to the mix.

This semester we got a new filler with no information regarding the absorption or the gravity. Hence, these two parameters are needed to be determined to reach the right amounts in the concrete mix. AASHTO T84 / C 128 [70] is the standard method of test for the specific gravity and absorption of fine aggregate which was followed in this thesis. The relative density or specific gravity test will identify the physical properties of the fine aggregate. A change in this number will increase or decrease the amount of fine aggregate in the concrete mixture. Absorption as a measurement of water that is in the concrete pours. When the pores are filled, but there is no surface moisture, the sample is considered to be in the S.S.D condition (Saturated surface dry), i.e., the surfaces of the samples are dry. Meaning, if the moisture content is higher than the absorption limit (the aggregates are in a surface wet condition), this raises the water-to-cement ratio and affects strength and durability of the concrete mixture. While using dry aggregates with no moisture in their pores into the wet concrete mixture will absorb water from the paste and fill their pores. This lead to a reduction in the amount of available water.

Table 6-1 gives a summary of the previously mentioned cases.

Table 6-1 The moisture of fine aggregate effect on durability and strength

Over absorption limit	Filled pores+ wet surface (surface wet condition)	Less durability and strength due to more w/c ratio.
Under absorption limit	Empty pores+ dry surface	Less durability and strength due to absorbing water from the paste in the mix.
On absorption limit	Filled pores+ dry surface (S.S.D condition, Saturated surface dry)	meet the requirements of the mix.

It should be reviewing the steps of T-84 and C 128. The steps come directly from the technician's handbook. Testing fine aggregate for specific gravity and absorption is unique in the fact that it is done in two steps. First, it must to be sure that the sample is in the S.S.D condition then can proceed the rest of the experiment. The test must be done with a mold and a tamper. It will also be using a heat gun to provide a warm stream of air for getting the sample to S.S.D. To perform the contest, we want to hold the cone firmly on a flat non-absorbent surface. We do not want to add material into the cone filling it to overflowing keeping additional material over the top as necessary.

We then want to tamp the material into the mold with 25 light drops of the tamper. The temper should be approximately 5 mm above the fine aggregate for each drop. The cone should lift vertically. If moisture is still present define aggregate will retain its molded shape. However, when the fine aggregates slums slightly it is mean that the aggregate reached the saturated surface on dry condition. When the material is in the saturated surface dry condition, time for start the procedure. Figure 6-1 and Figure 6-1 illustrates the SSD condition.

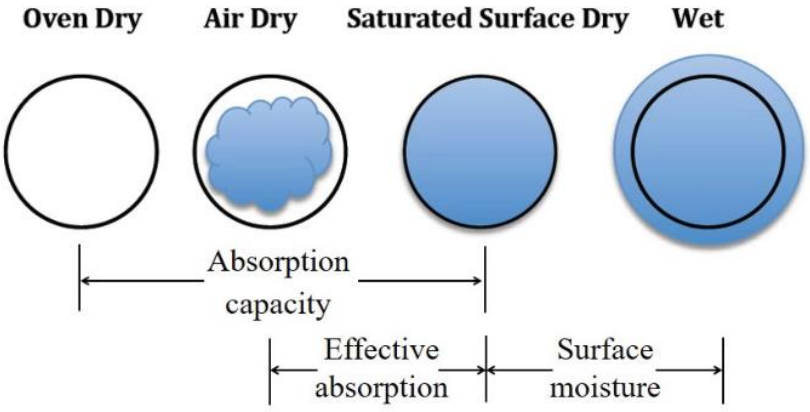

Figure 6-1 Saturated Surface Dry [71]

Figure 6-2 Saturated Surface Dry of our work in the lab

To perform the Specific Gravity and Absorption of the fine aggregate test we will need (Figure 6-3):

- Mason Jar and Lid.
- Mold (The inside diameter in the top 40 +/- 3 mm, the inside diameter of the bottom 90 +/- 3mm and height is 75 +/- 3 mm).
- Tamper (the tamper weight's 340 +/- 15 g. The Tamping face must be round and flat with a diameter of 25 +/- 3 mm).
- Heat gun.
- Sorbent surface.
- A balance (AASHTO-meet classification to M231-class G2, while for ASTM it must be accurate to 0.1 grams or 0.1% of the sample mass).
- An oven with a range of 110 +/- 5 degrees Celsius.

Figure 6-3 Types of equipment of the test

To begin the test, we want to fill a Mason Jar with water partially. Next, we want to weight out 500 +/-10 grams of saturated surface dry fine aggregate. It has to be recorded the exact amount that is weighted out. Now we want to introduce our saturated surface dry specimen into the Mason Jar. Once the symbol is into the Mason Jar, we want to reintroduce water into the Mason Jar and fill to 90% of capacity. Now that all of our materials are back into the Mason Jar then we want to roll, invert and agitate the Mason Jar. We can also use mechanical methods to ensure that we remove all of the air bubbles. Once all the air bubbles have been removed we want to adjust the water temperature if necessary, to 23 +/ - 1.7 degrees Celsius (for ASTM this is 23 + / - 2 degrees Celsius by immersion in a circulating water bath). Once this is complete, we can bring the water level back to the calibrated mark. We now want to record the weight of the Mason Jar, the specimen and the water filled to the calibration mark. All subsequent has to be weighted to the nearest 0.1 gram. We can now remove the fine aggregate from the Mason Jar, place it in a bowl and dryer to a constant mass. We draw a sample by placing it in an oven that has a temperature of 110 +/ - 5 degrees Celsius. Once we move our sample from the oven and allow to cool for a 1 + / - 0.5 hours and again record the mass of the now dry sample. We now want to fill the Mason Jar with just water back to the calibrated mark (the water temperature is 23 + / - 1.7 degrees Celsius) then recorded this way to the nearest 0.1 grams. As we have completed our physical aspects of tests, we can go ahead and do our calculations.

When we have completed our test, we should have four weights recorded as are listed:
A = Mass of Oven Dry Test Sample (gram).
B = Mass of Pycnometer Filled with Water to the calibration line (gram).
S = Mass of S.S.D Sample (gram).
C = Mass of Pycnometer with Specimen and water filled to the calibration line (gram).

Our first calculation to be to calculate the bulk specific gravity of material in the SSD condition.

The calculation for the specific Gravity of the fine aggregate:

$$\frac{\mathrm{S}}{(\mathrm{B}+\mathrm{S}-\mathrm{C})} = Specific\ Gravity\ (SSD)$$

The calculation for the Absorption of the fine aggregate:

$$\frac{\mathrm{S}-\mathrm{A}}{\mathrm{A}} \times 100\% = Absorption\ percent\ of the\ fine\ aggregate$$

6.2.3. Casting and curing

The chemical reaction between the pozzolanic particles and calcium hydroxide (Ca(OH)2) resulting calcium silicate (C-S-H). C-S-H increase the hydration rate which in turns enhanced the strength of the mixture. In other words, the small particles of pozzolan fill in the voids of the mixture which increase the density of concrete and a stronger transition zone between matrix and aggregate. On the other hand to achieve an acceptable level of hydration and confirm that the used material has Ultra- High-Performance properties, specific curing regime needs to be conducted. The curing regime includes steam treatment at 90 degrees for 48 hours to accelerate the hydration process and improve the mechanical properties [6].

Moreover, the curing regime of beams was chosen to be at 20 degrees for 14 days. Several reasons lead to this chosen including the size of the water bath and the deadline to submit the thesis.

Figure 6-4 shows the total of 104 specimens that were cast and then tested at the laboratory of Agder University (Norway).

Figure 6-4 The cast specimens

Table 6-2 gives an overview of curing regimes that the various test specimens have undergone.

Table 6-2 Curing regime

Stages	Specimens Type	Casting type	Dimension (cm)	Curing regime				
				Nr.	Time before dissembling	The °C at the water vessel	Tim at water vessel at 90° C	Time at room °C
The first stage	**Beams**	F1, G1, H1	10x20x150	3	2 days	20°C	-	14 days
	Cube	F1, G1, H1	10x10x10	9	2 days	20°C	-	14 days
	Cube	F1, G1, H1	10x10x10	9	2 days	90°C	3 days	14 days
	Prism	F1, G1, H1	4x4x16	9	2 days	20°C	-	14 days
The second stage	**Prism**	F2, G2, H2	15x15x60	9	2 days	20°C	-	14 days
	Cylinder	F2, G2, H2	10x20	9	2 days	20°C	-	14 days
	Cylinder	F2, G2, H2	10x20	9	2 days	20°C	-	28 days
	Cube	F2, G2, H2	10x10x10	9	2 days	90°C	3 days	14 days
The third stage	**Cylinder**	I1, J1, K1	10x20	18	2 days	20°C	-	14 days
	Cylinder	I1, J1, K1	10x20	18	2 days	90°C	3 days	14 days

6.2.4. Specimens

After several trials, the absorption of fine aggregate has been determined according to section 6.2.2. Hence, a water-cement ratio of 0.2 was used to the final mixture.

The compressive strength was obtained by applying the compressive test on cubes of 10 x 10 x 10 cm and on cylinders (diamerer= 10 cm and height= 20 cm) according to NS-EN 12390-3:2009. The three-point bending test was implemented on small-scal prisms to obtained flexral strength according to EN 196-1:2016. The results of the compressive and flexural strength test will be used later in addition to the previous results in Table 5-2 as inputs in ANSYS.

All the specimens were covered with plastic sheets for 24 hours at laboratory temperature; then the specimens were taken out from the molds and stored into a water bath until the test day at 20 degrees. Eighteen cubes were cured at 90 degrees for 48 hours and then stored at water bath until test day.

The reason for curing 18 cubes and 18 cylinders at 90 degrees as in Table 6-2 is that we had three mixing stages. The UHPC properties, therefore, should be confirmed in the three-stage, where;

The first stage includes,
F1 0% fibre volume
G1 0.5% fibre volume
H1 1% fibre volume
The second stage includes;
F2 0% fibre volume
G2 0.5% fibre volume
H2 1% fibre volume
The third stage includes;
I1 0% fibre volume
J1 0.5% fibre volume
K1 1% fibre volume

The efforts were set to produce the same concrete of the three stages as possible in order to achieve the same properties of concrete such as compressive strength.

Testing procedures on fresh concrete, small- scale prisms (4x4x16)cm, large- scale beams, cubes, and cylinders are explained in detail in Annex D (section 6.5.2).

6.2.5. Modulus of elasticity

To obtain the modulus of elasticity, several cylinders were tested in the University of Agder lab according to (EN12390/13:2013). These cylinders need to be loaded up to (60%) of the ultimate cylinder compressive strength. Hence, the compressive strength test should be conducted on concrete cylinders having the same dimensions of the cylinders used to determine the modulus of elasticity before starting the modulus of elasticity test. The loading rate was (0.6 ± 0.2) MPa/sec. The test machine was connected to the software so that the load-strain curve can be drawn as well. The test will be then terminated at 60% of the ultimate load where the test parameters have to be entered to the software in order to calculate initial and stabilized secant modulus of elasticity as shown in Figure 6-5. The initial secant modulus of elasticity $(E_{c,0})$is measured at the first loading while the stabilized secant modulus of elasticity $(E_{c,s})$ is measured after three loading cycles.

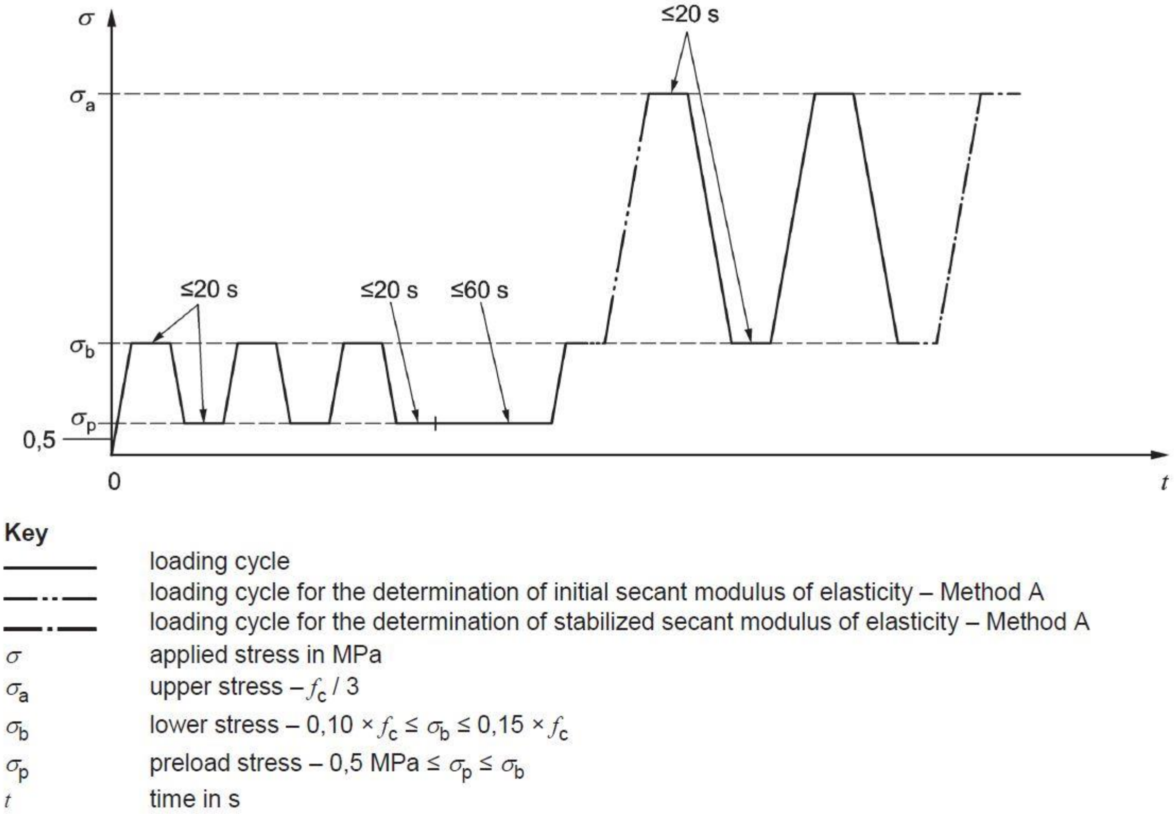

Figure 6-5 The applied cycles to determine initial and stabilized modulus of elasticity [72]

6.2.6. Poisson's ratio

It was found to be 0.19 by Bonneau et al. [73] and 0.2 by Simon [74] and 0.21 by Ahlborn et al. [75]. Hence, we chose it to be 0.2 in ANSYS.

6.2.7. DIC technique

As earlier mentioned, the DIC method was adopted to investigate the specimen deformation and to some extent the crack growth based on the camera database.

All the beams were brushed with white paint from one side and then dotted with black paint to form a random pattern of dots. The dots size was tiny where the maximum diameter was $3\mu m$.

To capture the painted specimens accurately, two anti-shading lens with 1.3” 12-megapixel sensor with micro-lenses were focused on one shear span of the beam. This span has no stirrups or inclined shear reinforcement at all. The cameras were set at a distance a bit less than one meter from the beams. To improve the capturing process, a flashlight was focused on the investigated shear span.

On the computer, the used software called Vicsnap and Vic3D which was developed by the University of South Carolina (USC). Every one second, 15 images were taken of the beams up to the failure. The resulting image provided information of the deflections in x,y and z directions as well as strains for several chosen points within the beams. The mechanism in obtaining the results is by comparing the pattern in each image with the initial reference image and by omitting any motion from the support settlement.
Figure 6-6 shows the two digital cameras and the used equipment.

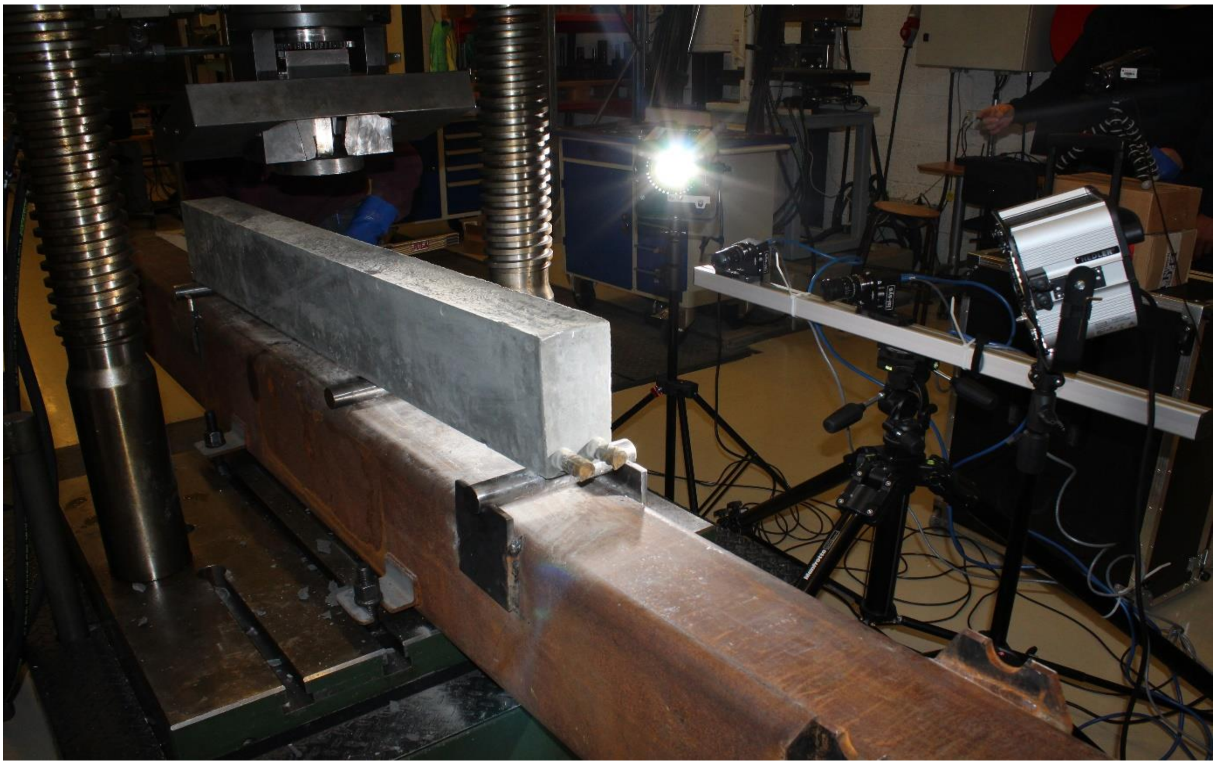

Figure 6-6 Digital image correlation system setup

6.3. Estimated shear strength based on different standards and guidelines

The shear failure in conventional concrete is difficult to be predicted correctly. This challenge is moreover identified in UHPFRC beams. Much experimental research and highly advanced analytical ways are not yet entirely described shear behavior. To be more specified, there is not enough understanding of rectangular UHPFRC beams without stirrups. Accordingly, in this section, several guidelines, and standards are utilized to investigate the shear strength of rectangular UHPFRC beams with longitudinal tension rebar and without shear reinforcement and further are linked to the results achieved from our experimental work, more details will be in the results section.

6.3.1. Australian Design Guidelines for Ductal Prestressed Concrete Beams

If the CMOD test result cannot be obtained, then the "Australian Guideline" may be used without the need for any test result to estimate the shear capacity.

The following method provides the shear strength of a prestressed concrete section [76]:

$$V_u = V_{uc} + V_{us} + P_s \qquad (6\text{-}1)$$

Where V_{uc} is the contribution of the concrete to the shear strength; V_{us} is the contribution of the transverse shear reinforcement; Pv is the transverse component of the prestressing force. When shear reinforcement and inclined tendons are out, then the shear strength for beams are defined from:

$$V_u = V_{uc}$$

To get the highest value based on the uncracked section in flexure. The following equations are given:

$$v_c = 5 + 0.13\sqrt{f_c'}$$

$$V_c = v_c \times b_w \times d \qquad (6\text{-}2)$$

6.3.2. Design guideline ACI 544 (1988)

This design code gives the nominal shear strength V_n for FRC members as [77]:

$$V_n = \frac{2}{3} f_{ct} (\frac{d}{a})^{0.25} b_w d \qquad (6\text{-}3)$$

Where,

f_{ct}: the tensile strength of FRC.
a: is the distance from the loading point to the support.
d: the effective depth.
b_w: the web width.

6.3.3. Narayan and Darwish (1987) Model

They proposed that the shear capacity of fibre reinforced concrete beam can be calculated as follows [78]:

$$V_u = e\left[0.24 f_{spfc} + 80\rho(\frac{d}{a})\right] + v_b \ \ (MPa) \qquad (6\text{-}4)$$

where,

V_u= shear capacity (MPa).
ρ = flexural reinforcement ratio.
d = effective depth of the beam.

a = shear span.
e = arch action factor (1.0 for a/d> 2.8 and 2.8 d/a for a/d< 2.8).
f_{spfc}= split cylinder strength (MPa).

$$f_{spfc} = \frac{f_{cuf}}{20 - \sqrt{F}} + 0.7 + \sqrt{F}$$

Where,
f_{cuf} = cube strength of fibre concrete.
$F = (\frac{L_f}{D_f})v_f d_f$, in which,
L_f = fibre length.
D_f = fibre diameter.
v_f = The volume fraction of steel fibre.
d_f = bond factor (0.5 for round, 0.75 for crimped, and 1.0 for independent fibre).
Again, $v_b = 0.41\tau F$
Where τ = average fibre-matrix interfacial bond stress (assumed to be 4.15 MPa).

6.3.4. Sharma

Sharma proposed an empirical equation for predicting the shear strength of fibre reinforced concrete beams [34].

$$V_u = kf't(d/a)^{0.25}\ (MPa) \qquad (6\text{-}5)$$

Where,
V_u = Average Shear stress at shear failure.
K = 2/3
d/a = Shear span -depth ratio.
f_t' = Tensile strength of concrete.
f_t' = 0,95(f_c')^0,5 MPa. If tensile strength is unknown.
f_t' = concrete cylinder compressive strength.

6.3.5. Ashour, Hasanain, and Wafa

They tested 18 beams made of high strength fibre reinforced concrete [34].

For a/d > 2.5

$$\mathrm{V_u} = (2{,}11\sqrt[3]{\mathrm{f'_c}} + 7\mathrm{F})(\rho\frac{\mathrm{d}}{\mathrm{a}})^{0{,}333} \quad (\mathrm{MPa}) \qquad (6\text{-}6)$$

For a/d < 2.5

$$\mathrm{V_u} = [\mathrm{Eq}\cdot(5\mathrm{a})] \times (\frac{2{,}5}{\frac{\mathrm{a}}{\mathrm{d}}}) + \mathrm{Vb}\,(2{,}5 - \mathrm{a/d}) \quad \mathrm{MPa} \qquad (6\text{-}7)$$

6.3.6. Imam and Vandewalle

They developed the following equation to predict the shear strength of standard concrete beams [34];

$$Vu = 0.6\Psi\sqrt{\omega}[\,(f'_c)^{0.44} + 275\sqrt{\frac{\boldsymbol{\omega}}{(a/d)^5}}\,]\ \ (MPa)\ \ (6\text{-}8)$$

$$\Psi = \frac{1 + \sqrt{(5.08/d_a}}{\sqrt{1 + d/(25d_a\,)}}$$

Where,

ψ size effect factor= 1.01

d_a Maximum aggregate size= 0.250 mm

ω reinforcement factor= $\boldsymbol{\rho}$(1+4F)

F fiber factor $(Lf/Df)\;Vf\;df$

df bond factor, equal to 0.50 for smooth fiber, 0.9 for deformed fibers, and 1.0 for hooked fibers.

6.4. Numerical calibration- ANSYS

Under this section, the analytical part of our thesis will be covered by applying finite element analysis. Finite element modeling was performed to calibrate the experimental results by using ANSYS v.19.2. In recent years, using computer software become quite significant to sufficiently understand the behavior of the structural elements. The reason is that finite element modeling is faster and cost-effective method if it is compared to other available methods. However, the calibration process is critical to verify that the outputs of the software are correct.

6.4.1. Experimental Beam

As it has been mentioned previously, a method based on Eurocode 2 was applied to reinforce a UHPC beam to achieve shear failure in our preliminary report (Annex D). The study introduced experimental testing of six beams from the previous work (C1, C2, D1, D2, E1, and E2) and three beams more in this semester (F1, G1 and H1) that can be utilized for calibration of finite element models.

The width and height of the beams tested were 200mm and 100mm, respectively. The length of the beam was 1500 mm with a simply supported span of 1400 mm. The tension reinforcements used were $2\emptyset25\,mm$ bars with $\emptyset16\,mm$ partial shear reinforcements on one side without stirrups. The cover was set to 2 mm in all directions. The dimensions and reinforcement details of the beam is shown in Figure 6-7.

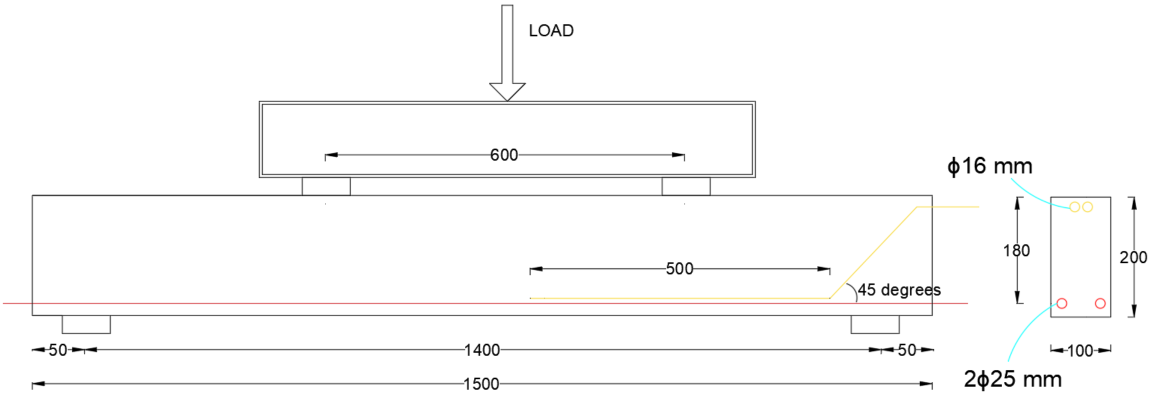

Figure 6-7 Geometry of test specimens- All dimensions are in millimeters

The area and yield stress of steel reinforcement are included in Table 6-3.

Table 6-3 Properties for Steel

Area of $\mathbf{2\emptyset25}$ ($\boldsymbol{mm^2}$)	981.747
yield stress (MPa)	600

The applied loading along with beam deflection were recorded at the midspan. The beams were loaded to shear failure as shown in Figure 6-8.

Figure 6-8 Failure in shear

Table 6-4 shows the experimental ultimate shear loads.

Table 6-4 Peak load results of UHPC beams

Fibre volume %	Beam type	Shear strength (kN)
0	C1	64.61
	C2	59.80
	F1	161.68
0.5	D1	175.33
	D2	181.18
	G1	173.4
1	E1	236.13
	E2	222.48
	H1	262.82

6.4.2. ANSYS

The calibration process on ANSYS aims to model the UHPC beams that were tested by us including 0%, 0.5%, and 1% fibre volume as shown in Table 6-4. The whole beam was simulated since there is a partial shear reinforcement on one side.

To make the model run correctly, several tasks demand to be performed by using a Graphical User Interface (GUI). This section will illustrate the different steps that were conducted to generate the model.

6.5. Element type

In this section, it shall be explained how to simulate concrete, reinforcing steel and loading plate in Ansys. The modeling process involves the creation of nodes and the elements to represent the correct size and shape of the experimental model.

6.5.1. Concrete

The solid65 element was utilized to represent the concrete. A sketch of the element is shown in Figure 6-9. This element owns eight nodes with three degrees of freedom per node – translations in the nodal x, y, and z directions. Besides, solid65 can model plastic crushing, cracking in three orthogonal directions, and deformation [45].

It is possible to add reinforcement to SOLID65 through its "real constants." This can be employed to simulate the nonlinear behavior of the reinforced concrete as well as fiber reinforcement. The "real constants" support defining three different reinforcing elements with:
1- Individual material models.
2- Volume fractions.
3-Orientations in two directions (θ, φ).

The reinforcement, across the SOLID65, is smeared and can resist tensile as well as compression forces, but it does not resist shear forces. This reinforcement and steel fiber are activated once the SOLID65 element itself cracks or crushes [45].

The ANSYS program lists a crack pattern at every implemented load step. At places of cracking or crushing in concrete elements, the ANSYS program performs circles with an octahedron outline. The first crack at the integration point is presented with a red circle outline, the second crack with a green outline, and the third crack with a blue outline [79].

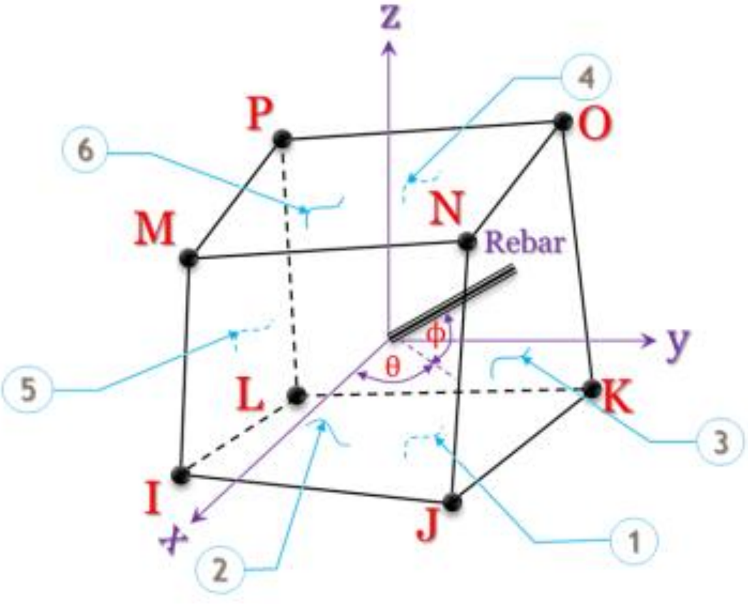

Figure 6-9 SOLID65 element with Smeared reinforcement (rebar) [45]

6.5.2. Reinforcing Steel

The reinforcement can be presented in two different ways. The smeared approach in which a longitudinal reinforcement is defined as an extra stiffness within the centroids of solid65 elements. Whereas, in the discrete approach, the steel reinforcements were simulated by defining Link section element which has two nodes. Each node has three degrees of freedom, - translations in the nodal x, y, and z directions. The element is also capable of plastic deformation [45] [80]. The geometry and node locations for this element type are shown in Figure 6-10.

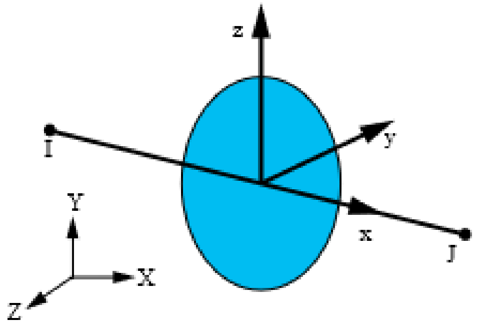

Figure 6-10 Link element geometry [46]

6.5.3. Steel plates

In this study, bearing plates were used in the loading points and supports by using solid185 element. SOLID185 is used for 3-D modeling of solid structures. It is defined by eight nodes having three degrees of freedom at each node: translations in the nodal x, y, and z directions [45]. This element (Figure 6-11) is used to avoid the concentration of stresses in areas that are exposed to high and variable forces and stresses.

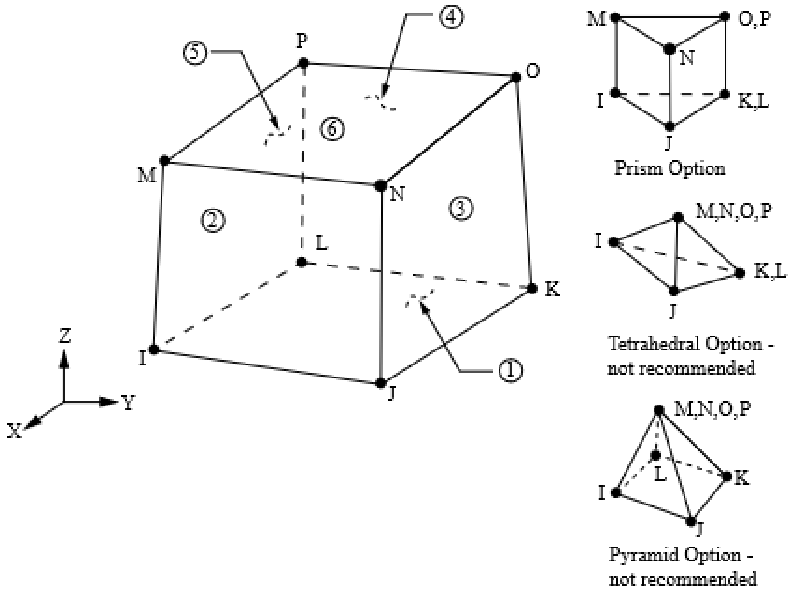

Figure 6-11 SOLID185 Structural Solid Geometry [45]

6.6. Real constant

The real constants for this model are shown in Table 6-5. As ANSYS 19.2 is utilized, no real constant exists for the Solid45 element and link section is used to represent reinforcement since LINK 8 has no real constant in this version as well (Table 6-6).

Table 6-5 Real Constants For Calibration Model

Real constant set	**Element type**	**Constants**			
150	Solid 65		Real constants for rebar 1	Real constants for rebar 2	Real constants for rebar 3
		Material number	0	0	0
		Volume ratio	0	0	0
		Orientation angle THETA	0	0	0
		Orientation angle PHI	0	0	0

Table 6-6 Link section to model the reinforcements

Section name	**Link area (mm^2)**
Stirrups	$\frac{\pi \times 16^2}{4} = 201.062$
Main bar	$\frac{\pi \times 25^2}{4} = 490.87$

The parameters in Table 6-5 can be clarified as follows; the model needs real constant to active the smeared reinforcement (embedment reinforcement) model within SOLID 65 element. ANSYS enables the user to insert three rebar materials in x, y, and z directions in the element (Figure 6-9). The material number refers to the reinforcement type. Volume ratio and orientation refer to the reinforcement percentage and direction in the element, respectively.

As the LINK section is defined in this study which represents the discrete reinforcement, zero values have been entered for all real constants to deactivate the smeared reinforcement type.

6.7. Material properties

6.7.1. Material models

The material models for 0%, 0.5%, and 1% are represented in Table 6-7, Table 6-8 and Table 6-9, respectively.

Table 6-7 Material Models in ANSYS- 0% fibre volume- C1, C2, and F1 beams

Material model number	Element type	Material properties		
150	SOLID 65	**Linear isotropic**		
		EX	38146	
		PRXY	0.2	
		Multilinear isotropic		
			Strain	Stress
		Point 1	0.001	38.146
		Point 2	0.0015	55.921
		Point 3	0.002	71.623
		Point 4	0.0025	83.285
		Point 5	0.003	87.211
		Concrete		
		Open shear transfer coef	0.2	
		Closed shear transfer coef	0.8	
		Uniaxial cracking stress	4	
		Uniaxial crashing stress	83.5	
		Tensile crack factor	0.6	
280	LINK SECTION	**Linear isotropic**		
		EX	200000	
		PRXY	0.3	
		Bilinear isotropic		
		Yield stress	600 MPa	
		Tang mod	1000 MPa	
1	SOLID 45	**Linear isotropic**		
		EX	200000	
		PRXY	0.3	

Table 6-8 Material Models in ANSYS- 0.5% fibre volume- D1, D2 and G1 beams

Material model number	Element type	Material properties		
150	SOLID 65	**Linear isotropic**		
		EX	37845	
		PRXY	0.2	
		Multilinear isotropic		
			Strain	Stress
		Point 1	0.001	37.845
		Point 2	0.0015	56.049
		Point 3	0.002	73.292
		Point 4	0.0025	88.912
		Point 5	0.003	101.819
		Point 6	0.0035	110.244
		Point 7	0.004	111.318
		Concrete		
		Open shear transfer coef	0.2	
		Closed shear transfer coef	0.8	
		Uniaxial cracking stress	12	
		Uniaxial crashing stress	107.1	
		Tensile crack factor	0.6	
280	LINK SECTION	**Linear isotropic**		
		EX	200000	
		PRXY	0.3	
		Bilinear isotropic		
		Yield stress	600 MPa	
		Tang mod	1000 MPa	
1	SOLID 45	**Linear isotropic**		
		EX	200000	
		PRXY	0.3	

Table 6-9 Material Models in ANSYS- 1% fibre volume- E1, E2 and H1 beams

Material model number	Element type	Material properties		
150	SOLID 65	**Linear isotropic**		
		EX	38495	
		PRXY	0.2	
		Multilinear isotropic		
			Strain	Stress
		Point 1	0.001	38.495
		Point 2	0.0015	56.833
		Point 3	0.002	73.870
		Point 4	0.0025	88.591
		Point 5	0.003	99.245
		Point 6	0.0035	102.838
		Concrete		
		Open shear transfer coef	0.2	
		Closed shear transfer coef	0.8	
		Uniaxial cracking stress	18.9	
		Uniaxial crashing stress	98.7	
		Tensile crack factor	0.6	
280	LINK SECTION	**Linear isotropic**		
		EX	200000	
		PRXY	0.3	
		Bilinear isotropic		
		Yield stress	600 MPa	
		Tang mod	1000 MPa	
1	SOLID 45	**Linear isotropic**		
		EX	200000	
		PRXY	0.3	

To model SOLID 65 element correctly, linear and multilinear isotropic material properties are required. The multilinear isotropic material applies the von Mises failure criterion along with the Willam and Warnke (1974) model to determine the failure of the concrete (as explained in detail in section 3.6.1, 3.6.2 and 3.7.1). EX is the modulus of elasticity of the concrete based on Hooke's Law, and PRXY is the Poisson's ratio (ν). To implement the multilinear isotropic stress-strain material model, the first point of the curve must meet Hooke's Law and be set by the user;

$$EX = \frac{\sigma}{\varepsilon}$$

The modulus of elasticity that were used to obtain the other points of stress-strain curve were obtained from our lab work as shown in the results section and summerized here (Table 6-10);

Table 6-10 Modulus of Elasticity

Fibre volume %	Modulus of Elasticity (MPa)
0	39128
0.5	38376
1	38955

The multilinear isotropic stress-strain curve for the concrete model was obtained utilizing the following equations (Graybeal equation [8]):

$$f_c = \varepsilon_c E(1 - \alpha)$$
$$\alpha = a e^{\frac{\varepsilon_c E}{b f_c'}} - a$$

Where;
f_c: Actual stress.
ε_c: Actual strain.
α: The percent stress decrease from linear elastic behavior.
E: Modulus of elasticity.
f_c': Compressive strength of cylinders experimentally determined at 14-day.

Uniaxial cracking stress and uniaxial crushing stress refer to the flexural tensile strength of small-scale prisms and compressive strength of cylinders after 14 days and at 20 degrees, respectively, which were obtained experimentally as well.

However, the negative slope portion will lead to convergence problems. Therefore, the negative slope was ignored in the stress-strain curve in the finite element material model. The stress-strain relation shown in Figure 6-12 was used for the material model in ANSYS.

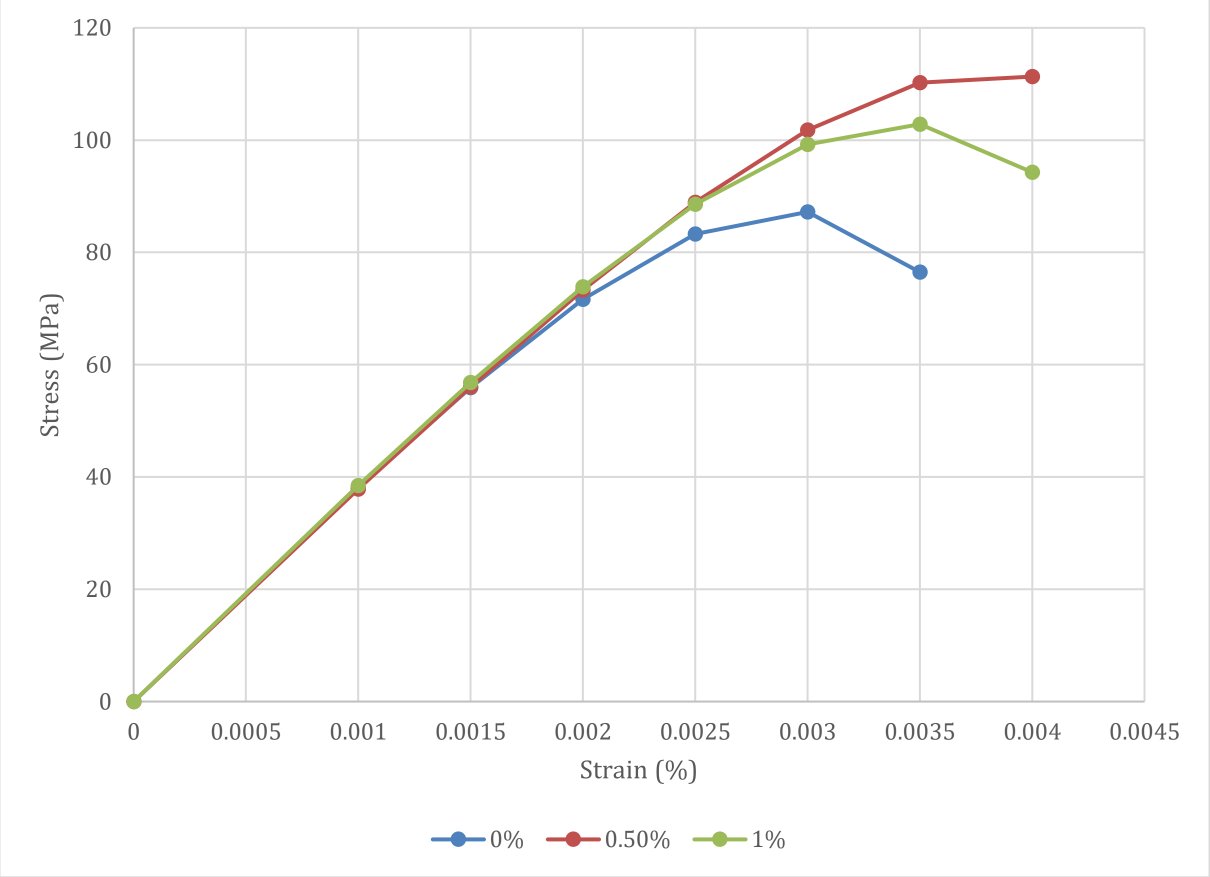

Figure 6-12 Stress-Strain Curve

At loading points and supports on the beam, the steel plates were represented by applying material model number 1. For this model, the SOLID 45 element is being utilized. This element is modeled as a linear isotropic with a modulus of elasticity for the steel (Es), and Poisson's ratio (0.3).

Regarding the steel reinforcement in the beam, the LINK element is being used corresponding to material model number 280. LINK element is assumed to be bilinear isotropic which is based on von Mises failure criteria. The yield stress was defined as 600 MPa, and the hardening modulus was 1000 MPa.

6.8. Modeling

All the elements were modeled as volumes. The model is 1500 mm long, 200 mm high and 100 mm width. The zero values for the X, Y, and Z- global coordinates coincide with the center of the cross-section for the concrete beam. The steel plate at the load point and support are an 80 mm x 30 mm x 100 mm. The volumes of the plate, support, and beam are shown in Figure 6-13. The FE mesh for the beam model is shown in Figure 6-14.

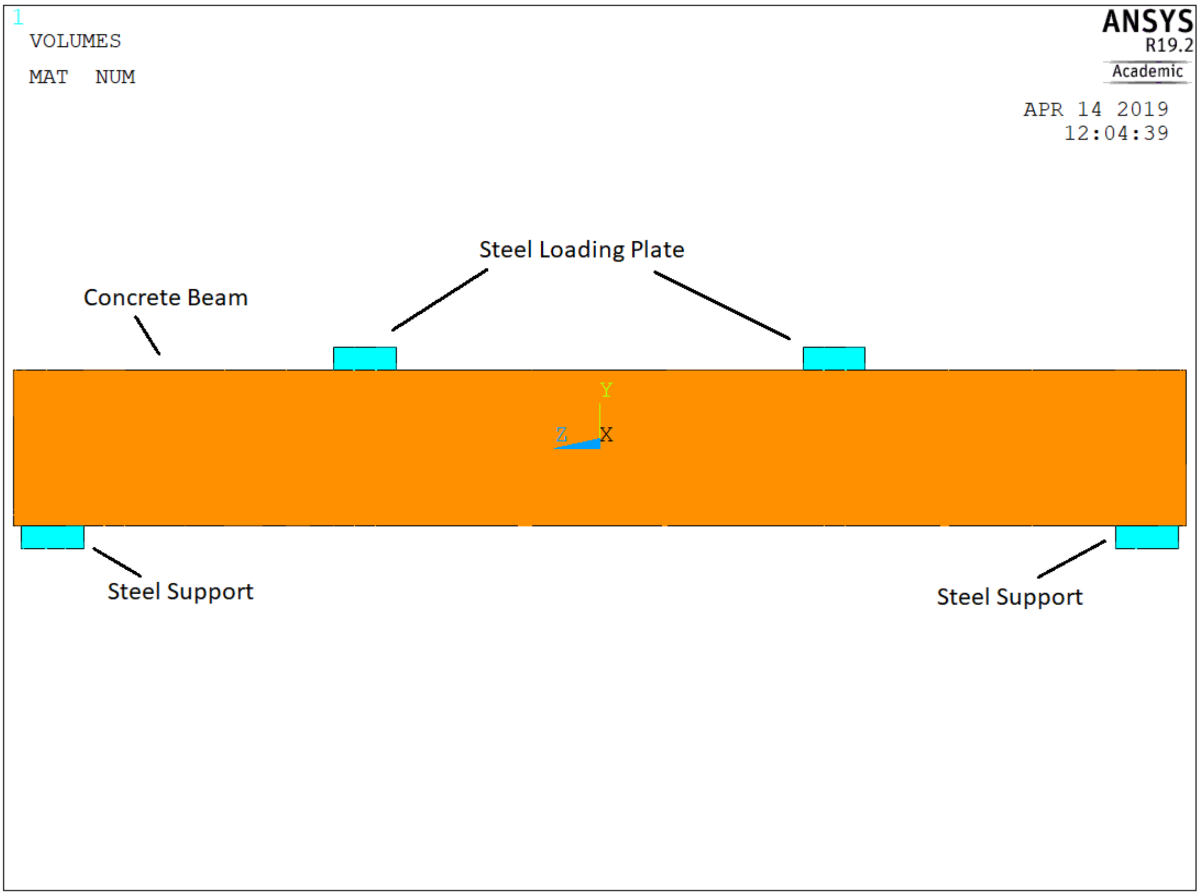

Figure 6-13 Volumes used in ANSYS

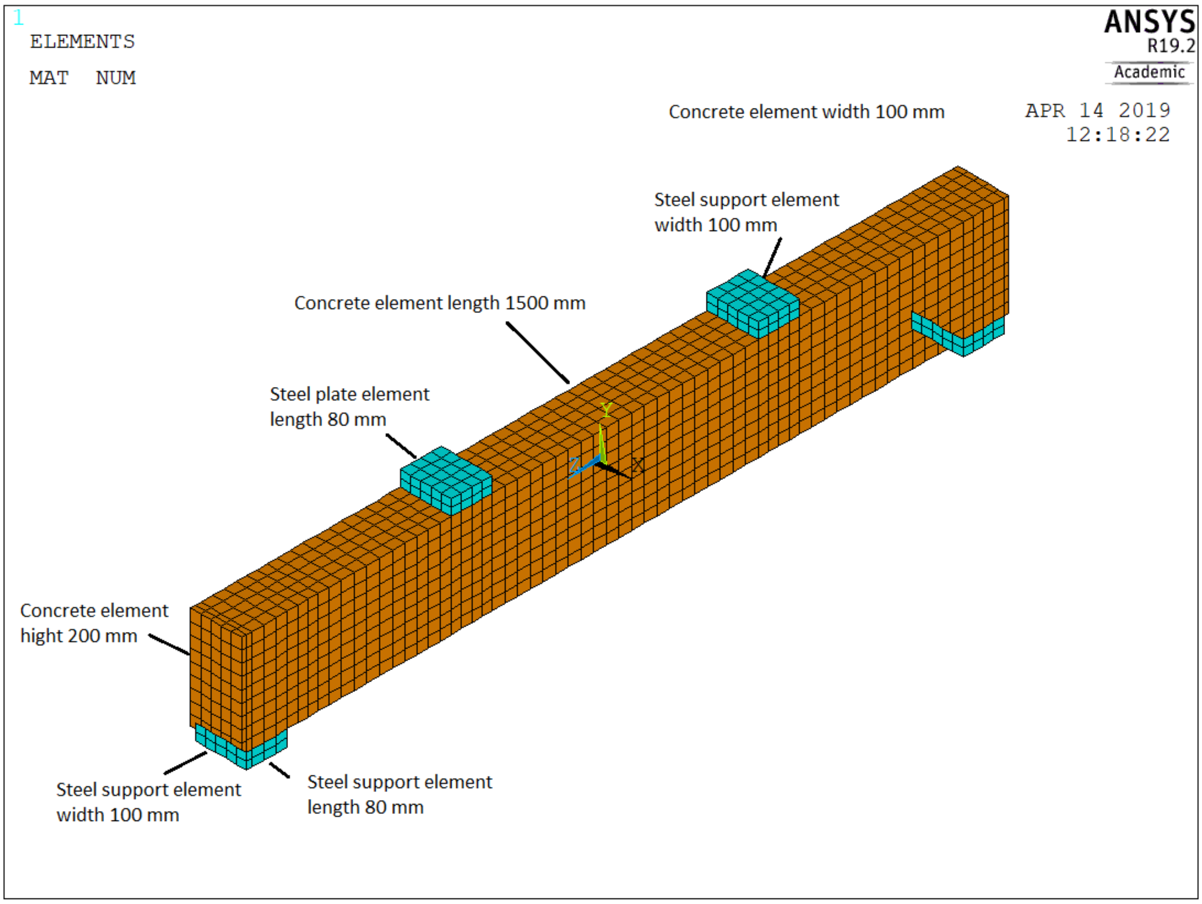

Figure 6-14 Mesh of components in ANSYS

LINK sections were used to simulate longitudinal reinforcement and portion shear reinforcement. For simplicity, inclined shear reinforcements were substituted by vertical stirrups. Figure 6-15 demonstrates the used reinforcements in the ANSYS model. The material number, element type number, and real constant set number are shown in Table 6-11.

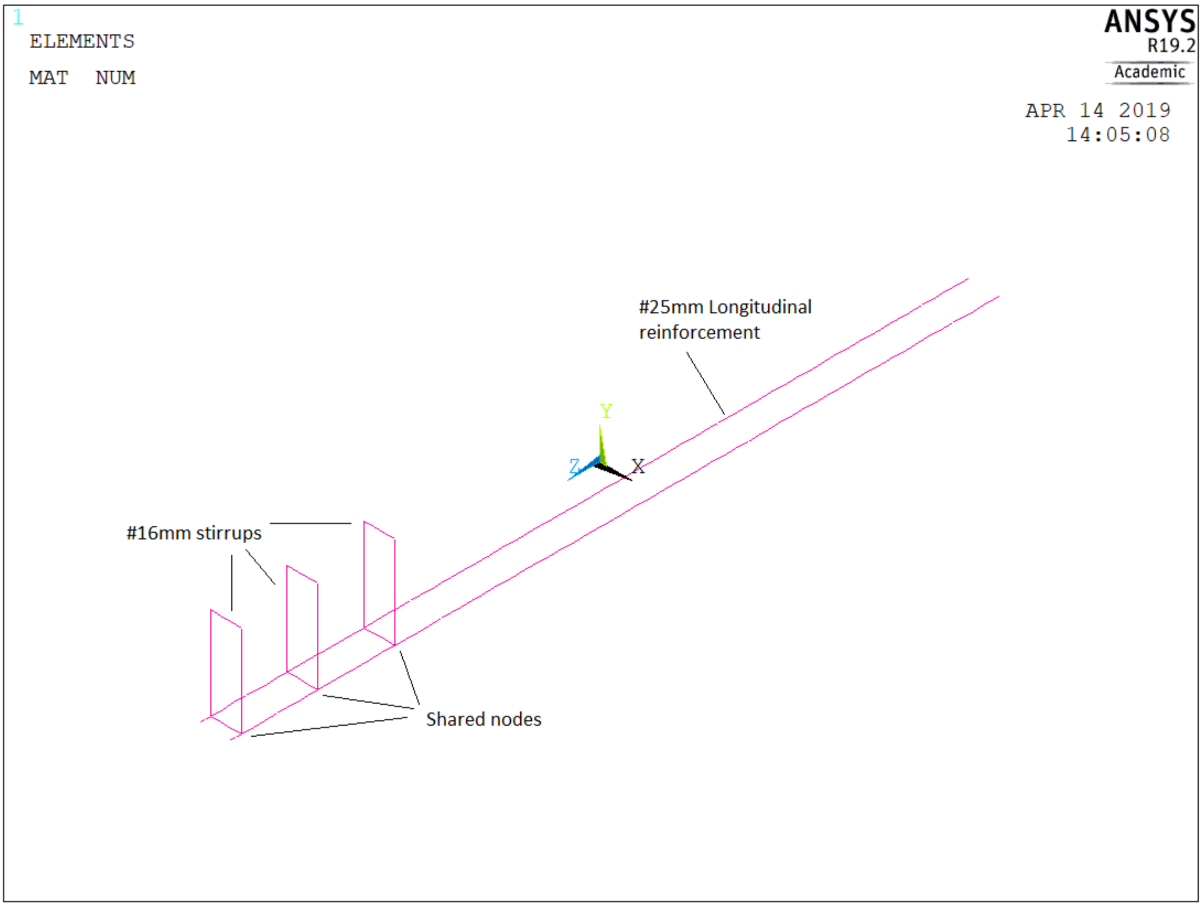

Figure 6-15 Reinforcement Form

Table 6-11 Mesh Attributes

Component	Material number	Element type	Real constant set
Concrete Beam	150	150	150
Steel Plate	1	1	Not applicable
Steel Support	1	1	Not applicable
Longitudinal reinf.	280	LINK	Not applicable
Stirrups	280	LINK	Not applicable

6.9. Meshing

The rectangular mesh was used to get good results from SOLID 65 as shown in Figure 6-14. To obtain compatibility between the nodes and the elements in the plates and supports with their correspondings of the concrete component, the volume sweep command was used to mesh. Regarding the reinforcement mesh, they were divided as lines to be in coincide with the other meshed elements.

6.10. Numbering Controls

An important command that has to be kept in mind before starting the solution is merging items. All cares must be taken to ensure that everything was merged in the proper order. Merge process should be performed before the meshing. If it is implemented after the meshing, then several nodes may lose their position in the model and become separate. This will lead to primary fail in transfer loads.

6.11. Loads and Boundary Conditions

To reflect the behavior of the experimental beam as possible and get an innovative solution, correct boundary conditions have to be set. Therefore, one of the support was constrained in Y-direction (UY= 0) while the other was constrained in Y and Z-directions (UY= UZ= 0). The force at the steel plate is applied across the entire centerline of the plate. The loading and support condition are shown in Figure 6-16.

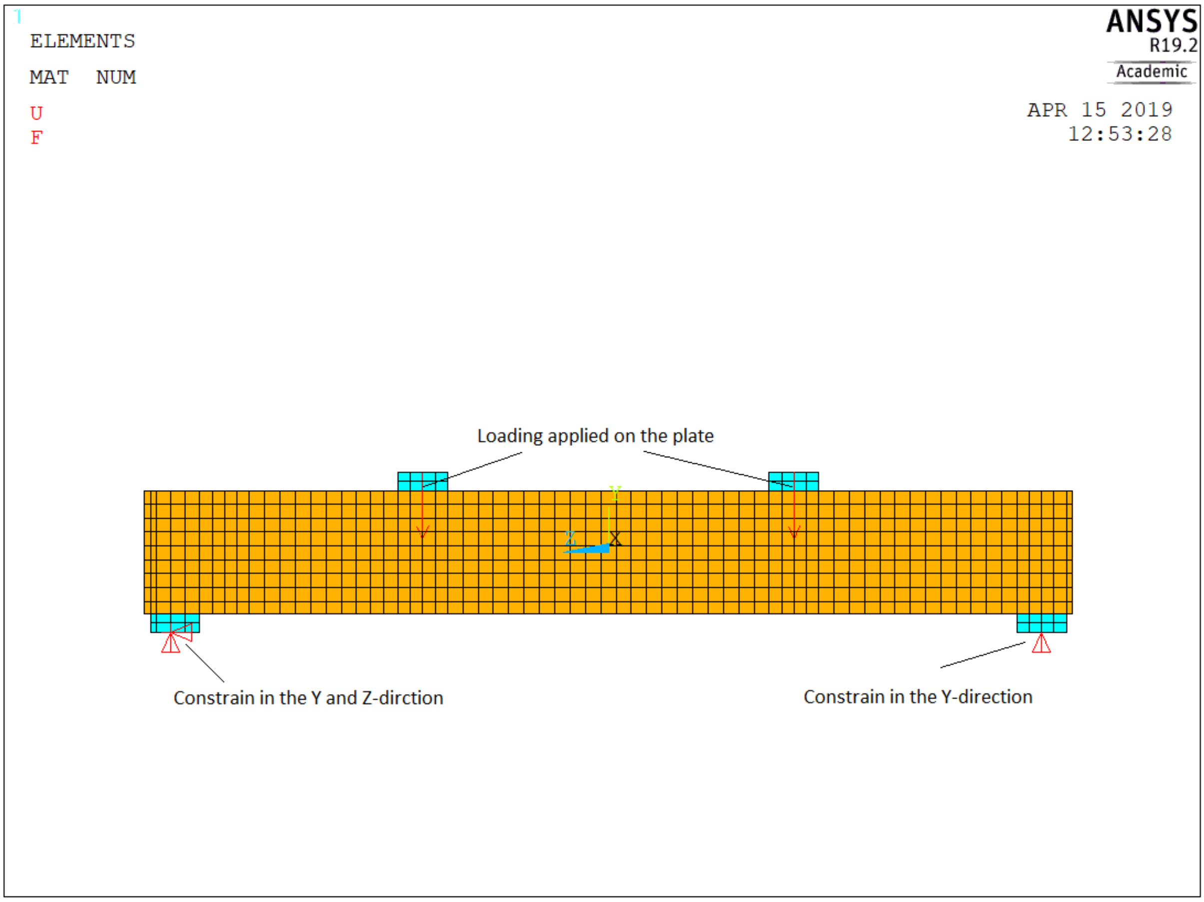

Figure 6-16 Loading and boundary conditions in the beampixel

6.12. Analysis Type

The static analysis was adopted since the FE model is for a simple beam. To manage the non-linear behavior, the Sol'n Controls command was used as shown in Table 6-12, Table 6-13 and Table 6-14.

Table 6-12 Typical commands utilized in nonlinear static analysis for 0% fibre volume

AnalySIs optiontion	**Small displacement static**
Time at the end of Loadstep	86
Automatic Time Stepping	Prog chosen
Number of Substeps	300
Max no. of Substeps	300
Min no. of Substeps	10

Table 6-13 Typical commands utilized in nonlinear static analysis for 0.5% fibre volume

AnalySIs optiontion	**Small displacement static**
Time at the end of Loadstep	182
Automatic Time Stepping	Prog chosen
Number of Substeps	300
Max no. of Substeps	300
Min no. of Substeps	10

Table 6-14 Typical commands utilized in nonlinear static analysis for 1% fibre volume

AnalySIs optiontion	**Small displacement static**
Time at the end of Loadstep	237
Automatic Time Stepping	Prog chosen
Number of Substeps	300
Max no. of Substeps	300
Min no. of Substeps	10
Write Items to Results File	All solution items
Frequency	Write every substep

From Table 6-14, it can be seen that the used analysis is small displacement static. The time at the end of the load step chose to be equal to the applied load so that every load step equal to 1 kN. To control the outputs, the commands in Table 6-15 are used.

Table 6-15 Commands Used to Control Output

Equation Solvers	**Program chosen solver**
Number of Restart Files	0
Frequency	Write Every Substep

In the non-linear options, all values are set to default as shown in Table 6-16. Also, convergence criteria are shown in Table 6-16.

Table 6-16 Nonlinear algorithm

Line Search	**Prog chosen**
DOF solution predictor	Prog chosen
VT speedup	off
Maximum number of iteration	Prog chosen
Cutback Control	Limits on physical values to perform bisection
Equiv. Plastic Strain	0.15
Explicit Creep ratio	0.1
Implicit Creep ratio	0
Incremental displacement	10000000
Points per cycle	13

All values are set to defaults except for the tolerances in Table 6-17. The program will then terminate but not exit upon non-convergence. Two criteria for the solution were used at the beginning; Force and Displacement. However, it turned out to be challenging to get convergence for the non-linear analysis by applying Force criteria. Hence, the convergence criteria for Force was dropped while only displacement criteria were used to achieve a proper response as possible.

Table 6-17 Convergence Criteria

Nonlinear Convergence Criteria for U (displacement)	
Tolerance about value	0.05
Convergence norm	L2 norm
Minimum reference value	Not applicable

6.13. Analysis Process

As it has been mentioned in section 3.8.5, Newton-Raphson method was used for the nonlinear analysis. A listing of the load steps is shown in Table 6-18, Table 6-19 and Table 6-20.

Table 6-18 Load Increment for 0% fibre volume beam

SET	TIME/FREQ	SUBSTEP	Load increment (kN)
1	0.28667	1	0.28667
2	0.57333	2	0.28666
3	1.0033	3	0.42997
4	1.6483	4	0.645
5	2.6158	5	0.9675
6	4.0671	6	1.4513
7	6.244	7	2.1769
8	9.5093	8	3.2653
9	14.407	9	4.8977
10	21.754	10	7.347
11	30.354	11	8.6
12	38.954	12	8.6
13	47.554	13	8.6
14	56.154	14	8.6
15	64.754	15	8.6
16	73.354	16	8.6
17	81.954	17	8.6
18	82.241	18	0.287
19	82.528	19	0.287
20	82.814	20	0.286
21	86	999999	-

Table 6-19 Load Increment for 0.5% fibre volume beam

SET	TIME/FREQ	SUBSTEP	Load increment (kN)
1	0.60667	1	0.60667
2	1.2133	2	0.60663
3	2.1233	3	0.91
4	3.4883	4	1.365
5	5.5358	5	2.0475
6	8.6071	6	3.0713
7	13.214	7	4.6069
8	20.124	8	6.91
9	30.49	9	10.366
10	46.038	10	15.548
11	64.238	11	18.2
12	82.438	12	18.2
13	100.64	13	18.202
14	118.84	14	18.2
15	137.04	15	18.2
16	155.24	16	18.2
17	173.44	17	18.2
18	174.04	18	0.6
19	174.65	19	0.61
20	175.26	20	0.61
21	182	999999	-

Table 6-20 Load Increment for 1% fibre volume beam

SET	TIME/FREQ	SUBSTEP	Load increment (kN)
1	0.79	1	0.79
2	1.58	2	0.79
3	2.765	3	1.185
4	4.5425	4	1.78
5	7.2088	5	2.67
6	11.208	6	4
7	17.207	7	6
8	26.206	8	9
9	39.704	9	13.5
10	59.951	10	20.25
11	83.651	11	23.7
12	107.35	12	23.7
13	131.05	13	23.7
14	154.75	14	23.7
15	178.45	15	23.7
16	202.15	16	23.7
17	225.85	17	23.7
18	226.64	18	0.79
19	227.43	19	0.79
20	237.00	999999	-

Time/FREQ refers to the applied load. For instance, at the 10th set, 59.951 kN was applied at the steel plate.

Up to the initial cracking of the beam, the loading steps increment increase very slightly. Once the load exceeded the initial crack 9.5093 kN, 30.49 kN and 39.704 kN for 0%, 0.5%, and 1%, respectively, the load increment increased up to yielding of steel point. After that, the load increment size decreased to capture the failure of the beam. The failure happens when convergence fails.

7. Results

The statistical method that was used to determine the acceptable range of the experimental results was explained in the preliminarily report (ANNEX D- section 6.4).

7.1.1. Determination of specific gravity & water absorption of fine aggregate

The following table shows the weights of the test's components.

Table 7-1 The weights of the considered components in specific gravity and water absorption test

DESCRIPTION		SAMPLE
	Weight of sample taken (g)	**2000**
S	Mass of SSD Sample (g)	**510**
C	Mass of Pycnometer with Specimen and Water filled to the Calibration Mark (g)	**2745,8**
B	Mass of Pycnometer Filled with Water to the Calibration Mark (g)	**2429,6**
A	Mass of Oven Dry Test Sample (g)	**496,9**

A = 496,9 g B = 2429,6 g S = 510 g C = 2745,8 g

The calculation for the specific Gravity of the fine aggregate:

$$\frac{S}{(B+S-C)} = Value\ of\ Specific\ Gravity\ of\ the\ fine\ aggregate \quad (7\text{-}1)$$

$$\frac{510}{(2429{,}6 + 510 - 2745{,}8)} = 2{,}63\ g$$

The calculation for the Absorption of the fine aggregate:

$$\frac{S-A}{A} \times 100\% = percent\ of\ water\ absorption \quad (7\text{-}2)$$

$$\frac{510 - 496{,}9}{496{,}9} \times 100 = 2.63\ \%$$

7.1.2. Compressive and flexural strength

Table 7-2 and Figure 7-1 show the mean values and standard deviations (S.D) of flexural strength of small-scale prisms at 20 degrees of F1, G1 and H1 mix after 14 days. The red bars in all charts refer to standard deviations as well.

Table 7-2 Mean values and standard deviations of flexural strength

No	Date of Casting	Date of Test	Curing regime	v_f%	l_f/d_f	Flexural strength (MPa)		
						Measured values	Mean values	S.D
1	29/03/2019	12/04/2019	20°C	0.0 %	13/0,2	12.4	12.5	0.5
2						13.1		
3						12.1		
1	29/03/2019	12/04/2019	20°C	0.5 %	13/0,2	12.9	12.2	0.6
2						12		
3						11.7		
1	29/03/2019	12/04/2019	20°C	1.0 %	13/0,2	13.7	13.1	1.3
2						13.9		
3						11.6		

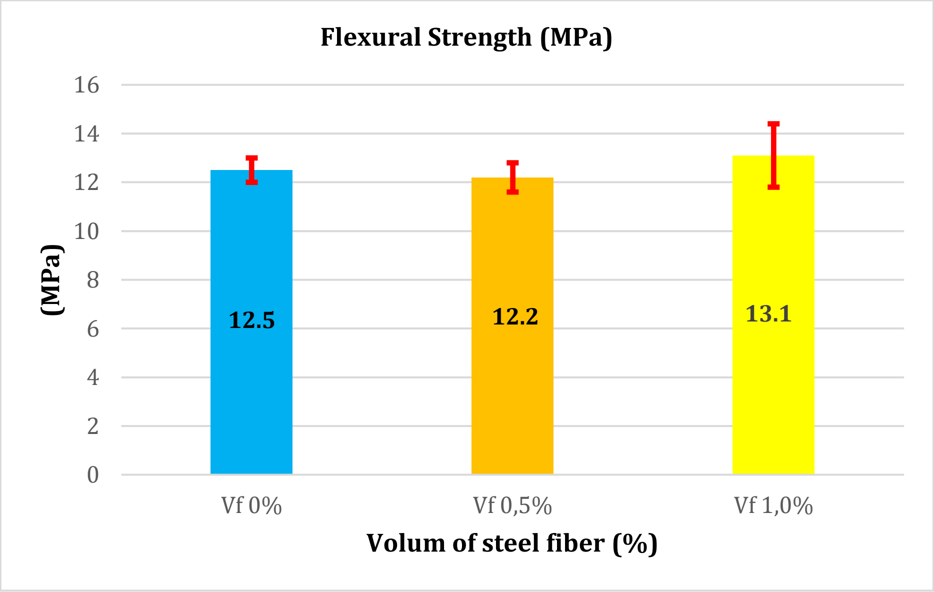

Figure 7-1 Mean values and standard deviations of flexural strength

Table 7-3 and Figure 7-2 show mean values and standard deviations (S.D) of compressive strength of cylinders at 20 degrees of F2, G2 and H2 mix after 14 days.

Table 7-3 Mean values and standard deviations of cylinder compressive strength

No.	Date of Casting	Date of Test	Curing regime	$v_f\%$	l_f/d_f	compressive strength (MPa)		
						Measured values	Mean values	S.D
1	02/04/2019	16/04/2019	20°C	0.0 %	13/0,2	49.5	83.6	29.6
2						103.2		
3						98		
1	29/03/2019	16/04/2019	20°C	0.5 %	13/0,2	102.6	107.1	4.8
2						106.7		
3						112.1		
1	29/03/2019	16/04/2019	20°C	1.0 %	13/0,2	84.9	98.7	12.2
2						108		
3						103.2		

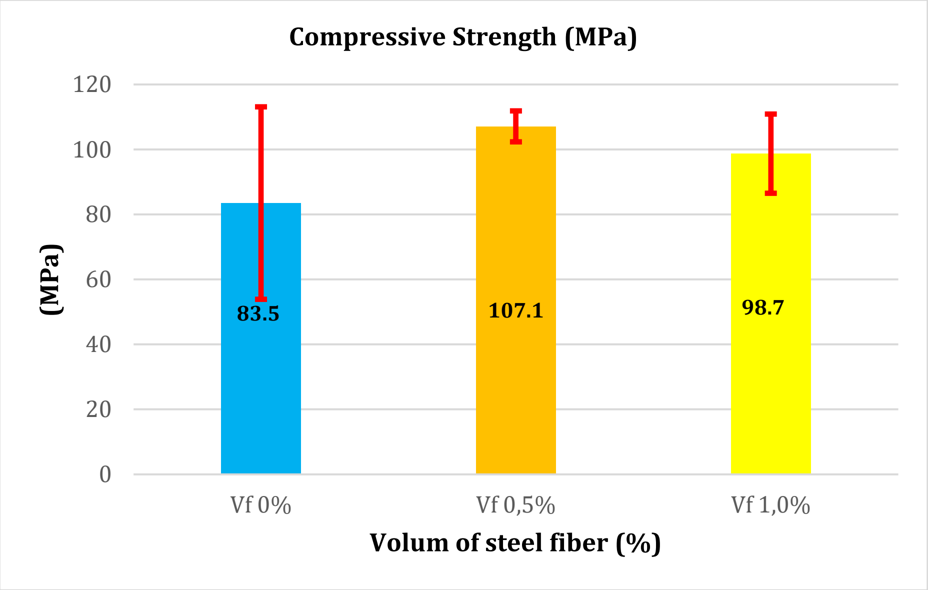

Figure 7-2 Mean values and standard deviations of cylinder compressive strength

Table 7-4 and Figure 7-3 show mean values and standard deviation (S.D) of compressive strength of cylinders at 20 degrees of F2, G2 and H2 mix after 28 days.

Table 7-4 Mean values and standard deviations of cylinder compressive strength after 28 days

No.	Date of Casting	Date of Test	Curing regime	$v_f\%$	l_f/d_f	compressive strength (MPa)		
						Measured values	Mean values	S.D
1	02/04/2019	30/04/2019	20°C	0.0 %	13/0,2	100.6	95.9	18.9
2						112		
3						75.1		
1	29/03/2019	30/04/2019	20°C	0.5 %	13/0,2	113.7	117.9	5.8
2						115.4		
3						124.5		
1	29/03/2019	30/04/2019	20°C	1.0 %	13/0,2	110.2	115.0	4.3
2						118.3		
3						116.5		

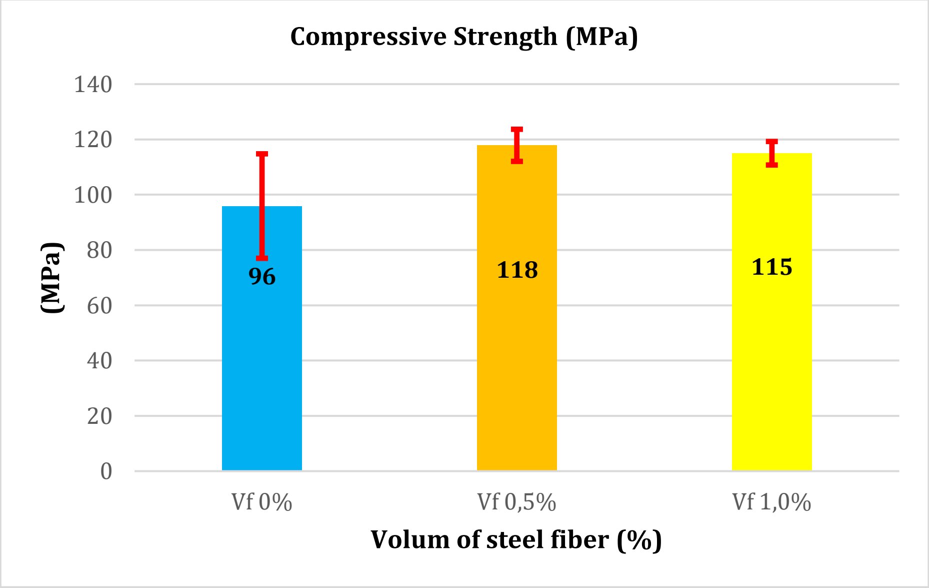

Figure 7-3 Mean values and standard deviations of cylinder compressive strength after 28 days

7.1.3. E- modulus

Table 7-5 and Figure 7-4 show mean values and standard deviation (S.D) of E-modulus at 20 degrees after 14 days.

Table 7-5 Mean values and standard deviations of E- modulus

No.	Date of Casting	Date of Test	Curing regime	v_f%	LOAD [kN]	STRESS [MPa]	STRAIN [%]	E-modulus [GPa]	Mean values	S.D
1	30.04.19	14.05.19	20°C	0.0 %	104.8	16.66	0.044	38.53	38.95	0.48
2						16.66	0.043	38.86		
3						16.67	0.043	39.48		
1	30.04.19	14.05.19	20°C	0.5 %	103.3	16.67	0.045	38.27	38.38	0.14
2						16.66	0.044	38.33		
3						16.67	0.045	38.53		
1	30.04.19	14.05.19	20°C	1.0 %	106.2	16.66	0.042	39.39	39.13	0.24
2						16.67	0.043	39.07		
3						16.67	0.06	38.92		

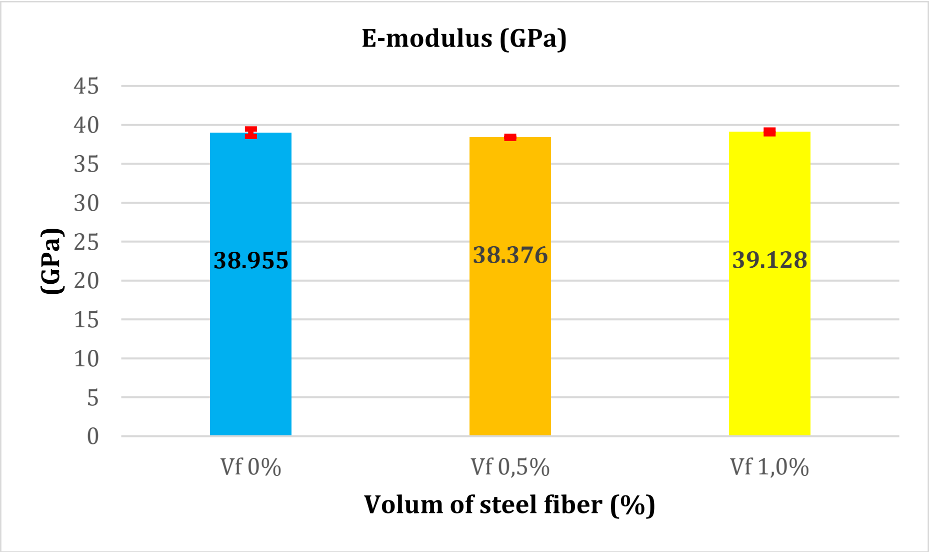

Figure 7-4 Mean values and standard deviations of E-modulus after 14 days

Table 7-6 and Figure 7-5 show mean values and standard deviation (S.D) of E-modulus at 90 degrees after 14 days.

Table 7-6 Mean values and standard deviations of E- modulus

No.	Date of Casting	Date of Test	Curing regime	$v_f\%$	Last [kN]	Stress [MPa]	Strain [%]	E-modulus [GPa]	Mean values	S.D
1	30.04.19	14.05.19	90°C	0.0 %	150.8	16.66	0.041	42.96	42.5	0.40
2						16.67	0.041	42.18		
3						16.66	0.041	42.37		
1	30.04.19	14.05.19	90°C	0.5 %	148.8	16.37	0.041	42.03	41.9	0.36
2						16.67	0.041	41.45		
3						16.66	0.041	42.11		
1	30.04.19	14.05.19	90°C	1.0 %	143.5	16.67	0.04	41.14	43.1	2.35
2						16.66	0.039	42.5		
3						16.66	0.038	45.7		

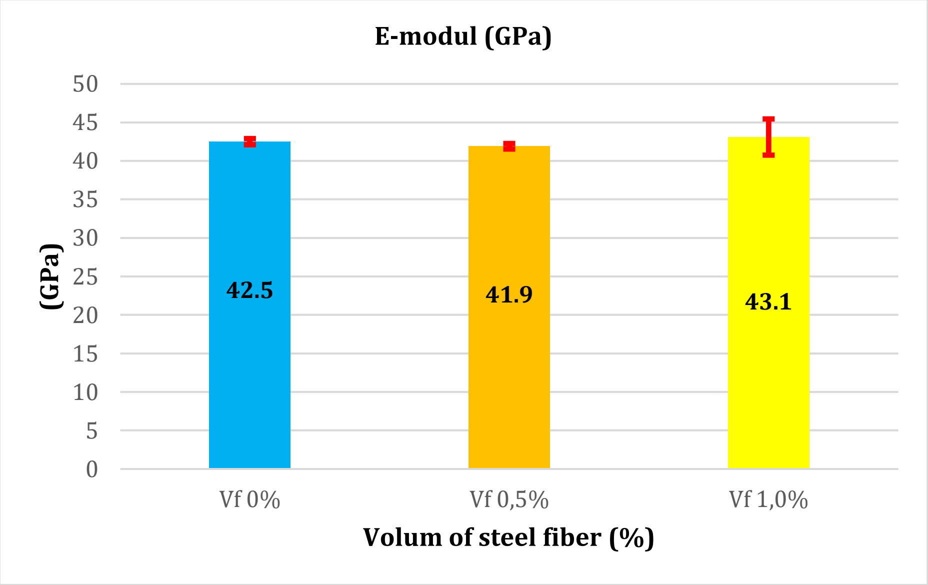

Figure 7-5 Mean values and standard deviations of E-modulus after 14 days

7.1.4. Failures of the beams

Figure 7-6, Figure 7-7and Figure 7-8 show crack patterns and failures of beams F1, G1, and H1.

Figure 7-6 Shear crack pattern of the beam- F1- 0% fibre

Figure 7-7 Shear crack pattern of the beam- G1- 0.5% fibre

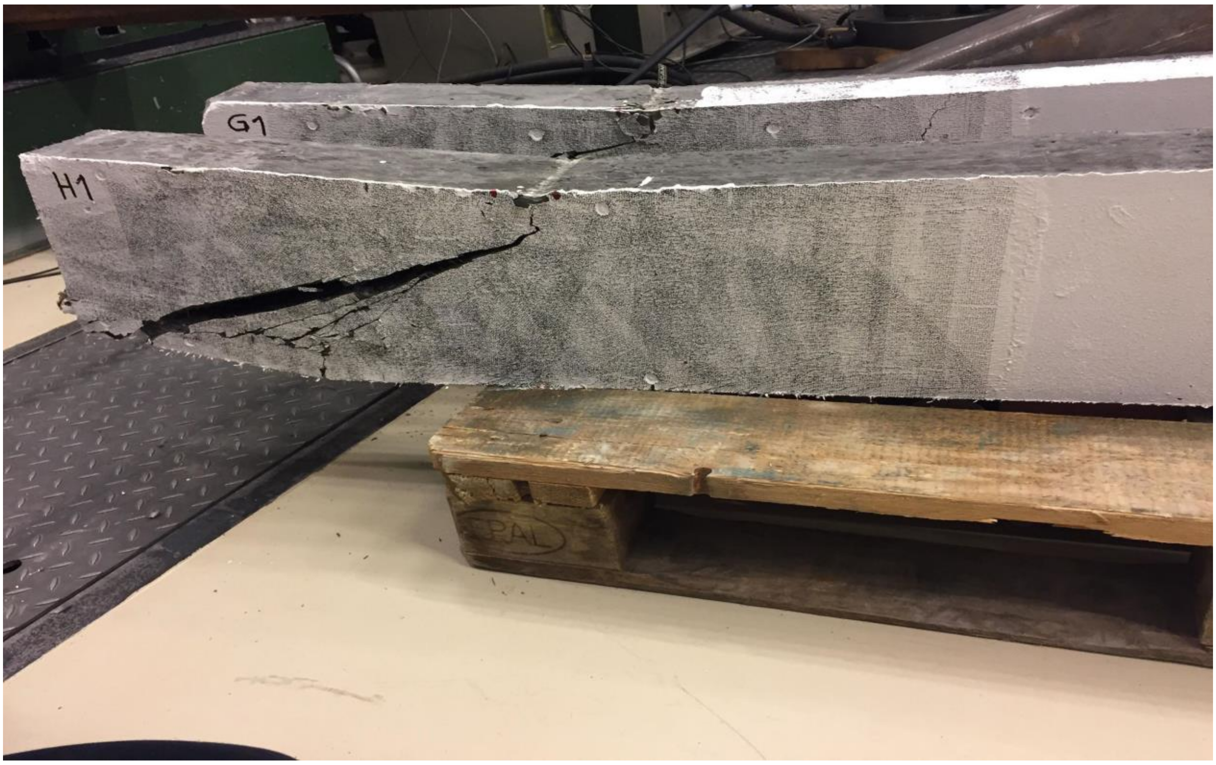

Figure 7-8 Shear crack pattern of the beam- H1- 1% fibre

7.2. Estimated shear strength out from standards

All the mentioned formulas in section 6.3 give the shear stress except Australian guideline, ACI 544 and our lab results. Therefore, it was decided to convert all the values to represent shear stress. The compressive strength values were obtained from the cylinders compressive strength which were tested after 14 days at 20 degrees. The flexural strength values were calculated as the mean value of all the small-scale prisms test from this semester and the last semester. The following formula is used to obtain shear stress;

$$\tau = \frac{\mathrm{Q\,V_{rd}}}{\mathrm{I_b\,b}} \qquad (7\text{-}3)$$

Where,

τ = Shear stress (MPa).

Q = Calculated statical moment = $\sum A_i y_i = (200 \times 100) \times 100 = 2000000\ mm^3$

y= Vertical distance away from the neutral axis.

A: cross-sectional area.

V_{rd}= Shear force (N).

I_b = moment of inertia around the neutral axis= $\frac{bh^3}{12} = \frac{100 \times 200^3}{12} = 66666666.7\ mm^4$

b = width of the beam (mm).

h = The hight of the beam.

Table 7-7, Table 7-8, Table 7-9,
Table *7-10* and Table 7-11 show the comparison process between experimental and calculated results.

Out from Figure 7-11, Figure 7-12 and Figure 7-13, the average shear strength was calculated as follows;

$$V_{rd,0\%} = \frac{64614+59795+161678}{3} = 62204.5\ \text{(N)}$$
$$V_{rd,0.5\%} = \frac{175332+181179+173440}{3} = 176650.333\ \text{(N)}$$
$$V_{rd,1\%} = \frac{236128+222481+262822}{3} = 240477\ \text{(N)}$$

Table 7-7 Shear stress of our experimental results

Q	V_{rd} (N) 0%	V_{rd} (N) 0.5%	V_{rd} (N) 1%	bw (mm)	h (mm)	$I_b (mm^4)$	$\tau_{exp.}\ (MPa)$ 0%	$\tau_{exp.}\ (MPa)$ 0.5%	$\tau_{exp.}\ (MPa)$ 1%
2.0E6	6.2E4	1.7E4	2.4E4	100	200	6.7E7	18.66	52.99	72.14

Table 7-8 Shear stress for the used formulas

Formula	$\tau_{cal.}$ (MPa) **0%**	$\tau_{cal.}$ (MPa) **0.5%**	$\tau_{cal.}$ (MPa) **1%**
Sharma	6.9	6.7	7.20
Narayana and Darwish	4.1	33.4	61.8
Ashour, Hasanain, and Wafa for a/d > 2,5	2.5	34.8	66.5
Ashour, Hasanain, and Wafa for a/d < 2,5	2.9	47.8	91.1
Imam and Vandewalle	3.4	15.2	114.9

Table 7-9 Shear stress for the Australian guideline

Q	f'_c	v_c (N)	b_w	d	V_c (N)	V_{us}	P_v	$V_u(KN)$	I	$\tau_{cal.}$ (MPa)
2.0E6	83.5	6.18	100	180	111382.53	0	0	111.38	6.67E7	33.41
2.0E6	107.1	6.34	100	180	114216.4	0	0	114.21	6.67E7	34.26
2.0E6	98.7	6.29	100	180	113247.4	0	0	113.24	6.67E7	33.97

Table 7-10 Shear stress for ACI 544

Q	f_{ct} (MPa)	d (mm)	a (mm)	d/a	V_n (N)	$\tau_{cal.}(MPa)$
2.0E6	10.1	180	400	0.45	99763.53	29.929
2.0E6	13.9	180	400	0.45	137298.32	41.189
2.0E6	18.9	180	400	0.45	186686.21	56.005

Table 7-11 comparisons of the experimental results to the calculated one

Formula	$\tau_{exp.}/\tau_{cal.}$ (MPa) **0%**	$\tau_{exp.}/\tau_{cal.}$ (MPa) **0.5%**	$\tau_{exp.}/\tau_{cal.}$ (MPa) **1%**
Sharma	2.71	7.91	10.01
Narayana and Darwish	4.57	1.58	1.17
Ashour, Hasanain, and Wafa for a/d < 2,5	6.34	1.11	0.79
Imam and Vandewalle	5.48	3.48	0.63
Australian guidline	0.558	1.546	2.123
ACI 544	0.623	1.286	1.288

Figure 7-9 illustrates and summarize all the results where the blue line shows the experimental values;

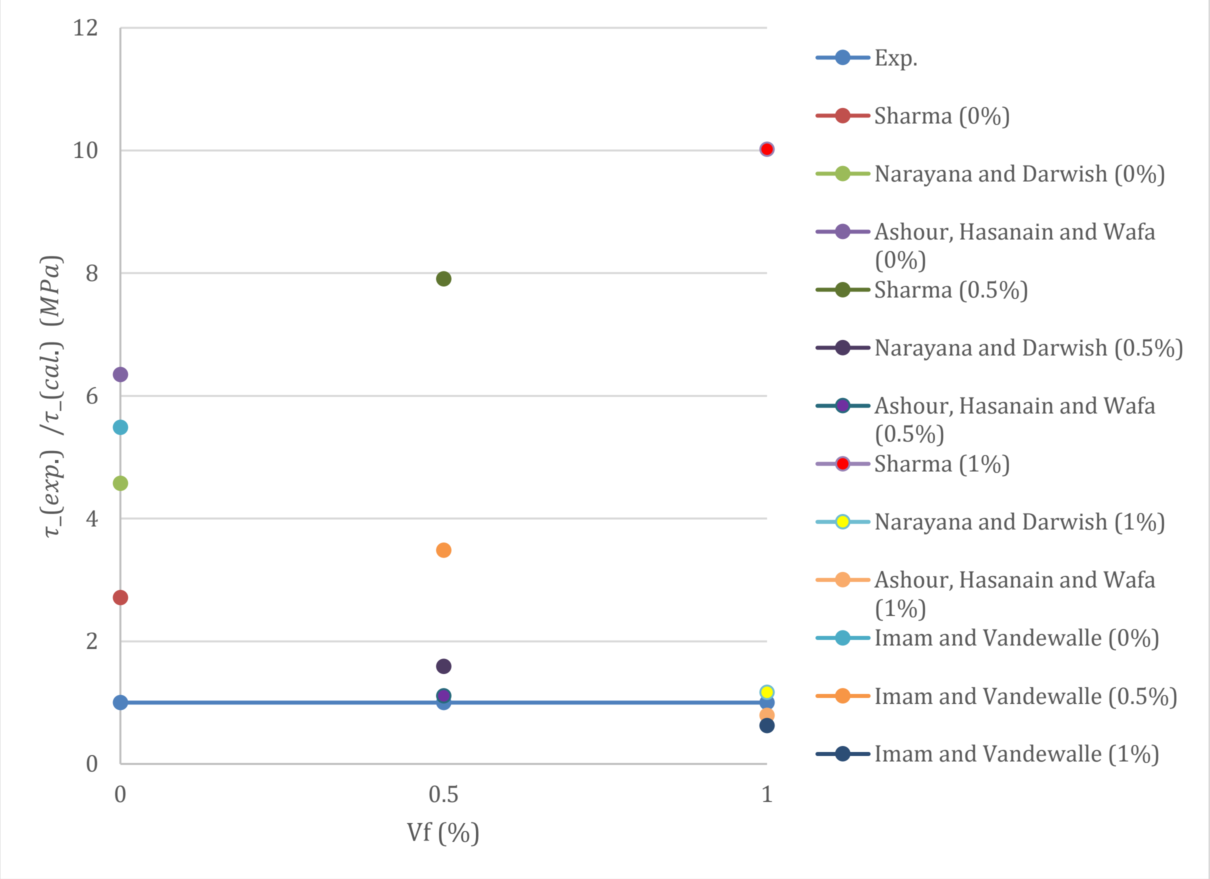

Figure 7-9 Evaluation of the used formulas

7.2.1. Proposed formula

The following equation has been developed based on our experimental results. Table 7-12 shows the calculations process and the results.

$$V_{rd}(N) = \left[4\left(\frac{F_{cu}}{20-v_f}\right)^{0.36} + f_t^{0.01}\left(\frac{d}{a}\right) + 110(v_f)^{0.54}\right] bw.d \quad \text{(7-4)}$$

Where,

V_{rd}= shear capacity (N).

f_t= flexural tensile strength.

d = effective depth of the beam.

a = shear span.

f_{cu} = cylinder compressive strength of UHPC.

v_f = The volume fraction of steel fibre.

Table 7-12 shear strength out from the proposed formula

Q	$bw(mm)$	f_{cu} (Mpa)	$d(mm)$	$a(mm)$	f_t	$v_f\%$	V_{rd} (N)	V_{rd} (kN)	$\tau_{exp.}$ (MPa)	$\tau_{exp.}$ $/\tau_{cal.}$
2.0E6	100	83.5	180	400	11.3	0.01	222593.39	222.59	66.778	1.08
2.0E6	100	107.1	180	400	13.05	0.005	175830.08	175.83	52.749	1.004
2.0E6	100	98.7	180	400	16	0	61001.86	61.001	18.300	1.01

Figure 7-10 compares the results of Australian guideline, ACI 544 and the proposed formula. The proposed formula is represented by the HP symbol.

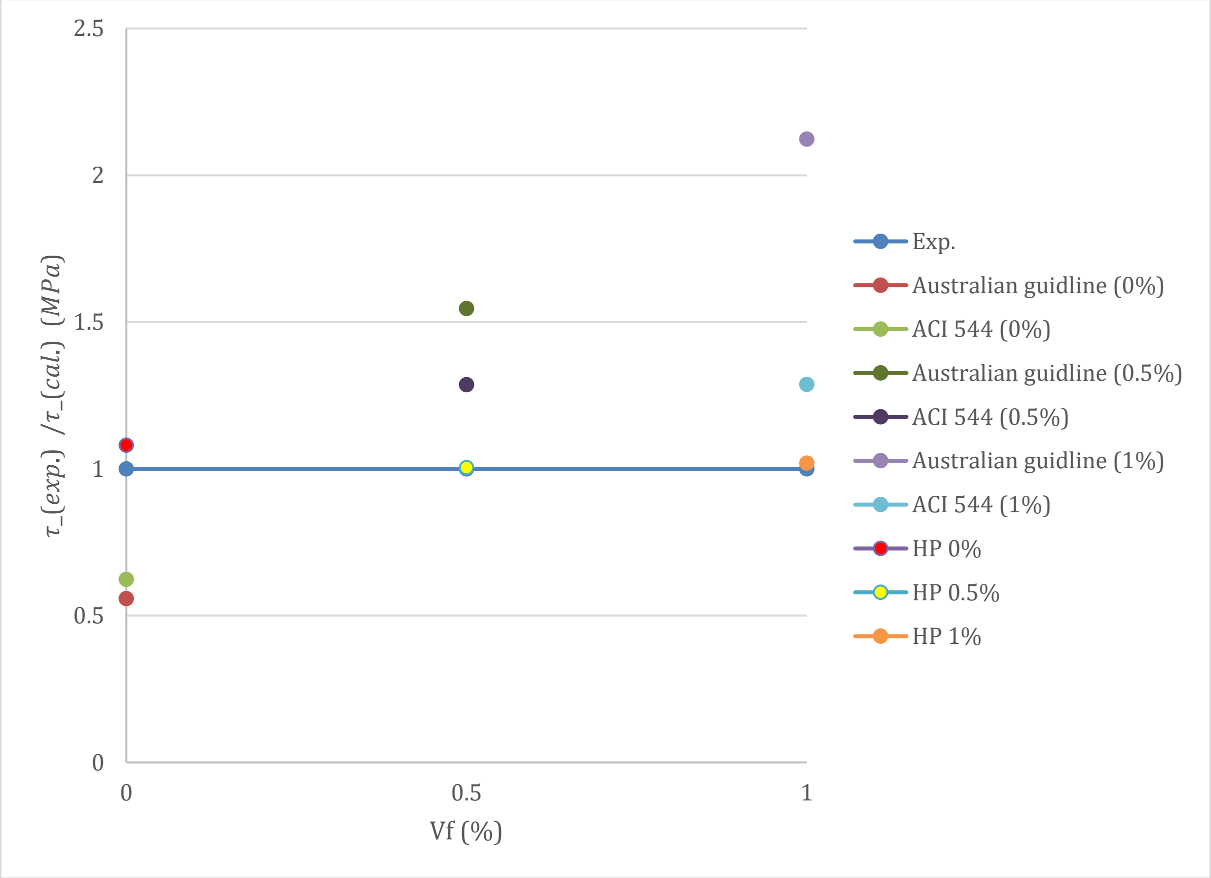

Figure 7-10 Evaluation of Australian guideline, ACI 544 and proposed formulas

7.3. ANSYS vs. Experimental results

The purpose of the calibration of the finite element model is to provide confidence in the use of the model developed in ANSYS (v.19.2). The results show that steel fiber content had a limited effect on the first crack strength and first crack deflection of load-deflection curve of UHPC, but showed considerable effects on the peak load. Figure 7-11, Figure 7-12 and Figure 7-13 show the load-deflection curves obtained from ANSYS as well as the experimental tests at the mid-span of the beams.

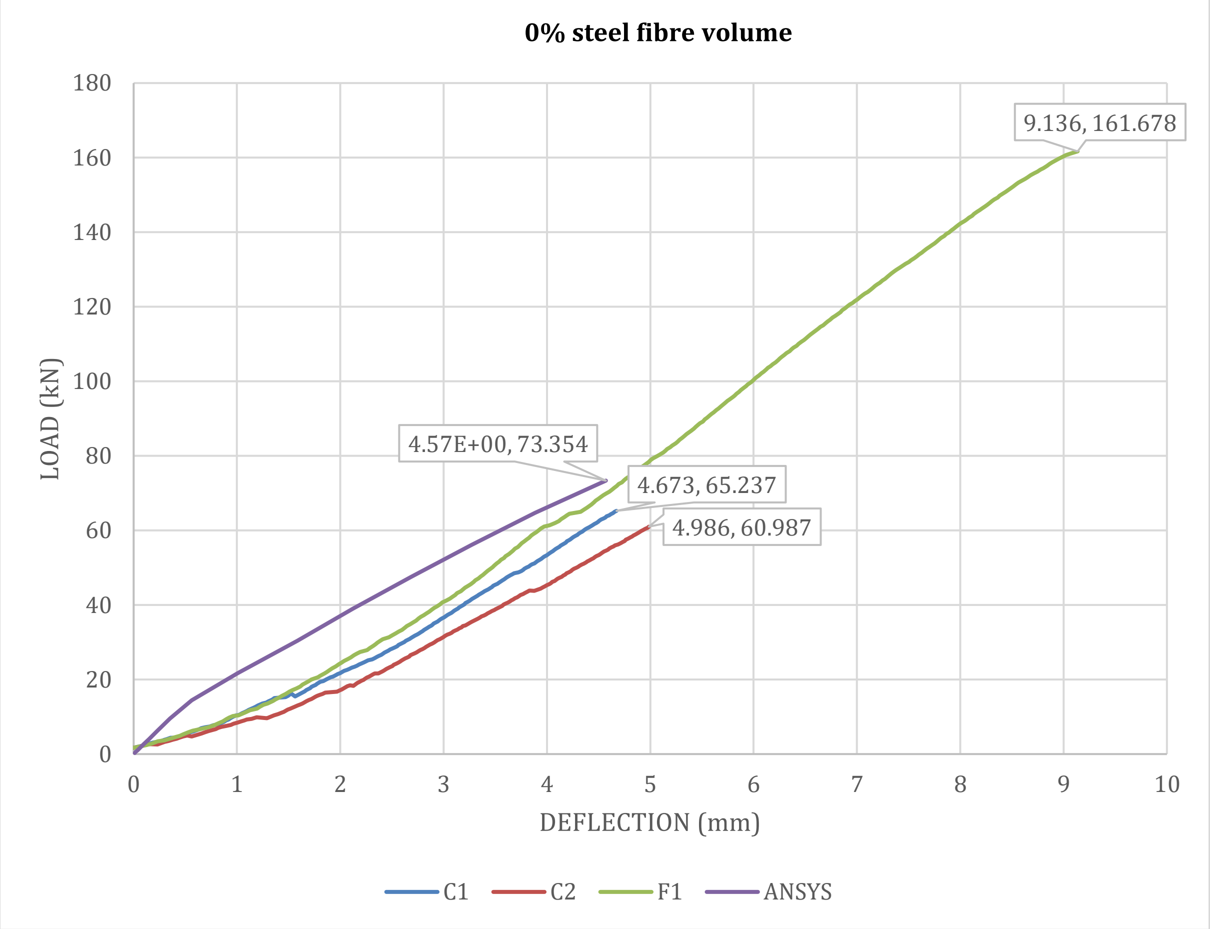

Figure 7-11 ANSYS vs. Experimental results for 0% fibre volume at mid-span of the beams

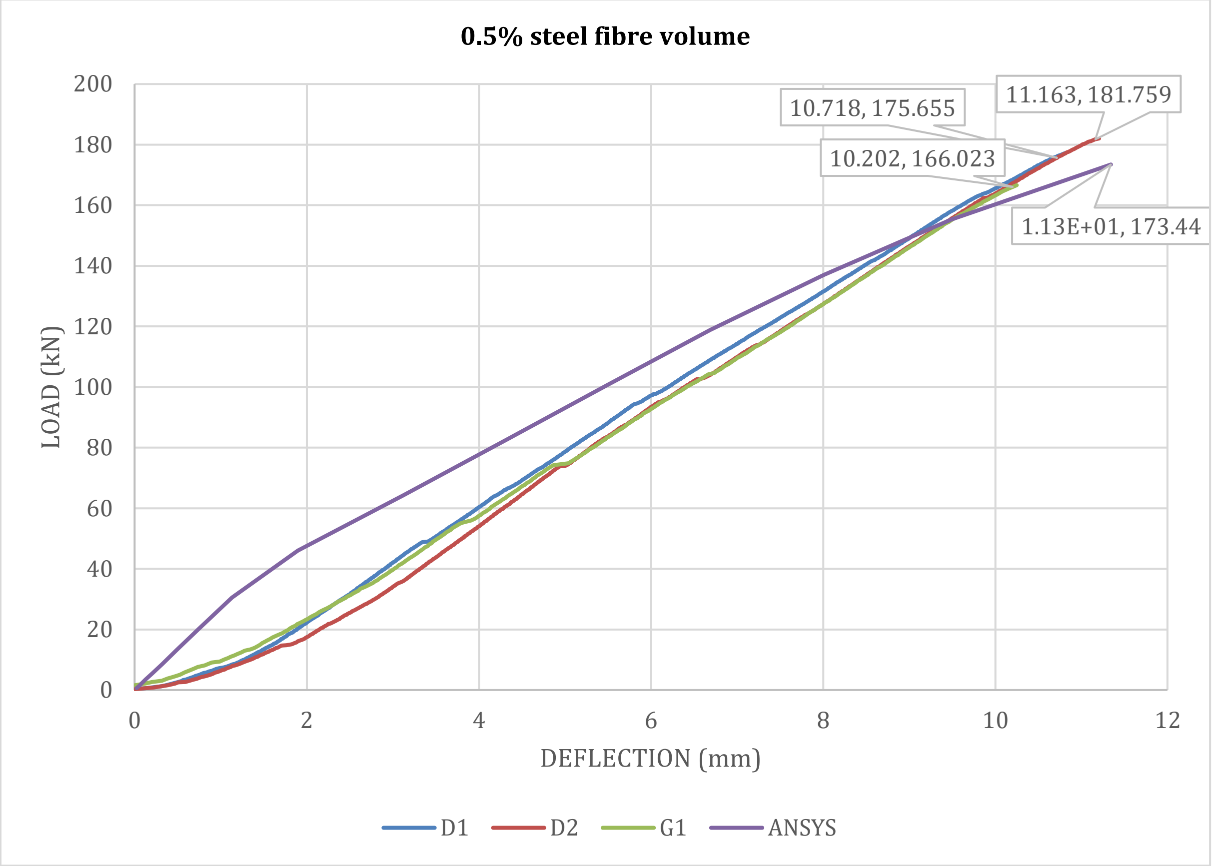

Figure 7-12 ANSYS vs. Experimental results for 0.5% fibre volume at mid-span of the beams

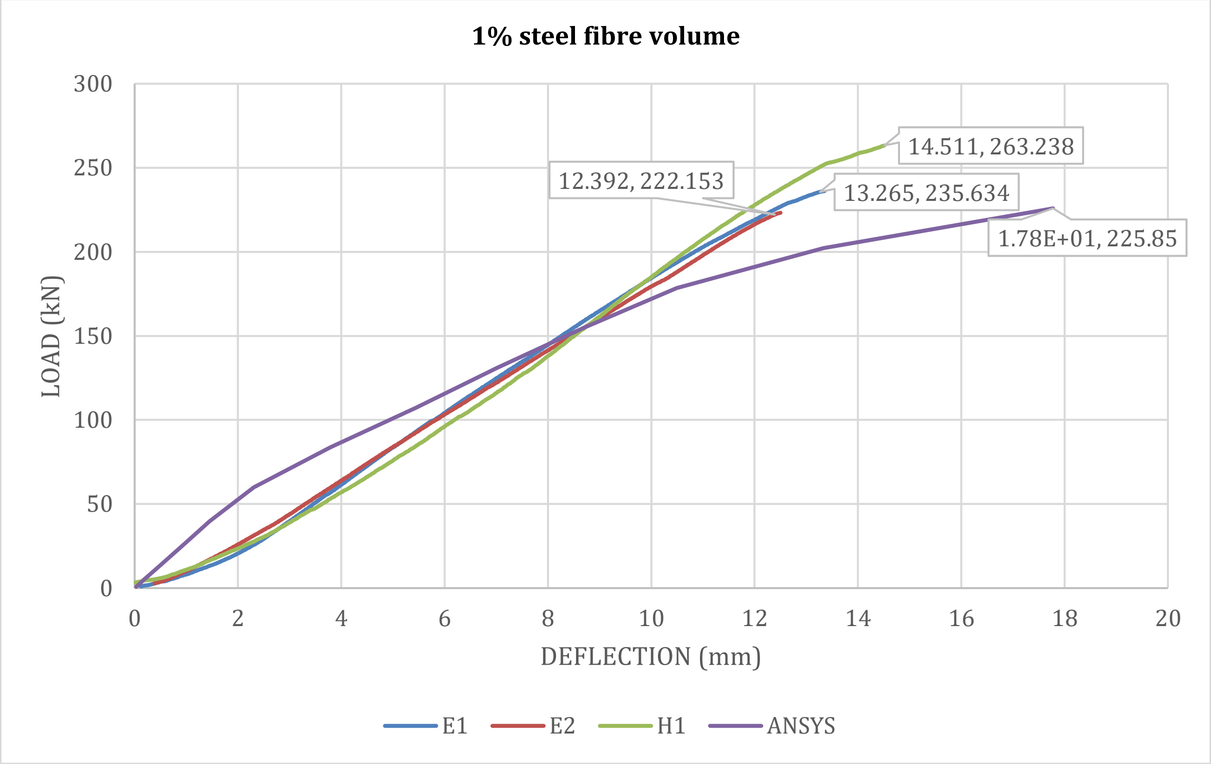

Figure 7-13 ANSYS vs. Experimental results for 1% fibre volume at mid-span of the beams

7.4. ANSYS vs. DIC-camera results

Several points were extracted from the DIC-camera. The load-deflection curves of these points compared to ANSYS as the following figures demonstrate.

7.4.1. Beam- C1

Figure *7-14* shows the positions of the points that were obtained from DIC- camera for C1 beam.

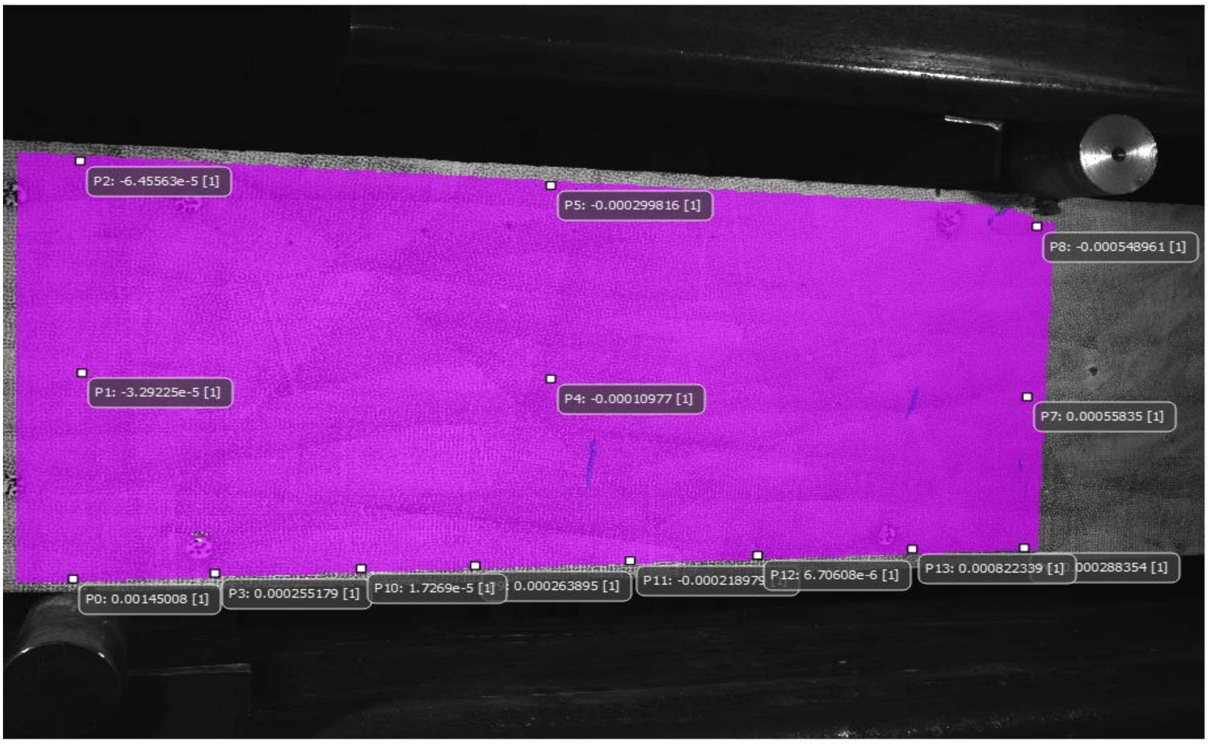

Figure 7-14 The extracted points from DIC- camera for beam C1- 0% fibre volume

The following figure shows the points that represent the best match between DIC- camera results and ANSYS.

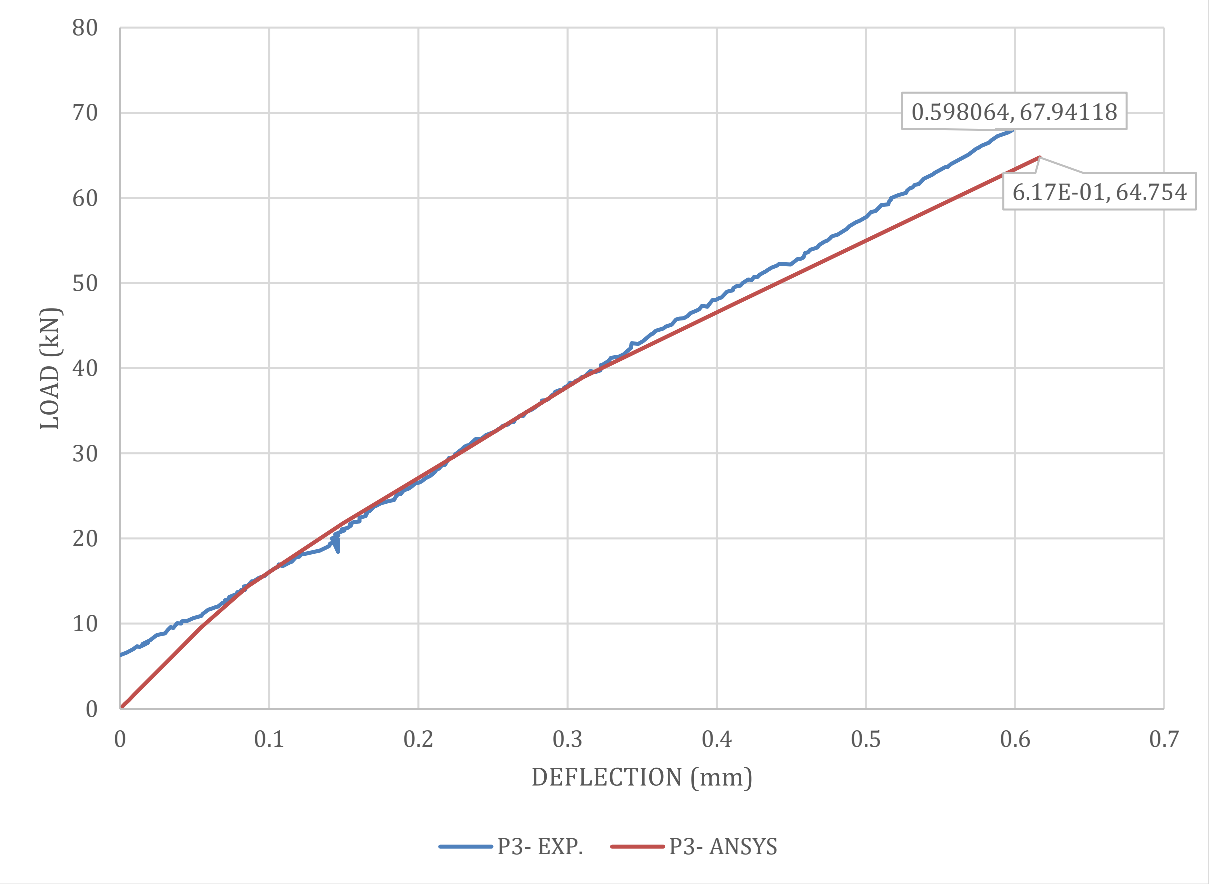

Figure 7-15 ANSYS vs. DIC-camera results for point 11 within C1 beam

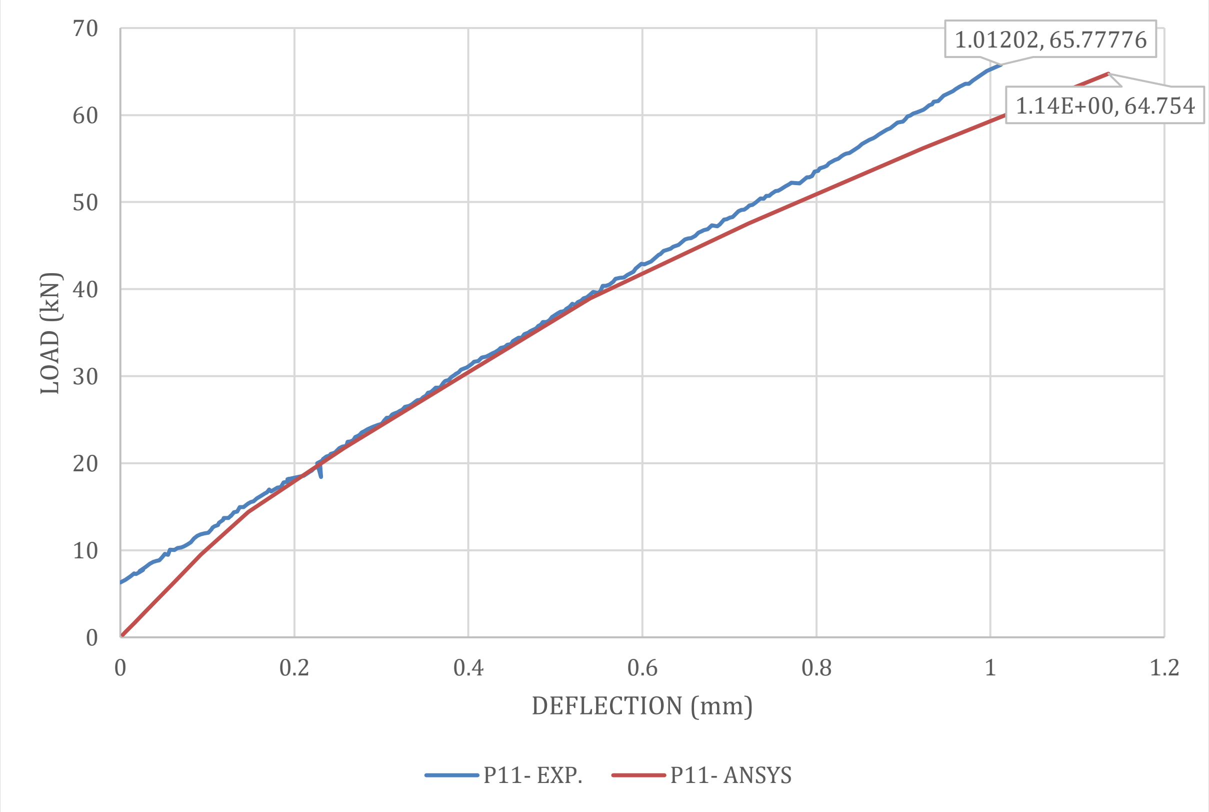

Figure 7-16 ANSYS vs. DIC-camera results for point 11 within C1 beam

7.4.2. Beam- C2

Figure 7-17 shows the positions of the points that were obtained from DIC- camera for C2 beam.

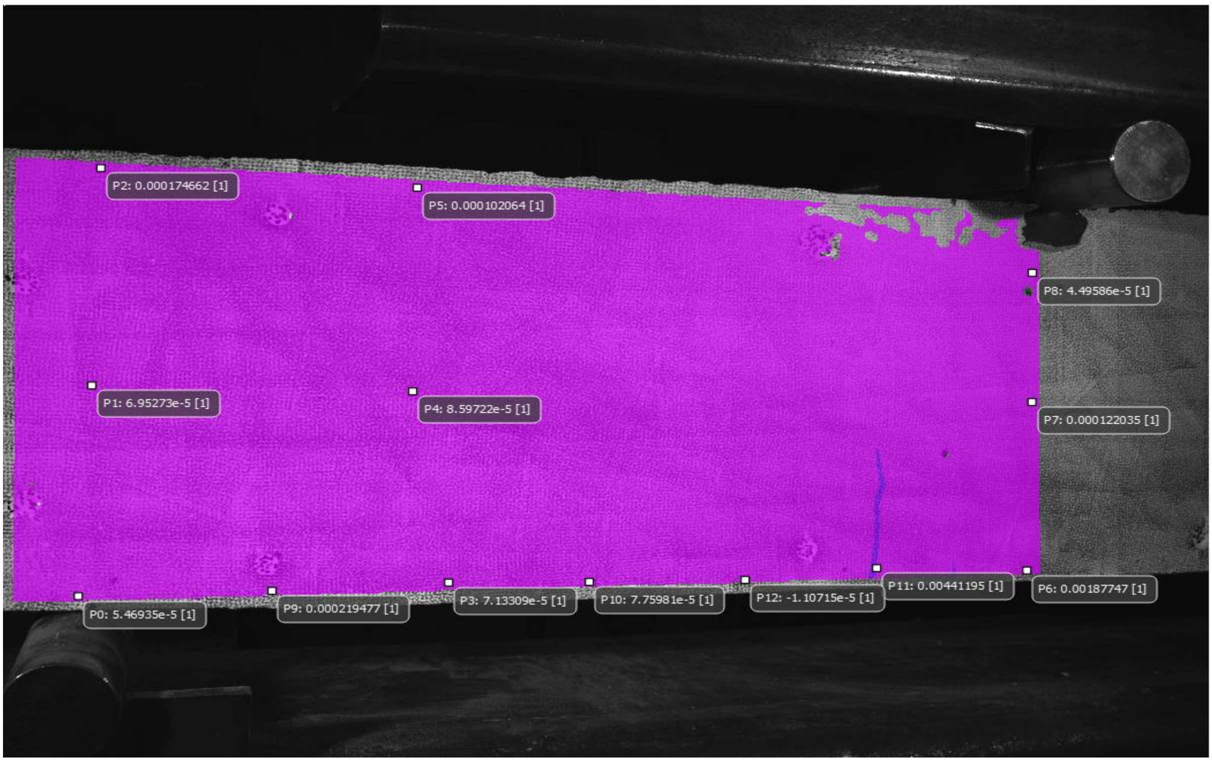

Figure 7-17 The extracted points from DIC- camera for beam C2- 0% fibre volume

The following figure shows the points that represent the best match between DIC- camera results and ANSYS.

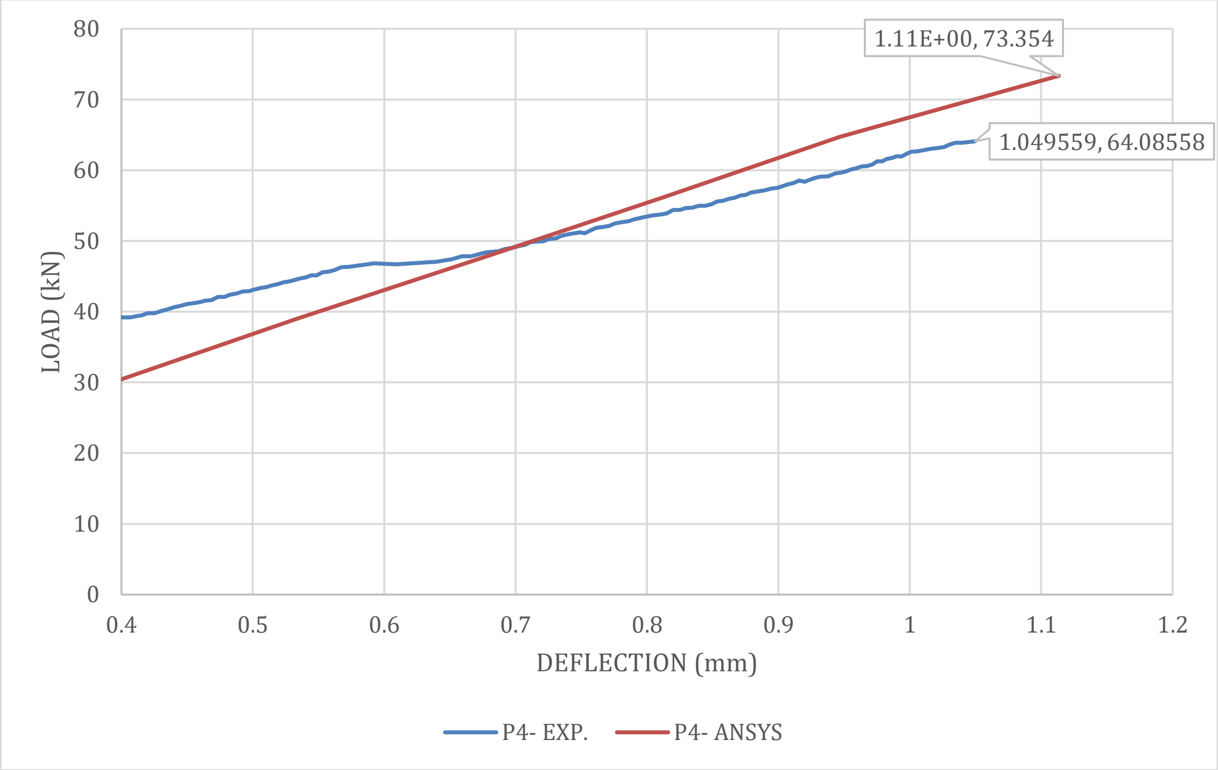

Figure 7-18 ANSYS vs. DIC-camera results for point 4 within the C2 beam

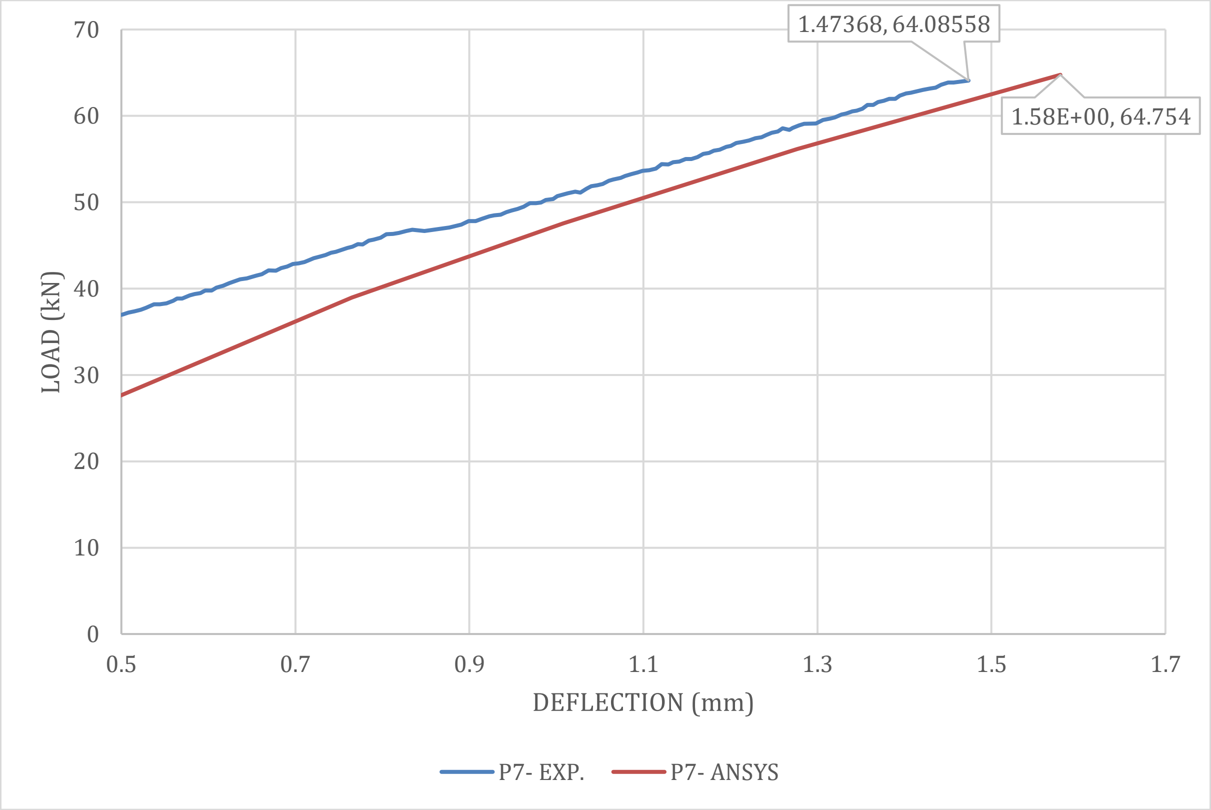

Figure 7-19 ANSYS vs. DIC-camera results for point 7 within the C2 beam

7.4.3. Beam- F1

Figure 7-20 shows the positions of the points that were obtained from DIC- camera for F1 beam.

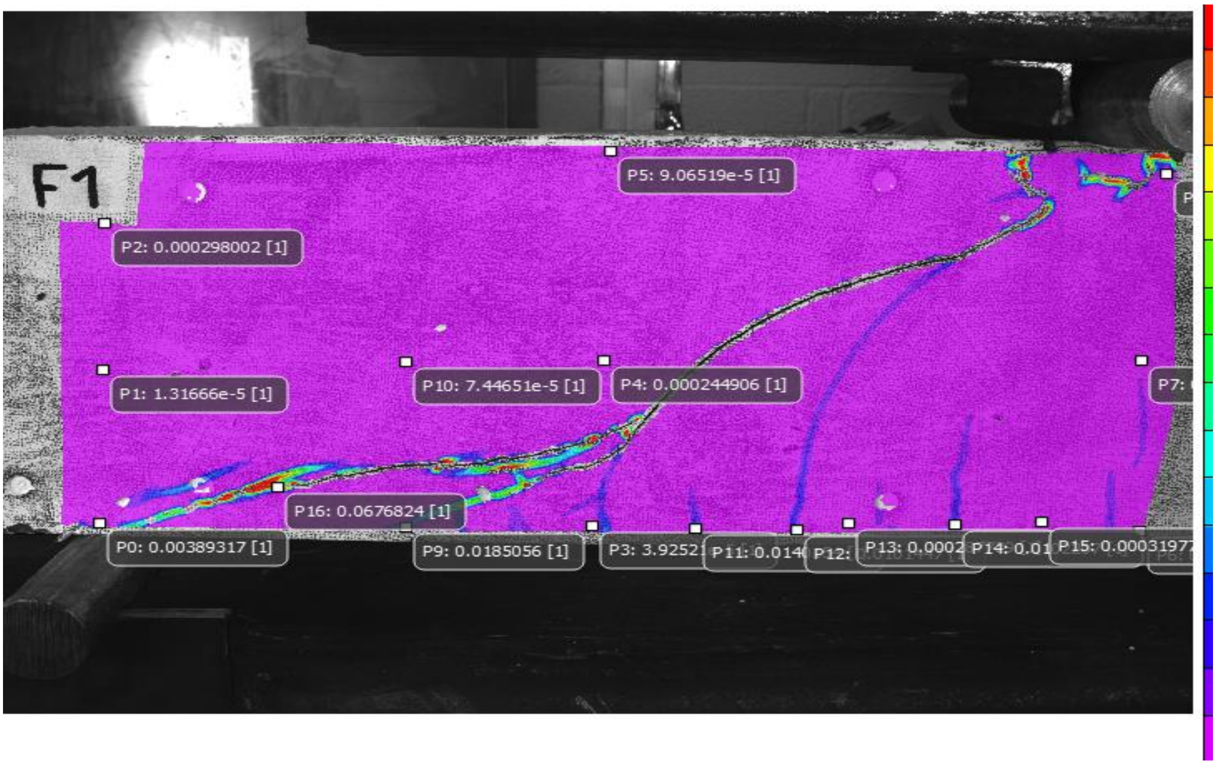

Figure 7-20 The extracted points from DIC- camera for beam F1- 0% fibre volume

The following figure shows the points that represent the best match between DIC- camera results and ANSYS.

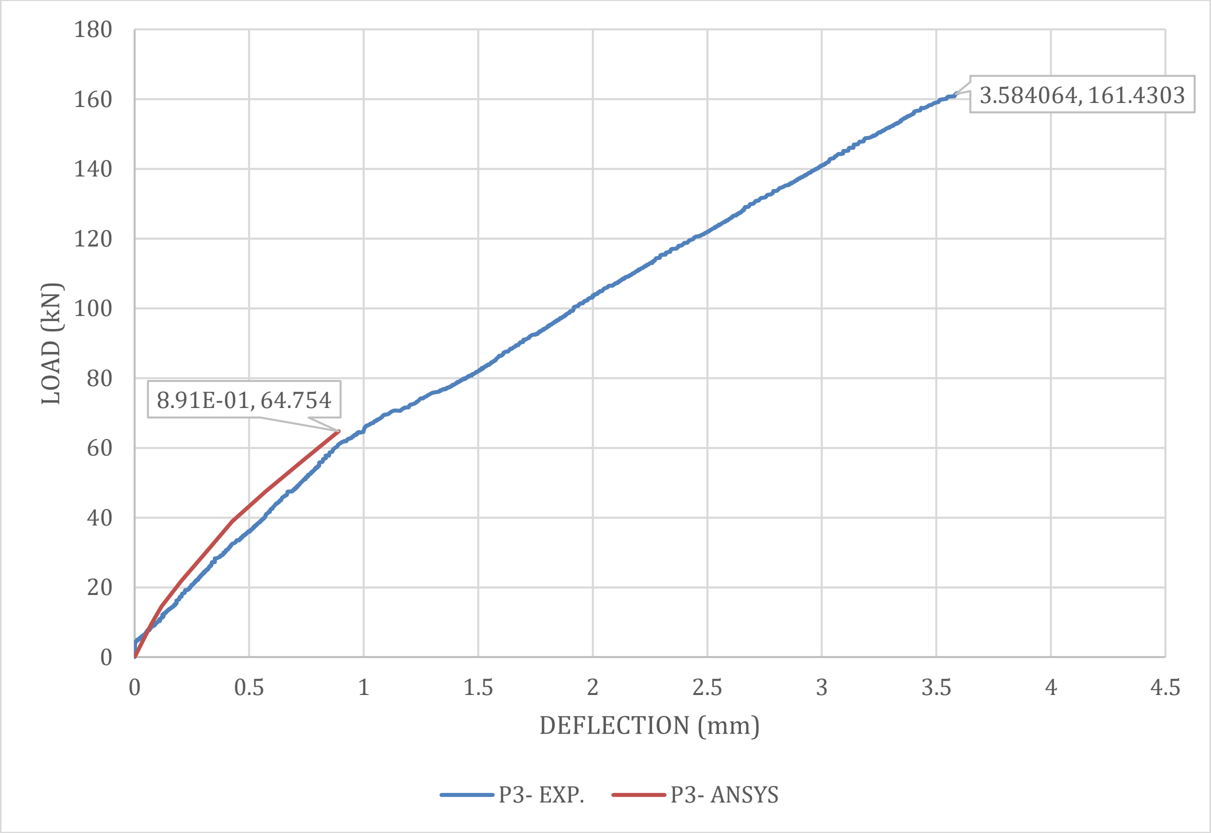

Figure 7-21 ANSYS vs. DIC-camera results for point 3 within F1 beam

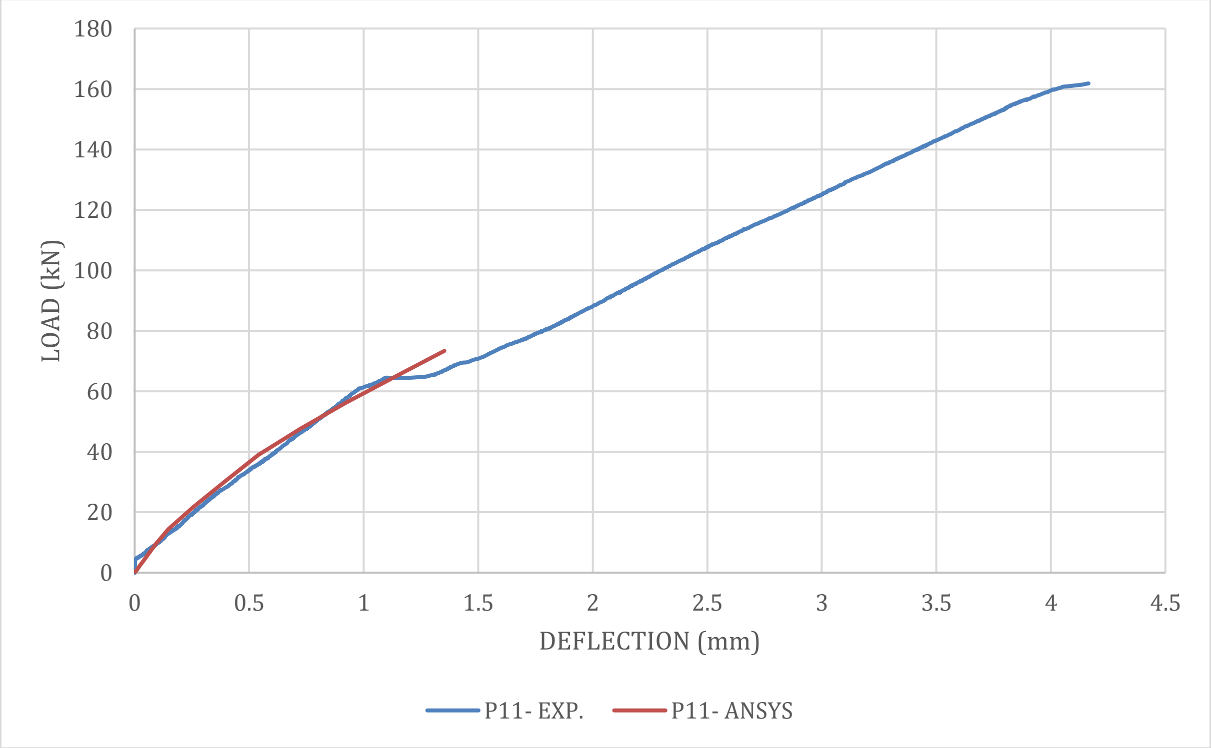

Figure 7-22 ANSYS vs. DIC-camera results for point 11 within F1 beam

7.4.4. Beam- D1

Figure 7-23 shows the positions of the points that were obtained from DIC- camera for D1 beam.

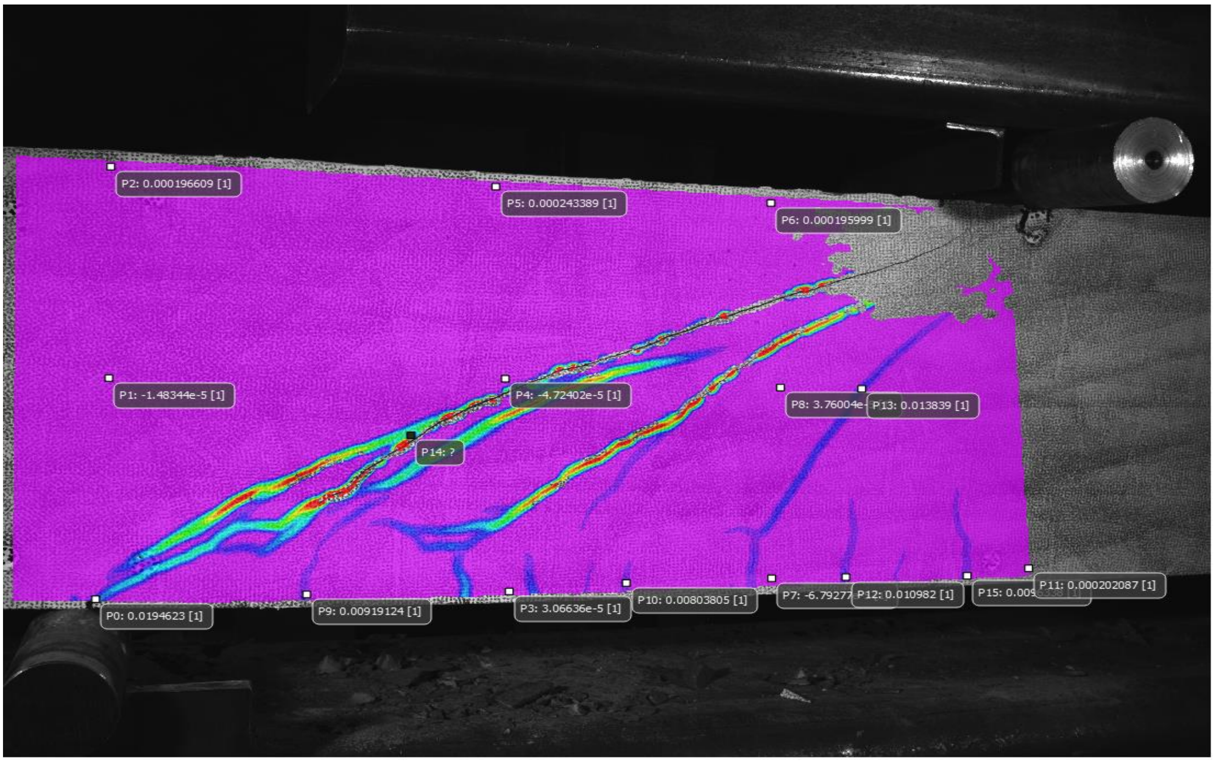

Figure 7-23 The extracted points from DIC- camera for beam D1- 0.5% fibre volume

The following figure shows the points that represent the best match between DIC- camera results and ANSYS.

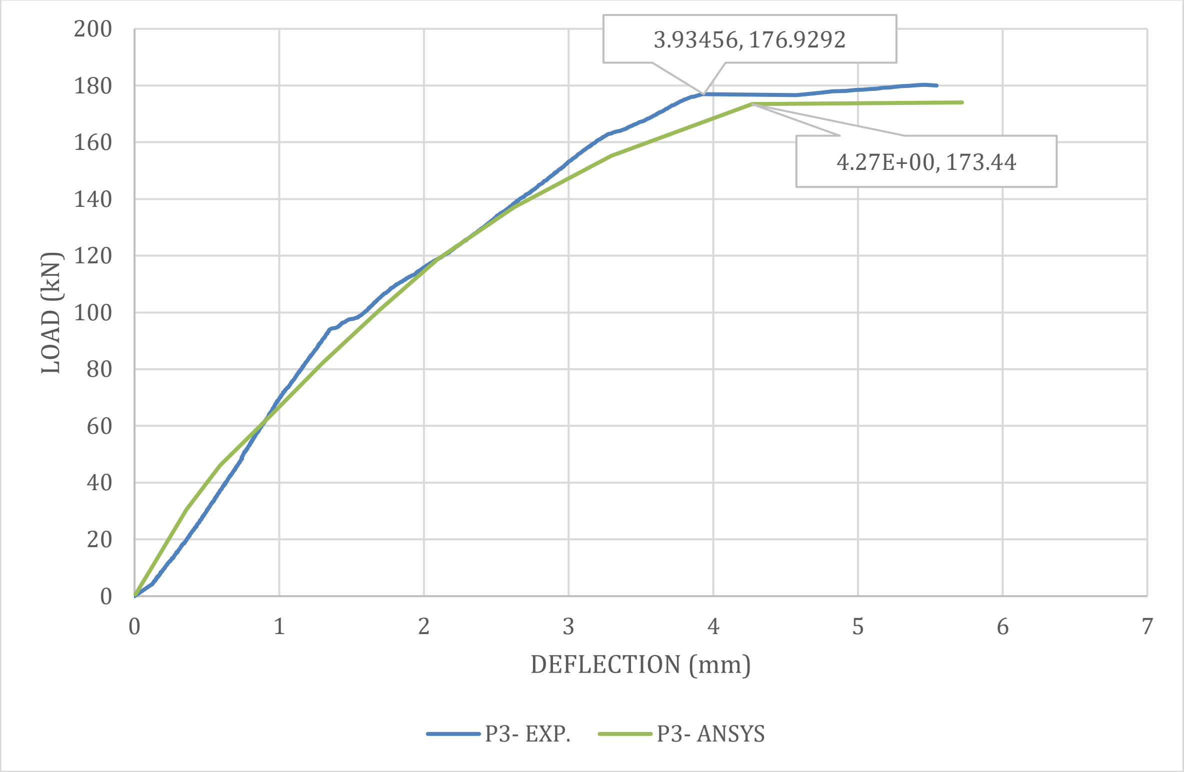

Figure 7-24 ANSYS vs. DIC-camera results for point 3 within the D1 beam

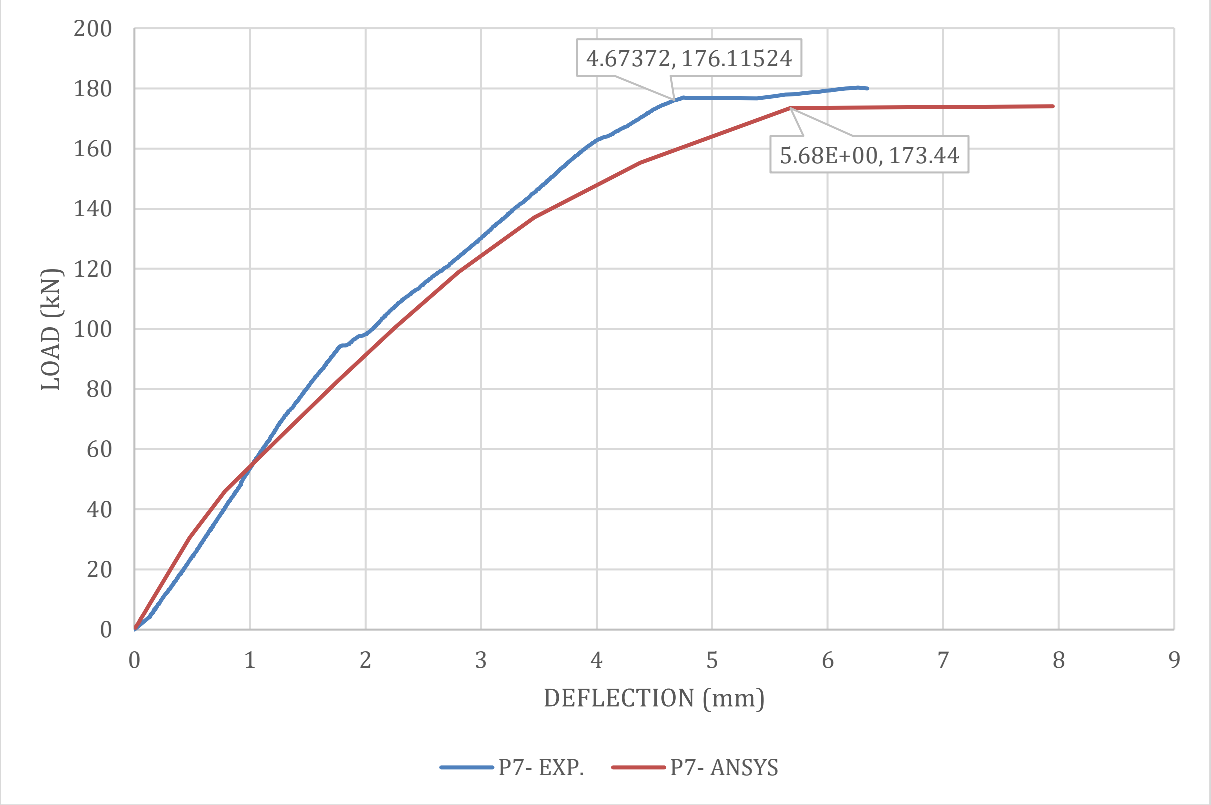

Figure 7-25 ANSYS vs. DIC-camera results for point 7 within the D1 beam

7.4.5. Beam- D2

Figure 7-26 shows the positions of the points that were obtained from DIC- camera for D2 beam.

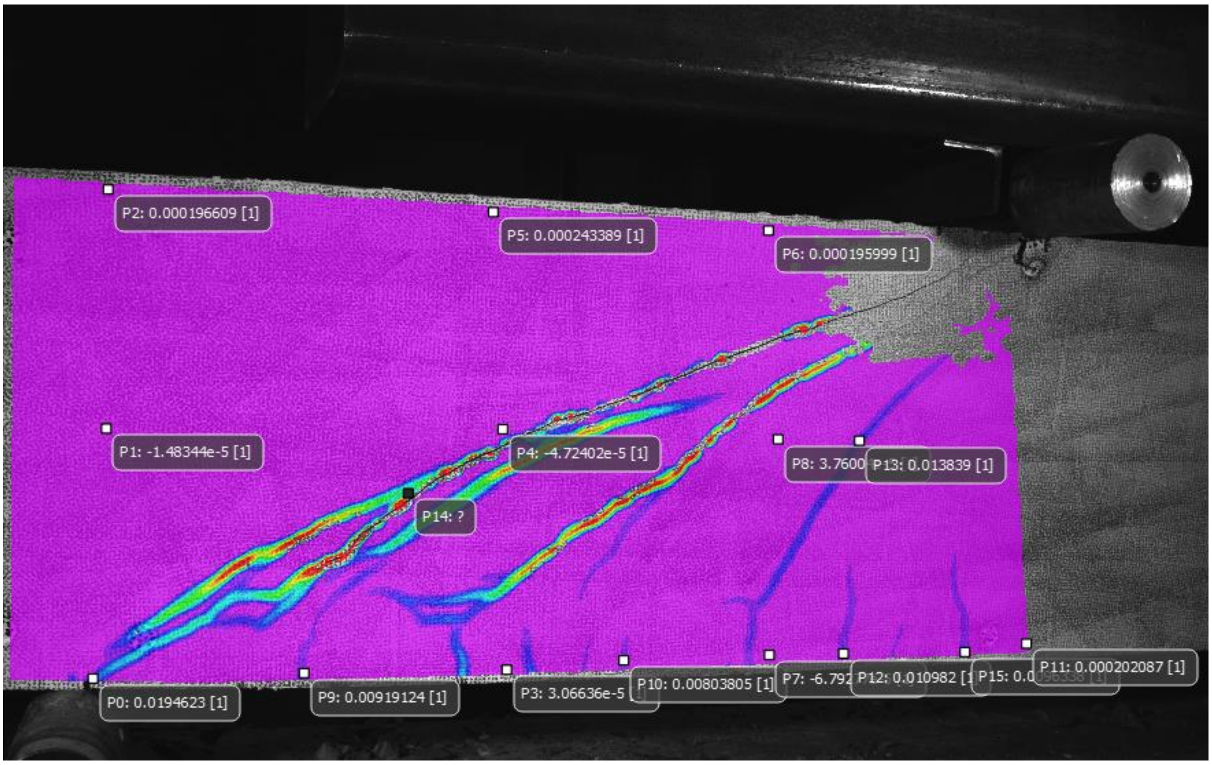

Figure 7-26 The extracted points from DIC- camera for beam D1- 0.5% fibre volume

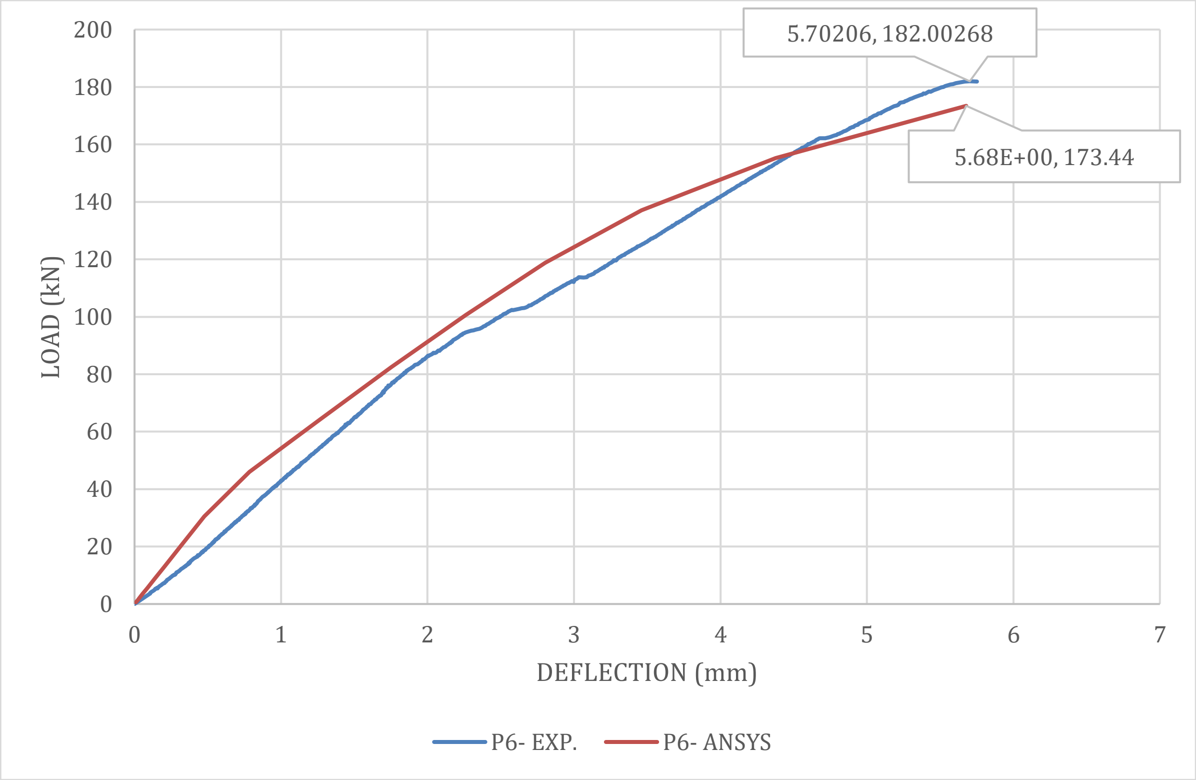

Figure 7-27 ANSYS vs. DIC-camera results for point 6 within D2 beam

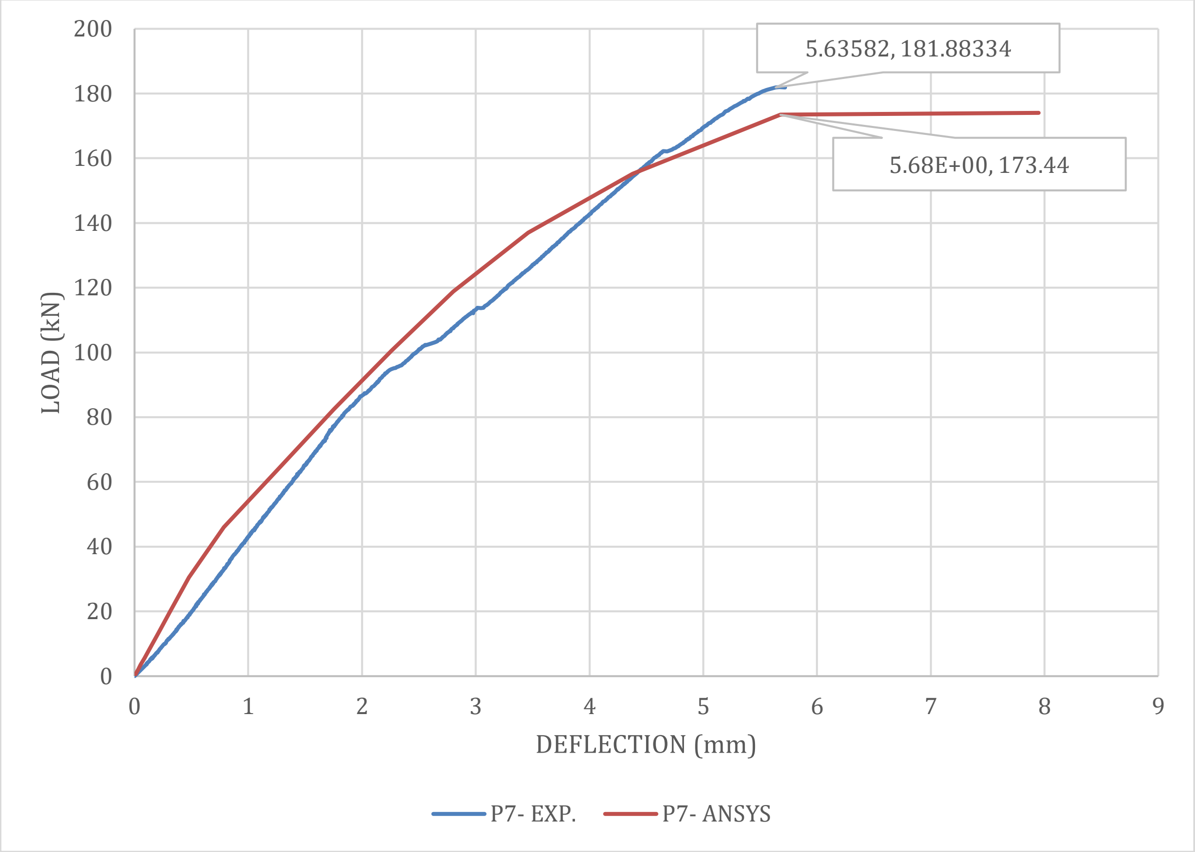

Figure 7-28 ANSYS vs. DIC-camera results for point 7 within D2 beam

7.4.6. Beam- G1

Figure 7-29 shows the positions of the points that were obtained from DIC- camera for G1 beam.

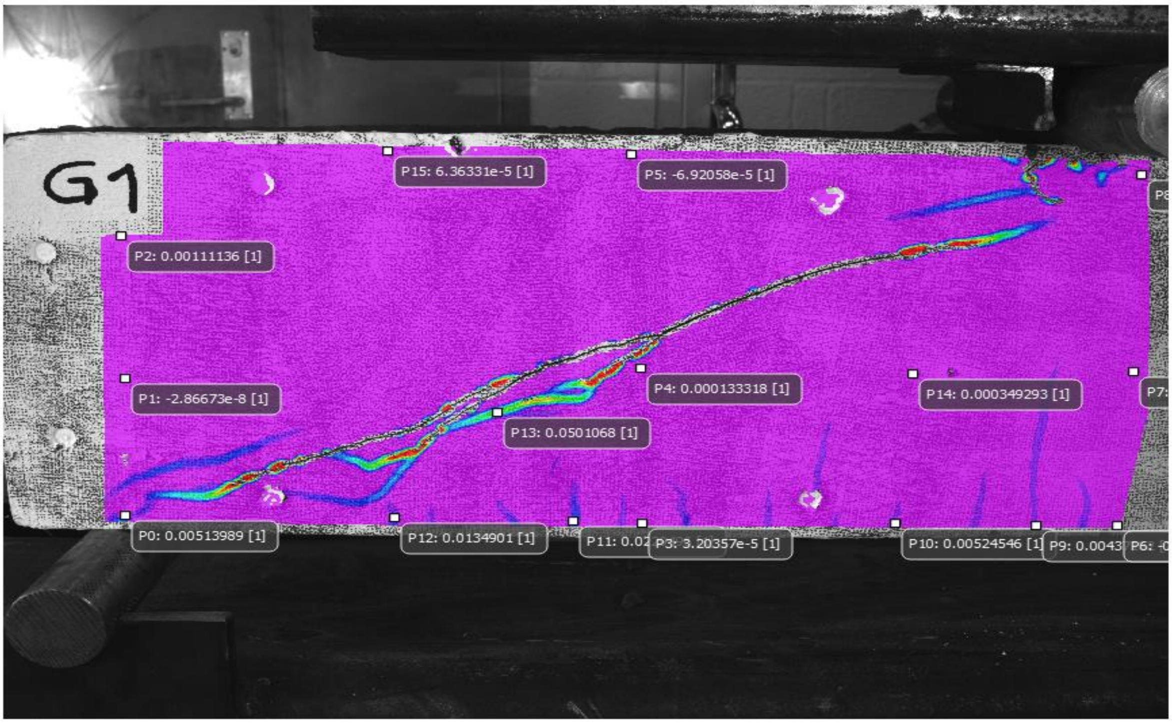

Figure 7-29 The extracted points from DIC- camera for beam G1- 0.5% fibre volume

The following figure shows the points that represent the best match between DIC- camera results and ANSYS.

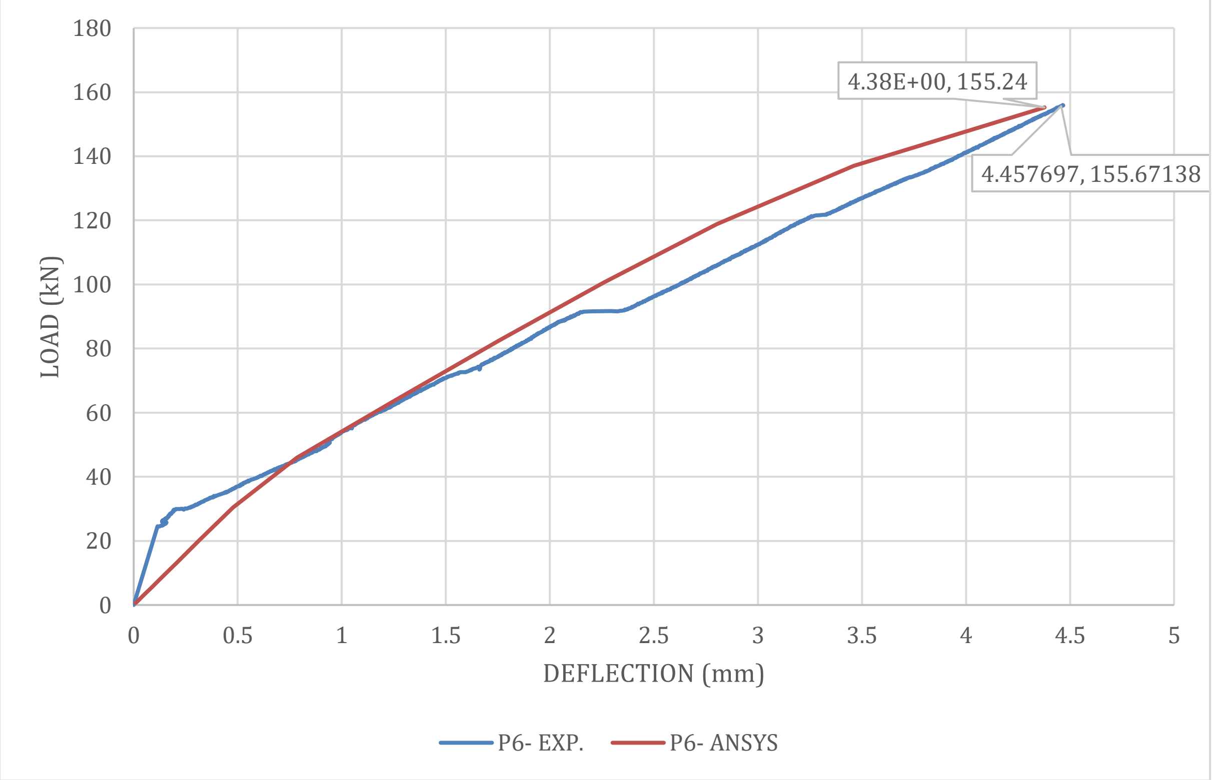

Figure 7-30 ANSYS vs. DIC-camera results for point p6 within G1 beam

7.4.7. Beam- E1

Figure 7-31 shows the positions of the points that were obtained from DIC- camera for E1 beam.

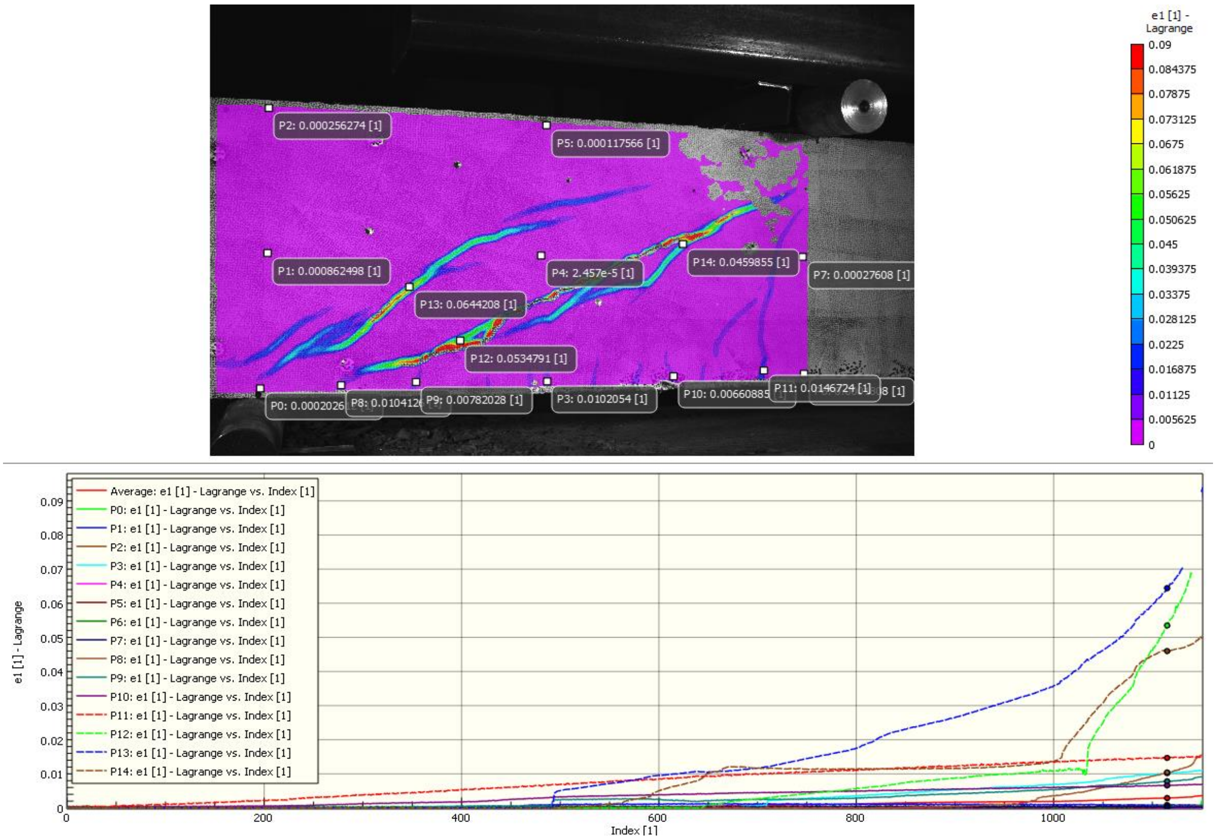

Figure 7-31 The extracted points from DIC- camera for beam E1- 1% fibre volume

The following figure shows the points that represent the best match between DIC- camera results and ANSYS.

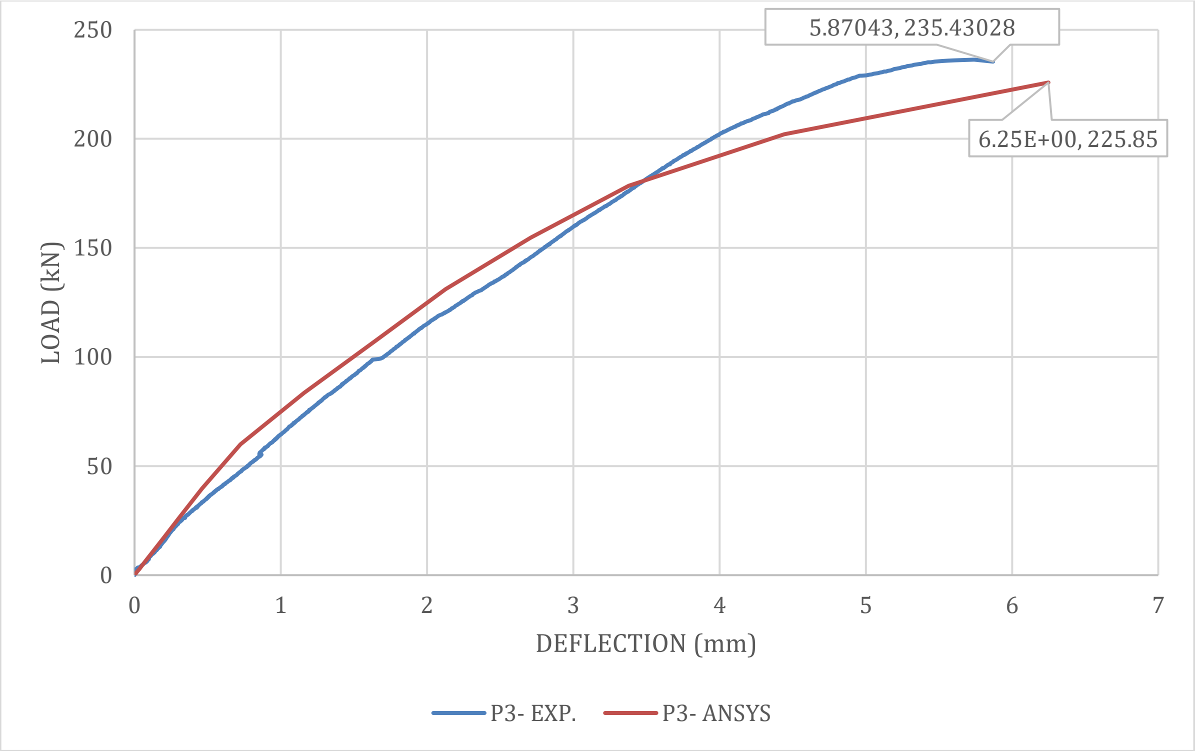

Figure 7-32 ANSYS vs. DIC-camera results for various points within the E1 beam

7.4.8. Beam- E2

Figure 7-33 shows the positions of the points that were obtained from DIC- camera for E2 beam.

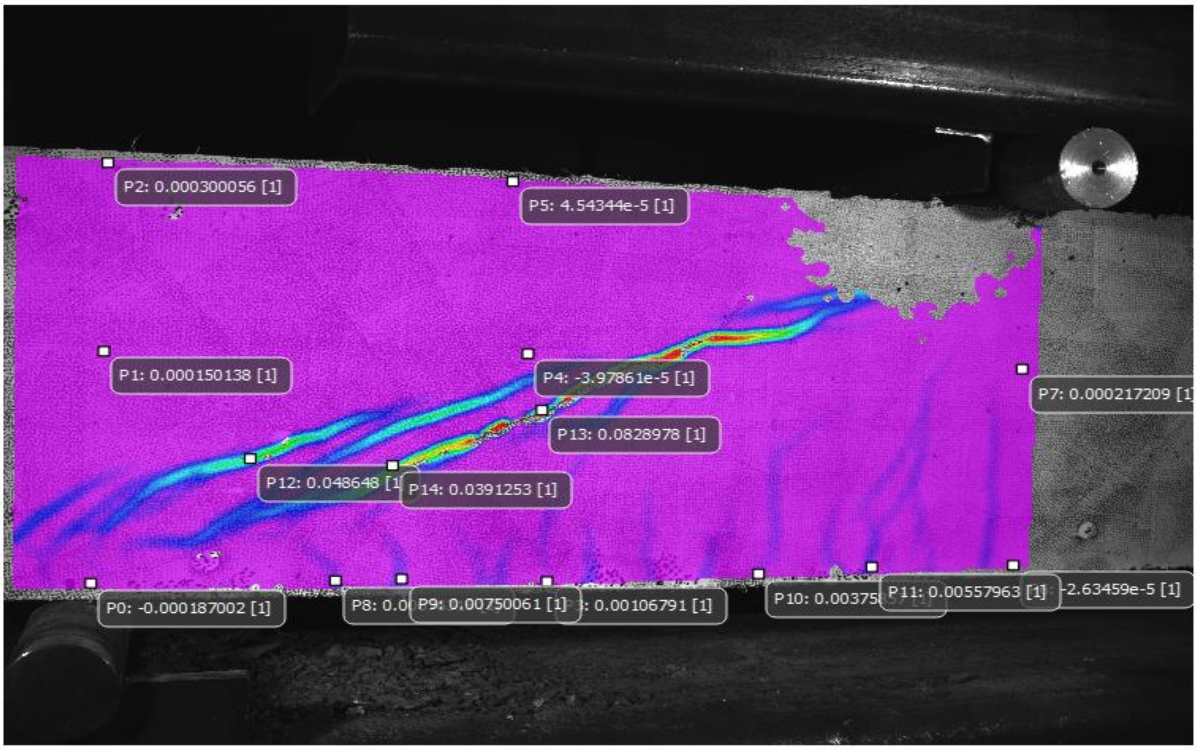

Figure 7-33 The extracted points from DIC- camera for beam E2- 1% fibre volume

The following figure shows the points that represent the best match between DIC- camera results and ANSYS.

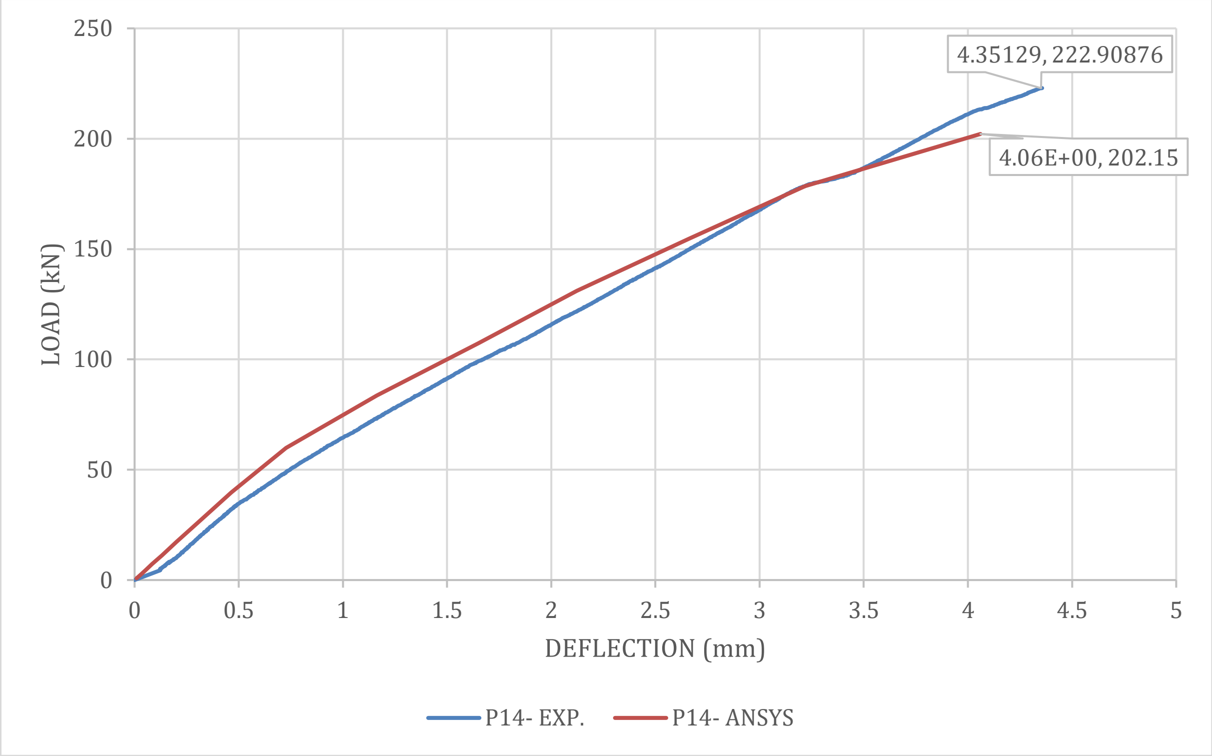

Figure 7-34 ANSYS vs. DIC-camera results for point 14 within the E2 beam

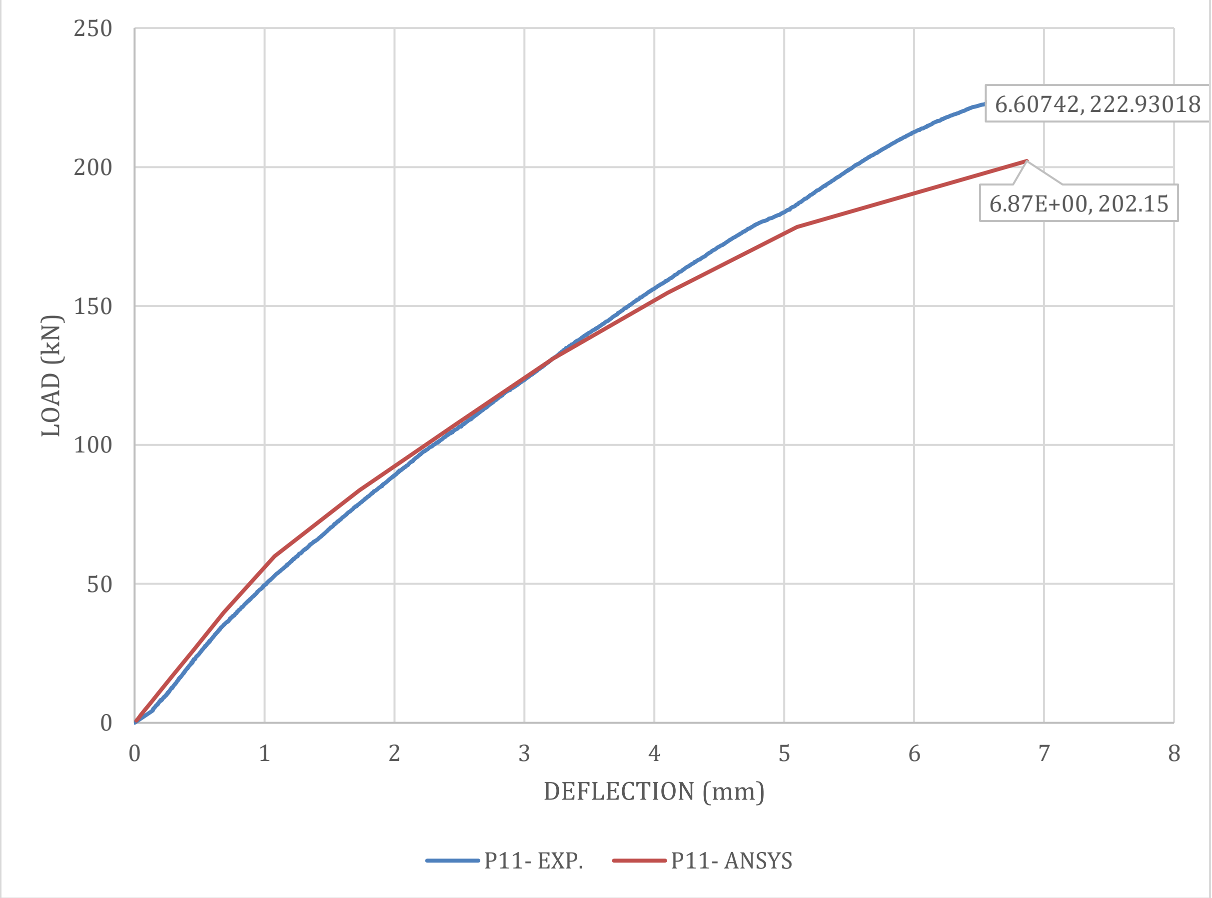

Figure 7-35 ANSYS vs. DIC-camera results for point 11 within the E2 beam

7.4.9. Beam- H1

Figure 7-36 shows the positions of the points that were obtained from DIC- camera for H1 beam.

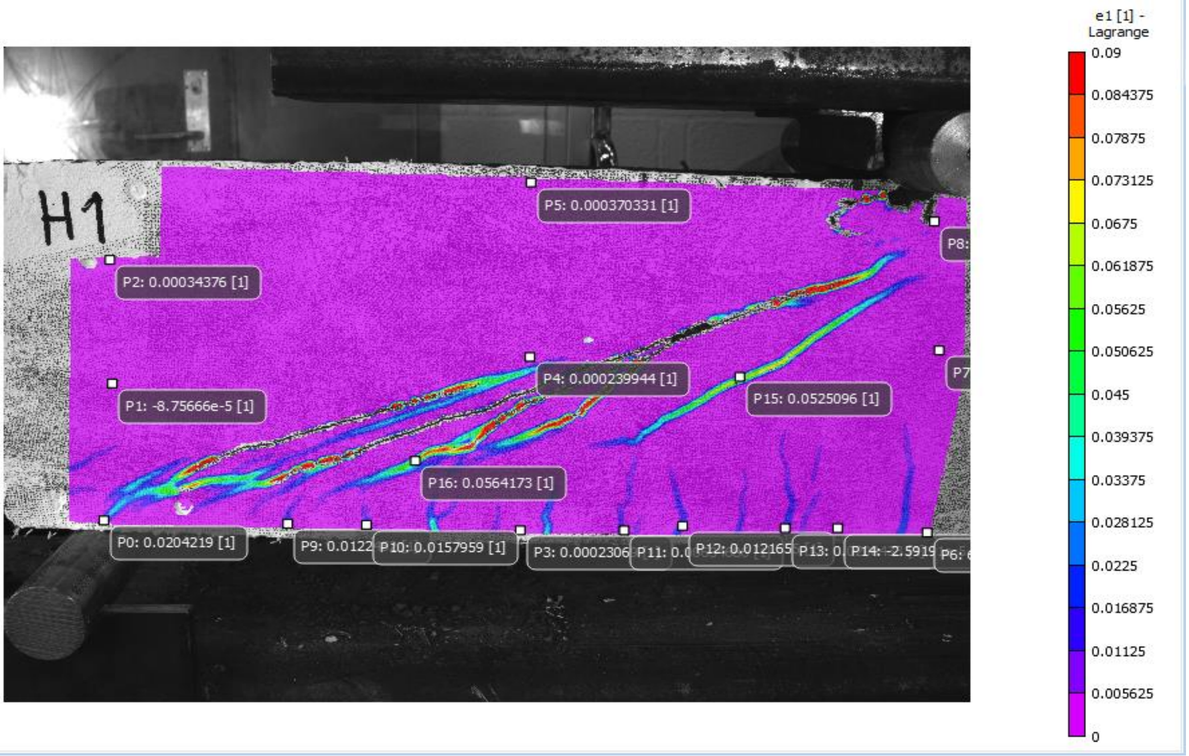

Figure 7-36 The extracted points from DIC- camera for beam H1- 1% fibre volume

The following figure shows the points that represent the best match between DIC- camera results and ANSYS.

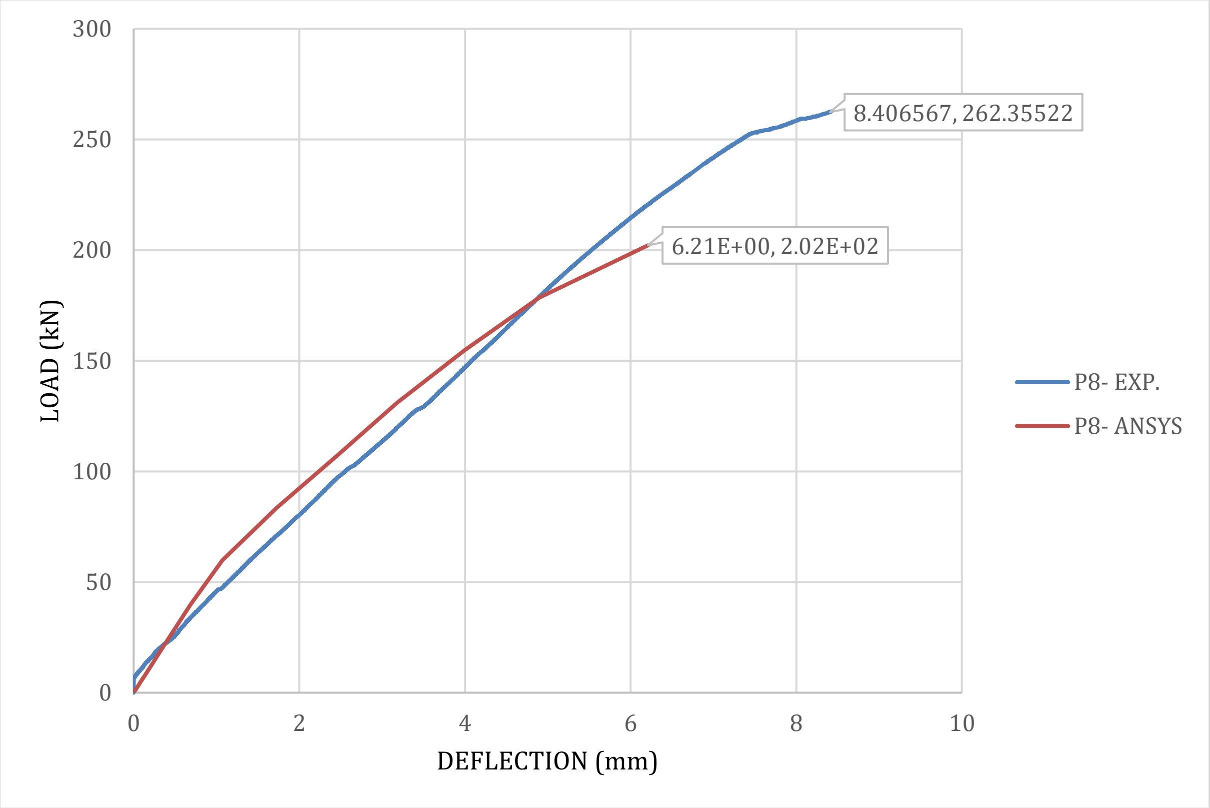

Figure 7-37 ANSYS vs. DIC-camera results for point 8 within the H1 beam

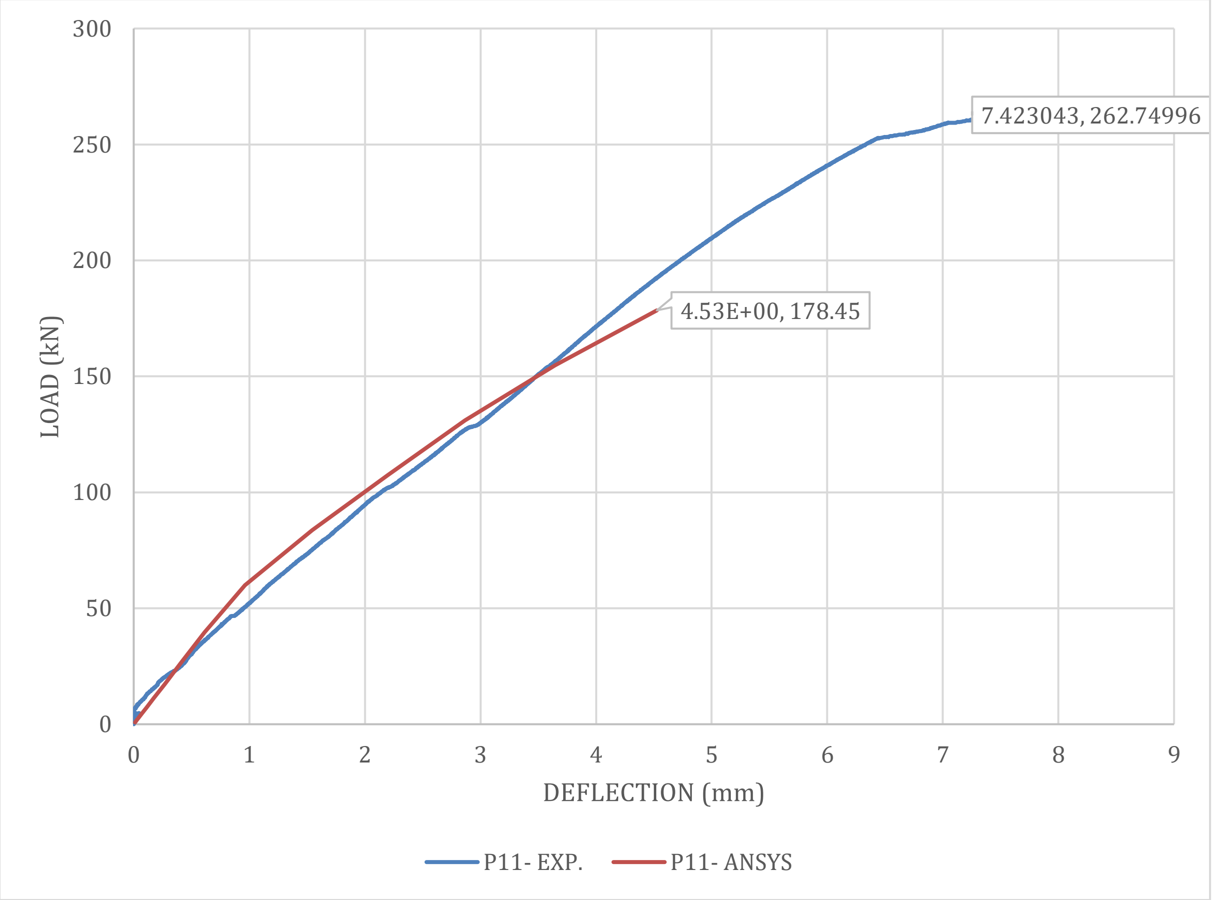

Figure 7-38 ANSYS vs. DIC-camera results for point 11 within the H1 beam

7.5. Cracking behaviour

7.5.1. First cracking load

The first cracking load refers to the load step where the first crack can be detected in the concrete of the finite element model. Out from Figure 7-39, Figure 7-40 and Figure 7-41, it can be seen that the first crack occurs as a flexural crack.

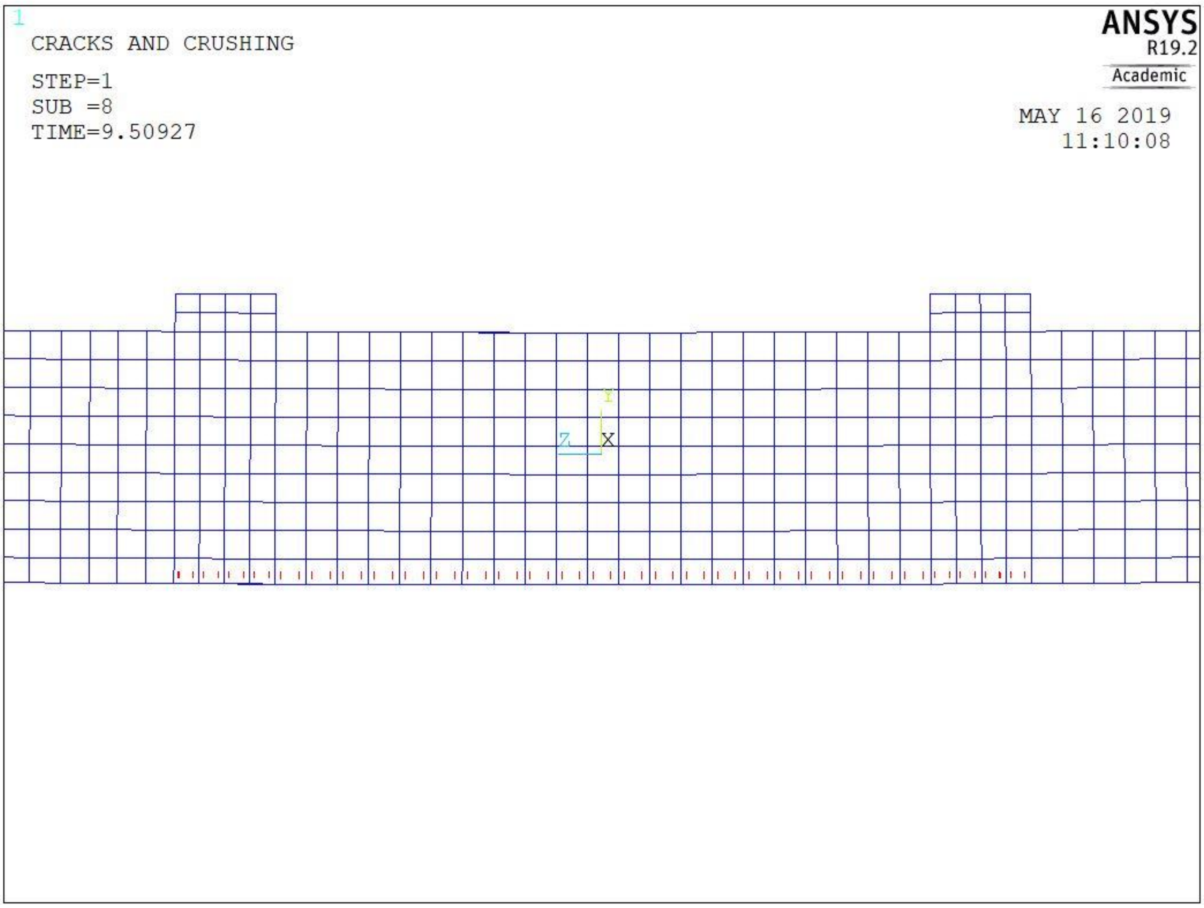

Figure 7-39 First crack of the concrete model for 0% fibre volume at 9.50927 kN

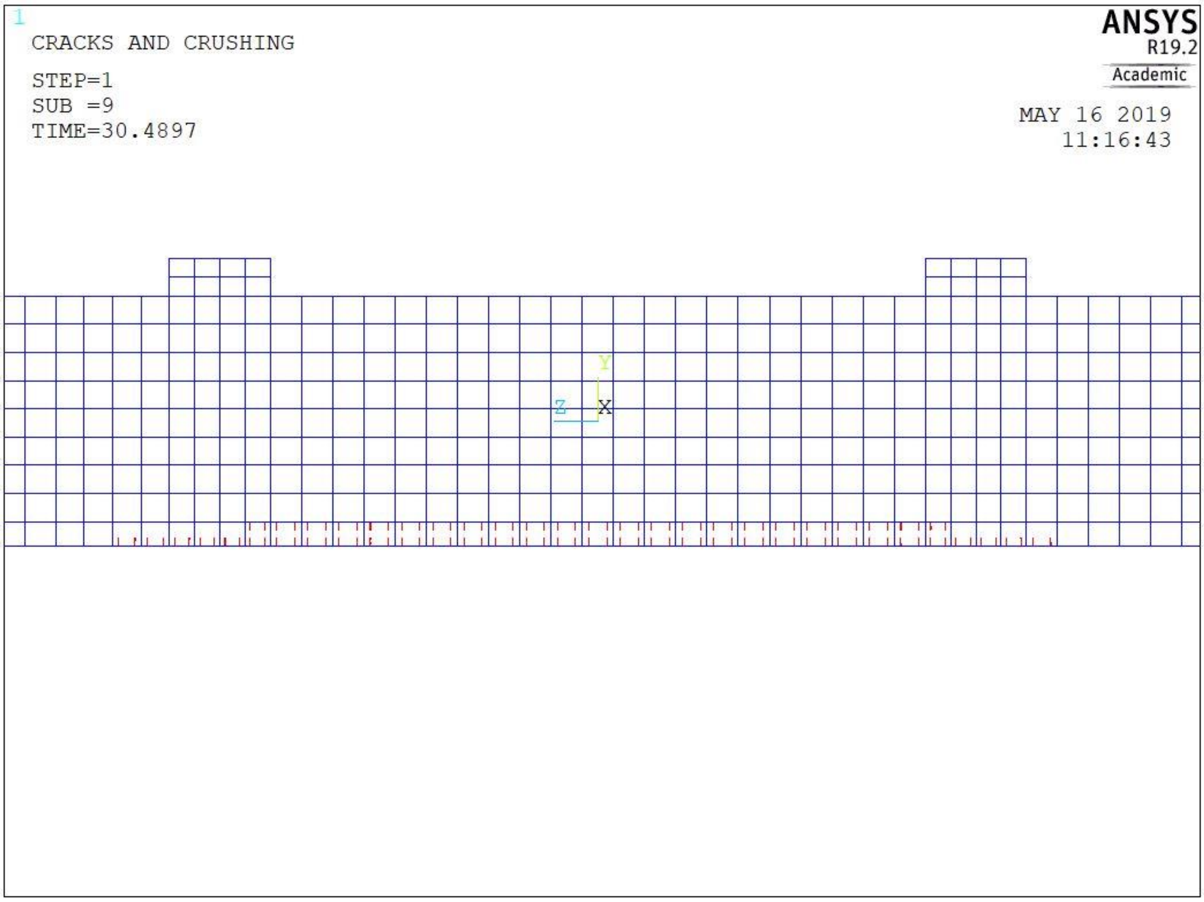

Figure 7-40 First crack of the concrete model for 0.5% fibre volume at 30.4897 kN

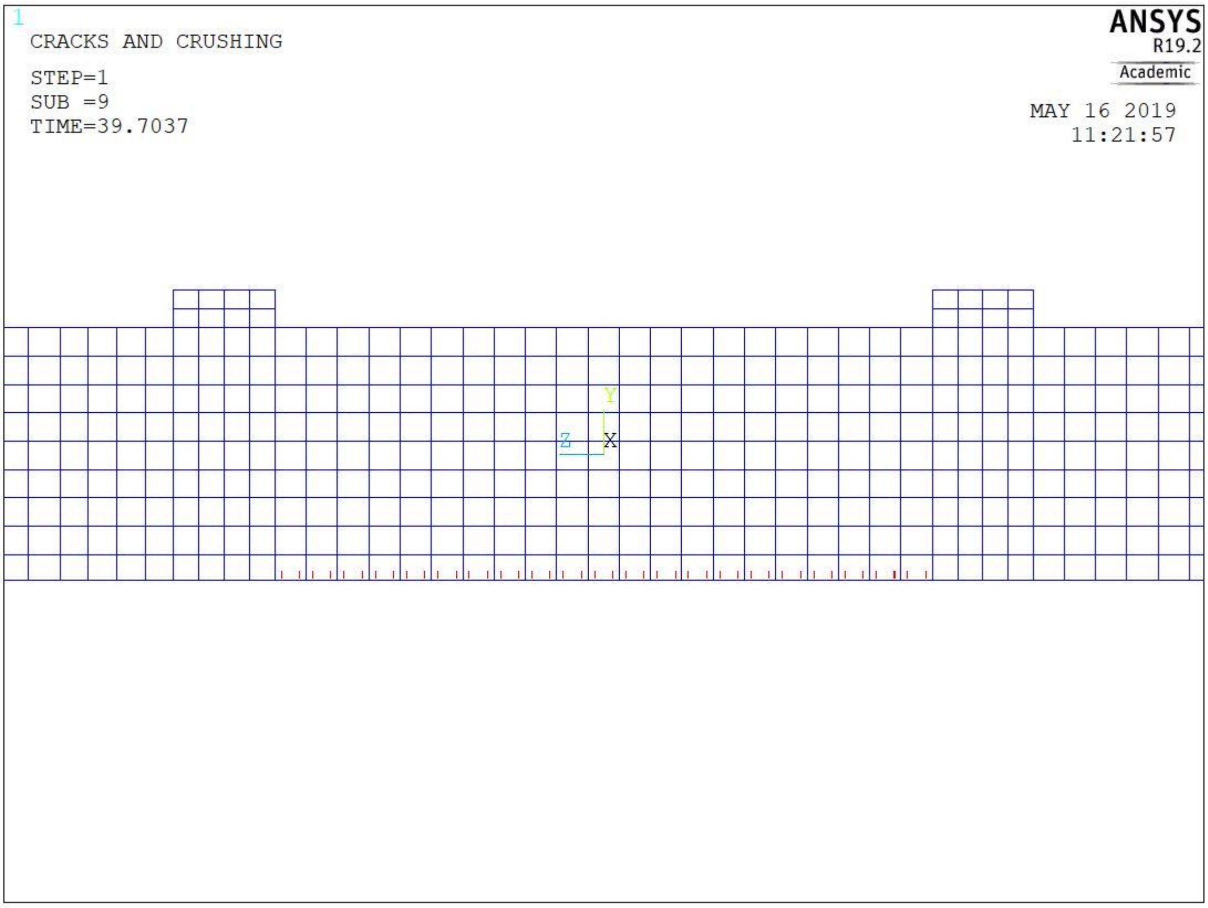

Figure 7-41 First crack of the concrete model for 0% fibre volume at 39.7037 KN

7.5.2. The behaviour of Reinforcement Yielding and Beyond

Figure 7-42 and Figure 7-43 show that yielding of the reinforcements happened at 155.238 KN and 178.451 kN for 0.5% and 1% volume fibre, respectively. For 0% fibre volume, there was no yielding of the reinforcement.

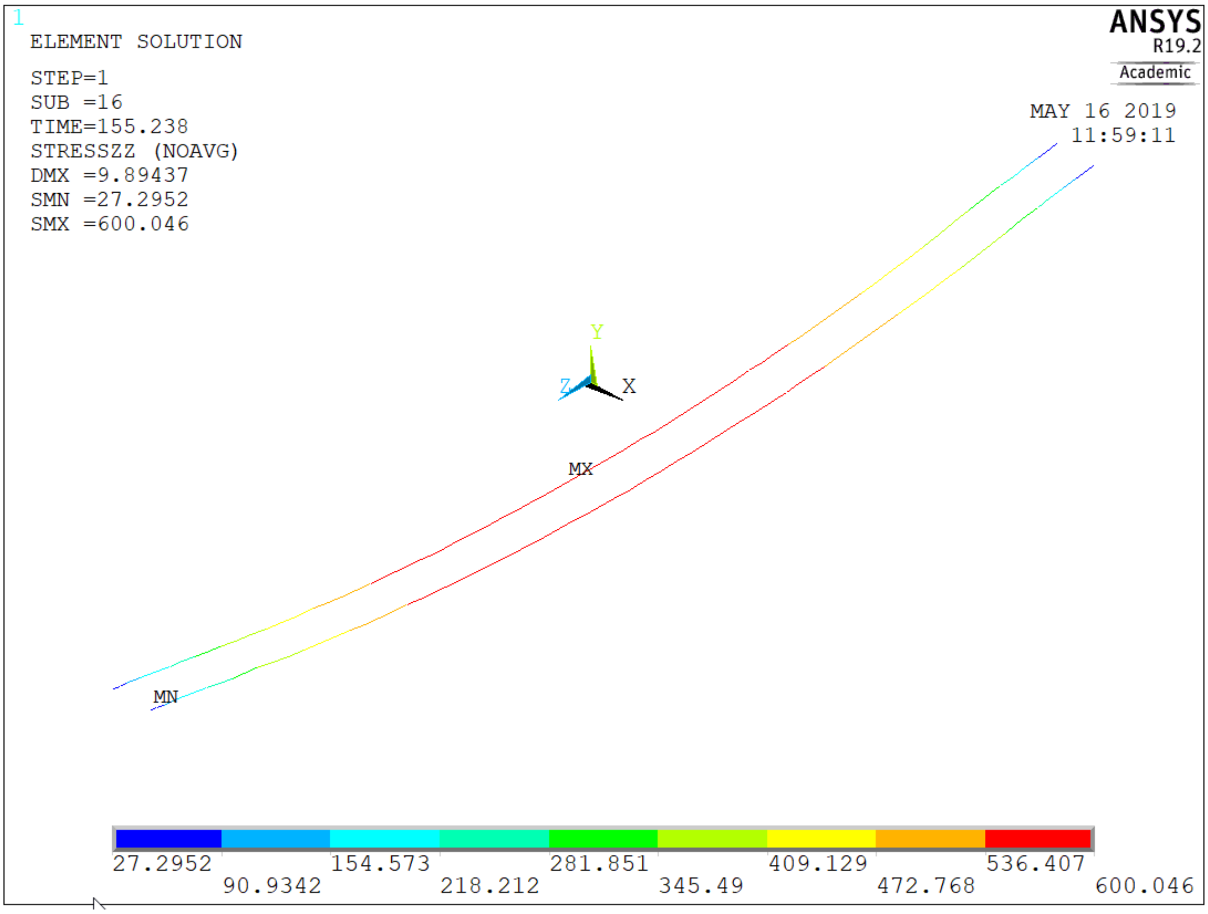

Figure 7-42 Yielding of reinforcement at 155.238 kN for 0.5% fibre volume

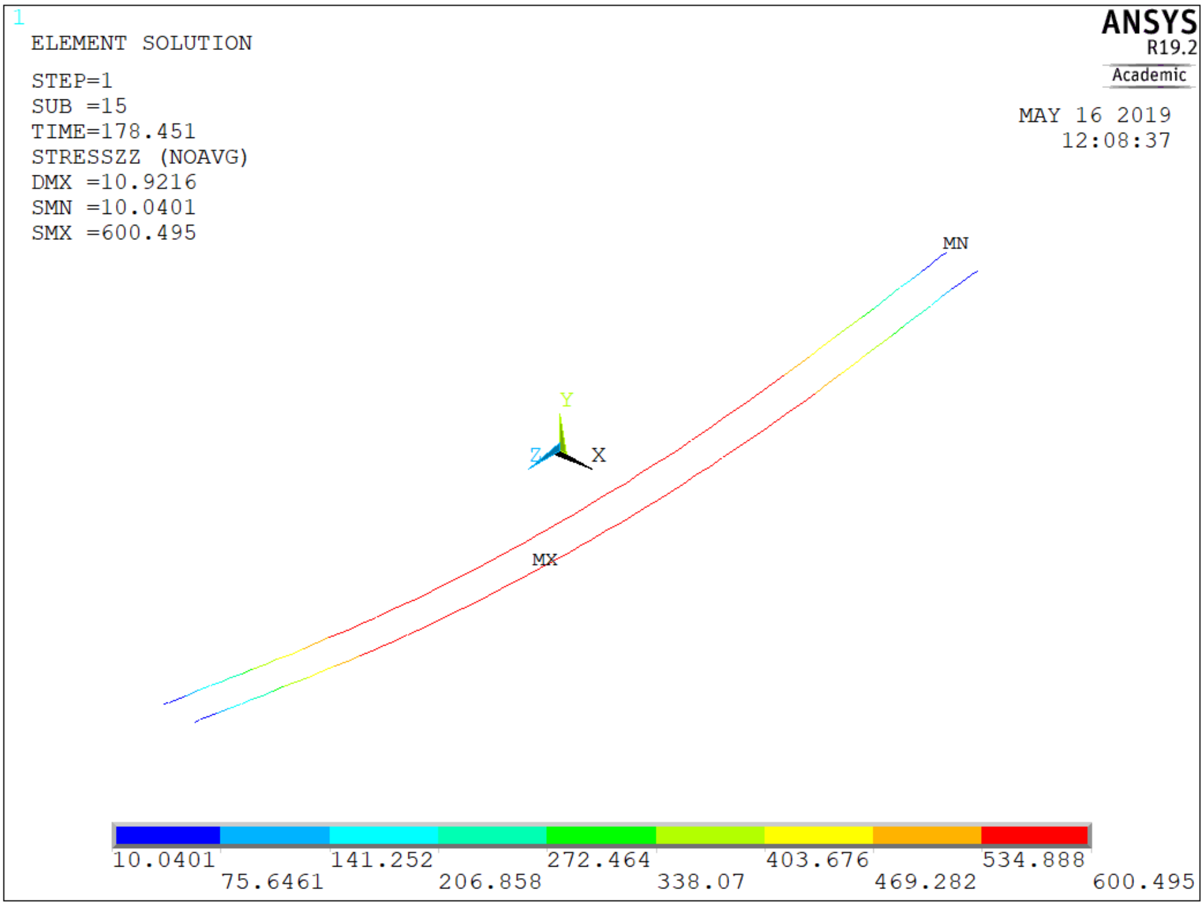

Figure 7-43 Yielding of reinforcement at 178.451 kN for 1% fibre volume

As extra load is applied after yielding, the displacements of the beam begin to increase at a larger rate. A progressive cracking of the concrete beam after yielding of the reinforcement can be observed in Figure 7-44.

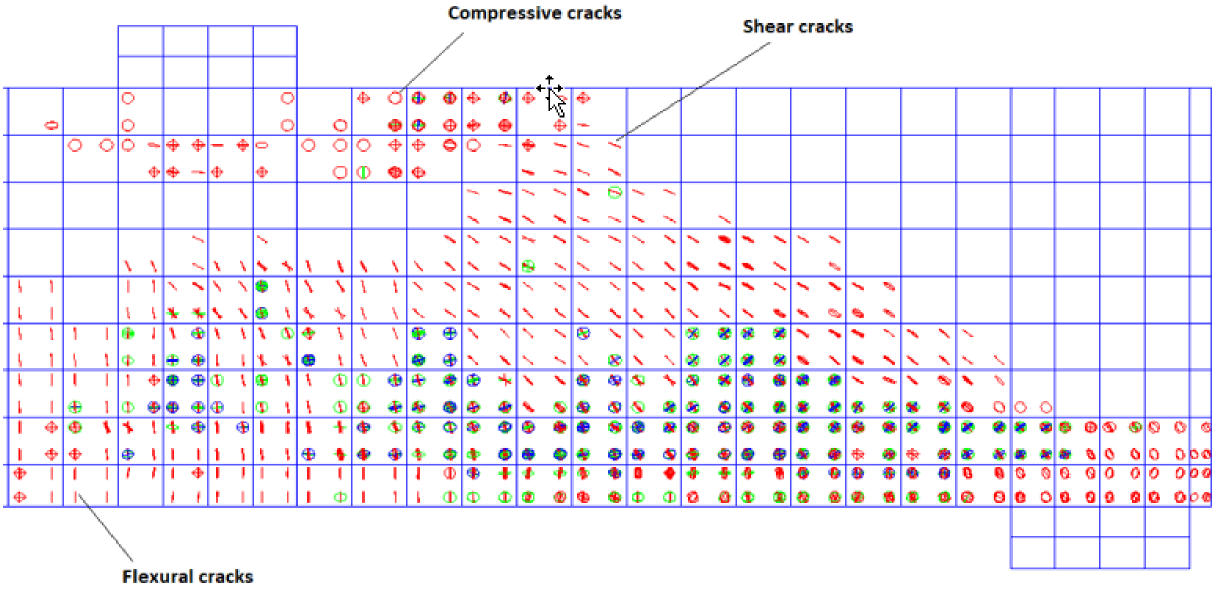

Figure 7-44 Crack types after yielding of reinforcement

Figure 7-45 shows the crack pattern in the concrete model near to failure

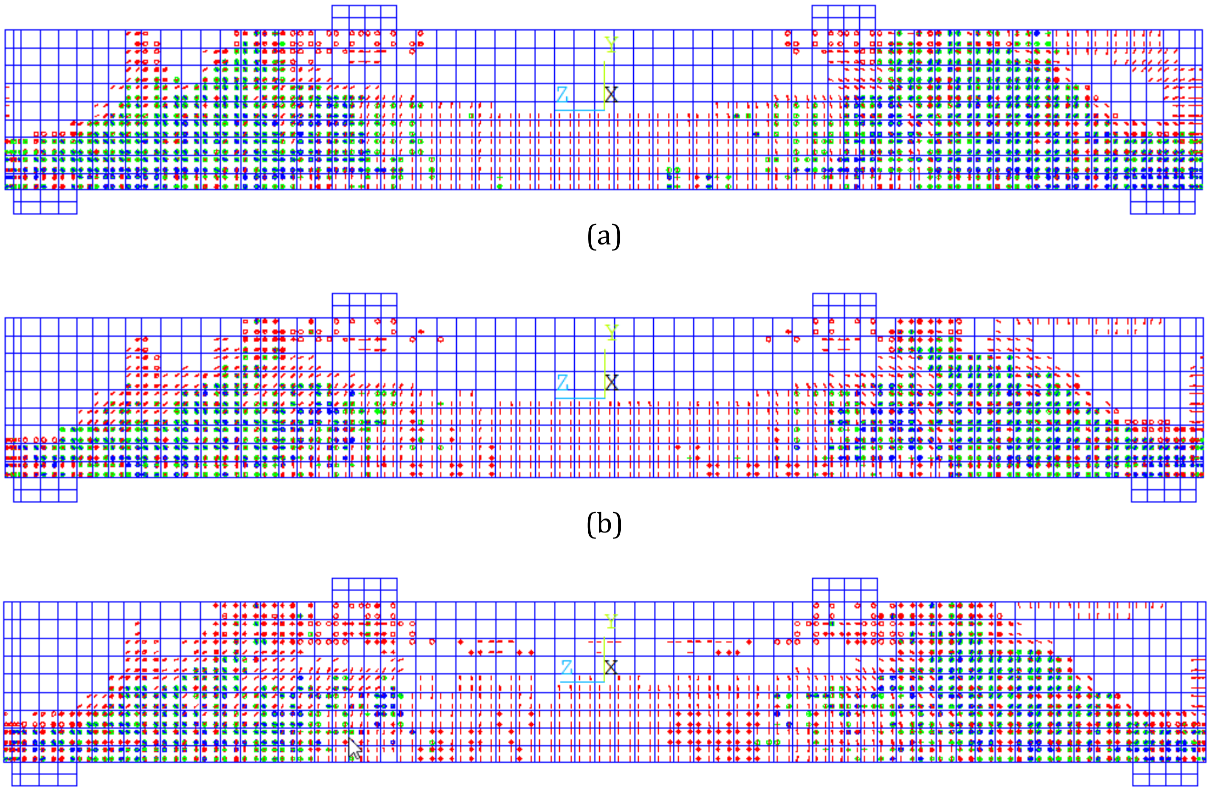

(a)

(b)

(c)

Figure 7-45 Cracking pattern near to failure; (a) 0%, (b) 0.5% and (c) 1%

8. Discussion

8.1. Experimental work

8.1.1. Casting and UHPC properties

Mixing

We got Velde- filler in early April. The material was wet, and we had to do the water absorption test to verify the proper mixing ratio so that the filler did not absorb the concrete mixture water and lead to a lower compressive strength. The water absorption test result proved that the ratio is 2.63%. This result is very similar to the one obtained by Prabhat et al. [81]. However, in our preliminarily report the used percentage was 2.8 %. Since these two percentages are close, there will be no significant impact on the results. Hence, we decided to use 2.8% so that we keep the same mixing procedure as in the first semester. The results of the compressive strength test on cubes were close to the previous semester results. This confirms to a large extent that the mixture is very much the same.

Casting

The casting process was one of the most critical challenges to get similar properties to what we got in the previous semester. Generally, handling UHPC is not easy because of the low water/cement ratio. However, the tiny particles of UHPC manage to spread well around the longitudinal reinforcement and let the mixing flow to get better fibre orientation.

Properties

During the casting, we noticed that the fibre has an essential effect on the air content and flowability of UHPC. It is obvious from our results (Annex D) that as the fibre dosage increases, the air content decreases while the flowability increases which can be explained by the good dispersion of the fibre as been also found by Wang et al. [82].

As expected, the cubes and cylinder that were cured at 90 degrees show higher compressive strength. This confirms the fact that heat treatment is valuable for the activation of the hydration reaction. In addition, at 20 degrees and 14 days, the compressive strength of cylinders were almost 96% of the compressive strength of the cubes. This coincided with Graybeal and Davis test results, who examined 1000 specimens using different curing regimes, including treatment at 90 degrees for 48 hours and also used similar fibre to our case [83]. This may be due to the confinement effect of the testing machine platens.

As can be seen in Figure 8-1, it is obvious that UHPC is an explosive material while the addition of fibre ensures ductile behavior, this coincides with the results obtained by by Graybeal and Fehling et al. [16] [57]. In general, when the fiber rate increases, the flexural strength of UHPC increasesdue to the bridging mechanics of fibre, which restrain the propagation and growth of cracks.

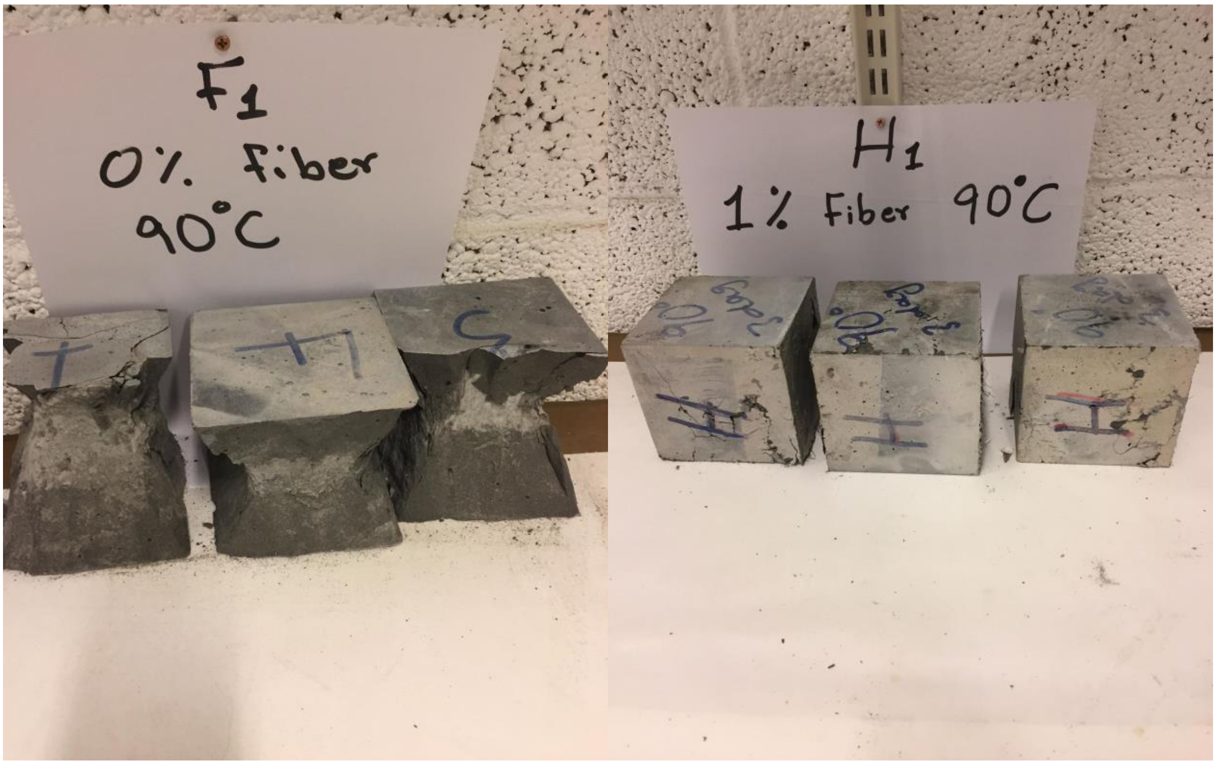

Figure 8-1 Cubes at failure due to compressive strength test with different fiber content

Regarding E- modulus and compressive strength, tt was observed that UHPC compressive strength and elastic modulus was not significantly affected by the addition of steel fibers. Higher steel fibers dosage can lead to gathering the fibre in the same place, this driving to weakness in this place and reduce the efficiency of fibers. Hence compressive strength is decreased. This was also found by Schmidt et al. [84]. Besides, with the addition of 1% fibre, the modulus of elasticity was almost the same compared to 0% and 0.5% fibre volume. This was also stated by Bonneau et al. [85]. Furthermore, the elastic modulus of UHPC increaing follows the curing regime process. This coincide with Graybeal experimental results [57]. For instance, the modulus increased from 39 to 43 GPa when specimens were subjected to 90 degrees for 2 days.

8.1.2. Large- scale prisms

The results of the large- scale prisms, have not been included in this thesis. These results will be used further to be puplished beside the results obtained in this thesis as well as the experimental results of two extra beams reinforced by 0% steel fibre.

8.1.3. Shear strength

In this work, three large- scale UHPC beams (F1, G1, and H1) were tested. A shear span-to-depth ratio (a/d) of (2) was held constant by maintaining the shear span, a, at 400 mm.

Failure load

The experimental observations show that the inclined stirrups that were located on one side served as shear reinforcement to provide more shear capacity in addition to the contribution of the fibre and the concrete towards the ultimate shear capacity, where there was no failure crack on that side.

On the other side, there were no shear reinforcements. The failure loads were 161.67 kN and 175.33 kN of the beams F1 and G1, respectively. These results are very near to each other. Also, the failure mode of F1 as shown in Figure 7-6, was sudden and catastrophic.

Compared with the results of the previous semester for C1, C2, D1, and D2, the result of G1 is quite acceptable while the result of F1 is approximately three times the value of the shear strength of C1 and C2. It should be noted that the concrete mix as we mentioned earlier is almost the same where the results of the compressive strength tests were close, and all the treatment conditions were the same. The reason behind this high strength of F1 is because we attach the longitudinal reinforcing steel with an additional connection to fix the rebars in place. This point is undoubtedly significant and must not be passed unnoticed as a simple change in the beam installation process led to a significant increase in resistance. This point needs a more in-depth study in the future.

The third beam H1 was strengthened by 1% fibre volume. This beam failed in shear as well where fewer vertical cracks started and propagated, as shown in Figure 7-8. The ultimate load was found to be 262.82 kN (50% greater than G1 beam) with corresponding midspan displacement of 14.468 mm. The higher fibre volume in this beam has an additional improvement in the failure load with a ductile failure. This can be due to the bridging mechanism of the fibre which passes through the cracks and hold them together. Such results were stated by several researches [38] [39].

Generally, the shear capacity of UHPC beams reinforced with 1% fibre was 58.3% higher than UHPC beams reinforced with 0.5% fibre. Moreover, 1% fibre volume specimens experienced 42% higher deflection than their 0.5% counterparts.

Modes of failure

All beams failed in shear. Tow kinds of failure were observed; shear-compression and diagonal tension. F1 failed in shear-compression as shown in Figure 7-6. The diagonal crack under this failure is not a consequence of earlier flexural cracks, but it develops separately within the shear-span. The diagonal crack extended towards the compression zone at the loading point resulting in the crushing of the concrete in an explosive behavior due to a sudden release of stored energy.

On the other hand, G1 and H1 failed in diagonal tension. The shear crack at failure come mainly from several flexural cracks within the shear span. The shear crack spreads approaching the loading point as shown in Figure 7-7 and Figure 7-8. As a consequence, the shear crack works to split the beam into two pieces. This model of failure is less explosive and may be associated with a horizontal crack at the lower part of the shear crack. The horizontal crack destroys the bond between the concrete and rebars. In this case, in contrast to shear-compression failure, the stored energy releases gradually so that the ultimate amount is less than the ultimately released energy of F1 case. Consequently, a less explosive failure happened. This results coincide with the investigation conducted by Bazat and Kazemi [86] and Hai H. Dinh et al. [36].

This difference in failure between F1, G1, and H1 is due to the occurrence of fibres, where there is no fibre in F1 beam. In G1 and H1 beams, fibre serves in transfer tension over the inclined crack which enables new shear forces to be transferred across aggregate interlock and dowel action.

Crack pattern

For G1 and H1 beams, the hairline vertical crack propagates near to the diagonal shear crack with an evenly spacing to some extent. This mechanism enhances the shear resistance of the beam and creates a more ductile failure. As it was mentioned, usually a horizontal crack results along with the longitudinal reinforcement at the downward end of the shear crack as in G1 beam (Figure *7-7*). This may be due to the span-to-depth ratio. As we have it here 2, the load cannot be directly transferred from the loading plate to the support which causes such a horizontal crack.

The continuously increased applied load was countered by fibre which holds the shear crack opening together up to failure. While the behaviour of F1 is brittle, the shear failure of G1 and H1 showed ductility characteristics. One additional reason for that may be that there was no crushing in the compressive zone in the concrete of G1 and H1 beams which confirm that randomly dispersed fibers could have useful application for the crack resistance due to fiber bridging effect mechanism.

Furthermore, inclined strut action was detected through the development of diagonal shear cracking in the beams. The slopes of the diagonal cracks were almost the same for G1 and H1 beams. The diagonal crack was unique and inclined at 20° to the horizontal axis of the beam (Figure 7-29 and Figure 7-36), whereas for F1, the diagonal crack was more horizontal (about 10°) and then became to 20° (Figure 7-20).

8.2. Prediction of the ultimate shear strength of beams

The ideal situation was represented by a blue line in Figure 7-9 and Figure 7-10, where the same shear strength could be obtained from experimental, standard and other proposed formulas.

Figure 7-9 and Figure 7-10 show that all the formulas are extremely conservative regarding 0% fibre volume specimens. While the closest predictions to the experimental results for 0.5% and 1% are Ashour et al. and Narayana et al. formulas, respectively. Sharma's formula shows very conservative prediction due to the huge gap between the calculated stress and the experimental results of the nine beams. By reviewing Table 7-11, the minimum difference between the predicted stress and the experimental results is 1.11 which belong to Ashour, Hasanain, and Wafa formula. Moreover, the next nearest prediction relates to ACI 544 following by Australian guideline which shows a reasonable conservative compared to Sharma and Imam et al. formulas. The highest ratio of experimental to predicted shear stress is for Sharma, where it was 7.91 and 10.01 for 0.5% and 1% fibre volume, respectively.

As it can be concluded, Sharma's formula is quite simple and does not provide a good prediction of the shear strength. In fact, this formula does not include the factors that have the main effect on the results, such as fibre volume, flexural strength, and tension reinforcement ratio.

When it comes to Narayana and Darwish formula, it is considered several significant factors like compressive strength, tension reinforcement, fibre volume, and shape. This formula provides more reliable results but still conservative as it overestimated the experimental results by 17% for 1% fibre volume and 58% for 0.5% fibre volume.

Ashour, Hasanain, and Wafa considered the compressive strength, tension reinforcement and fibre volume as the main factors. This formula reflects our experimental results with more accuracy than Narayana and Darwish formula regarding the beams reinforced by 0.5% fibre. The difference range was 11% for 0.5% fibre volume.

Although Imam et al. formula included important factors, it does not reflect well the experimental results. Australian guideline and ACI 544 do not include tension reinforcement ratio or flexural strength within their formulas.

It is evident that including factors related to the flexural mechanism within the formula reflect more accurately the real results, such as flexural strength or flexural reinforcement.

8.2.1. The proposed formula

By reviewing the theoretical models in the literature, it has been found that several researchers attempted to determine the shear strength of fibre reinforced concrete in general, but little research has been conducted to determine the strength properties of UHPC beams. It has also been observed that the available formulas do not consider the fibre contribution immediately. Also, some of the formulas required experimental work to find the fibre contribution by finding the residual tensile strength and crack width. Hence, a new equation for shear strength was developed by combining Narayana and Darwish formula (section 7.2.1) with UHPC properties and the contribution of fibre. We have tried to consider three main contributors to the shear strength of beams. The first part refers to the contribution of fibre in terms of the compressive strength of the

UHPC cylinder. The second part refers to the flexural tensile strength. While the third part refers to the fibre contribution across the crack. Table 7-12 shows that this formula accurately reflects the shear strength of our case. Meaning, it represents the fibre, flexural reinforcement, shear span, and compressive strength effects on shear strength considering the properties that we have. However, since we have a deadline for delivering our thesis, we could not be able to apply this formula on a high number of beams and compare the results with a higher number of formulas.

8.3. Finite element modeling

8.3.1. General issues within ANSYS

With limited previous experience of simulating and analyzing in ANSYS, it was very time-consuming to get to know the software more deeply. The official website of ANSYS was not so helpful, and there were very few published articles that deal with UHPC beams and fibre in ANSYS APDL, which delayed the process of creating the correct model. As a consequence, a considerable part of the work done in this thesis has been utilized to address many outstanding issues that appear while preparing the model.

In the early phase of the project, we started modeling the UHPC beam in ANSYS without having all the necessary data from the lab work, such as cylinder compressive strength and modulus of elasticity. Besides, we had to wait for Velde- filler to be in the lab, which is a part of the mix recipe. These issues lead to challenges in modeling the beams. However, we had started modeling before all the results were in hands by using several available formulas in the literature to convert cube strength to cylinder strength and determine the modulus of elasticity.

For a time, ANSYS provided incorrect results concerning load-deflection curves. It was observed that using force norm to get convergence is almost not achievable. Hence, by using only the displacement norm, the problem was solved, and more reasoning and smooth curves were obtained.

The obtained curves did not match with the experimental one. Therefore, we decided first to use smeared reinforcement model. In this model, the fibre and longitudinal reinforcement were represented as a layer in the SOLID 65 element. This was not helpful. Finally, we utilized the proper characteristics of every beam in ANSYS and applied discrete reinforcement model, which was much reliable and competent.

8.3.2. Finite element modeling Results Compared with Experimental Data

At the lab, sensors were used to measure deflections for the experimental beams at the centre of the beams (i.e., at the middle of length and cross-section). For ANSYS, deflections were measured at the same position as for the experimental beams. Figure 7-11, Figure 7-12, and Figure 7-13 give the load-deflection curves from the finite element modeling and the experimental results for all nine beams. Upon comparison of the failure load, it is evident that FE models estimated the failure load with 1%, 4.4% and 4.4% range difference for D1, D2, and G1, respectively. In the 0% case, the FE modeling appears to overestimate the failure load by 13% and 22% for the “C1”, and “C2” beams, respectively. In the same manner, the case of “1%” FE models evaluated the failure load with 4.55%, 1.5% and 16.37% range difference for E1, E2, and H1, respectively. Furthermore, the load-deflection curve from the finite element analysis is stiffer than that from the experimental results up to the yielding points where the curve changes its direction, and the stiffness becomes less.

At 2mm deflection for the finite element models of 0%, 0.5%, and 1%, the load differences were close to 200%, 400%, and 300%, respectively, compared to the experimental result. In general, the results do not match well. The reason for this is the chosen point (the centre of the beam) to measure the loads, as well as deflections. There might be no or very tiny cracks in the centre of the beams. This might be explained by that sensors that measured our experimental results were fixed in the centre of the beam and cracks may have started in other regions of the beam, which our experimental equipment would have been unable to detect. Thus, the experimental curves reflect an entirely linear behaviour. As the material model in ANSYS is nonlinear, it was not possible to get acceptable results. Fortunately, the DIC-camera was used to record several parameters throughout the experimental process. Hence, we decided to use the camera database to extract the load-deflection curves out from several points, on and around the diagonal shear crack, so that we could investigate the nonlinear behavior as much as possible.

However, it is obvious that there is an acceptable matching among the observed and predicted crack patterns (shear failure), which demonstrate the ability of the FE model to predict the crack pattern correctly. Besides, a crushing in the concrete was recognized in the experimental test at loading location, which was in accordance with the prediction of the FE model, as shown in Figure 7-45.

8.3.3. Finite element modeling Results Compared with DIC-camera Data

Beam- C1

Figure 7-15 and Figure 7-16, illustrate that there is good correlation between the load-deflection plots for several points extracted from the beam C1 (0% fibre volume) from the DIC- camera, and the finite element model. The finite element model shows higher stiffness for the point P3, and P11 up to the first crack, and then the stiffness becomes less gradually. The results show that FE modeling underetimates the data from DIC- camera at failure by 4.9% and 1.5 % for point P3 and point P11, respectively.

Beam- C2

Several attempts were made to extract the results from the DIC-camera for this beam, but we kept getting the same results as shown in Figure 8-2. The horizontal axis represents the vertical deflection, while the vertical axis represents the applied load in kN.

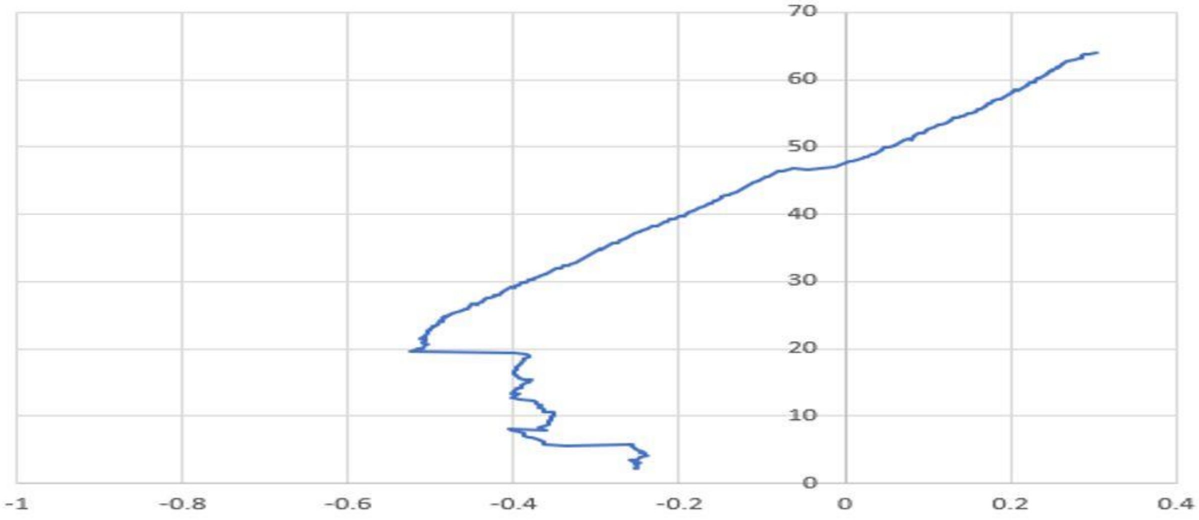

Figure 8-2 The extracted curve from DIC-camera for C2 before editing

Therefore, the curve was pulled horizontally by add 0.5 to all the points of the vertical deflection axes so that the straight line starts from the vertical axis near to 20 KN. Then the first point will be (0, 20). Hence, the numerical analysis results can be compared to the experimental one as shown in Figure 7-17. By extracting the curves of ANSYS and considering the above adjustment, it will be large spacing from zero on the horizontal axis until 0.4. At 0.4, the curves from DIC data and FE modeling begin to convergence again. Therefore, the curves in Figure 7-18 and Figure 7-19 start at 0.4. Additional detailed information can be obtained from the attached Excel files in Annex C.

However, the results show that there is a reasonable agreement between the curves from the DIC-camera and FE modeling in terms of the load at failure, where convergence is 1% for point P7 and 14% for point P4. This corresponded to a range of differences between the DIC-camera and FE modeling in deflections equal to 5.8% and 7.5% at failure for points P4 and P7, respectively.

Beam- F1

The model that was used for calibrating the beams with 0% fibre volume was used to calibrate the F1 beam. The results from Figure 7-21 and Figure 7-22 show that there is a good correlation between the curves extracted from DIC- camera and FE modeling to the point of collapse of the numerical model. As we mentioned earlier, the F1 beam showed unexpected resistance and higher failure value than the other beams reinforced by 0% fibre volume. However, the results indicate clearly that the stiffness of the numerical model is higher than the experimental one.
Moreover, the first part of the curves from the DIC- camera for this beam were being completely horizontal and irregular (up to 0.215 mm). Hence, the horizontal and irregular part were deleted so that the curves started from (0, 0).

Beam- D1

Figure *7-24* and Figure 7-25 confirm that the numerical and experimental results agree well. At peak, the differences for the investigated points were 2% and 1.5% for points P3 and P7, respectively. It is evident that the stiffness of the finite element model becomes less than the experimental one prior to the first crack. The nonlinear behaviour is also more apparent in this beam.

Beam- D2

Figure 7-27 and Figure 7-28 show as in beam D1 that there is a good agreement between the experimental and numerical model. The differences near the failure are 4.9% for points P6 and P7. For these points, the finite element model is stiffer than the experimental one up to the yielding point and then reduced gradually.

Beam- G1

Figure 7-30**,** shows that the numerical and experimental results correlate well. It is obvious that the stiffness of the finite element model is higher than the experimental one up to failure. In this beam also, the first part of the curves from DIC- camera were completely horizontal and irregular (up to 0.787 mm). Hence, the horizontal and irregular part were deleted so that the curves started from (0, 0).

Beam- E1

Figure 7-32, shows that the load-deflection plots for the numerical and experimental results agree well up to failure. The differences at failure are approximately 4.2%. The stiffness of the finite element model is higher than the experimental one, and was then reduced as the reinforcement started to yield at 178.451 KN.

Beam- E2

Figure 7-34 and Figure 7-35 show that only for points 11 and 14, the load-deflection plots for the numerical and experimental results agree reasonably up to failure. The differences at failure are approximately 9.9%. The stiffness of the finite element model ,was higher than the experimental up to the first crack load, and then started to reduce.

Beam- H1

The model that was used for calibrating the beams with 1% fibre volume, was used to the calibrate the H1 beam. The results from Figure 7-37 and Figure 7-38, show that there is (a) good correlation between the curves extracted from the DIC- camera, and the FE modeling, to the point of failure of the numerical model. However, the results indicate clearly that the stiffness of the numerical model, is higher than the experimental one, up to yielding point at 178.451 KN.
Moreover, the first part of the curves from the DIC- camera for this beam, were completely horizontal and irregular (up to 0.632 mm). Hence, the horizontal and irregular part were deleted so that the curves started from (0, 0).

Summary

The previous results give confidence in the use of ANSYS and our model, to predict the shear behaviour of UHPC beams.

The differences in load-deflection curves (especially after the first crack initiated), for some of the extracted points from DIC- camera, compared to the numerical one, may be due to the impact of material models. Besides, higher stiffness of FE curves could be due to many factors such as tensile strength of concrete, crack patterns, and fibre orientations, which affect experimental outcomes.

Why does ANSYS underestimate the strength of the beams?

Generally, ANSYS underestimate the ultimate strength of most of the beams. One reason may be Toughening mechanisms. These mechanisms at the crack faces may cause little enhance in the failures loads of the experimental beams before the final collapse. This means that additional energy is required in creating the crack propagation due to the interlock between the faces of the crack. The aggregate causes the interlock action so that as the crack propagate, the aggregate continues to transfer stress across the crack. This mechanisms was explained by Shah et al. [87]. The finite element models do not have such mechanisms.

Another reason may be due to the stress-strain curve of the UHPC should be obtained from the test which was not available in our lab machine. In addition, the stress-strain curve of the reinforcing of the real beam is different from the one used in the finite element modeling. This may assist to produce the higher ultimate strength in the experimental beams.

Why does the stiffness of FEM higher than Experimental one?

As mentioned before, when the first crack initiated, the stiffness started to reduce, which affected the load- deflection slope. This may have been due to that the principal tensile stress surpassed the tensile strength of the concrete on that crack along with curing regim effeccts and shrinkage of the real beam. This lead to a reduction in the bonding between the concrete and steel reinforcement of the beams. While in FE modeling, the bond between the reinforcing and concrete is assumed to be perfect. Consequently, the overall stiffness of the real beams could be lower than the stiffness of the finite element models.

However, the degradation of beam stiffness slowed down after the yielding of tensile reinforcement. It also became apparent that, as the tensile reinforcement reached the yielding, the deflection would (will be) increase, and more crushing was noticed at the compression zone of the concrete within the beam, which may have been due to the reduction in the flexural strength of the beam.

The fibre effect on the first cracking load

Regarding the fibre effect on the first cracking load, when the fibre volume increased from 0% to 0.5%, the first crack load increased significantly from 9.5 to 30.48 KN, respectively. This was due to the bridging mechanism as well, which prevented the starting of the cracks and hindered it from being propagated. When we increased the fibre volume to 1%, the crack load only increased to 39.79KN, indicating that a fractional increase in fiber volume does not result in a proportional increase in the first crack load. Moreover, from load-deflection curves, it is clear that as the fibre volume increased, the stiffness increased. Generally, the fibre enhanced the shear strength, as well as the stiffness of the UHPC beams, even if the reinforcement ratio of the beam was not so high.

8.3.4. Crack pattern

When the principle stress exceeds the tensile strength of the concrete, cracks starts to appear in ANSYS as lines. These lines are a gathering of small circles, perpendicular to the principal stress in the z-direction (z-direction in our model is the horizontal axis) to form the flexural cracks.

The compression cracks, as shown in Figure 7-44, show up underneath the loading plate where there is a compressive load. These cracks propagate parallel to the compressive load. The reason that these cracks occurred, is the tensile strain that develops out from Poisson ratio. This was also stated by Mindess et al. [60]. This means, as the load applied in the y-direction, the circles in the finite element model will be perpendicular to the principal tensile strain in the x-direction in the concrete near to the loading plate.

The shear cracks are also shown in Figure 7-44. In this region, normal tensile stress effect in the z-direction and shear stress take place at zy plane. As the principal tensile stress became inclined to the horizontal and passed the tensile strength of the concrete, the circles started to gather as inclined lines perpendicular to the principal stress in the concrete element.

Figure 7-39 to Figure 7-45, confirms that the flexural cracks first initiated in mid-span near to the maximum moment, and then propagated toward the supports. As the load increased, the flexural cracks started to form shear cracks. By increasing the applied load, close to the point of failure, compressive cracks appeared along with more shear and flexural cracks.

All the beams failed as expected. The beams failed in shear where the yielding was reached for 0.5% and 1% fibre volume and followed by a compression failure at the top of the beam. This coincides with the experimental results on our beams and confirms that this model can be used to predict the shear crack pattern of UHPC.

9. Conclusion

An experimental and numerical study was carried out on 102 specimens, which were made based on an UHPC developed recipe by the University of Agder (UiA). All of the specimens were prepared and tested at the UiA. The only test variable was the fibre volume, where the type of concrete (UHPC), shear span - to - depth ratio (2) and reinforcement ratio (4.9 %) were kept constant. All specimens had the same lengths and cross-sections.

The influence of using steel fiber on UHPC capacity was presented in this thesis. The results prove that the ultimate shear strengths were enhanced as the steel fiber content increased. On average, the shear capacity of UHPC beams reinforced with 1% fibre, was 58.3% higher than UHPC beams reinforced with 0.5% fibre. Moreover, 1% fibre volume specimens experienced 42% higher deflection, than their 0.5% counterparts.

In addition, the beam reincorced with 0% fibre, failed suddenly and explosively by shear-compressive failure. While the beams reinforced by 0.5% and 1% failed in diagonal- tension, this indicates the brittle behaviour of UHPC and that as the fibre volume increases (up to 1% in this case), more ductility behaviour can be obtained. This also let the structures achieve higher safety requirements.

Furthermore, test results indicate that the predictive models of both Ashour et al. and Narayana et al. are the nearest predictions to the experimental results for 0.5% and 1% beams,while ACI 544 following by Australian guideline equation is reasonably conservative. On average, for 0% fibre, all the formulas are remarkably conservative.

Based on data and analyses of the calibration models of the UHPC beams in ANSYS,

it can be concluded that the load-deflection curve of the finite element model, does not match well to the experimental data at the centre of the beam, where there might be no or very tiny cracks. The initial and continuous cracking of the finite element model, does however compare well to the experimental data obtained from the UHPC beams.

Finally, the failure mechanism of UHPC beams, is represented considerably well utilizing Finite element modeling, and the failure load predicted is quite near to the failure load measured near the shear crack during experimental testing by DIC technique.

10. Further work

The experimental and numerical study that was prepared in this thesis, confirms the benefits of using steel fiber reinforcement in enhancing the shear capacity of ultra-high-performance concrete beams. This thesis will help in one way or another in developing the structural field in Norway.

However, more experimental and numerical research on the shear strength of large- scale UHPC beams with stirrups, is needed. In addition, the effect of the shear span- to- depth ratio, longitudinal reinforcement ratio, and reinforcement anchorage, need to be investigated in the future. Moreover, the explosive behaviour of the reinforced beam by 0% fibre volume needs to be examined experimentally more deeply in the future.

11. References

[1] R. Zagon, S. Matthys and Z. Kiss, "Shear behaviour of SFR-UHPC I-shaped beams," *Construction and Building Materials ,* vol. 124, p. 258–268, 2016.

[2] S. Ahmad, I. Hakeem and M. Maslehuddin, "Development of UHPC Mixtures Utilizing Natural and Industrial Waste Materials as Partial Replacements of Silica Fume and Sand," *The Scientific World Journal,* Vols. 2014, Article ID 713531, 2014.

[3] P. Colajanni, A. Recupero and N. Spinella, "Generalization of shear truss model to the case of SFRC beams with stirrups," *Computers and Concrete ,* vol. 9, no. 3, pp. 227-244, 2012.

[4] P. K. MEHTA, "Reducing the environmental impact of concrete," *Concrete international,* 2001.

[5] P. Hájek and C. Fiala, "Environmentally optimized floor slabs using UHPC -contribution to sustainable building," in *Ultra High Performance Concrete (UHPC) Proceedings of the Second International Symposium on Ultra High Performance Concrete*, Kassel, University of Kassel, Germany, 2008, pp. 879-886.

[6] F. H. Administration, ""Ultra-High Performance Concrete: A State-of-the-Art Report for the Bridge Community," Georgetown Pike, McLean, 2013.

[7] N.M.Azmee and N.Shafiq, "Ultra-high performance concrete: From fundamental to applications," *Case Studies in Construction Materials,* vol. 9, 2018.

[8] B. A. Graybeal, "Compressive Behavior of Ultra-High-Performance Fiber-Reinforced Concrete," *Materials Journal,* vol. 104, no. 2, pp. 146-152, 2007.

[9] J. López, P. Serna and E. Camacho, "Structural Design and Previous Tests for a Retaining Wall Made with Precast Elements of UHPFRC," in *High Performance Fiber Reinforced Cement Composites 6*, RILEM , 2012, pp. 437-444.

[10] J. Resplendino, " Introduction: What is UHPFRC?, in Designing and building with UHPFRC - State of the Art and Development," *ISTE ltd,* pp. 3-12, 2011.

[11] "Norsk Betongforenings miljøkomite," 2009. [Online]. Available: https://fabeko.no/assets/CO2_rapport-2009-02.pdf.

[12] P. Rossi, "Ultra high performance fiber reinforced concrets," *concrete international,* pp. 46-52, 2001.

[13] H. Mari, B. Eide and Jorun-Marie, "Ultra High Performance Fibre Reinforced Concrete (UHPFRC) – State of the art," SINTEF Building and Infrastructure, COIN Project report 44 – 2012.

[14] F. Toutlemonde and J. Resplendino, Designing and Building with UHPFRC- State of the Art and Development, USA: John Wiley & Sons, Inc., 2011.

[15] A. E. Naaman, "Engineered steel fiber with optimal proprties for reinforcement of cement composites," *J adv. technol,* vol. 1, no. 3, pp. 241-252, 2003.

[16] Fehling, A. L. Hoang and Ekkehard, "Influence of steel fiber content and aspect ratio on the uniaxial tensile and compressive behavior of ultra high performance concrete," *Construction and Building Materials,* no. 153, pp. 790-806, 2017.

[17] M. Schmidt, E. Fehling, C. Glotzbach, S. Frohlich and S. Piotrowski, in *Third International Symposium on UHPC and Nanotechnology for High Performance Construction Materials*, Kassel, Germany (p. 1036), 2012.

[18] "French standard NF P18-470," Afnor, 2016.

[19] U. Muller, H. Kuhne, P. Fontana, B. Meng and J. Nemecek, "Micro texture and mechanical properties of heat treated and autoclaved ultra-high performance concrete (UHPC)," *International Symposium on UHPC,* p. 213–220, 2008.

[20] P. R. PREM, B. H. BHARATKUMAR and N. R. IYER, "Influence of curing regimes on compressive strength of ultra high performance concrete," *Indian Academy of Sciences,* vol. 38, no. 6, p. 1421–1431, 2013.

[21] F. Xing, D. Huang, L. Cao and L. Deng, "Study on preparation technique for low-cost green reactive powder concrete," *Key Engineering Materials,* pp. 302–303, 405–410, 2006.

[22] G. H. Russel and B. a. Graybeal, "Ultra-High Performance Concrete : A State-of-the-Art Report for the Bridge Community," 2013.

[23] B. Graybeal and F. Baby, "Development of a Direct Tension Test Method for UHPFRC," *ACI Materials Journal,* vol. 110, no. 2, 2013.

[24] D.-L. Nguyen, D.-K. Thai and D. J. Kim, "Direct tension-dependent flexural behavior of ultra-high-performance fiber reinforced concretes," *The Journal of Strain Analysis for Engineering Design,* vol. 52, no. 2, pp. 121-134, 2017.

[25] N. Long, O. Manager and D. Clark, "High-Speed Cameras Help Digital Image Correlation Show Its Strength," [Online]. Available: https://www.phantomhighspeed.com/-/media/project/ameteksxa/visionresearch/documents/whitepapers/english/web/wpdicweb.pdf?la=en.

[26] N. Mccormick, "Digital image correlation for structural measurements," *Proc Inst Civ Eng,* vol. 4, pp. 185-190, 2012.

[27] M. F. Smrkić, J. Košćak and D. Damjanović, "Application of 2D digital image correlation for displacement and crack width measurement on RC elements," *GARDEVINAR,* vol. 70, pp. 771-781, 2018.

[28] B. Gencturk, K. Hossain, A. Kapadia, E. Labib and Y.-L. Mo, "Use of digital image correlation technique in full-scale testing of prestressed concrete structures," vol. 47, pp. 505-515, 2014.

[29] D. Corr, M. Accardi, L. Graham-Brady and S. Shah, "Digital image correlation analysis of interfacial debonding properties and fracture behavior in concrete," *Engineering Fracture Mechanics,* vol. 74, p. 109–121, 2007.

[30] G. L. Balázs, "A historical Review of Shear," *Shear and punching shear in RC and FRC elements,* pp. 1-13, 2010.

[31] J. A.-A. C. 445, "Recent approaches to shear design of structural concrete," *J. Structural Engineering,* vol. 124, no. 12, pp. 1375-1417, 1998.

[32] R. S. Pendyala and P. Mendus, " Experimental study on shear strength of high-strength concrete beams," *ACI Journal Structural ,* vol. 97, no. 4, pp. 564-571, 2000.

[33] R. L. Sudheer, R. N. V. Ramana and T. Gunneswara Rao, "Shear resistance of high strength concrete beams without shear reinforcement," *International Journal of Civil and Structural Engineering,* vol. 1, no. 1, pp. 101-113, 2010.

[34] Y. L. Voo, W. K. Poon and S. J. Foster, "Shear Strength of Steel Fiber-Reinforced Ultrahigh- Performance Concrete Beams without Stirrups," *Journal of Structural Engineering,* vol. 136, no. 11, 2010.

[35] J. Xia, K. R.Mackie, M. A. Saleem and A. Mirmiran, "Shear failure analysis on ultra-high performance concrete beams reinforced with high strength steel," *Engineering Structures,* vol. 33, no. 12, pp. 3597-3609, 2011.

[36] I. F. Kara, "Prediction of shear strength of FRP-reinforced concrete beams without stirrups based on genetic programming," *Advances in Engineering Software,* vol. 42, p. 295–304, 2011.

[37] J. Xia, Y. Xiao, K. R. Mackie, A. Mirmiran and M. A. Al-Ramahee, "Dowel action and shear strength contribution of high strength rebar embedded in ultra-high performance fiber reinforced concrete," *Engineering Structures,* vol. 83, pp. 223-232, 2015.

[38] F. Baby, P. Marchand and F. Toutlemonde, "Shear Behavior of Ultrahigh Performance Fiber-Reinforced Concrete Beams. I: Experimental Investigation," *Journal of structural engineering, ASCE, 04013111,* vol. 140, no. 5, 2013.

[39] F. Bab, P. Marchand and F. Toutlemonde, "Shear Behavior of Ultrahigh Performance Fiber-Reinforced Concrete Beams. II: Analysis and Design Provisions," *Journal of Structural Engineering, ASCE, 4013112,* vol. 140, no. 5, 2014.

[40] "Recommendation provisories, Ultra High Performance Fibre-Reinforced Concrete, Interim recommendations, SETRA-AFGC," BFUP, Paris, France, cited 2011. [Online]. Available: http://www.afgc.asso.fr/index.php/presentation-afgc/fonctionnement/statuts.

[41] S. H. Ahmad, A. R. Khaloo and A. Poveda, "Shear Capacity of Reinforced High-Strength Concrete Beams," *International Concrete Abstracts Portal,* vol. 83, no. 2, pp. 297-305, 1986.

[42] H. H. Dinh, G. J. Parra-Montesinos and J. K. Wight, "Shear Strength Model for Steel Fiber Reinforced Concrete Beams without Stirrup Reinforcement," *Journal of Structural Engineering,* vol. 137, no. 10, pp. 1039-1051, 2011.

[43] E. Madenc and I. Guven, The Finite Element Method and Applications in Engineering Using ANSYS- Second Edition, Springer is a brand of Springer US, 2015.

[44] M. K. Thompson and J. M. Thompson, ANSYS Mechanical APDL for Finite Element Analysis, Joe Hayton, 2017.

[45] A. Inc., ANSYS User's Manual Revision 19.2, Canonsburg, Pennsylvania, 2019.

[46] K. Vertes, "BYG 506, Advanced finite element method," UiA, Grimstad, 2017.

[47] M. Bangash, Numerical modelling and applications, 1989.

[48] M. Zhou, "Application of Finite Element Method for Nonlinear Analysis in Reinforced Concrete Structures," *Applied Mechanics and Materials,* pp. 935-938, 2012.

[49] D. Cotsovos and M. Pavlovic, "Numerical investigation of concrete subjected to high rates of uniaxial tensile loading," *International Journal of Impact engineering,* vol. 35, no. 5, pp. 319-335, 2008.

[50] J. Georgin and J. Reynouard, "Modeling of structures subjected to impact: concrete behaviour under high strain rate," *Cement & Concrete Composites,* vol. 25, no. 1, pp. 131-143, 2003.

[51] A. Barbosa and G. Ribeiro, Analysis of reinforced concrete structures using ANSYS nonlinear concrete model, 1998.

[52] G. Hughes and D. Speirs, An investigation of the beam impact problem, 1982.

[53] Ø. GRØSTAD and E. SANDBERG, "Master thesis: Analysing UHPFRC beams with ANSYS," University of Agder, Grimstad, 2017.

[54] A. 18.2, "Academic Teaching Introductory, documentation embedded in the software," 2017.

[55] Eurocode 2: Design of concrete structures - Part 1-1 : General rules and rules for buildings, 2004.

[56] COIN, "State of the art - UHPFRC," SINTEF- NTNU, 2013.

[57] B. Graybeal, "Material property charecteraization of Ultra-High Performance Concrete," FHWA, U.S. department of transportation, 2006.

[58] J. K. J. William and E. Warnke, "Constitutive model for the triaxial behaviour of concrete," in Concrete structures subjected to triaxial stress, Bergamo, Italy, 1974.

[59] S. P. Shah, S. E. Swartz and C. Ouyang, Fracture Mechanics of Concrete, New York: John Wiley & Sons, Inc., 1995.

[60] S. Mindess and J. F. Young, Concrete, Prentice-Hall, Inc., New Jersey: Englewood Cliffs, 1981.

[61] N. D and S. AC, "Finite element analysis of reinforced concrete beams," *Journal of the American Concrete Institute,* vol. 64, pp. 152-163, 1967.

[62] R. YR., "Analysis of reinforced concrete pressure vessels," *Nuclear Engineering and Design ,* vol. 7, p. 334–344, 1968.

[63] R. d. Borst, J. J. C. Remmers, A. Needleman and M.-A. Abellan, "Discrete vs smeared crack models for concrete fracture: bridging the gap," *INTERNATIONAL JOURNAL FOR NUMERICAL AND ANALYTICAL METHODS IN GEOMECHANICS,* vol. 28, p. 583–607, 2004.

[64] K. Habel, "Structural Behaviour of Elements Combining Ultra high Performance Fibre Reinforced Concretes (UHPFRC) and Reinforced Concrete. Ph.D. thesis," 2004.

[65] Y. Lin, "TENSION STIFFENING MODEL FOR REINFORCED CONCRETE BASED ON BOND STRESS SLIP RELATION, master thesis," The Pennsylvania State University, Pennsylvania, August 2010.

[66] H. H. Abrishami and D. Mitchell, "Influence of Steel Fibers on Tension Stiffening," *Structural Journal,* vol. 94, no. 6, pp. 769-776, 1997.

[67] P. H. Bischoff, "Tension Stiffening and Cracking of Steel Fiber-Reinforced concrete," *Journal of Materials in Civil Engineering,* vol. 15, no. 2, 2003.

[68] Ø. T. Moltubakk, "Nonlinear Analysis of Fibre Reinforced concrete beams," NTNU, Trondheim, 2014.

[69] J. Qi, X. Ding, Z. Wang and Y. Hu, "Shear strength of fiber-reinforced high-strength steel ultra-high performance concrete beams based on refined calculation of compression zone depth considering concrete tension," *Advances in Structural Engineering,* pp. 1-13, 2019.

[70] "Standard Method of Test for Specific Gravity and Absorption of Fine," AASHTO Designation: T 84-00 (2004) , ASTM Designation: C 128-97 .

[71] S. Noor-E-Khuda, "ENEC13016- Concrete Technology and Design".

[72] E. c. f. standardization, "Testing hardened concrete - Part 13: Determination of secant modulus of elasticity in compression," CEN management centre, Brussels, 2013.

[73] O. e. a. Bonneau, "Mechanical Properties and Durability of Two Industrial Reactive Powder Concretes," *ACI Materials Journal,* vol. 94, no. 4, p. 286–290, July–August 1997.

[74] A. Simon, "Updated AFGC Recommendations: Chapter 1 Materials," in *Designing and Building with UHPFRC: State of the Art Development*, Marseille, France, Proceedings of the International Workshop on Ultra High Performance Fibre Reinforced Concrete, November 2009, p. 17–19.

[75] T. e. a. Ahlborn, "Durability and Strength Characterization of Ultra-High Performance Concrete Under Variable Curing Regimes," *Proceedings of the Second International Symposium on Ultra High Performance Concrete,* p. 197–204, 2008.

[76] G. N. I. R. Gibert, "Design Guidelines for RPC Prestressed Concrete Beams," School of Civil and Environmental Engineering, The university of New South Wales, 2000.

[77] A. C. 5. (. 544), "Design considerations for steel fiber reinforced concrete," *ACI Structural Journal,* vol. 85, no. 5, p. 563–579, 1988.

[78] R. Narayanan and D. S., "Use of Steel Fibres as Shear Reinforcement," *ACI structural journal,* vol. 84, no. 3, pp. 216-227, 1987.

[79] H. Q. Majeed, "Nonlinear Finite Element Analysis of Steel Fiber Reinforced Concrete Deep Beams With and Without Opening," *Journal of Engineering,* vol. 18, no. 12, 2012.

[80] I. Saifullah1, M. Hossain, S.M.K.Uddin, M. Khan and M. Amin, "Nononlinear Analysis of RC Beam for Different Shear Reinforcement Patterns by Finite Element Analysis," *International Journal of Civil & Environmental Engineering,* vol. 11, no. 1, pp. 63-74, 2011.

[81] P. R. Prem, B.H.Bharatkumar and N. R. Iyer, "Mechanical Properties of Ultra High Performance Concrete," *International Journal of Civil and Environmental Engineering,* vol. 6, no. 8, 2012.

[82] R. Wang and X. Gao, "Relationship between Flowability, Entrapped Air Content and Strength of UHPC Mixtures Containing Different Dosage of Steel Fiber," *Applied science,* vol. 216, no. 6, 2016.

[83] B. Graybeal and M. Davis, "Cylinder or Cube: Strength Testing of 80 to 200 MPa (11.6 to 29 ksi) Ultra-High-Performance Fiber-Reinforced Concrete," *ACI MATERIALS JOURNAL,* 2008.

[84] M. Schmidt, E. Fehling, T. Teichmann, K. Bunje and R. Bornemann, "Ultra-high performance concrete: Perspective for the precast concrete industry," *Concr Pre-casting Plant Tech.,* vol. 69, no. 3, p. 16–29, 2003.

[85] O. Bonneau, C. Poulin, J. Dugat, P. Richard and P. Aitcin, "Reactive powder concretes: From theory to practice," *Concrete International,* vol. 18, no. 4, p. 47–49, 1996.

[86] Z. P. Bazant and M. T. Kazemi, "Size dependence of concrete fracture energy determined by RILEM work-of-fracture method," *Civil and Environmental Engineering,* vol. 51, no. 2, pp. 121-138, 1991.

[87] S. S.P, S. S.E. and O. C., Fracture Mechanics of Concrete: Applications of Fracture Mechanics to Concrete, Rock, and other Quasi-brittle Materials, New York: John Wiley & Sons. LTD., 1995.

12. Annexes

12.1. Annex A- Guidance meeting

12.2. Annex B- Experimental process

12.3. Annex C- Numerical analysis- ANSYS

12.4. Annex D- Preliminary report

Annex A- Guidance meeting

Dato: 14.01.2019	**Place: University of Agder and Oslomet**
Presents	Kataline, Ingrid, Haidar, Perooz
This was the first meeting held, where the outline of the work was drawn. First we queried what type of recipe to be used. Then, the temperature at which the UHPC would be treated was discussed. It was decided that some specimens would be cured at 90 degrees for 48 hours, and then at the lab's room temperature continuously for 14 days, while the other specimens cured at 20 degrees for 14 days , this was done to replicate the curing regime of the first semester. The discussion also extended to determine the statistical method that would be used in the inventory of results. That was postponed until we obtained the results of the laboratory work. As for the design of the beams, it was agreed to keep the design we previously obtained, as the collapse of the shear had been achieved.	

Dato: 28.01.2019	Place: University of Agder and Oslomet
Present	Kataline,Ingrid,Haidar, Perooz

We started by discussed the number of beams that will be cast and the appropriate type of fibres. It was decided that the primary point was to complement the laboratory work of the first semester, also, to we investigated new fibre ratios to cover the behavior of the shear resistance as much as possible. We reviewed the recipe to be used in the laboratory and we received a new type of filler to utilizise. Based on a basic program of laboratory work, we developed the casting process and decided on the test days.

The preliminary report was used as a reference for our theoretical section and we then developed a numerical study based on the experimental results, using Ansys program.

The characteristics of the materials and the most critical parameters to be used in numerical modeling were discussed, as well as the following research questions
How does the steel fiber content affect the behavior of Ultra-High-Performance Concrete (UHPC)?
Sub-questions:
How does fiber reinforcement affect the shear behavior of UHPC-beams?
How to model an UHPC-beam on Ansys?
How to calculate the shear capacity of UHPC-beam from standards?

The Solid65 element requires linear isotropic and multilinear isotropic material properties to accurately model concrete. The multilinear isotropic material uses the von Mises failure criterion, along with the Willam and Warnke (1974) model to define the failure of the concrete.
Rankine maximum principal stress theory.
Drucker-Prager yield criterion.
The William-Warnke 5-parameter constitutive model for triaxial behavior in concrete.
Tresca yield criterion.
Von Mises yield criterion.

Finally, the method of determining the failure load and how to draw a load-deflection curve out from ANSYS in order to compare it with the results of laboratory work were discussed.

Dato: 19.03.2019	**Place: University of Agder and Oslomet**
Present	Kataline,Ingrid,Haidar, Perooz
During this meeting, the results from ANSYS of 0%, 0.5%, and 1% fibre volume were presented. The outcomes from the numerical simulation were not comparable. The reason was determined to be an incorrectly chosen beam comparison point(mid-span point). Therefore, it was concluded that load-displacement curves of several points within the beams, needed to be extracted from the DIC camera, in order to show as much non-linear behavior as possible, and to match it further to ANSYS. In addition, a proposed formula was developed to determine the most accurate shear strength of our specimens.	

Dato: 10.04.2019	**Place: University of Agder and Oslomet**
Present	Kataline,Ingrid,Haidar, Perooz
Out from DIC camera, 11-points from beam (C1- 0%), 11-points from beam (C2- 0%), 14-points from beam (D1- 0.5%), 14-points from beam (D2- 0.5%), 14-points from beam (E1- 1%) and 14-points from beam (E2- 1%) were chosen to be compared to ANSYS. These beams were tested last semester experimentally (Annex D). The comparative results were presented during this meeting. They showed that ANSYS reflected the experimental results and non-linear behavior very well. Also, the next steps were determined; the test results of our lab work for this semester will be obtained soon and compared to Ansys as well.	

Date: 24.04.2019	**Place: University of Agder and Oslomet**
Present	Kataline,Ingrid,Haidar, Perooz
The test results of our lab work for this semester were obtained and compared to Ansys as well. Out from the DIC camera, 14-points from the beam (F1- 0%), 14-points from the beam (G1- 0.5%), 14-points from the beam (H1- 1%) were chosen to be compared to ANSYS. These beams were tested this semester experimentally. The comparative results were presented during this meeting. They showed that ANSYS reflected the experimental results and non-linear behavior very well.	

Annex B- Experimental process

Curing regime of specimens

Lab plan to be cast

Mix F1

Type	Liters specimens	Form	Size(cm)	Test	curing	Number of specimens
0%Fibre	30	Beam	20x10x150	Shear	20°C	1
	3	Cube	10x10x10	compression/14 days	20°C	3
	3	Cube	10x10x10	compression/14 days	90°C	3
	0,768	Prism	4x4x16	Flexural /14 days	20°C	3
	8	Air content				1
	1	Slump				1
Sum	45,768					

Mix F2

Type	Liters specimens	Form	Size(cm)	Test	curing	Number of specimens
0%Fibre	40,5	Prism	15x15x60	Flexural tensile strength	20°C	3
	3	Cube	10x10x10	compression/ 14 days	90°C	3
	4.71	Cylinder	10x20	compression/ 14 days	20°C	3
	4.71	Cylinder	10x20	compression/ 28 days	20°C	3
	8	Air content				1
	1	Slump				1
Sum	61,92					

Mix G1

Type	Liters specimens	Form	Size(cm)	Test	curing	Number of specimens
0,5%Fibre	30	Beam	20x10x150	Shear	20°C	1
	3	Cube	10x10x10	compression/14 days	20°C	3
	3	Cube	10x10x10	compression/14 days	90°C	3
	0,768	Prism	4x4x16	Flexural /14 days	20°C	3
	8	Air content				1
	1	Slump				1
Sum	45,768					

Mix G2

Type	Liters specimens	Form	Size(cm)	Test	curing	Number of specimens
0,5%Fiber	40,5	Prism	15x15x60	residual tensile strength	20°C	3
	3	Cube	10x10x10	compression/14 days	90°C	3
	4.71	Cylinder	10x20	compression/14 days	20°C	3
	4.71	Cylinder	10x20	compression/28 days	20°C	3
	8	Air content				1
	1	Slump				1
Sum	61,92					

Mix H1

Type	Liters specimens	Form	Size(cm)	Test	curing	Number of specimens
1%Fiber	30	Beam	20x10x150	Shear	20°C	1
	3	Cube	10x10x10	compression/14 days	20°C	3
	3	Cube	10x10x10	compression/14 days	90°C	3
	0,768	Prism	4x4x16	tensile strength/14 days	20°C	3
	8	Air content				1
	1	Slump				1
Sum	45,768					

Mix H2

Type	Liters specimens	Form	Size(cm)	Test	curing	Number of specimens
1%Fiber	40,5	Prism	15x15x60	residual tensile strength	20°C	3
	3	Cube	10x10x10	compression/14 days	90°C	3
	4.71	Cylinder	10x20	compression/14 days	20°C	3
	4.71	Cylinder	10x20	compression/28 days	20°C	3
	8	Air content				1
	1	Slump				1
Sum	61,92					

Mix I1

Type	**Liters specimens**	**Form**	**Size(cm)**	**Test**	**curing**	**Number of**
0 % fiber	4.71	Cylinder	10x20	compression/14 days	20°C	3
	4.71	Cylinder	10x20	E- modul /14 days	20°C	3
	4.71	Cylinder	10x20	compression/14 days	90°C	3
	4.71	Cylinder	10x20	E- modul /14 days	90°C	3
	8	Air content				1
	1	Slump				1
sum	27,84	We have mixed 25 l of concrete and used a small amount of concrete from the air content test to cast the cylinders.				

Mix J1

Type	Liters specimens	Form	Size(cm)	Test	curing	Number of
0 % fiber	4.71	Cylinder	10x20	compression/14 days	20°C	3
	4.71	Cylinder	10x20	E- modul /14 days	20°C	3
	4.71	Cylinder	10x20	compression/14 days	90°C	3
	4.71	Cylinder	10x20	E- modul /14 days	90°C	3
	8	Air content				1
	1	Slump				1
sum	27,84	We have mixed 25 l of concrete and used a small amount of concrete from the air content test to cast the cylinders.				

Mix K1

Type	Liters specimens	Form	Size(cm)	Test	curing	Number of
0 % fiber	4.71	Cylinder	10x20	compression/14 days	20°C	3
	4.71	Cylinder	10x20	E- modul /14 days	20°C	3
	4.71	Cylinder	10x20	compression/14 days	90°C	3
	4.71	Cylinder	10x20	E- modul /14 days	90°C	3
	8	Air content				1
	1	Slump				1
sum	27,84	We have mixed 25 l of concrete and used a small amount of concrete from the air content test to cast the cylinders.				

Mixing recipe of F1, G1 and H1

material	0% Fibre		0.5% Fibre		1% Fibre	
	Kg/m^3	Kg/50L	Kg/m^3	Kg/50L	Kg/m^3	Kg/50L
Cement	727,709	36,385	724,071	36,204	720,432	36,022
Microsilica	181,930	9,096	181,020	9,051	180,111	9,006
filler(mellom)	1237,099	61,855	1230,913	61,546	1224,728	61,236
Water	144,380	7,219	143,658	7,183	142,936	7,147
SP	72,770	3,638	72,406	3,620	72,042	3,602
Steel fiber	0,000	0,000	39,000	1,950	78,000	3,900

Mixing recipe of F2, G2, and H2

material	0% Fiber		0.5% Fiber		1% Fiber	
	Kg/m^3	Kg/65L	Kg/m^3	Kg/65L	Kg/m^3	Kg/65L
Cement	727,709	47,301	724,071	47,065	720,432	46,828
Microsilica	181,930	11,825	181,020	11,766	180,111	11,707
filler(mellom)	1237,099	80,411	1230,913	80,009	1224,728	79,607
Water	144,380	9,385	143,658	9,338	142,936	9,291
SP	72,770	4,730	72,406	4,706	72,042	4,683
Steel fiber	0,000	0,000	39,000	2,535	78,000	5,070

Mixing recipe of I1, J1, and K1

material	0 % Fiber		0.5% Fiber		0.1% Fiber	
	Kg/m^3	Kg/25L	Kg/m^3	Kg/25L	Kg/m^3	Kg/25L
Cement	727,709	18,193	724,071	18,102	720,432	18,011
Microsilica	181,930	4,548	181,020	4,526	180,111	4,503
filler(mellom)	1237,099	30,927	1230,913	30,773	1224,728	30,618
Water	144,380	3,609	143,658	3,591	142,936	3,573
SP	72,770	1,819	72,406	1,810	72,042	1,801
Steel fiber	0,000	0,000	39,000	0,975	78,000	1,950

TEST RESULTS

Mean values and standard deviation of compressive strength of cubes at 20 degrees of F1, G1 and H1 mix after 14 days.

No.	Date of Casting	Date of Test	Curing regime	v_f%	l_f/d_f	compressive strength (MPa)		
						Measured values	Mean values	S.D
1	29.03.19	12.04.19	20°C	0.0 %	13/0,2	107.8	108.6	0.9
2						108.4		
3						109.5		
1	29.03.19	12.04.19	20°C	0.5 %	13/0,2	106.1	108.7	4.3
2						106.3		
3						113.7		
1	29.03.19	12.04.19	20°C	1.0 %	13/0,2	110.8	106.8	8.3
2						97.3		
3						112.4		

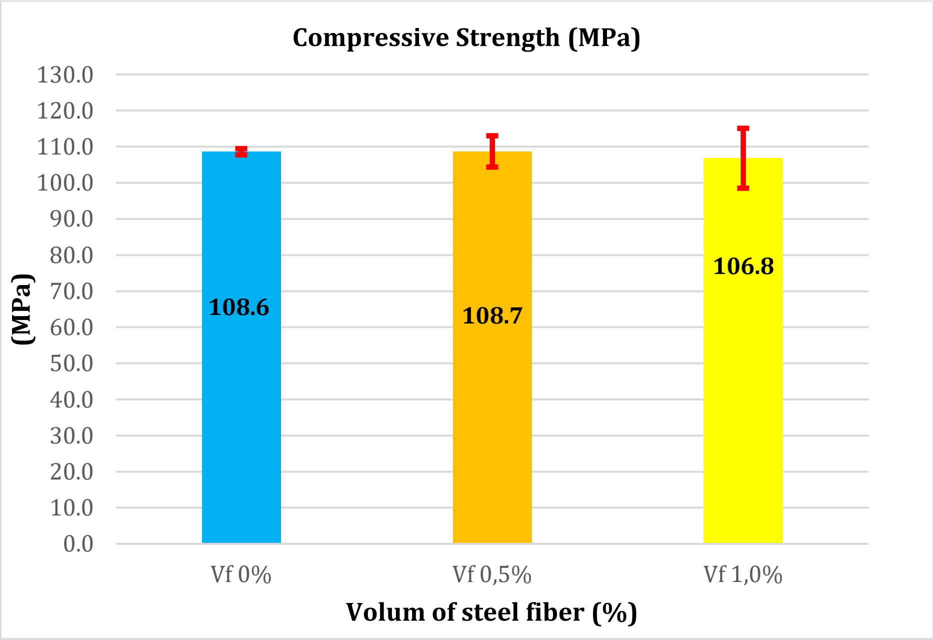

Mean values and standard deviation of densities at 20 degrees of F1, G1 and H1 mix after 14 days.

No	Date of Casting	Date of Test	Curing regime	v_f%	l_f/d_f	Density		
						Measured values	Mean values	S.D
1	29.03.19	12.04.19	20°C	0.0 %	13/0,2	2255.7	2279.5	3.9
2						2248.7		
3						2249.5		
1	29.03.19	12.04.19	20°C	0.5 %	13/0,2	2279.3	2276.49912	5.7
2						2270.0		
3						2280.3		
1	29.03.19	12.04-19	20°C	1.0 %	13/0,2	2315.7	2310.73402	5.1
2						2305.6		
3						2310.8		

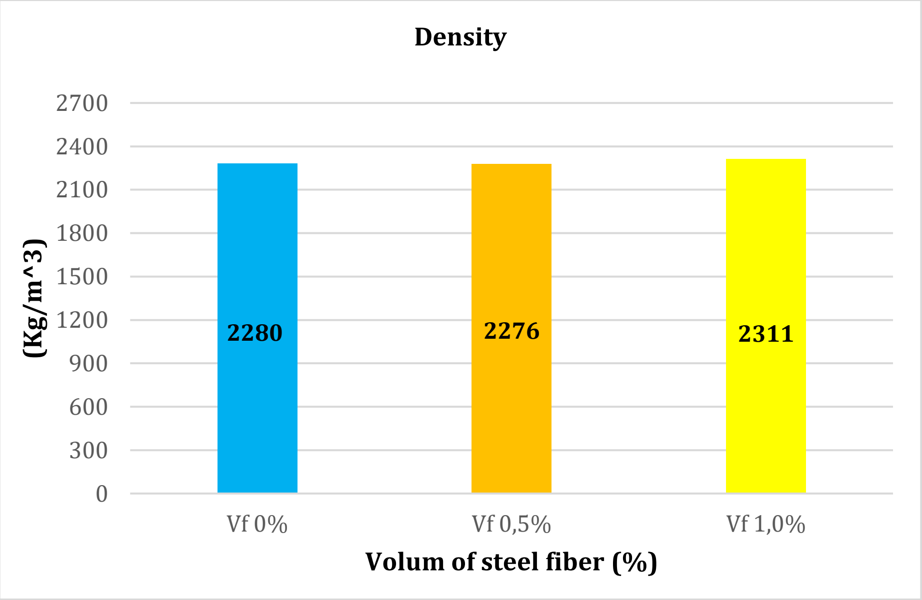

Mean values and standard deviation of compressive strength of cubes at 90 degrees of F1, G1 and H1 mix after 14 days.

No	Date of Casting	Date of Test	Curing regime	$v_f\%$	l_f/d_f	f_c compressive strength (MPa)		
						Measured values	Mean values	S.D
1	29.03.19	12.04.19	90°C	0.0 %	13/0,2	140.9	139.4	5.6
2						144		
3						133.2		
1	29.03.19	12.04.19	90°C	0.5 %	13/0,2	150.6	147.9	5.5
2						151.5		
3						141.6		
1	29.03.19	12.04.19	90°C	1.0 %	13/0,2	148.1	149.8	3.9
2						147		
3						154.3		

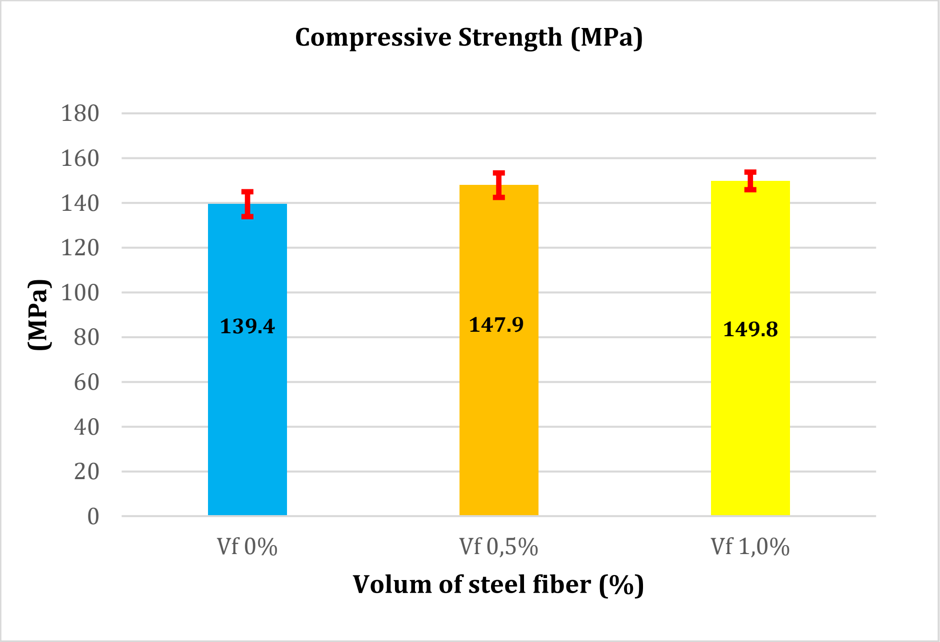

Mean values and standard deviation of densities at 90 degrees of F1, G1 and H1 mix after 14 days.

No	Date of Casting	Date of Test	Curing regime	v_f%	l_f/d_f	Density		
						Measured values	Mean values	S.D
1	29.03.19	12.04.19	90°C	0.0 %	13/0,2	2253.6	2282.6	1.3
2						2253.7		
3						2255.9		
1	29.03.19	12.04.19	90°C	0.5 %	13/0,2	2284.9	2284.0	1.3
2						2282.6		
3						2284.6		
1	29.03.19	12.04.19	90°C	1.0 %	13/0,2	2307.0	2309.2	4.7
2						2306.0		
3						2314.7		

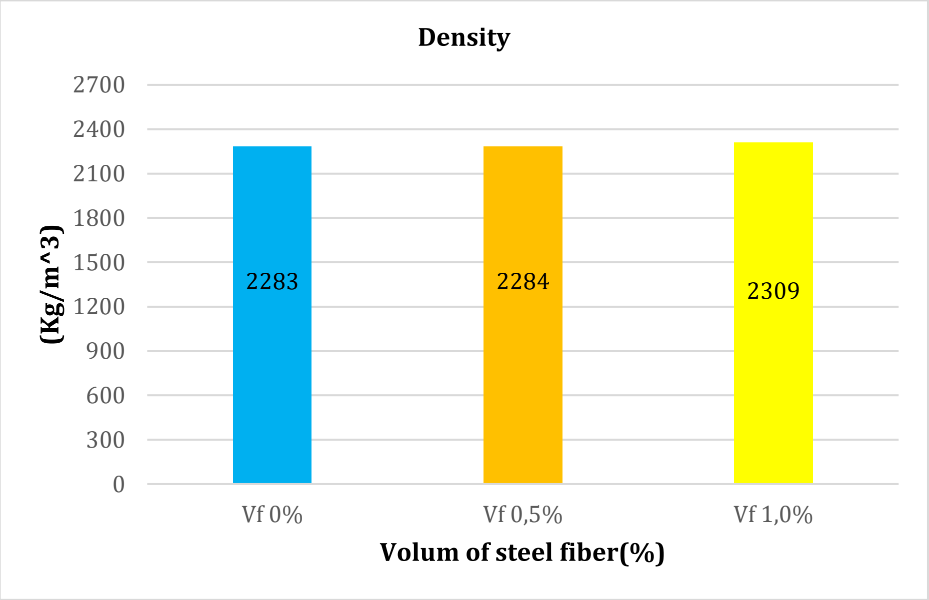

Mean values and standard deviation of compressive strength of cubes at 90 degrees of F2, G2 and H2 mix after 14 days.

No	**Date of Casting**	**Date of Test**	**Curing regime**	$v_f\%$	l_f/d_f	**compressive strength (MPa)**		
						Measured values	Mean values	S.D
1	02.04.19	16.04.19	90°C	0.0 %	13/0,2	136.3	133.2	7.0
2						138.2		
3						125.2		
1	29.03.19	16.04.19	90°C	0.5 %	13/0,2	136.2	141.2	5.1
2						146.3		
3						141.1		
1	29.03.19	16.04.19	90°C	1.0 %	13/0,2	137.2	143.3	5.3
2						147		
3						145.8		

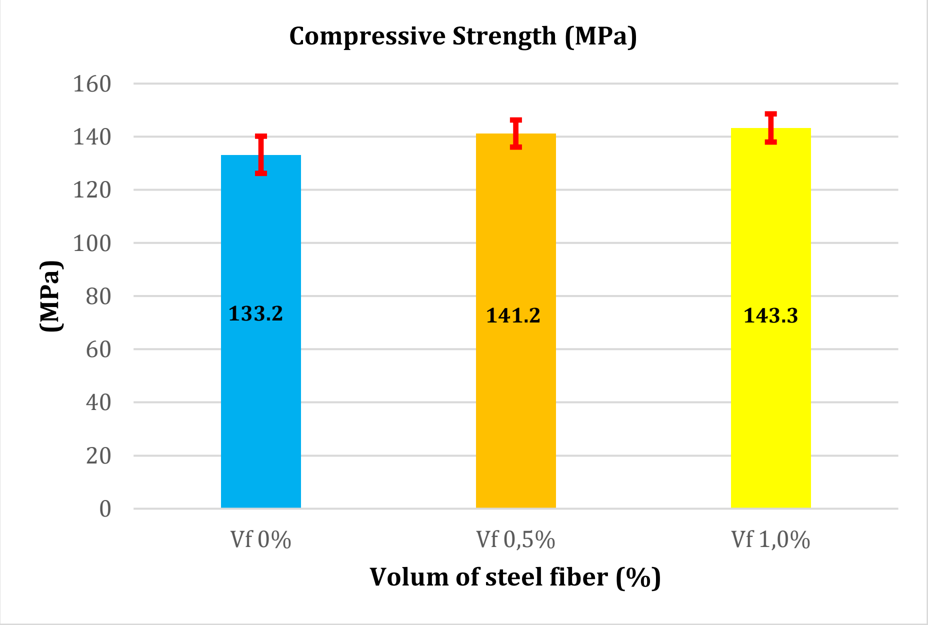

Mean values and standard deviation of densities at 90 degrees of F2, G2 and H2 mix after 14 days.

No	Date of Casting	Date of Test	Curing regime	$v_f\%$	l_f/d_f	Density		
						Measured values	Mean values	S.D
1	02.04.19	16/04/2019	90°C	0.0 %	13/0,2	2232.8	2230.5	4.6
2						2225.2		
3						2233.5		
1	02.04/2019	16/04/2019	90°C	0.5 %	13/0,2	2273.6	2274.1	3.6
2						2278.0		
3						2270.8		
1	02/04/2019	16/04/2019	90°C	1.0 %	13/0,2	2295.4	2294.6	6.9
2						2287.3		
3						2301.0		

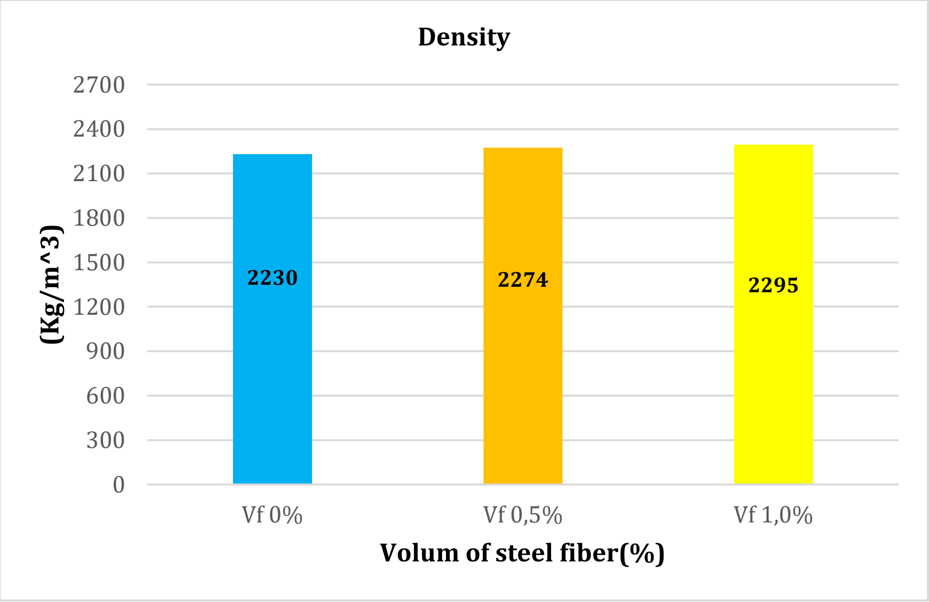

Mean values and standard deviation of densities at 20 degrees of F2, G2 and H2 mix after 14 days.

No.	Date of Casting	Date of Test	Curing regime	v_f%	l_f/d_f	Density		
						Measured values	Mean values	S.D
1	02/04/2019	16/04/2019	20°C	0.0 %	13/0,2	2220.7	2223.9	4.8
2						2221.6		
3						2229.4		
1	02/04/2019	16/04/2019	20°C	0.5 %	13/0,2	2268.3	2268.0	4.9
2						2272.8		
3						2263.1		
1	02/04/2019	16/04/2019	20°C	1.0 %	13/0,2	2314.1	2300.0	12.2
2						2293.6		
3						2292.3		

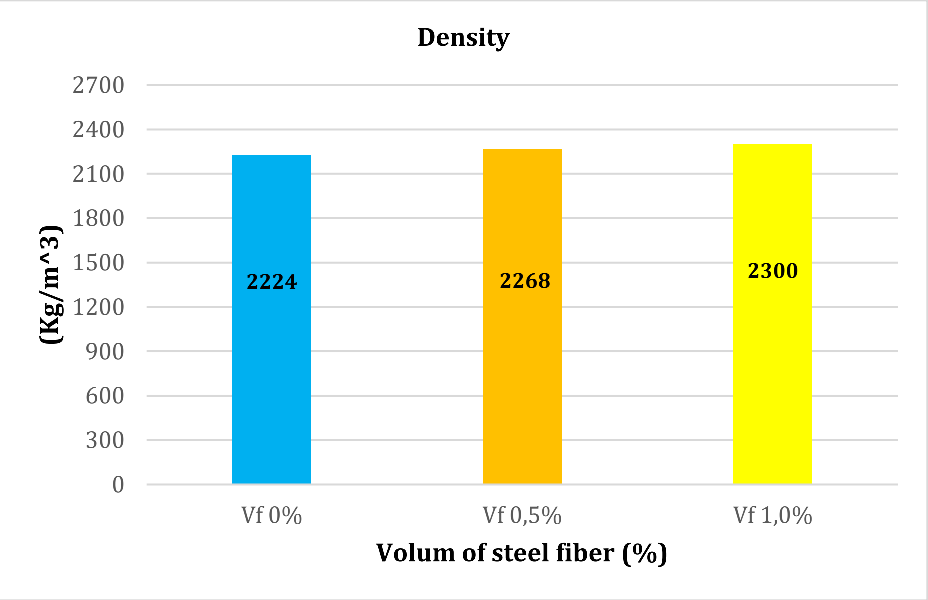

Mean values and standard deviation of densities at 20 degrees of F2, G2 and H2 mix after 28 days.

No	Date of Casting	Date of Test	Curing regime	v_f%	l_f/d_f	Density		
						Measured values	Mean values	S.D
1	02.04.19	16.04.19	20°C	0.0 %	13/0,2	2221.9	2220.6	2.3
2						2221.9		
3						2218.0		
1	02.04.19	16.04.19	20°C	0.5 %	13/0,2	2268.9	2264.6	6.2
2						2267.5		
3						2257.5		
1	02.04.19	16.04.19	20°C	1.0 %	13/0,2	2292.2	2286.9	5.5
2						2281.3		
3						2287.2		

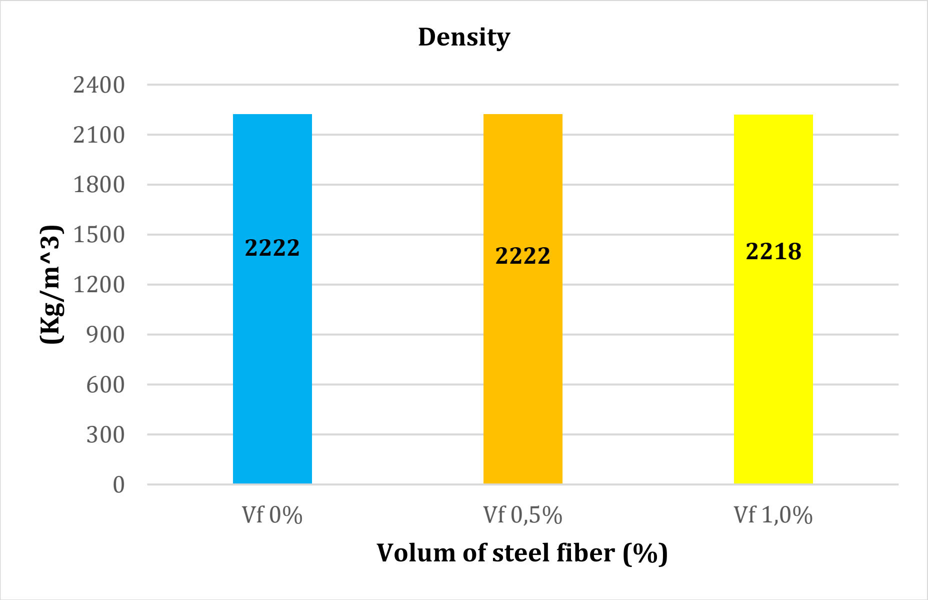

Fresh concrete properties:

F1, G1 and H1 mix:

Flowability without energy

No	Diameter	Date of test	$V_f(\%)$	flow without energy [cm]		
				Measured values	Mean values	S.D
F 1	D1	29.04.19	0%	12.5	12.8	0.4
	D2	29.04.19	0%	13		
G1	D1	29.04.19	0.5 %	16.2	17.1	1.2
	D2	29.04.19	0.5 %	17.9		
H1	D1	29.04.19	1.0 %	16	17.1	1.6
	D2	29.04.19	1.0 %	18.2		

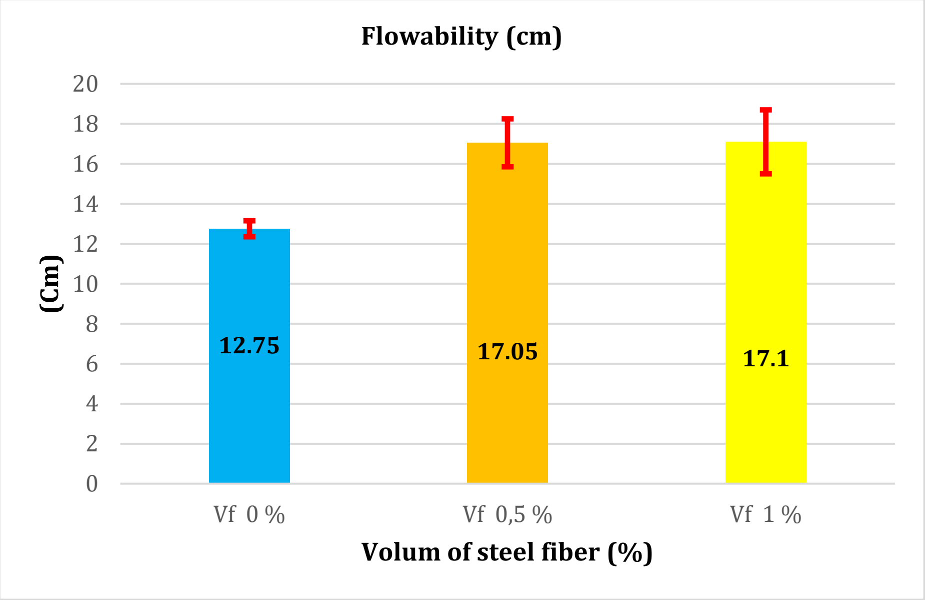

Flowability with energy

No	**Diameter**	**Date of test**	$V_f(\%)$	**flow with energy [cm]**		
				Measured values	Mean values	S.D
F1	D 1	29.04.19	0%	15.6	15.7	0.1
	D 2	29.04.19	0%	15.7		
G1	D 1	29.04.19	0.5 %	20.2	20.95	1.1
	D 2	29.04.19	0.5 %	21.7		
H1	D 1	29.04.19	1.0 %	19.1	20.1	1.4
	D 2	29.04.19	1.0 %	21.1		

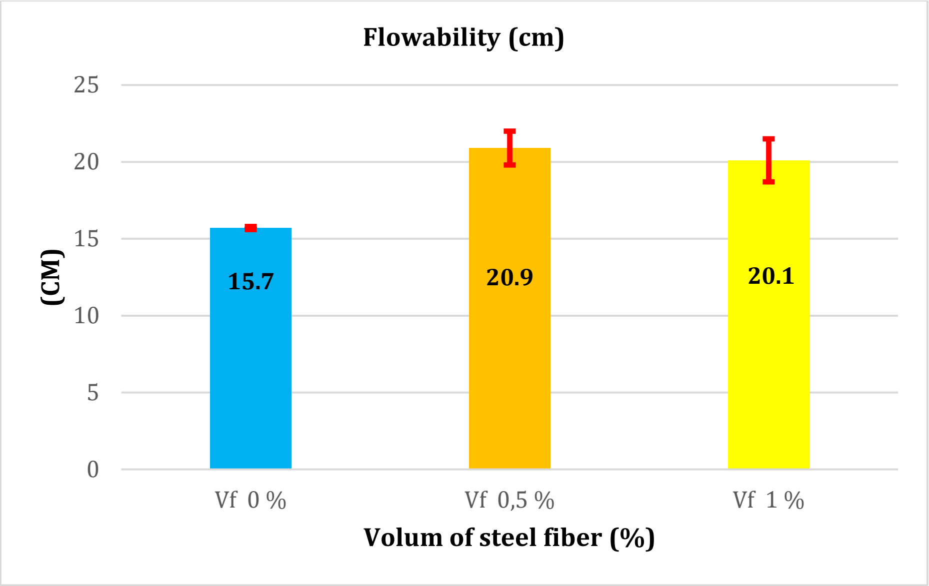

Air content and Fresh density

No.	Date of test	$V_f\,(\%)$	M1	M2	Fresh density	Air content
			Kg	Kg	[kg/m3]	[%]
F1	29.04.19	0%	4.6782	22.252	2196.8	4.8
G1	29.04.19	0.5 %	4.6768	22,738,4	2257.7	4.5
H1	29.04.19	1.0 %	4.6854	23.089	2300.5	3.3

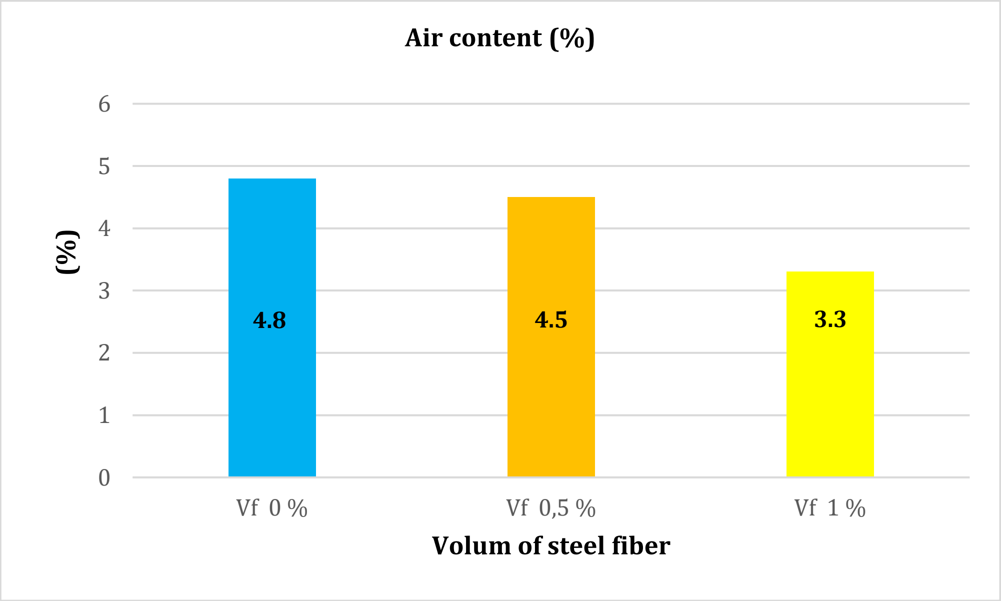

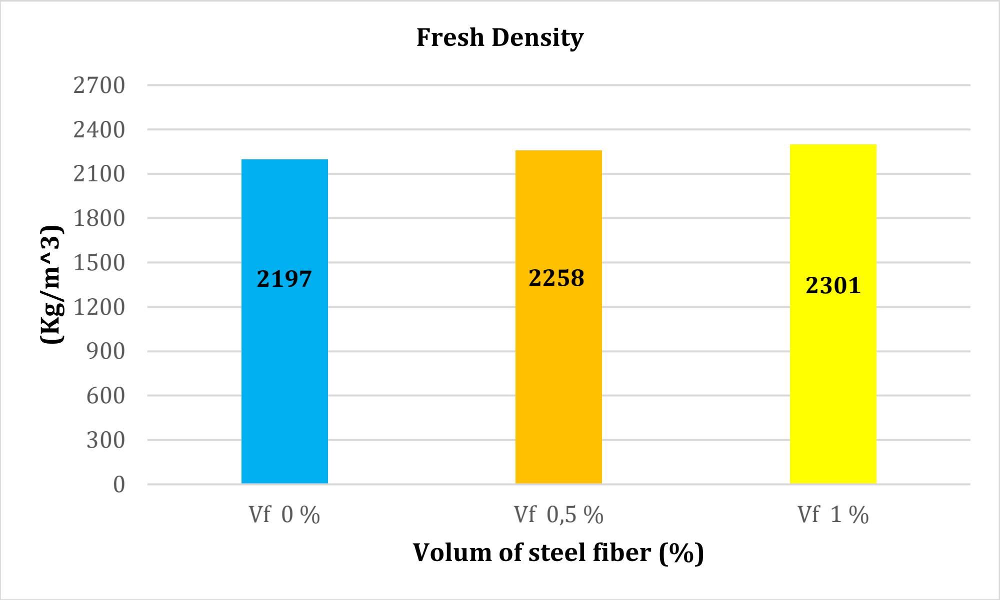

F2, G2 and H2 mix:

Flowability without energy

No	Diameter	Date of test	V_f (%)	flow without energy [cm]		
				Measured values	Mean values	S.D
F 2	D1	02.04.19	0%	13.9	14.6	0.9
	D2	02.04.19	0%	15.2		
G2	D1	02.04.19	0.5 %	15.2	15.9	1.0
	D2	02.04.19	0.5 %	16.6		
H2	D1	02.04.19	1.0 %	17	17.3	0.4
	D2	02.04.19	1.0 %	17.5		

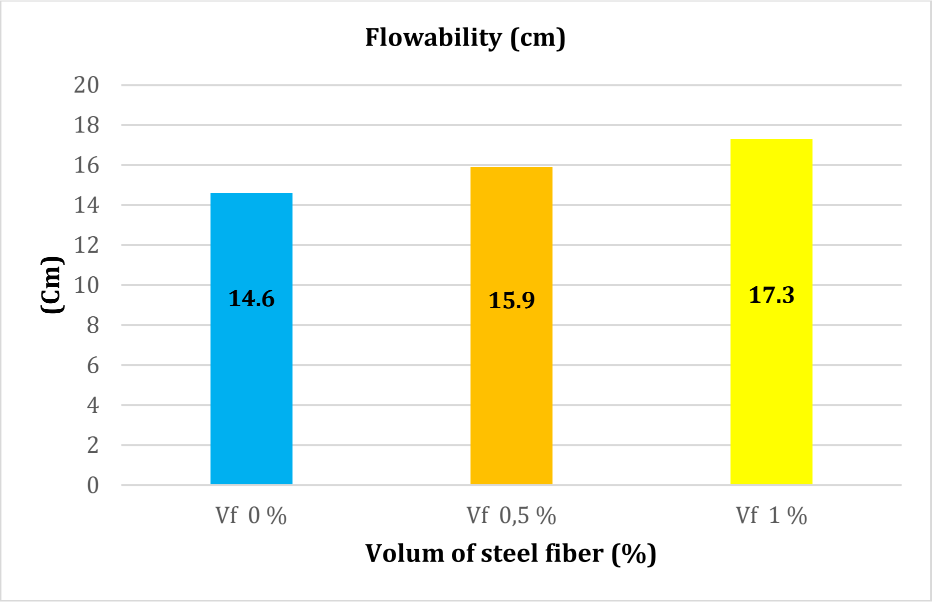

Flowability with energy

No.	Diameter	Date of test	V_f (%)	flow with energy [cm]		
				Measured values	Mean values	S.D
F2	D 1	02.04.19	0%	16	16.3	0.4
	D 2	02.04.19	0%	16.6		
G2	D 1	02.04.19	0.5 %	19.2	19.7	0.7
	D 2	02.04.19	0.5 %	20.2		
H2	D 1	02.04.19	1.0 %	19.8	19.9	0.1
	D 2	02.04.19	1.0 %	19.9		

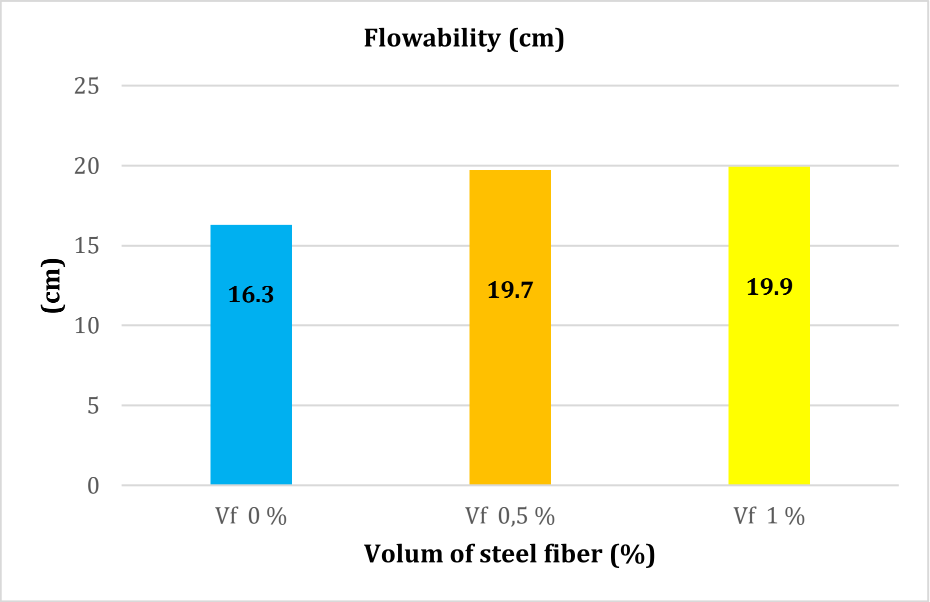

Air content and Fresh density

No.	Date of test	V_f (%)	M1	M2	Fresh density	Air content
			Kg	Kg	[kg/m3]	[%]
F2	02.04.19	0%	4.6804	22.352	2209.0	4.5
G2	02.04.19	0.5 %	4.6638	22.355	2211.4	3
H2	02.04.19	1.0 %	4.7	22.385	2210.7	4.25

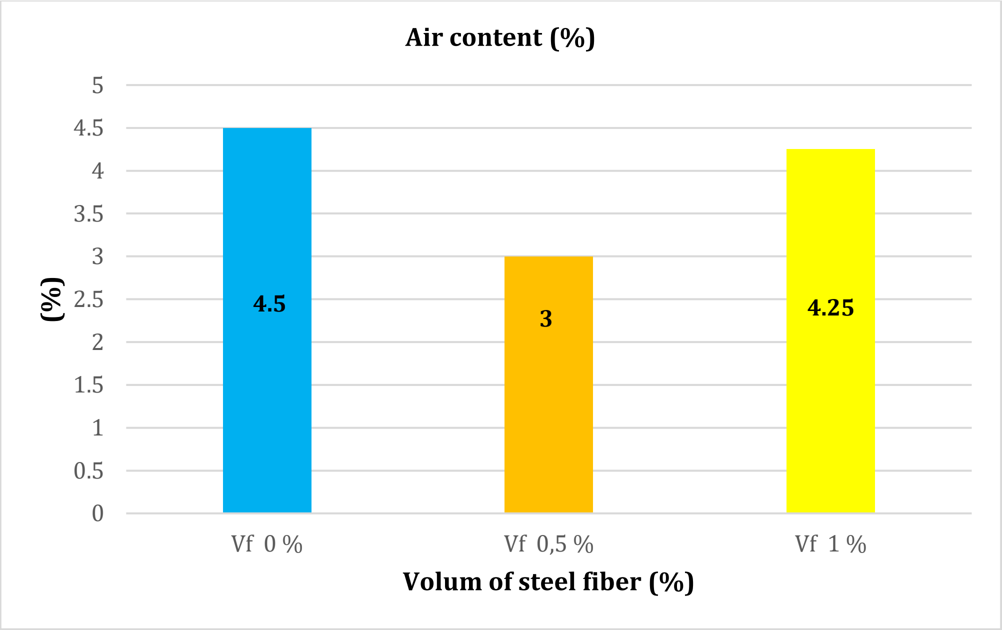

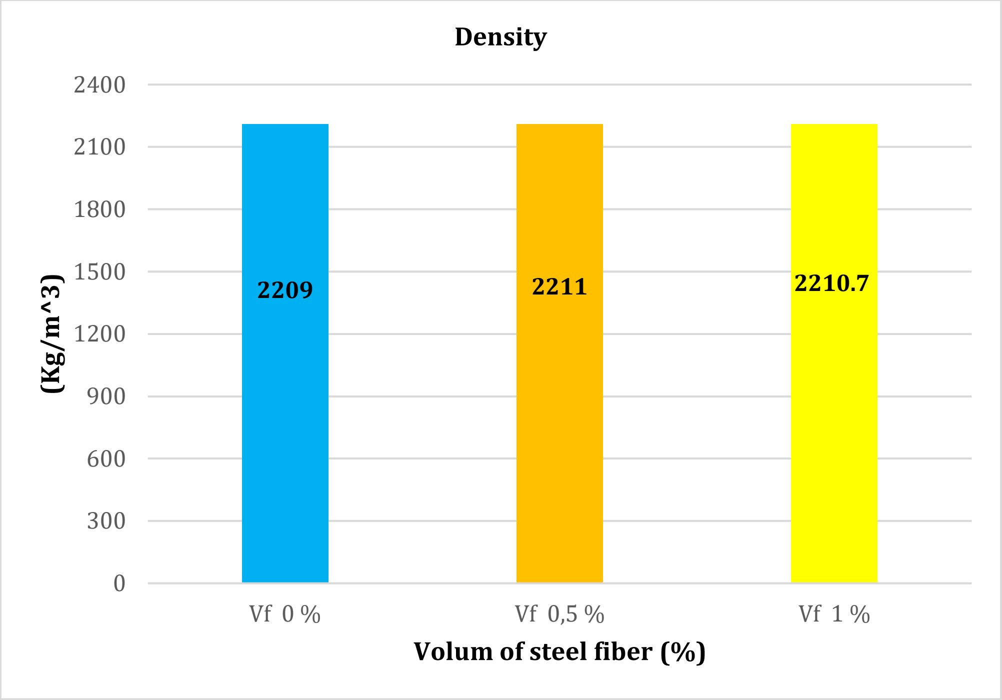
Density
2400
2100
1800
1500
1200
900
600
300
0
(Kg/m^3)
2209
2211
2210.7
Vf 0 %
Vf 0,5 %
Vf 1 %
Volum of steel fiber (%)

LABORATORIEBETONG-UHPC

Data: 29.03.2019
Navn: Perooz & Haidar
Støpe .Nr: F1 (0% fiber)

Delmateriale	**kg/m³**	**Oppmålt masse g/ 50 L betong**		Kommentar:
Microsilica	181,930	9,096		
Sement	727,709	36,385		
Filler (2,8 % fuktet)	1237,099	61,855		
Vann	144,380	7,219		
SP	72,770	3,638		
Stålfiber	0,0	0,0		

Prøvestykker	**Antall**	**Harderegime** 90°C	**Antall**	**Harderegime 45°C**	**Antall**	**Harderegime 20°C**	**Antall**
Terning	6	x	3			x	3
Sylinder							
Prismer	3 små					x	3
Bjelker	1					x	1

Fersk betong , kontrolldata

Start blanding kl	**Slutt blanding kl**	**Temperatur (°C) Start**		**Temperatur (°C) Slutt**		**RF (%)**
		Luft	Betong	Luft	Betong	
09^{15}	09^{45}	22		22	27,6	

Flyt utan energi (mm)		**Flyt med energi (mm)**		**Fersk densitet**			**Luft (%)**
Diameter 1	Diameter 2	Diameter 1	Diameter 2	Masse beholder (g)	Masse m/betong (g)	Densitet (Kg/m3)	
12,3	13	15,6	15,7	4678,2	22252,4	2196,8	4,8

90°C Herding		**45°C Herding**		**20°C Herding**	
Start Herderegime kl	Avsluttet Herderegim kl	Start Herderegime kl	Avsluttet Herderegim kl	Start Herderegime kl	Avsluttet Herderegim kl
13^{00} / 31.03.19	13^{00} / 03.04.19			13^{00} /31.03.19	13^{00} /12.04.19

Herdetbetong,kontrolldatap

Test (Trykkfasthet ,bøyestrekkfasth, skjær, E-modul)	**Prøvedato**	**Prøvestykke type** (terning ,prisme, sylinder, bjelke)	**Nummer**	**Alder** (Døgn)	**Harderegime** (90°C, 45°C,20°C)	**Vekt i luft (g)**	**Vekt i vann (g)**	**Densitet (Kg/m³)**	**Bruddlast (kN)**	**Fasthet (MPa)**
trykkfasthet	12.04.19	Terning	1	14 døgn	20°C	2206,9	1230,5	2255,7	1077,8	107,8
trykk	12.04.19	Terning	2	14 døgn	20°C	2195,3	1221	2255,7	1084,4	108,4
trykk	12.04.19	Terning	3	14 døgn	20°C	2200,1	1224	2249,5	1094,6	109,5
Bøyestrekkfasthet	12.04.19	Prisme	1	14 døgn	20°C	561,9	314,5	2263,9	5,31	12,4
Bøyestrekkfasthet	12.04.19	Prisme	2	14 døgn	20°C	566,2	318.2	2278,5	5,59	13,1
Bøyestrekkfasthet	12.04.19	Prisme	3	14 døgn	20°C	564,1	317	2278,3	5,1	12,1
trykk	12.04.19	Terning	1	14 døgn	3 dag 90°C /res 20°C	2225,6	1240	2253,7	1409,3	140,9
trykk	12.04.19	Terning	2	14 døgn	3 dag 90°C /res 20°C	2223,7	1239	2253,7	1439,9	144
trykk	12.04.19	Terning	3	14 døgn	3 dag 90°C /res 20°C	2191,5	1222	2255,9	1332,2	133,2

LABORATORIEBETONG-UHPC

Data: 02.04.2019

Navn: Perooz & Haidar

Støpe .Nr: F2 (0% fiber)

Delmateriale	kg/m³	Oppmålt masse g/ 65 L betong		Kommentar:
Microsilica	181,93	11,825		
Sement	727,709	47,301		
Filler (2,8 % fuktet)	1237,099	80,411		
Vann	144,380	9,385		
SP	72,770	4,730		
Stålfiber	0,0	0,0		

Prøvestykker	Antall	Harderegime 90°C	Antall	Harderegime 45°C	Antall	Harderegime 20°C	Antall
Terning	3	x	3				
Sylinder	6					x	6
Prismer	3					x	3
Bjelker							

Fersk betong , kontrolldata

Start blanding kl	Slutt blanding kl	Temperatur (°C) Start		Temperatur (°C) Slutt		RF (%)
		Luft	Betong	Luft	Betong	
08^{35}	09^{00}					

Flyt utan energi (mm)		Flyt med energi (mm)		Fersk densitet			Luft (%)
Diameter 1	Diameter 2	Diameter 1	Diameter 2	Masse beholder (g)	Masse m/betong (g)	Densitet (Kg/m3)	
15,2	13,9	16	16,6	4680,4	22352,2	2209	4,5

90°C Herding		45°C Herding		20°C Herding	
Start Herderegime kl	Avsluttet Herderegim kl	Start Herderegime kl	Avsluttet Herderegim kl	Start Herderegime kl	Avsluttet Herderegim kl
12^{00} / 04.04.19	12^{00} / 07.04.19			12^{00} / 04.04.19	12^{00} / 30.04.19

Herdetbetong,kontrolldatap

Test (Trykkfasthet ,bøyestrekkfasth, skjær, E-modul)	Prøvedato	Prøvestykke type (terning ,prisme, sylinder, bjelke)	Nummer	Alder (Døgn)	Harderegime (90°C, 45°C,20°C)	Vekt i luft (g)	Vekt i vann (g)	Densitet (Kg/m³)	Bruddlast (kN)	Fasthet (MPa)
trykk	16.04.19	Terning	1	14 døgn	3 dag 90°C /res 20°C	2194,5	1213,6	2232,8	1362,8	136,3
trykk	16.04.19	Terning	2	14 døgn	3 dag 90°C /res 20°C	2178,8	1201,6	2225,2	1382,4	138,2
trykk	16.04.19	Terning	3	14 døgn	3 dag 90°C /res 20°C	2182,9	1207,5	2233,5	1251,7	125,2
trykk	16.04.19	sylinder	1	14 døgn	20°C	3378,2	1860	2220,7	388,7	49,5
trykk	16.04.19	sylinder	2	14 døgn	20°C	3382,5	1863	2221,6	810,9	103,2
trykk	16.04.19	sylinder	3	14 døgn	20°C	3365,6	1859	2225,0	769,3	98,0
trykk	30.04.19	sylinder	1	28 døgn	20°C	3394,8	1870	2221,9	790,5	100,6
trykk	30.04.19	sylinder	2	28 døgn	20°C	3400,3	1873	2221,9	879,5	112,0
trykk	30.04.19	sylinder	3	28 døgn	20°C	3403,4	1872	2218,0	590,1	75,1

LABORATORIEBETONG-UHPC

Data: 29.03.2019

Navn: Perooz & Haidar

Støpe .Nr: G1 (0,5 % fiber)

Delmateriale	**kg/m³**	**Oppmålt masse g/ 50 L betong**		Kommentar:
Microsilica	181,02	9,051		
Sement	724,071	36,204		
Filler (2,8 % fuktet)	1230,913	61,546		
Vann	143,658	7,183		
SP	72,406	3,620		
Stålfiber	39	0,0		

Prøvestykker	**Antall**	**Harderegime** 90°C	**Antall**	**Harderegime 45°C**	**Antall**	**Harderegime 20°C**	**Antall**
Terning	6	x	3			x	3
Sylinder							
Prismer	3 små					x	3
Bjelker	1					x	1

Fersk betong , kontrolldata

Start blanding kl	**Slutt blanding kl**	**Temperatur (°C) Start**		**Temperatur (°C) Slutt**		**RF (%)**
		Luft	Betong	Luft	Betong	
10^{25}	10^{55}	23		22	27,6	

Flyt utan energi (mm)		**Flyt med energi (mm)**		**Fersk densitet**			**Luft (%)**
Diameter 1	Diameter 2	Diameter 1	Diameter 2	Masse beholder (g)	Masse m/betong (g)	Densitet (Kg/m3)	
16,2	17,9	20	21,7	4676,8	22738,4	2257,7	4,5

90°C Herding		**45°C Herding**		**20°C Herding**	
Start Herderegime kl	Avsluttet Herderegim kl	Start Herderegime kl	Avsluttet Herderegim kl	Start Herderegime kl	Avsluttet Herderegim kl
13^{00} / 31.03.19	13^{00} / 03.04.19			13^{00} /31.03.19	13^{00} /12.04.19

Herdetbetong,kontrolldatap

Test (Trykkfasthet ,bøyestrekkfasth, skjær, E-modul)	**Prøvedato**	**Prøvestykke type** (terning ,prisme, sylinder, bjelke)	**Nummer**	**Alder** (Døgn)	**Harderegime** (90°C, 45°C,20°C)	**Vekt i luft (g)**	**Vekt i vann (g)**	**Densitet (Kg/m³)**	**Bruddlast (kN)**	**Fasthet (MPa)**
trykkfasthet	12.04.19	Terning	1	14 døgn	20°C	2243,2	1261	2279,3	1060,5	106,1
trykk	12.04.19	Terning	2	14 døgn	20°C	2239,7	1255	2270,0	1066,3	106,3
trykk	12.04.19	Terning	3	14 døgn	20°C	2254,9	1268	2280,3	1136,9	113,7
Bøyestrekkfasthet	12.04.19	Prisme	1	14 døgn	20°C	570,8	323	2298,9	5,5	12,9
Bøyestrekkfasthet	12.04.19	Prisme	2	14 døgn	20°C	567,2	320	2289,9	5,14	12
Bøyestrekkfasthet	12.04.19	Prisme	3	14 døgn	20°C	564,1	319,7	2303,5	5,0	11,7
trykk	12.04.19	Terning	1	14 døgn	3 dag 90°C /res 20°C	2246	1265	2284,9	1506,2	150,6
trykk	12.04.19	Terning	2	14 døgn	3 dag 90°C /res 20°C	2246	1264	2282,6	1514,7	151,5
trykk	12.04.19	Terning	3	14 døgn	3 dag 90°C /res 20°C	2221,4	1251	2284,6	1415,9	141,6

LABORATORIEBETONG-UHPC

Data: 02.04.2019

Navn: Perooz & Haidar

Støpe .Nr: G2 (0,5% fiber)

Delmateriale	**kg/m³**	**Oppmålt masse g/ 65 L betong**
Microsilica	181,02	11,766
Sement	724,071	47,065
Filler (2,8 % fuktet)	1230,913	80,009
Vann	143,658	9,338
SP	72,406	4,706
Stålfiber	39,0	2,535

Kommentar:

Prøvestykker	**Antall**	**Harderegime** 90°C	**Antall**	**Harderegime 45°C**	**Antall**	**Harderegime 20°C**	**Antall**
Terning	3	x	3				
Sylinder	6					x	6
Prismer	3					x	3
Bjelker							

Fersk betong , kontrolldata

Start blanding kl	**Slutt blanding kl**	**Temperatur (°C) Start**		**Temperatur (°C) Slutt**		**RF (%)**
		Luft	Betong	Luft	Betong	
10^{30}	11^{00}					

Flyt utan energi (mm)		**Flyt med energi (mm)**		**Fersk densitet**			**Luft (%)**
Diameter 1	Diameter 2	Diameter 1	Diameter 2	Masse beholder (g)	Masse m/betong (g)	Densitet (Kg/m3)	
16,6	15,2	19,6	20,2	4553,8	22355,3	2211,4	3

90°C Herding		**45°C Herding**		**20°C Herding**	
Start Herderegime kl	Avsluttet Herderegim kl	Start Herderegime kl	Avsluttet Herderegim kl	Start Herderegime kl	Avsluttet Herderegim kl
12^{00} / 04.04.19	12^{00} / 07.04.19			12^{00} / 04.04.19	12^{00} / 30.04.19

Herdetbetong,kontrolldatap

Test (Trykkfasthet ,bøyestrekkfasth, skjær, E-modul)	**Prøvedato**	**Prøvestykke type** (terning ,prisme, sylinder, bjelke)	**Nummer**	**Alder** (Døgn)	**Harderegime** (90°C, 45°C,20°C)	**Vekt i luft (g)**	**Vekt i vann (g)**	**Densitet (Kg/m³)**	**Bruddlast (kN)**	**Fasthet (MPa)**
trykk	16.04.19	Terning	1	14 døgn	3 dag 90°C /res 20°C	2200	1234,3	2273,6	1361,8	136,2
trykk	16.04.19	Terning	2	14 døgn	3 dag 90°C /res 20°C	2180,3	1225,1	2278,0	1463,3	146,3
trykk	16.04.19	Terning	3	14 døgn	3 dag 90°C /res 20°C	2200	1233,1	2270,8	1414	141,4
trykk	16.04.19	sylinder	1	14 døgn	20°C	3421,3	1916	2268,3	805,8	102,6
trykk	16.04.19	sylinder	2	14 døgn	20°C	3383,9	1898	2272,8	837,8	106,7
trykk	16.04.19	sylinder	3	14 døgn	20°C	3398,9	1900	2263,1	880,7	112,1
trykk	30.04.19	sylinder	1	28 døgn	20°C	3420,6	1916	2268,9	893	113,7
trykk	30.04.19	sylinder	2	28 døgn	20°C	3395,4	1901	2267,5	906,5	115,4
trykk	30.04.19	sylinder	3	28 døgn	20°C	3400,1	1896	2257,5	977,6	124,5

LABORATORIEBETONG-UHPC

Data: **29.03.2019**

Navn: **Perooz & Haidar**

Støpe .Nr: **H1 (1 % fiber)**

Delmateriale	**kg/m³**	**Oppmålt masse g/ 50 L betong**		Kommentar:
Microsilica	180,111	9,006		
Sement	720,432	36,022		
Filler (2,8 % fuktet)	1224,728	61,236		
Vann	142,936	7,147		
SP	72,024	3,602		
Stålfiber	78	3,90		

Prøvestykker	**Antall**	**Harderegime 90°C**	**Antall**	**Harderegime 45°C**	**Antall**	**Harderegime 20°C**	**Antall**
Terning	6	x	3			x	3
Sylinder							
Prismer	3 små					x	3
Bjelker	1					x	1

Fersk betong , kontrolldata

Start blanding kl	**Slutt blanding kl**	**Temperatur (°C) Start**		**Temperatur (°C) Slutt**		**RF (%)**
		Luft	Betong	Luft	Betong	
11^{30}	12^{00}	23		23,3	27	

Flyt utan energi (mm)		**Flyt med energi (mm)**		**Fersk densitet**			**Luft (%)**
Diameter 1	Diameter 2	Diameter 1	Diameter 2	Masse beholder (g)	Masse m/betong (g)	Densitet (Kg/m3)	
16	18,2	19,1	21,1	4685,4	23089,4	2300,5	3,3

90°C Herding		**45°C Herding**		**20°C Herding**	
Start Herderegime kl	Avsluttet Herderegim kl	Start Herderegime kl	Avsluttet Herderegim kl	Start Herderegime kl	Avsluttet Herderegim kl
13^{00} / 31.03.19	13^{00} / 03.04.19			13^{00} /31.03.19	13^{00} /12.04.19

Herdetbetong,kontrolldatap

Test (Trykkfasthet ,bøyestrekkfasth, skjær, E-modul)	**Prøvedato**	**Prøvestykke type** (terning ,prisme, sylinder, bjelke)	**Nummer**	**Alder** (Døgn)	**Harderegime** (90°C, 45°C,20°C)	**Vekt i luft (g)**	**Vekt i vann (g)**	**Densitet (Kg/m³)**	**Bruddlast (kN)**	**Fasthet (MPa)**
trykkfasthet	12.04.19	Terning	1	14 døgn	20°C	2245,9	1278	2315,7	1108,4	110,8
trykk	12.04.19	Terning	2	14 døgn	20°C	2301,0	1305	2305,6	9729	97,3
trykk	12.04.19	Terning	3	14 døgn	20°C	2281.2	1296	2310,8	1124,2	112,4
Bøyestrekkfasthet	12.04.19	Prisme	1	14 døgn	20°C	569,2	325	2326,2	5,83	13,7
Bøyestrekkfasthet	12.04.19	Prisme	2	14 døgn	20°C	575,9	328	2318,5	5,93	13,9
Bøyestrekkfasthet	12.04.19	Prisme	3	14 døgn	20°C	583,8	313,2	2153,1	4,9	11,6
trykk	12.04.19	Terning	1	14 døgn	3 dag 90°C /res 20°C	2273,5	1290	2307	1481,4	148,1
trykk	12.04.19	Terning	2	14 døgn	3 dag 90°C /res 20°C	2277,8	1292	2306	1469,9	147
trykk	12.04.19	Terning	3	14 døgn	3 dag 90°C /res 20°C	2292,4	1304	2314,7	1542,9	154,3

LABORATORIEBETONG-UHPC

Data: 02.04.2019
Navn: Perooz & Haidar
Støpe .Nr: H2 (1% fiber)

Delmateriale	kg/m³	Oppmålt masse g/ 65 L betong		Kommentar:
Microsilica	181,111	11,707		
Sement	720,432	46,828		
Filler (2,8 % fuktet)	1224,728	79,607		
Vann	142,936	9,291		
SP	72,042	4,683		
Stålfiber	78	5,070		

Prøvestykker	Antall	Harderegime 90°C	Antall	Harderegime 45°C	Antall	Harderegime 20°C	Antall
Terning	3	x	3				
Sylinder	6					x	6
Prismer	3					x	3
Bjelker							

Fersk betong , kontrolldata

Start blanding kl	Slutt blanding kl	Temperatur (°C) Start		Temperatur (°C) Slutt		RF (%)
		Luft	Betong	Luft	Betong	
11^{40}	12^{15}					

Flyt utan energi (mm)		Flyt med energi (mm)		Fersk densitet			Luft (%)
Diameter 1	Diameter 2	Diameter 1	Diameter 2	Masse beholder (g)	Masse m/betong (g)	Densitet (Kg/m3)	
17	17,5	19,9	19,8	4700	22385,2	2210,7	4,25

90°C Herding		45°C Herding		20°C Herding	
Start Herderegime kl	Avsluttet Herderegim kl	Start Herderegime kl	Avsluttet Herderegim kl	Start Herderegime kl	Avsluttet Herderegim kl
12^{00} / 04.04.19	12^{00} / 07.04.19			12^{00} / 04.04.19	12^{00} / 30.04.19

Herdetbetong,kontrolldatap

Test (Trykkfasthet ,bøyestrekkfasth, skjær, E-modul)	Prøvedato	Prøvestykke type (terning ,prisme, sylinder, bjelke)	Nummer	Alder (Døgn)	Harderegime (90°C, 45°C,20°C)	Vekt i luft (g)	Vekt i vann (g)	Densitet (Kg/m³)	Bruddlast (kN)	Fasthet (MPa)
trykk	16.04.19	Terning	1	14 døgn	3 dag 90°C /res 20°C	2252,6	1273,2	2295,4	1372	137,2
trykk	16.04.19	Terning	2	14 døgn	3 dag 90°C /res 20°C	2272,6	1281	2287,3	1470,41	147
trykk	16.04.19	Terning	3	14 døgn	3 dag 90°C /res 20°C	2258,6	1279	2301	1457,5	145,8
trykk	16.04.19	sylinder	1	14 døgn	20°C	3449,8	1962	2314,1	866,6	84,9
trykk	16.04.19	sylinder	2	14 døgn	20°C	3466,3	1958	2292,3	848,2	108
trykk	16.04.19	sylinder	3	14 døgn	20°C	3458,9	1953	2292,3	810,4	103,2
trykk	30.04.19	sylinder	1	28 døgn	20°C	3457,2	1952	2292,2	865,5	110,2
trykk	30.04.19	sylinder	2	28 døgn	20°C	3462,9	1948	2281,3	928,8	118,3
trykk	30.04.19	sylinder	3	28 døgn	20°C	3458,9	1941	2287,2	914,8	116,5

LABORATORIEBETONG-UHPC

Data: **30.04.2019**

Navn: **Perooz & Haidar**

Støpe .Nr: **I1 (0% fiber)**

Delmateriale	kg/m³	Oppmålt masse g/ 25 L betong		Kommentar:
Microsilica	181,930	4,548		
Sement	727,709	18,193		
Filler (2,8 % fuktet)	1237,099	30,927		
Vann	144,380	3,609		
SP	72,770	1,819		
Stålfiber	0,0	0,0		

Prøvestykker	Antall	Harderegime 90°C	Antall	Harderegime 45°C	Antall	Harderegime 20°C	Antall
Terning							
Sylinder	12	x	6			x	6
Prismer							
Bjelker							

Fersk betong , kontrolldata

Start blanding kl	Slutt blanding kl	Temperatur (°C) Start		Temperatur (°C) Slutt		RF (%)
		Luft	Betong	Luft	Betong	
08^{35}	09^{00}					

Flyt utan energi (mm)		Flyt med energi (mm)		Fersk densitet			Luft (%)
Diameter 1	Diameter 2	Diameter 1	Diameter 2	Masse beholder (g)	Masse m/betong (g)	Densitet (Kg/m3)	
14,5	16,7	16,5	17,8	4644,6	22215	2196,3	5,6

90°C Herding		45°C Herding		20°C Herding	
Start Herderegime kl	Avsluttet Herderegim kl	Start Herderegime kl	Avsluttet Herderegim kl	Start Herderegime kl	Avsluttet Herderegim kl
13^{00} / 02.05.19	13^{00} / 05.05.19			13^{00} /02.05.19	13^{00} /14.05.19

Herdetbetong,kontrolldatap

Test (Trykkfasthet ,bøyestrekkfasth, skjær, E-modul)	Prøvedato	Prøvestykke type (terning ,prisme, sylinder, bjelke)	Nummer	Alder (Døgn)	Harderegime (90°C, 45°C,20°C)	Vekt i luft (g)	Vekt i vann (g)	Densitet (Kg/m³)	Bruddlast (kN)		Fasthet (MPa)
trykk	14.05.19	Sylinder	1	14 døgn	3 dag 90°C /res 20°C	3383	1877	2241,9	1203,1		152
trykk	14.05.19	Sylinder	2	14 døgn	3 dag 90°C /res 20°C	3370,4	1875	2249,7	1154		146,5
trykk	14.05.19	Sylinder	3	14 døgn	3 dag 90°C /res 20°C	3369,9	1885	2264,9	1204,5		153,4
trykk	14.05.19	Sylinder	1	14 døgn	20°C	3356,1	1873	2258,4	879,3		112
trykk	14.05.19	Sylinder	2	14 døgn	20°C	3373,1	1885	2262,2	-		-
trykk	14.05.19	Sylinder	3	14 døgn	20°C	3358,3	1876	2261,1	751,8		97,5
									Spenning (MPa)	Tøyning (_%)	E-modul (Gpa)
E-modul	14.05.19	Sylinder	1	14 døgn	20°C	3339	1872	2271,5	16,66	0,044	38,529
E-modul	14.05.19	Sylinder	2	14 døgn	20°C	3341	1865	2259	16,66	0,043	38,856
E-modul	14.05.19	Sylinder	3	14 døgn	20°C	3353	1859	2239,8	16,67	0,043	39,48
E-modul	14.05.19	Sylinder	1	14 døgn	3 dag 90°C /res 20°C	3383,2	1894	2263,9	16,66	0,041	42,957
E-modul	14.05.19	Sylinder	2	14 døgn	3 dag 90°C /res 20°C	3395	1884	2242,4	16,67	0,041	42,184
E-modul	14.05.19	Sylinder	3	14 døgn	3 dag 90°C /res 20°C	3396,7	1900	2264,9	16,66	0,041	42,369

LABORATORIEBETONG-UHPC

Data:	**30.04.2019**
Navn:	**Perooz & Haidar**
Støpe .Nr:	**J1 (0,5 % fiber)**

Delmateriale	**kg/m³**	**Oppmålt masse g/ 25 L betong**
Microsilica	181,020	4,526
Sement	724,071	18,102
Filler (2,8 % fuktet)	1230,913	30,773
Vann	143,658	3,591
SP	72,406	1,810
Stålfiber	39,00	0,975

Kommentar:

Prøvestykker	**Antall**	**Harderegime 90°C**	**Antall**	**Harderegime 45°C**	**Antall**	**Harderegime 20°C**	**Antall**
Terning							
Sylinder	12	x	6			x	6
Prismer							
Bjelker							

Fersk betong , kontrolldata

Start blanding kl	**Slutt blanding kl**	**Temperatur (°C) Start**		**Temperatur (°C) Slutt**		**RF (%)**
		Luft	Betong	Luft	Betong	
09^{30}	10^{05}					

Flyt utan energi (mm)		**Flyt med energi (mm)**		**Fersk densitet**			**Luft (%)**
Diameter 1	Diameter 2	Diameter 1	Diameter 2	Masse beholder (g)	Masse m/betong (g)	Densitet (Kg/m3)	
12,5	13,5	15,5	16,2	4650,4	22519,4	2233,6	5

90°C Herding		**45°C Herding**		**20°C Herding**	
Start Herderegime kl	Avsluttet Herderegim kl	Start Herderegime kl	Avsluttet Herderegim kl	Start Herderegime kl	Avsluttet Herderegim kl
13^{00} / 02.05.19	13^{00} / 05.05.19			13^{00} /02.05.19	13^{00} /14.05.19

Herdetbetong,kontrolldatap

Test (Trykkfasthet,bøy estrekkfasth, skjær, E-modul)	**Prøvedato**	**Prøvestykke type** (terning ,prisme, sylinder, bjelke)	**Nummer**	**Alder** (Døgn)	**Harderegime** (90°C, 45°C,20°C)	**Vekt i luft (g)**	**Vekt i vann (g)**	**Densitet (Kg/m³)**	**Bruddlast (kN)**		**Fasthet (MPa)**
trykk	14.05.19	Sylinder	1	14 døgn	3 dag 90°C /res 20°C	3488,1	1974,3	2299,6	1100,4		140,1
trykk	14.05.19	Sylinder	2	14 døgn	3 dag 90°C /res 20°C	3479,5	1963,8	2291	1247		158,8
trykk	14.05.19	Sylinder	3	14 døgn	3 dag 90°C /res 20°C	3470,4	1953	2282,5	1158,4		147,5
trykk	14.05.19	Sylinder	1	14 døgn	20°C	3489,7	1958	2273,8	835		106,3
trykk	14.05.19	Sylinder	2	14 døgn	20°C	3462,4	1948	2281,7	740,1		94,2
trykk	14.05.19	Sylinder	3	14 døgn	20°C	3441	1938	2284,8	858,7		109,3
									Spenning (MPa)	Tøyning (%)	E-modul (GPa)
E-modul	14.05.19	Sylinder	1	14 døgn	20°C	3453	1949	2291,3	16,67	0,045	38,268
E-modul	14.05.19	Sylinder	2	14 døgn	20°C	3484	1955	2274,1	16,66	0,044	38,327
E-modul	14.05.19	Sylinder	3	14 døgn	20°C	3476,5	1954	2278,8	16,67	0,045	38,534
E-modul	14.05.19	Sylinder	1	14 døgn	3 dag 90°C /res 20°C	3482,4	1964	2288,9	16,67	0,041	42,028
E-modul	14.05.19	Sylinder	2	14 døgn	3 dag 90°C /res 20°C	3402,3	1907	2270,8	16,67	0,041	41,455
E-modul	14.05.19	Sylinder	3	14 døgn	3 dag 90°C /res 20°C	3430,8	1925	2273,8	16,66	0,041	42,107

LABORATORIEBETONG-UHPC

Data: **30.04.2019**
Navn: **Perooz & Haidar**
Støpe .Nr: **K1 (1 % fiber)**

Delmateriale	kg/m³	Oppmålt masse g/ 25 L betong
Microsilica	180,111	4,503
Sement	720,432	18,011
Filler (2,8 % fuktet)	1224,728	30,618
Vann	142,936	3,573
SP	72,042	1,801
Stålfiber	78,00	1,950

Kommentar:

Prøvestykker	Antall	Harderegime 90°C	Antall	Harderegime 45°C	Antall	Harderegime 20°C	Antall
Terning							
Sylinder	12	x	6			x	6
Prismer							
Bjelker							

Fersk betong , kontrolldata

Start blanding kl	Slutt blanding kl	Temperatur (°C) Start		Temperatur (°C) Slutt		RF (%)
		Luft	Betong	Luft	Betong	
10^{30}	11^{05}					

Flyt utan energi (mm)		Flyt med energi (mm)		Fersk densitet			Luft (%)
Diameter 1	Diameter 2	Diameter 1	Diameter 2	Masse beholder (g)	Masse m/betong (g)	Densitet (Kg/m3)	
11	10,6	13,2	13,2	4648	22786	2267,3	5,1

90°C Herding		45°C Herding		20°C Herding	
Start Herderegime kl	Avsluttet Herderegim kl	Start Herderegime kl	Avsluttet Herderegim kl	Start Herderegime kl	Avsluttet Herderegim kl
13^{00} / 02.05.19	13^{00} / 05.05.19			13^{00} /02.05.19	13^{00} /14.05.19

Herdetbetong,kontrolldatap

Test (Trykkfasthet ,bøyestrekkfasth, skjær, E-modul)	Prøvedato	Prøvestykke type (terning ,prisme, sylinder, bjelke)	Nummer	Alder (Døgn)	Harderegime (90°C, 45°C,20°C)	Vekt i luft (g)	Vekt i vann (g)	Densitet (Kg/m³)	Bruddlast (kN)		Fasthet (MPa)
trykk	14.05.19	Sylinder	1	14 døgn	3 dag 90°C /res 20°C	3492,3	1981,9	2307,5	1101		140,2
trykk	14.05.19	Sylinder	2	14 døgn	3 dag 90°C /res 20°C	3490,2	1978	2303,4	1108,2		141,1
trykk	14.05.19	Sylinder	3	14 døgn	3 dag 90°C /res 20°C	3439,8	1949	2302,7	1172,2		149,2
trykk	14.05.19	Sylinder	1	14 døgn	20°C	3475,3	1975	2311,8	847,2		107,9
trykk	14.05.19	Sylinder	2	14 døgn	20°C	3464,4	1967	2309,0	801,7		102,1
trykk	14.05.19	Sylinder	3	14 døgn	20°C	3479,2	1973	2305,3	857,8		109,2
									Spenning (MPa)	Tøyning (%)	E-modul (GPa)
E-modul	14.05.19	Sylinder	1	14 døgn	20°C	3475,8	1965	2296	16,66	0,042	39,393
E-modul	14.05.19	Sylinder	2	14 døgn	20°C	3433,8	1946	2303,4	16,67	0,043	39,067
E-modul	14.05.19	Sylinder	3	14 døgn	20°C	3469,9	1966	2302,7	16,67	0,06	38,923

E-modul	14.05.19	Sylinder	1	14 døgn	3 dag 90°C /res 20°C	3472,8	1969	2304,7	16,67	0,040	41,143
E-modul	14.05.19	Sylinder	2	14 døgn	3 dag 90°C /res 20°C	3493	1984	2310,1	16,66	0,039	42,498
E-modul	14.05.19	Sylinder	3	14 døgn	3 dag 90°C /res 20°C	3488,4	1981	2309,6	16,66	0,038	45,71